UC Berkeley
UC Berkeley Electronic Theses and Dissertations

Title
Novel Physical Phenomena in Oxide Superlattices

Permalink
https://escholarship.org/uc/item/916058t1

Author
Yadav, Ajay Kumar

Publication Date
2016

Peer reviewed|Thesis/dissertation

eScholarship.org Powered by the California Digital Library
University of California

Novel Physical Phenomena in Oxide Superlattices

by

Ajay Kumar Yadav

A dissertation submitted in partial satisfaction of the

requirements for the degree of

Doctor of Philosophy

in

Engineering – Materials Science and Engineering

in the

Graduate Division

of the

University of California, Berkeley

Committee in charge:

Professor Ramamoorthy Ramesh, Chair
Professor Oscar Dubon
Professor Joel E. Moore

Spring 2016

Novel Physical Phenomena in Oxide Superlattices

Copyright 2016

by

Ajay Kumar Yadav

Abstract

Novel Physical Phenomena in Oxide Superlattices

by

Ajay Kumar Yadav

Doctor of Philosophy in Materials Science and Engineering

University of California, Berkeley

Professor Ramamoorthy Ramesh, Chair

It is historically proven that artificial heterostructures are of paramount importance for both fundamental research and technological application. One distinguishable example is superlattices and quantum-well heterostructures of conventional semiconductors (III-V). Several fundamental observations such as two-dimensional electron gas, quantum confinement effect, quantum Hall effect and fractional quantum Hall effect, were first realized in artificial heterostructures of conventional semiconductors. On the technological front, artificial heterostructures of conventional semiconductors were found to revolutionize optoelectronic and high-speed electronic industry. Given the capability of artificial heterostructures to enable new physical phenomena, with an appropriate choice of material system, these heterostructures hold the potential to uncover hidden physical phenomena and exotic phases, which are otherwise not observed in bulk systems. One choice of such a system could be a strongly correlated material where the presence of strong electronic correlations has been known to enable unique electronic and magnetic properties. Complex oxides, in particular, are known to exhibit a strong interaction between various degrees of freedom available such as spin, charge, orbital and lattice degree, and thus offer a suitable choice of material system. In literature, one can find plenty of examples from different areas of research such as superconductivity, magnetism, ferroelectricity and thermoelectricity, where artificial superlattices led to the observation of fundamentally different behavior, compared to bulk superlattice constituents. These artificial superlattices and heterostructures continue to be the most promising candidate for exploring new phenomena and enhancing physical properties in complex oxide material systems. In this dissertation, artificial superlattices of complex oxides were synthesized in a thin-film geometry to enable the observation of fundamentally new physical phenomena, compared to their bulk counterparts, in few selected areas of investigation.

First, I will present the experimental results on heat transport across superlattice structures composed of insulating perovskite oxides. The measured thermal conductivity of these artificial superlattices exhibited a unique phonon transport, *i.e.* coherent phonon transport, phenomenon that is extremely rare to observe in bulk form. The key element for

enabling the coherent transport of phonon in these superlattice systems is the range of phonon wavelengths, which carry most of the heat in the material. The critical range being between 1-3 nanometers, the size of the system needs to reduce to this length scale in order to observe the effect of the wave nature of phonons on heat transport. Thus, superlattice structures offer an ideal candidate to search for this novel phenomenon. Several theoretical studies predicted the existence of these phenomena, but the experimental evidence of their existence remained largely absent or inconclusive. By synthesizing the superlattice of perovskite oxides, I've observed unambiguous evidence of the coherent transport of phonons at short-period superlattices of $SrTiO_3$-$CaTiO_3$ and $BaTiO_3$-$SrTiO_3$. In contrast to conventional heat conduction mechanisms, where phonon transport can be described by energy-carrying particles, the uniqueness of this phenomenon is highlighted by the fact that the wave aspect of phonons needs to be invoked to understand their transport behavior. After observing the wave nature of phonons in dictating heat conduction across periodic superlattices, other artificial heterostructures were studied to understand the nature of coherent phonon transport at the superlattice interfaces. Designed superlattice-like sequences, where the structural order can be controlled from a periodic sequence to a completely random sequence, were synthesized to further understand the role of the coherent scattering of phonons in thermal transport across superlattice structures.

Next, I will discuss the experimental observation of another unique phenomenon, which was enabled by artificial superlattices of complex oxides in a different subject of research, *i.e.* ferroelectricity. Several theoretical studies on nanostructured ferroelectric systems such as nanodisc, nanocomposites, superlattices *etc.*, predicted the stabilization of novel ferroelectric ground states. A number of different topologies of electrical polarization such as vortices and skyrmions, were predicted in ferroelectric nanostructures, which showed a strong resemblance to spin topologies such as skyrmion, merons *etc.* found in magnetic systems. Experimental confirmation for the existence of these exotic polarization states, however, remained absent. By leveraging the competition among charge, orbital and lattice degrees of freedom in superlattices of a paraelectric ($SrTiO_3$) and ferroelectric ($PbTiO_3$) material, vortex-antivortex structures of electrical polarization were stabilized in ferroelectric ($PbTiO_3$) layers of $PbTiO_3$-$SrTiO_3$ superlattice. Only for a narrow range of superlattice periods, the polarization vortices are stabilized with a balance between one gradient energy associated with the non-uniform polarization profile of the vortex structure and the other's electrostatic and elastic energies associated with depolarization fields and epitaxial constraints from the substrate, respectively.

In the last section, I will describe unique and unusual phenomena associated with the existence of polarization vortices in paraelectric/ferroelectric superlattices. Superlattices of $PbTiO_3$-$SrTiO_3$ with varying periodicity showed a rich spectrum of characteristically different ferroelectric domains. Specifically, in the short-period regime, domain size was observed to evolve with a negative scaling coefficient, which is unusual for typical ferroelectrics. When the superlattice periodicity was increased, the average domain size decreased, suggesting an opposite behavior to the universal Kittel's Law, where in the latter, an increase in ferroelectric thickness leads to an increase in the average domain size. Second, I will present intriguing results on the fundamental characteristics of polarization vortices as revealed from X-ray circular dichroism studies. The finite

difference in absorption spectra of left-circular vs. right-circular polarized light from vortex structures, suggested that vortex-antivortex arrays are chiral in nature. The presence of chirality in polarization vortex structures is a characteristically different behavior compared to bulk ferroelectric systems where uniformly polarized regions are expected to exhibit a linear X-ray dichroism (*i.e.* a difference in the absorption spectra of linearly polarized light in a direction parallel and perpendicular to ferroelectric order). Lastly, a possibility of manipulating phonon dispersion using vortex ordering or vortex "lattice" is discussed, along with a hypothesis of inducing localization in propagative phonons.

To my family

Table of Contents

List of Figures v

List of Tables xvi

1 Introduction **1**
1.1 Brief History 1
1.2 Complex Oxides 4
1.2.1. Introduction 4
1.2.2. Crystallographic structure 5
1.2.3. Electronic structure 8
1.3 Superlattice structures and their Importance 15
1.3.1. Introduction 15
1.3.2. Superlattice structures 16
1.3.3. Significance of Artificial Superlattices 21
1.4 Summary 26

2 Synthesis and Characterization **27**
2.1 Synthesis 27
2.1.1. Pulsed Laser Deposition 27
2.2 Characterization Methods 29
2.2.1. *In situ* characterization: Reflection High Energy Electron Diffraction ..29
2.2.2. Laboratory-based X-ray Diffraction 36
2.2.3. Synchrotron-based X-ray Diffraction 46
2.2.4. Scanning Probe Microscopy 52
2.2.5. Transmission Electron Microscopy 59
2.2.6. Rutherford Backscattering Spectrometry 65
2.3 Thermal Conductivity measurement 67
2.4 Spectroscopic measurement 75
2.5 Summary 83

3 An overture to the Dissertation **84**
3.1 Introduction 84
3.2 Combinatorial Approach: Complex Oxides in Superlattice geometry 85
3.2.1 Employing only one degree of freedom: *Lattice* 85

3.2.2 Utilizing more than one degree of freedom: *Charge*, *Orbital* and *Lattice* 88
3.3 Organization of the dissertation 90

4 Demonstration of Coherent Phonon transport in Superlattice structures 91
4.1 Introduction 91
4.2 Theoretical predictions of Coherent Phonon transport in Superlattices 94
4.2.1 Fundamentals of Thermal Conductivity 94
4.2.1.1 Phonons 95
4.2.1.2 Heat Capacity 97
4.2.1.3 Lattice Thermal Conductivity 100
4.2.1.4 Phonon Scattering Mechanisms 103
4.2.2 Theoretical models predicting Coherent Phonon transport 108
4.3 Experimental Demonstration of Coherent Phonon Transport in Periodic Superlattices 114
4.3.1 Background 115
4.3.2 Experimental Methods 116
4.3.3 Results and Discussion 117
4.4 Role of Coherent Phonon scattering in Aperiodic Superlattices 128
4.4.1 Background 128
4.4.2 Experimental Methods 131
4.4.3 Results and Discussion 131
4.4.3.1 Measure of Disorder 140
4.4.3.2 Quasi-incoherent model 142
4.4.3.3 Coherent Effects 145
4.5 Summary and future directions 147

5 Observation of Polarization Vortices in $PbTiO_3$-$SrTiO_3$ Superlattices 150
5.1 Introduction 150
5.2 Theoretical predictions of Polarization Vortices in Ferroelectric Nanostructures 153
5.2.1 Fundamentals of Ferroelectricity 153
5.2.1.1 Definitions 153
5.2.1.2 Hysteresis Loop 155
5.2.1.3 Ferroelectric Phase Transition 157
5.2.1.4 Bulk Ferroelectrics 162
5.2.1.5 Thin-film Ferroelectrics 165
5.2.2 Theoretical models predicting Vortex structures 169
5.3 Experimental observation of Polarization Vortices in $PbTiO_3$-$SrTiO_3$ Superlattices 177
5.3.1 Background 177
5.3.2 Experimental Methods 180
5.3.3 Results and Discussion 180
5.4 Summary and future directions 196

6 Novel phenomena associated with Polarization Vortices 198
6.1 Introduction 198
6.2 Unusual ferroelectric domain evolution with Superlattice periodicity 200
6.2.1 Background 200
6.2.2 Experimental Methods 204
6.2.3 Results and Discussion 205
6.3 Emerging Chirality in Polarization Vortices 225
6.3.1 Background 225
6.3.2 Experimental Methods 226
6.3.3 Results and Discussion 226
6.4 Possibility of Phonon Localization due to Vortex *Lattice* 229
6.4.1 Background 229
6.4.2 Hypothesis 233
6.5 Summary and implications 237

7 Conclusion and future prospects 239

Bibliography 242

List of Figures

1.1 Schematic of ideal perovskite unit cell, ABO_3. 6
1.2 Common crystal symmetries found in perovskites: (a) Cubic, (b) Tetragonal, (c) Rhombohedral, and (d) Octahedral symmetry. From [39]. 8
1.3 Electronic energy levels of 'Ti' *d*-orbital. The figure also depicts the shape of d-orbitals in t_{2g} (d_{xy}, d_{yz}, d_{zx}) and e_g ($d_{3z^2-x^2}$, $d_{x^2-y^2}$) levels. Figure adapted from [28; 41]. 9
1.4 Titanium d_{xy} orbitals are depicted on neighboring Ti-sites of a cubic STO structure, illustrating a stronger hopping along *x* and *y* directions (thicker arrows) compared to *z* direction (thin arrow). Figure adapted from [28]. 10
1.5 The effect of Jahn-Teller distortion on electronic structure of Titanium *d*-orbitals. [42] 11
1.6 Orbital ordering in orthorhombic $LaMnO_3$. From [44]. 12
1.7 A schematic of super exchange interaction in $LaMnO_3$. From [30]. 13
1.8 A schematic of indirect exchange interaction in $LaMnO_3$. From [30]. 13
1.9 A schematic of various degrees of freedom present in complex oxides. Figure adapted from [27]. 15
1.10 A schematic of 3 x 3 PTO-STO superlattice. Figure adapted from [55]. 17
1.11 A schematic of various possible superlattice structures of PTO-STO, (a) 3 x 3 symmetric superlattice, (b) 2 x 5 asymmetric superlattice and (c) complex unit-cell superlattice. The repeating unit, *i.e.* superlattice period (Δ_{SL}), is also highlighted for all three-superlattice structures. 18
1.12 The crystal structure of Ruddlesen-Popper phases of $Sr_{n+1}Ti_nO_{3n+1}$ for (a) $n = 1$, (b) $n = 2$, and (c) $n = 3$ is depicted in this diagram. Figure adapted from [56]. 19
1.13 Superlattice structures of complex oxide material system are shown. Cross-section TEM of bicolor superlattice (a) PTO-STO, (b) BTO-STO, (c) LSMO-STO, and tricolor superlattice (d) CTO-BTO-STO are depicted. These figures are adapted from [59-62]. 20

2.1 A schematic of a typical Pulsed-laser Deposition chamber. From [102]. 28
2.2 A schematic of *in situ* RHEED experimental set up (adapted from [112]). Inset shows a schematic of combined assembly of RHEED with PLD chamber (Courtesy of Jeroen Huijben). 30

2.3 A schematic of formation of RHEED diffraction using Ewald's sphere construction. Along with a 3D view, a side and front view are also drawn for better illustration. Figure is adapted from [114] and [115]. 31
2.4 RHEED diffraction pattern from a TiO_2-terminated STO (001) substrate. From [114]. 32
2.5 RHEED diffraction pattern for *Volmer-Weber* growth mode (a), along with a schematic (b) is shown. Figure adapted from [114]. 32
2.6 Different stages of layer-by-layer growth monitored via RHEED. Figure adapted from [116]. 33
2.7 RHEED oscillations for homoepitaxial growth of STO on a treated-STO (001) substrate and associated schematic of surface coverage. Figure adapted from [118]. 34
2.8 A schematic of RHEED diffraction pattern for (a) orthorhombic vs. (b) cubic crystal. Figure adapted from [121]. 35
2.9 A schematic of XRD experimental set up. Adapted from [124]. 37
2.10 A schematic of symmetric XRD scan is shown in the Ewald sphere construction. The region shaded in grey encompasses reciprocal lattice points which are not accessible in the normal reflection geometry, for the given incoming wave vector $\boldsymbol{k_{in}}$. From [132]. 38
2.11 Symmetric XRD scan of 126 unit cells of CTO grown on NGO (110) substrate. 39
2.12 Symmetric XRD scan of 200 nm thick 6 x 6 STO-CTO superlattice film grown on treated-NGO (110) substrate. 40
2.13 Evolution of structural ordering in aperiodic superlattice films of STO and CTO as characterized from symmetric XRD scans. 41
2.14 A schematic of rocking curve scan is shown in (a) under Ewald sphere construction, while (b) depicts a possible scenario, which can give rise to finite broadening in the rocking curve. Figure adapted from [132]. 42
2.15 Full-width-half-maximum (FWHM) of (a) superlattice film around (002) Bragg peak, and of (b) NGO (220) substrate peak. 43
2.16 Schematic of Asymmetric XRD scan is shown in the Ewald sphere construction. The arrows in grey show the scan direction for 'Ω'-scan or '2θ - Ω' scans for a given reciprocal lattice point (205). From [132]. 44
2.17 Asymmetric scan or reciprocal space maps of 200 nm thick 9 x 9 STO-CTO superlattice grown on NGO (110) substrate around 332 reciprocal lattice peak. 45
2.18 Experimental X-ray Reflectivity measurement of 25 unit cells of STO grown on NGO (110) substrate. 46
2.19 Three dimensional (3D) Reciprocal space map around (002) reciprocal point of STO (001) substrate, for a 16 x 16 PTO-STO superlattice film grown on STO (001) substrate. Courtesy of Dr. Christian Schlepütz. 47
2.20 An LK-cut taken at H = 0 overlaid on 3D RSM (a) yielding a two-dimensional map shown in (b). 48
2.21 A HK-cut taken at L = 0.965 overlaid on 3D RSM (a) yielding a two-dimensional map shown in (b). 49

2.22 Using a HK-cut (a) obtained from a 3D RSM around (001) peak of STO (001) substrate, a line scan taken along H at K = 0 and L = 0.965 is shown intensity profile in (b). 50
2.23 An LH-cut from a 3D RSM encompassing both (001) and (002) Bragg peak of 16 x 16 PTO-STO superlattice grown on STO (001) substrate is shown. 51
2.24 A line scan taken along L direction in the LH-cut obtained from 3D RSM having both (001) and (002) peak is shown as intensity profile vs. L values. 52
2.25 A schematic of typical scanning probe microscope. Figure adapted from [152]. 53
2.26 AFM image of a treated-STO (001) substrate. Figure adapted from [153]. 54
2.27 AFM image (a) of a 200 nm thick 2 x 2 STO-CTO superlattice grown on a STO (001) substrate imaged under non-contact mode is shown along with a line scan along the atomic steps in (b) to extract the step height for these films. 55
2.28 A schematic of tip-sample interaction for the case when the sample has polar domains aligned parallel or antiparallel to out-of-plane direction, with an external voltage applied across using a conductive tip. From [157]. 56
2.29 A schematic of piezoresponse signal as a function of time when bias voltage has small AC signal embedded in it. Figure also shows schematic of domains aligned parallel or antiparallel to electric field, at different intervals of time. Figure adapted from [159]. 57
2.30 Amplitude (a) and phase (b) image of ceramic PZT sample. From [157]. 58
2.31 In-plane (a) and Out-of-plane (b) PFM image of 600 nm thick (as-grown) $BiFeO_3$ on SRO (001) buffered with conducting SRO bottom electrode. From [162]. ... 59
2.32 A schematic of a conventional transmission electron microscope. Figure adapted from [164]. 60
2.33 Cross-sectional dark-field TEM images of a 12 x 12 PTO-STO superlattice film grown on a 5 nm SRO on DSO substrate is shown for two different tilt angles (a) and (b). Courtesy of Dr. Christopher Nelson. 61
2.34 A schematic of a scanning transmission electron microscope. Figure adapted from [167]. 62
2.35 A cross-sectional atomic-resolution HAADF Z-contrast TEM image of sub region of a 16 x 16 PTO-STO superlattice film grown on 5 nm SRO on DSO (110) substrate. Courtesy of Dr. Christopher Nelson. 63
2.36 A planar view dark-field TEM of 6 x 6 PTO-STO superlattice film grown on 5 nm SRO on DSO (110) substrate. Courtesy of ShangLin Hsu. 64
2.37 Polar displacements of A-site (Pb, Sr) atoms in a 16 x 16 PTO-STO superlattice film grown on a DSO substrate, extracted from atomic-resolution Z-contract STEM image is shown in (a), whereas the components of polar displacements along *x*- and *y*-direction is shown in (b) and (c) respectively. More analysis such as mapping *c*/*a* ratio (d) of unit cell lattice constant, and curl of polar displacement (e) based on the atomic resolution STEM image can be obtained. Courtesy of Dr. Christopher Nelson. 65

2.38 Experimental RBS spectra of a 200 nm PTO film grown on a $GdScO_3$ (110) substrate is shown, along with a simulated spectrum from which the stoichiometry of the film is extracted [168]. 66
2.39 A schematic of a typical transient pump-probe technique. 69
2.40 Schematic of main components of a standard TDTR equipment. Courtesy of Prof. Patrick Hopkins, UVa. 70
2.41 A schematic of laser output is shown as a train of delta functions in (a), while that of (b) shows the pump beam after going through a EO modulator, and finally choosing only the fundamental component results in beam profile shown in (c). Figure adapted from [182]. 72
2.42 A schematic of information revealed about the sample by the measured probe signal. Figure adapted from [182]. 73
2.43 A schematic of information revealed about the sample by the measured probe signal. 74
2.44 A typical TDTR signal is shown in (a) along with a critical time scale beyond which diffusive regime starts and thermal model can be used to extract the thermal conductivity of the thin film (b). 75
2.45 A schematic of resonant vs. non-resonant scattering of polarized X-rays (in transmission mode). From [218]. 77
2.46 A schematic of non-resonant vs. resonant scattering, where the latter can tell us the spatial distribution of |I>. [217] 79
2.47 A schematic X-ray Absorption spectroscopy is drawn, which illustrates various modes under which a XAS can be performed at resonant scattering condition. [222] 80
2.48 X-ray Absorption spectra obtained under Fluorescence Yield (FY) (a) and Total electron yield (TEY) (b), at the Cu-L_3 absorption edge for a LCMO/YBCO heterostructure is shown. Figure adapted from [214]. 81
2.49 Principle of X-ray circular magnetic dichroism is illustrated: (a) shows a schematic of sample incident with a circularly-polarized light with two possible opposite Helicity (H), where (b) depicts the dependence of light absorption on Helicity of circularly polarized light with a corresponding absorption spectra and circular dichroism shown in (c). Courtesy of Prof. Elke Arenholz. 82

3.1 Variety of complex oxides substrates commercially available are listed on an axis of their pseudo-cubic or pseudo tetragonal '*a*'-axis lattice parameter, along with few sample of thin-film complex oxides materials synthesized on selected substrates. From [52]. 86
3.2 A schematic of (a) '*n* x *n*' periodic $SrTiO_3$ - $CaTiO_3$ superlattice structure and (b) '*n* x *m*' periodic $SrTiO_3$ - $BaTiO_3$, where '*n*' and '*m*' represents no. of unit-cells. 87
3.3 Superlattice period dependent phase diagram differentiating coherent phonon transport in short-period superlattices to conventional incoherent phonon transport in thick-period superlattices. 88

3.4 A schematic of a '*n* x *n*' periodic superlattice of $SrTiO_3$-$PbTiO_3$, where 'n' represents no. of unit cells. 89
3.5 Phase diagram of PTO-STO superlattices, exhibiting novel ferroelectric ground states. 90

4.1 A schematic of range of electronic conductivity and thermal conductivity observed in material systems. 92
4.2 Phonon dispersion relation is shown for linear chain of atoms having two atoms in the unit cell. [259] 96
4.3 The generic trend of thermal conductivity as a function of temperature is illustrated by taking the example of bulk silicon. From [266]. 106
4.4 Phonon coherence length in bulk GaAs calculated as a function of temperature. From [267]. 108
4.5 Theoretical prediction of coherent phonon transport in superlattice systems. Figure adapted from [273]. 109
4.6 In the extended zone scheme, the effect of band folding effect on phonon dispersion curve is shown for the case of N equal to (a) 2, (b) 4, (c) 8, and (d) 16. From [273]. 112
4.7 Normalized thermal conductivity of STO-CTO superlattices calculated as a function of superlattice period. Courtesy of Prof. Joel Moore. 113
4.8 Effect of temperature on coherent phonon transport is calculated using molecular dynamics simulations for superlattice structures. From [274]. 114
4.9 (a) RHEED oscillations for the growth of CTO on NGO (110) substrate is shown, where the sustainability of oscillations was achieved by growing 4 unit cells (inset (b)) and giving sufficient time in between for surface recovery. RHEED diffraction pattern is also shown in (c) before and after the growth of 200 nm CTO film. 118
4.10 RHEED oscillations for five periods of 6 x 6 STO-CTO superlattice film grown on NGO (110) substrate are shown in (a), while Inset (b) shows the oscillations for one period. RHEED diffraction pattern is also shown before growth (*i.e.* of NGO substrate) and after the growth of 200 nm Superlattice film. 119
4.11 Reciprocal space map of 200 nm thick (a) 1 x 1 and (b) 2 x 2 STO-CTO superlattice film grown on NGO (110) substrate. 120
4.12 AFM (flattened) image of 200 nm thick superlattice films of (a) periodicity 2 x 2 grown on STO (001) and (b) periodicity 1 x 1 grown on NGO (110). 121
4.13 STEM image of a sub region of 200 nm thick 2 x 2 STO-CTO superlattice film grown on a NGO (110) substrate. 122
4.14 Thermal conductivity of STO-CTO superlattice films measured using TDTR at room temperature is shown. From [288]. 123
4.15 Normalized thermal conductivity calculated using modified Simkin-Mahan model to analyze the effect of interface disorder on coherent regime of thermal transport. Courtesy of Prof. Joel Moore. 124
4.16 Temperature-dependent thermal conductivity of STO-CTO superlattice films grown on NGO (110) substrate. From [288]. 126

4.17 Thermal conductivity of BTO-STO superlattice films, grown via MBE and measured using TDTR at room temperature. From [288]. 127
4.18 A schematic of an Aperiodic superlattice with average interface density equal to 0.86 nm^{-1}, *i.e.* average interface density equivalent to that of a periodic 3 x 3 superlattice, is shown in (a), along with a schematic for the reference 3 x 3 periodic structure. 130
4.19 (a) RHEED oscillations are shown for a part of an aperiodic sequence with average interface density of 0.65 nm^{-1} and Split 7. (b) shows the schematic of thin-film structure corresponding to the RHEED oscillations depicted in (a). 132
4.20 (a) shows low-magnification STEM image of sub region of an aperiodic superlattice film with average interface density 0.43nm^{-1} and Split 7. (b) shows colored STEM image based on A-site/B-site intensity ratio. (c) shows the same image recolored based on the histogram (inset) of overall intensity distribution of the image. A sub region is chosen within this image to analyze the variation of A-site atoms across the thickness of the thin-film, which is shown in (d) along with intensity profile across the highlighted region. TEM analysis courtesy of Dr. Christopher Nelson. 134
4.21 Evolution of structural order in aperiodic superlattice films with average interface density equal to 0.43 nm^{-1}. 135
4.22 Evolution of structural order in aperiodic superlattice films with average interface density equal to 0.43 nm^{-1}. 136
4.23 Reciprocal space map of an aperiodic superlattice film with an average interface density of 0.43 nm^{-1} and Split 7. 137
4.24 AFM (flattened) image of aperiodic superlattice film with an average interface density of 1.29 nm^{-1} and Split 3 grown on STO (001) substrate is shown. 137
4.25 Thermal conductivity of aperiodic superlattice as a function of average interface density for different Splits. 138
4.26 Thermal conductivity of aperiodic superlattices as a function of degree of disorder (local ID distribution width) at a given average interface density. 139
4.27 Degree of disorder calculated from the correlation function as a function of Split for various average interface density aperiodic superlattices. 141
4.28 Degree of disorder calculated from the local interface density distribution, as a function of Split for various average interface density aperiodic superlattices. 142
4.29 Thermal conductivity of aperiodic superlattices predicted using Quasi-incoherent model with L_theta value of (a) L_theta = 8, Linear Interpolation, (b) L_theta = 8, Cubic Interpolation, (c) L_theta = 2*n*, Linear Interpolation superlattices; (d) measured using TDTR. 144
4.30 Normalized coherent thermal conductivity predicted for various aperiodic superlattices as a function of degree of Disorder with (a) no cut-off, and cut-off at (b) 1000, (c) 500. Normalization is done with respect to respective periodic superlattice; (d) Thermal conductivity of ASLs measured using TDTR. 146
4.31 Normalized thermal conductivity as a function of superlattice period for two different mass ratio of superlattice constituents. From [274]. 148

5.1 Classification of crystal classes based on their structure-property relationship. [385]. 154
5.2 A schematic of Polarization-Electric field hysteresis loop is shown. [327] 156
5.3 Spontaneous polarization of various ferroelectric materials is listed. From [368]. 157
5.4 Ferroelectric phase transition described using Landau-Ginzburg-Devonshire theory. From [386]. 159
5.5 Ferroelectric distortion in a unit cell of PTO leading to a spontaneous polarization is shown. 160
5.6 Ferroelectric phase transition temperature for various types of ferroelectric materials is listed. From [368]. 161
5.7 Domain structure of a PZT single crystal. Figure adapted from [363] and [405]. 164
5.8 The schematic shows (a) 180° and (b) 90° degree domains walls which are commonly observed in multivariate domain structure. 165
5.9 Effect of electrical boundary conditions on the polarization distribution within a slab of ferroelectric material. From [368]. 167
5.10 Toroidal moment for a nanodisc, as calculated from first-principles-derived effective Hamiltonian method. From [372]. 172
5.11 Local polarization profiles within a nanorod is shown on the cross-sectional plane of (a) $yz = 0$ and (b) $zx = 0$, as predicted from first-principles-derived effective Hamiltonian method. From [372]. 173
5.12 Local polarization profiles within a sub region of a 6 x 6 PTO-STO superlattice predicted using first-principles-derived effective Hamiltonian method, is shown. From [432]. 174
5.13 Phase-field simulations for a 10 x 10 PTO-STO superlattice epitaxially strained on a DSO (110) substrate is shown in (a), which suggests existence of array of vortex-antivortex pairs (b) present in PTO layers of the superlattice structure. Courtesy of Zijian Hong, Penn State University. 177
5.14 First-principles calculations for a 1 x 1 PTO-STO superlattice epitaxially strained on a substrate is shown, illustrating the relative stability of various instabilities (individual or coupled) with respect to misfit strain for respective STO and PTO layers in the superlattice structure. From [86]. 179
5.15 Variation of RHEED intensity corresponding to the growth of PTO from a stoichiometric polycrystalline target is shown in (a), along with a RHEED pattern observed at the end of the growth. 181
5.16 Variation in RHEED intensity during the growth of PTO from a 20% lead-rich PTO target on TiO_2-terminated STO substrate is shown. Inset (a) shows the zoomed-in region to highlighting the 2D growth mode, while inset (b) shows the RHEED pattern after continuing the layer-by-layer growth till 13 nm. 182
5.17 RHEED oscillations for 1 oscillation of SRO, 5 unit-cells of STO, and then 4 unit-cells of PTO grown in that order is shown in (a), along with a zoomed-in section

for 4 unit-cells PTO growth in (b). RHEED pattern after growing PTO layer-by-layer up to 13 nm is shown in (c). 183

5.18 RHEED oscillations for five periods of a 6 x 6 PTO-STO superlattice grown on a DSO (110) substrate is shown in (a), along with a zoomed-in graph (b) showing oscillations for only one period. From [168]. 185

5.19 (a) A high-resolution symmetric XRD scan of a 10 x 10 PTO-STO superlattice [168] and a RSM around 113_{pc} of 6 x 6 PTO-STO superlattice (b), grown on DSO (110) substrate, are shown. 186

5.20 A 2D reciprocal space map, *i.e.* an LK-cut from 3D RSM around DSO 011_{pc} peak, of a 12 x 12 PTO-STO superlattice film grown on DSO (110) is shown. From [168]. 188

5.21 Low magnification STEM image of a 10 x 10 PTO-STO superlattice grown on a DSO (110) substrate is shown in (a), while (b) shows a High-resolution Z-contrast HAADF image of a sub region of the same 10 x 10 PTO-STO superlattice along with a schematic of one period of the superlattice structure. In the schematic, PTO (top) is drawn for the case of a $[001]_{pc}$ (upward) polarization, which results from the downward displacement of the Ti "centered" oxygen octahedral relative to Pb (Pb, red; Ti, blue; O, dark yellow). From [168]. 189

5.22 Cross-sectional HAADF STEM image with an overlay of the polar displacement vectors (yellow arrows) for a subregion of 10 x 10 PTO-STO superlattice showing an array of vortex-antivortex pairs, present in each PTO layers of the superlattice structure is shown in (a). A magnified image of a single vortex-antivortex pair (b) shows the full density of datapoints (displacement vectors are shown for both Pb-atoms and Ti-atoms) and the continuous rotation of the polarization state within such vortex-antivortex pairs. The curl of the polar displacement $(\nabla \times \boldsymbol{P_{PD}})_{[010]}$ for the same vortex-antivortex pair (c) reveals the alternating rotation directions the structures. Polarization distribution from a phase-field simulation of the same 10 x 10 superlattice (d), predicts vortex-antivortex pairs that closely matches the experimental observations. From [168]. 190

5.23 (a) Cross-section, DF-TEM images of a 10 x 10 PTO-STO superlattice revealing long-range ordering of vortices (where each bright/dark modulation corresponds to a period of the vortex-antivortex structure). The inset shows a SAED pattern for the sample with the g-vector of the two-beam imaging condition indicated by the yellow arrow. Close inspection of the SAED pattern reveals superlattice reflections both in- and out-of-the plane suggesting long-range ordering of the vortex structures (magnified $(00\bar{1})_{pc}$ reflection inset). (b) Planar-view DF-TEM imaging of a 16 x 16 superlattice which likewise exhibits long-range in-plane ordering associated with the vortex-antivortex pairs along the $[\bar{1}00]_{pc}$ and confirms the widespread occurrence of these vortex pairs in the superlattice films. The upper inset shows the SAED pattern for the sample with the g-vector of the two-beam imaging condition indicated by the yellow arrow. Again, close inspection of the diffraction pattern reveals in-plane superlattice reflections indicating long-range

ordering of the vortex structures. The lower inset shows a magnified view of the vortex structures – again revealing ~10 nm periodicities. From [168]. 191

5.24 (a) Cross-sectional DF-TEM of a 10 x 10 PTO-STO superlattice taken along $[010]_{pc}$ zone axis (inset shows the SAED diffraction pattern at-tilt along with g-vector for image formation). (b) Cross-sectional DF-TEM of the same 10 x 10 superlattice sample taken orthogonal $[001]_{pc}$ zone axis (inset shows SAED diffraction pattern at-tilt along with g-vector for image formation). From [168]. 193

5.25 The 3D geometry of the vortex-antivortex array from phase-field simulation of a 10 x 10 PTO-STO superlattice is shown. The front cross-section of the model shows the polarization vector ***P*** ordered into clockwise (blue) and counterclockwise (red) vortex-antivortex states which extend along the y ($[001]_{pc}$) axis. **Left**. For comparison, a cross-section HR-STEM image overlaid with a polar displacement vector map and a planar-view DF-TEM image are projected onto the front and top planes of the axes. Red/blue color scales correspond to the curl of the polarization (phase field model) and polar displacement (HR-STEM). Scale bar on P_x and P_z is from [-37.76, 37.76] μC/cm^2 and [-47.45, 47.45] μC/cm^2, respectively, whereas the vorticity is from [-17.07, 17.07] μC/cm^{2}nm (phase field). From [168]. 194

5.26 (a) HR-STEM polar displacement vector map of a single vortex in a 10 x 10 PTO-STO superlattice. (b) Phase-field calculated polarization vector map of a single vortex in a 10 x 10 PTO-STO superlattice. (c) Total energy density variation within a single vortex in a 10 x 10 PTO-STO superlattice calculated from Phase-field simulations. (d) HR-STEM polar displacement vector map of a 20 nm PTO in a heterostructure having same layer stacking as Tang *et. al.* [441] (e) Phase-field calculated polarization vector map of a flux-closure domain in a 20 nm PTO heterostructure. (f) Total energy density variation within a flux-closure domain calculated using Phase-field simulations. From [168]. 195

6.1 A schematic of Kittel domains in a ferroelectric slab (blue arrows indicate net polarization vectors within respective domains). From [446]. 200

6.2 Domain scaling law for 180° domain width as a function of thickness. Figure adapted from [386; 449]. 201

6.3 A schematic of Landau-Lifshitz domain in a ferroelectric slab of thickness 'T.' Figure adapted from [446]. 203

6.4 Theoretically predicted evolution of domain width with film thickness, for (a) c/a and (a) a_1/a_2 domains formed in tetragonal ferroelectric thin films strained on a cubic substrate. Regions exhibiting inverse domain scaling with thickness are highlighted in yellow. Figure adapted from [468]. 204

6.5 Low magnification STEM image of (a) 6 x 6 and (b) 16 x 16 PTO-STO superlattice is shown along with a zoomed-in sub region of the respective lattices in (c) and (d) showing high quality of superlattice interfaces. 205

6.6 In-plane PFM of (a) 6 x 6 and (b) 16 x 16 PTO-STO superlattice grown on STO (001) substrate is shown. 206
6.7 Phase diagram as function of superlattice periodicity with characteristic domain structure for the respective regimes in insets (a, b). 207
6.8 In-plane PFM of 4 x 4 PTO-STO superlattice grown on DSO (110) substrate is drawn, which shows a_1/a_2 type domain structure, along with a schematic of polarization distribution inside a_1 and a_2 domains. The schematic is taken from [469]. 208
6.9 Symmetric XRD of (a) 6 x 6, (b) 10 x 10, and (c) 12 x 12 PTO-STO superlattice films is drawn along with the in-plane PFM scans shown on right (d), (e) and (f) respectively. 209
6.10 (a) Average domain width of a_1 or a_2 domains observed in superlattice structures is plotted as a function of PTO thickness in superlattice periodicity. For comparison, domain size evolution of Landau-Lifshitz-Kittel domains is plotted in (b). 211
6.11 Symmetric XRD of 6 x 6 PTO-STO superlattice films grown on STO (001) (in blue) vs DSO (110) (in red) substrate. 212
6.12 HK-cut (a) and LHK-cut (b) obtained from a 3D RSM around DSO 202 peak is shown for a 6 x 6 PTO-STO superlattice film grown on DSO (110) substrate. 213
6.13 Evolution of polarization distribution for superlattice periodicity 4 x 4, 6 x 6, 12 x 12, as obtained experimentally from HR-TEM polar displacement map (a, b, c) and phase field simulations (d, e, f) respectively. 214
6.14 In-plane PFM of 16 x 16 PTO-STO superlattice film grown on a DSO (110) substrate. 215
6.15 AFM image of 16 x 16 PTO-STO superlattice film grown on DSO (110) substrate. 216
6.16 Symmetric XRD of 16 x 16 PTO-STO superlattice films grown on (a) STO (001) and (b) DSO (110) substrate. 217
6.17 Symmetric XRD of (a) 14 x 14, (b) 16 x 16, and (c) 18 x 18 PTO-STO superlattice films is shown along with the in-plane PFM scans shown on right (d), (e) and (f) respectively. 219
6.18 An HK-cut (a) and LHK-cut (b) is shown to highlight the a_1/a_2 periodicity in 16 x 16 superlattice film grown on DSO (110) substrate along specific crystallographic directions. 220
6.19 An LK-cut of 16 x 16 PTO-STO superlattice film grown on DSO (110) substrate showing vortex diffraction peaks. 222
6.20 In-plane PFM of a 27 x 27 PTO-STO superlattice film grown on DSO (110) substrate. 223
6.21 Symmetric XRD of 27 x 27 PTO-STO superlattice film grown on (a) DSO (110) and (b) STO (001) substrate. 224
6.22 XAS spectra of PZT thin film grown on SRO/STO (001) are shown in (a), along with X-ray Linear Dichroism signal shown in (b). Inset (c) shows the sample orientation with respect to incoming polarized soft X-ray light. From [211]. .. 226

6.23 A schematic of RSXS measurement is drawn in (a), with reciprocal space highlighting the difference between the spaces accessible by soft vs. hard X-rays. 227
6.24 A schematic of diffraction geometry is drawn in (a) showing the vortex orientation with respect to incoming X-ray beam, which results in diffracted intensities along H- and K-direction as shown in the schematic (b). Figure courtesy of Dr. Padraic Shafer, Prof. Elke Arenholz. 228
6.25 XAS spectra from a vortex diffraction peak in a 14 x 14 PTO-STO superlattice film grown on a DSO (110) substrate, obtained in FY mode is shown in (a) for both left- and right-circular polarized X-ray light. The difference in the absorption spectra between left- and right-circular polarized lights is shown in (b). The schematic of the particular diffraction peaks used for the XCD measurement is shown in (c). Figure courtesy of Dr. Padraic Shafer, Prof. Elke Arenholz. 229
6.26 (a) Average phonon transmission rate of phonon across a random multilayer of GaAs-AlAs vs a periodic superlattice (2 x 2). (b) Lyapunov exponent for a random multilayer as a function of phonon frequency corresponding to which the average transmission rate is shown in (a). For both graphs, solid lines correspond to analytical solution, while open circles indicate numerical data. From [312]. .. 230
6.27 (a), (c) present simulated phonon dispersion relation for clathrates Si_{46} and Ba_8Si_{46} respectively. (b) shows the crystal structure of Si_{46}, while (d) show building units of Ba_8Si_{46} with 'Ba' atoms occupying empty polyhedral cavities of 'Si' network. Figure adapted from [244; 483]. 231
6.28 (a) and (c) shows the map of simulated Inelastic X-ray Scattering (IXS) intensities of Longitudinal acoustic (LA_{001}) and Transverse acoustic (TA_{001}^{110}) phonons propagating along [001] respectively. The black dots in (a) and (c) represent the experimentally measured data points. (b) and (d) plots dynamic structure factor (DSF), measured in red squares, simulated in solid black line, for longitudinal and transverse acoustic phonons respectively, along with the intensities of optical phonons corresponding to 'Ba' guest sublattice at E_1. From [483]. 233
6.29 Time evolution of polarization distribution in 10 x10 PTO-STO superlattice as simulated using Phase-field Simulations is shown from (a) to (i) in chronological order. Time axis is also shown to highlight the evolution of vortex state from an unpolarized state. Courtesy of Zijian Hong. 234
6.30 (a) Contrast in diffraction TEM shows the wave-like modulation of lattice associated with polarization vortices in PTO layers of 16 x 16 PTO-STO superlattice film grown on DSO (110) substrate. (b) Polar displacement map showing the displacement vectors (in yellow) corresponding to A-site only, overlaid on HRSTEM image. The colorized map of 'c/a' ratio of the same superlattice film as extracted from a high-resolution STEM image is shown in (c). The displacement maps corresponding to both A-site (d) and B-site (e) extracted from HRSTEM image is shown in (d) and (e) respectively. Courtesy of Dr. Christopher Nelson. 236

List of Tables

4.1 Comparison of theoretical (aperiodic) sequence and as-grown aperiodic structure using RHEED-assisted Pulsed Laser Deposition as measured from TEM-based analysis is presented. 133

Acknowledgements

There are so many people to whom I would like to send my sincere thanks and appreciation for their help and support during the course of my graduate education at Berkeley. In the past five and a half years or so, I have had the opportunity to interact and work with a great set of people at and outside Berkeley. I learned a great deal from these fruitful collaborations and the work presented in this dissertation was only possible because of their constant help, support, and encouragement.

First and foremost, I would like to thank my advisor, Professor Ramamoorthy Ramesh for giving me this opportunity to pursue graduate studies at Berkeley. From the beginning of my graduate school, Ramesh gave me complete freedom to pursue my research interest and explore new ideas with full support. His belief in my research aptitude was a strong motivating force, and it encouraged me to take on exciting projects. He generously provided me with all the resources necessary to fulfill the goals of the project. His constant encouragement, guidance, and support helped me to grow as a researcher. I learned a lot from Ramesh, and I owe him a great deal of gratitude. I shall forever be in his debt for providing graduate education under his guidance.

I am also thankful to all the professors at Berkeley, who taught me graduate courses and gave me guidance on graduate research. I would first like to Prof. Daryl Chrzan, Prof. Oscar Dubon, Prof. Junqiao Wu, and Prof. Chris Dames for serving on my qualifying committee and giving me crucial feedback and advice to make progress towards a graduate degree. I would also like to thank Prof. Joel Moore and Prof. Oscar Dubon for being on my dissertation committee and providing me with advice and feedback on the thesis. Special thanks to Prof. Oscar Dubon for frequently advising me on various aspects of graduate research and giving very helpful suggestions from time to time. I am also grateful to Prof. Mark Asta for being my major field advisor and giving me advice on coursework required for this graduate program.

I was very fortunate to be a part of the thermoelectric program at Berkeley, which hosted a number of theoretical and experimental research groups. This tremendous opportunity allowed me to interact and collaborate with graduate students and post-docs from different research groups. In particular, I collaborated extensively with Prof. Joel Moore on a number of research projects and learned a lot working with him. I am thankful to Joel for providing theoretical calculations on these projects. I am also thankful to Prof. Arun Majumdar for his insightful suggestions and advice on various projects. I am very grateful to have received continuous financial support all throughout my graduate studies from this program.

While working towards my graduate studies, I collaborated with a number of talented individuals within and outside Berkeley. I will begin thanking first my research group - CONCEPT lab - members for their tremendous help and support. I would first like to thank Dr. Jayakanth Ravichandran who has been an excellent collaborator, a mentor, and a friend. From him I learned a lot about various aspects of research and am thankful for the countless number of discussions we had on various research topics. These discussions were very helpful in introducing me to physical concepts and insights. He has been extremely supportive and helpful during my graduate studies, and I owe him a lot. I

would like to thank Pim Rossen for training me on hybrid PLD growth chamber and for teaching me time-of-flight spectroscopy. From the fruitful discussions with Pim, Jayakanth, Dr. Balasubramaniam Kavaipatti, Dr. Morgan Trassin and Dr. Claudy Rayan Serrao, I learned a lot about PLD deposition process. Special thanks to Claudy for helping me with target synthesis and being very supportive and helpful in general. I am also very grateful for his brotherly advice and good times with him for the past four years. I would like to thank Morgan for teaching me scanning probe microscopy and for his helpful advice and discussions. It has been an excellent experience to collaborate with Dr. Christopher Nelson on a number of TEM-based projects. I am grateful for extensive TEM-based microscopy and analysis provided by him. He has been very helpful, and I would like to sincerely thank him for that. I also collaborated extensively with ShangLin-Hsu on several TEM-based projects, and I am thankful for his help in providing TEM-based microscopy and analysis on several projects. I would also like to give special thanks to Dr. Deyang Chen who greatly helped me in providing PFM-based measurements on my samples. I would like to thank Dr. Xavi Marti for his helpful advice and discussions. I also collaborated with Dr. Jian Liu and am thankful for his suggestions and advice on various projects. I am also thankful to Dr. Ying-Hao (Eddie) Chu for his guidance during the early stages of my graduate school. I am grateful to have started graduate school with my fellow graduate students – Dr. Di Yi, James Clarkson, and Anthony Diamond, with whom I discussed a lot on various research topics and graduate coursework. I will surely cherish the memories we shared during our graduate school. I am thankful to James Clarkson for helping me on various experiment-related hurdles from time to time and also providing PFM-based measurement on my samples. I should also thank all other former and current members of the CONCEPT group for all of their help and support: Dr. John Heron, Dr. S. J. Suresha, Dr. Shrawan Mishra, Dr. Jiun-Haw Chu, Dr. William Paschoal, Dr. Yeonbae Lee, Dr. Jeremey Turcaud, Dr. Julia Mundy, Dr. Zhiqi Liu, Suraj Cheema, Han EE Ong, Margaret McCarter, Oleg Sapunkov, Ya Gao, and Ryan Paul.

I also collaborated with several other research groups here at Berkeley and am thankful for learning a lot from these collaborative research projects. I am very grateful to have worked with Prof. Joel Moore's group, specifically with Aaron Szasz who has provided extensive theoretical calculations on a number of projects. Aaron's contribution was very valuable, and I am very thankful for it. I would also like to thank Prof. Ashwin Vishwanath for all of the useful discussions and physical insights on various projects. I am also thankful for fruitful collaboration with Prof. Sayeef Salahuddin and useful discussions with him. I would also like to thank Sayeef's group members for their help and suggestions: Dr. Asif Aslam Khan, Dr. Debanjan Bhowmik, Dr. Saidur Rahman Bakaul, Dr. Long You, Dr. Asis Sarker, Dr. Weiwei Gao, Sushant Gadgil, and Michelle Lee. In the last year or so of my graduate program, I collaborated extensively with Prof. Lane Martin and would like to sincerely thank him for his insightful suggestions and advice on several projects. I learned a lot from the interactions and discussions with Lane and his group members. I would like to thank Lane's group members for their help and suggestions: Dr. Anoop Rama Damodaran, Liv R. Dedon, Shishir Pandya, Thomas Mösl, Dr. Sungki Lee, Brent Apgar, Ruijuan Xu, Ran Gao, and Sahar Sareminaeini. I also worked with Prof. Elke Arenholz and Dr. Padraic Shafer at Advanced Light Source, LBL, in the last year of my graduate

studies, and I am thankful for their help with soft x-ray based spectroscopic measurements. Their contribution to this dissertation was very valuable. I would like to mention tremendous help from Dr. Kin Man Yu at LBL for RBS measurements time after time during my graduate research. I am also grateful to James Wu at LBL for his tremendous help with synthesizing a number of PLD targets for my projects.

I would like to give special thanks to Steven Montalvo and Daning Chow for their regular help with fixing the heater assembly and other chamber parts in the machine shop. I am also thankful for constant advising and help from Janene Martinez, Mei Griebenow, Ariana Castro, and Catalina Estrada in the MSE department.

I also had the great privilege to collaborate with excellent research groups outside Berkeley. First, I would like to thank Prof. Patrick Hopkins at UVa for being such an excellent collaborator and a great mentor, and a friend. I am indebted for his generous invitation to visit his lab at UVa and for allowing me work as a regular user on his TDTR equipment. I would like to thank Dr. Ramez Chaeito for being tremendously helpful with TDTR measurements and for all of those useful discussions and suggestions. It was a really fun experience working with Patrick and Ramez at UVa. I am also thankful for the collaboration with Prof. Darrell Schlom and his group at Cornell, especially for providing MBE-grown superlattice samples of BTO-STO. These samples were a critical part of a study we reported, and I am grateful for their valuable contribution to this thesis. I am also grateful for the fruitful collaboration with Prof. Long-Qing Chen and his group at Penn State. I am thankful for the phase-field calculations provided by his group, with special thanks to Zijian Hong who performed extensive simulations on different projects. Zijian's contribution was very valuable, and I would sincerely like to thank him for it. I was also fortunate to have collaborated with a great set of people at Advanced Photon source, Argonne National Laboratory. Special thanks to Dr. Christian Schlepütz for his tremendous help with providing 3D RSM measurements and data analysis on my samples. More thanks to Dr. Evguenia Karapetrova, Dr. Huajun Liu, and Dr. Dillon Fong at Advanced Photon source for their tremendous help and useful suggestions and discussions. I am also thankful to Prof. David Muller and his group at Cornell for providing TEM-based microscopy and analysis, providing valuable insights and contributions to the projects.

I have been extremely fortunate to have amazing friends with whom I had such good times at Berkeley. To Deepan, Shrikant, Shashank, Pallavi, Narayanan, Debanjan, Anthony, Suraj, and Rohit, thanks for all the fun times, and being extremely supportive and helpful. I will definitely cherish the memories of the time we spent at Berkeley. Special thanks to my roommates Deepan, Shrikant, and Shashank for being there at every stage of graduate school, and for being great friends and counselors. I owe you guys a great deal.

I have been blessed to have a family who gave me immense love and support all throughout my life. A deepest gratitude to my parents, dad and mom, for being extremely understanding, supportive, and encouraging me to pursue a career of my interest. I have so much to thank them for. I am also extremely fortunate to be blessed with amazing siblings, brother Badri and sister Shobha, who gave me their endless love and support all throughout my life. They deserve a special mention and a big thank-you note. I am also grateful to have received love and support from my sister-in-law Sonali and brother-in-law Shailesh. A heartfelt thanks to my family, and this is dissertation is solely dedicated to them

Chapter 1

Introduction

1.1 Brief History

The discovery of semiconductors heterostructures such as III-V quantum-well and superlattice, which later revolutionized the electronics industry, earned Herber Kroemer and Zhores I. Alferov a Nobel Prize in Physics. Semiconductor heterostructures had a massive impact on advancement of technologies because of their role in the development of applications ranging from high-speed electronic and optoelectronic devices. Some notable examples include high electron mobility transistors (HEMTs) for satellite television, heterostructures-based lasers for telecommunication, light-emitting diodes, solar cells and many others. The remarkable development in understanding the physics of semiconductor heterostructures, which resulted in an increase in their technological applications, was mainly driven by the necessity to control the fundamental properties of semiconductors using heterostructures. These properties include effective mass and mobility of charge carriers, electronic band gaps *etc.* Semiconductors with such tailored electronic and optical properties are achieved by combining different compounds (ex. III-V, II-VI, IV-VI) in a given sequence, thereby creating an "artificial" or "man-made" crystal with desired properties. Nobel Laureate Zhores I. Alferov also named these type of semiconductor materials as "Heterosemiconductors." Research on semiconductor heterostructures started as early as 1950 and from thereon interest in these materials only grew, primarily due to their technological and fundamental relevance. An excellent summary on the history of semiconductor heterostructures can be found in the Nobel Lecture of Zhores I. Alferov [1]. We shall use the discussion included therein as the primary reference for presenting a brief history of its evolution.

Research on semiconductor heterostructures started in the early 1950s [2-4] with theoretical studies proposing several new phenomena such as the *p*-*n* junction, which is based on a wide-band gap emitter, and solar cells based on single host semiconductor material (ex. p-n-p^+, n-p-p^+). In the late 1950s [5-9] , the experimental realization of the *p*-*n* junction based emitting diodes (LEDs) and lasers, based on GaAs as host semiconductor material, marked the advent of optoelectronics research. However, the performance of these devices suffered greatly from low efficiency due to high recombination and electrical losses. Remarkable improvement in the performance of these optoelectronic devices (LEDs and lasers) was achieved through their extensions to double heterostructures, *i.e.*

structures having more than one host semiconductor material such as AlAs-GaAs and GaP-GaAs systems. Using such optimized semiconductor systems, a number of important concepts were realized, including lower threshold current lasers, efficient LEDs, bipolar transistors and solar cells. Finally, we note that various new physical phenomena were discovered using semiconductor heterostructures such as one-side and super injection of carriers at an interface, diffusion of carriers in built-in electric field, confinement of electrons and photons in a layer, wide-band gap window effect and diagonal tunneling through an interface. The realization of such unique physical phenomena led to several applications in the electronic industry. Examples include semiconductor lasers, solar cells, LEDs, high-power diodes and bipolar wide-band gap transistors.

A decade later an important heterostructure called the quantum well structure was conceptualized [10-13], which was found to be very important from both fundamental physics and technology perspective. Quantum-well heterostructures are formed when the layer thickness reaches few hundreds of angstroms discretizing the energy levels due to the quantum confinement effect. The advancement of thin-film synthesis of III-V (ex. GaAs) semiconductors, through Molecular Beam Epitaxy (MBE), enabled the first observation of quantum confinement effect in the heterostructures of $Al_{0.2}Ga_{0.8}As/GaAs/Al_{0.2}Ga_{0.8}As$ (1974). The absorption spectra from the ultra-thin or quantum wells of GaAs layers showed characteristically different spectrum compared to bulk GaAs. The set of absorption peaks in the spectrum from quantum wells of GaAs layers was characterized as excitonic transitions associated with bound electrons and holes. In addition, a systematic shift of absorption peaks with a change in the quantum-well thickness was also observed. Also, resonant tunneling current was observed in quantum-well heterostructures of $GaAs/Al_xGa_{1-x}As$, resonant tunneling current was observed when tunneling current was measured as a function of applied voltage. During the same period [14-16], there was growing interest in the special kind of heterostructure called *superlattices*, which is a structure with periodic repetition of alternating layers of two (or more) materials. These semiconductor superlattices were also found to exhibit resonant tunneling current [17], which further generated more interest in these heterostructures due to its potential for high-speed electronics. In 1978, a two-dimensional electron gas (2DEG) was experimentally realized [18] in a modulation-doped semiconductor superlattice ($GaAs/Al_xGa_{1-x}As$). The electron mobility in these semiconductor superlattices were reported to be exceptionally higher than ever reported with GaAs based systems. Shortly after the realizations of 2DEGs in modulation-doped semiconductor superlattices, new field-effect transistors based on these 2DEGs were realized [19; 20].

During the same time period, quantum-well heterostructures were also studied for lasing action [21], but they mostly suffered from poor performance compared to the previously reported efficiency of lasers based on double heterostructures. However in the early 1980s, owing to significant improvement to the synthesis of quantum-well structures using the MBE technique, a tremendous improvement was observed in the laser performance with threshold currents as low as 160 A/cm^2 [22], over previously reported values of 900 A/cm^2 using double heterostructures [1]. A record-breaking improvement in laser performance was demonstrated in late 1980s by designing a heterostructure with a single quantum-well with short-period superlattices on either side [23]. In this short-period

superlattice quantum well, threshold currents as low as 40 A/cm^2 were observed [1]. During the same period, quantum-well structures were further employed to search for other novel phenomena based on the confinement of electrons in the quantum-well. A first of its kind, the discovery of the quantum hall effect [24] was experimentally realized in these quantum-well heterostructures. Soon after, an even more fundamental discovery was made using the quantum-well heterostructures of GaAs/$Al_xGa_{1-x}As$, the demonstration of Fractional Quantum Hall effect [25]. The observation of such new phenomenon demonstrates the potential of quantum-well heterostructures.

We summarize by noting some of the major discoveries enabled by semiconductor superlattices and quantum-well heterostructures [1]. These include the presence of two-dimensional electron gas (2DEG) in modulation-doped superlattices, the observation of step-like electron density of states from quantum confinement, the resonance tunneling in double-barrier quantum-well heterostructures, the stimulated emission of resonant tunneling, the quantum hall effect and the fractional quantum hall effect. Such fundamental observations were found to have a profound impact on the technological advancement of several devices, for example improved performance in semiconductor lasers (*i.e.* decreased current threshold and increased differential gain), high-electron mobility transistor (HEMTs), infra-red (IR) photodetectors, quantum cascade lasers and resonant tunneling diodes based on designed heterostructures. Thus, the discovery of semiconductor heterostructures, particularly quantum-well heterostructures and superlattices, had not only showed a multitude of new physical phenomena, but also has found applications so important that they revolutionized optoelectronic and high-speed electronic devices.

The above discussion on semiconductor heterostructures clearly emphasizes the importance of artificial heterostructures, or in this particular case *Heterosemiconductors*, in giving significant thrust to the field of conventional semiconductors (III-V, II-VI *etc.*). Additionally, synthesizing these heterostructures as thin-films enhanced the potential of these material system in exhibiting new phenomenon. This remarkable capability of artificial heterostructures to enable observation of fundamentally new physical phenomenon in conventional semiconductors, further invites the search of novel physics in other materials systems. An interesting class of material system could be those which possess strong electronic correlations, exhibiting properties found only in these materials such as metal-insulator transition (Mott insulator), high-temperature (high T_c) superconductivity, half-metallicity, giant magnetoresistance and many others [26]. Within the family of strongly correlated materials, transition metal oxides and complex oxides in particular attracted much attention owing to the strong interaction [27] among spin, charge, orbital and lattice degrees of freedom, exhibiting unique properties such as ferroelectricity, High-T_c superconductivity *etc.*, which are not observed in conventional semiconductors [28]. Using the inherent property of artificial heterostructures to form interfaces between two materials and choosing strongly correlated complex oxides as the materials system, one can create new structural and electronic phases at the interface [27], which rarely co-exist in conventional bulk systems.

In what follows, I will first provide an introduction to complex oxide materials along with the basic concepts involved in the context of structure-composition-property relationship. Then, an introduction to artificial superlattices will be given, which will be

followed by a discussion on significance advances enabled by superlattice structures in the field of complex oxides.

1.2 Complex Oxides

1.2.1 Introduction

In the last few decades, transition metal oxides attracted much attention, owing to their broad range of physical properties, examples of which include metals, semiconductors, superconductors, insulators, ferromagnetism, ferroelectricity, piezoelectricity, pyroelectricity, strong dielectric behavior, and multiferroicity [26]. While some of these properties found numerous applications already and across various industries, the remaining are being actively studied for their tremendous potential for the development of next generation devices [26]. Within the family of transition metal oxides, there are binary oxides, ternary oxides, and higher-order oxides [29; 30]. Binary oxides, depending on the valence state of the transition metal action, can be further classified into three categories: monovalent oxide, divalent oxide, and trivalent oxide [29; 30]. Examples of monovalent binary oxides include zinc oxide (ZnO), manganese oxide (MnO), cobalt oxide (CoO) and they are observed to crystallize in a variety of crystal structures such as rock salt structure (MnO, CoO) and Wurtzite structure (ZnO). Divalent binary oxides usually crystallize as rutile or fluorite structure. Examples of which include titanium dioxide (TiO_2), tungsten dioxide (WO_2), molybdenum dioxide (MnO_2), and zirconium dioxide (ZrO_2). Within this family of simple binary oxides, a range of physical properties such as metallic, semiconducting, insulating, magnetic, and superconducting behaviors were observed [29; 30].

Ternary transition metal oxides are found to crystallize in a variety of crystal structures such as spinel structure, perovskite structure and perovskite-derived structures such as Ruddlesen-Popper (RP) phases and limonite structures [30]. Examples of these oxides include cuprospinel ($CuFe_2O_4$), barium titanate ($BaTiO_3$), lanthanum-calcium-manganite ($La_{2/3}Ca_{1/3}MnO_3$), RP phases of $Sr_{n+1}Ti_nO_{3n+1}$ (n = 1, 2, 3,) and limonite $FeTiO_3$. As for the higher-order transition metal oxides, they are generally found to crystallize in layered crystal structure, which usually contains various atomic layers of metal oxides stacked on top of each other and forming blocks with dissimilar crystal symmetry. Finally, this results into a long (‘*c*’- axis) lattice parameter compared to the other two in-plane lattice parameters (‘*a*’ and ‘*b*’). Examples of these higher order transition metal oxides include Aurivillius compounds [31] such as strontium bismuth niobium oxide ($SrBi_2Nb_2O_9$), Dion-Jacobson phases [32], such as $RbYNb_2O_7$ and layered perovskites such as yttrium barium copper oxide ($YBa_2Cu_3O_7$) [31]. These ternary and higher-order complex oxides brought more functionality to the family of transition metal oxide such as ferroelectricity, high-temperature superconductivity, colossal magneto resistance and the electric-field control of magnetism [26; 29; 30]. Thus, these transition metal oxides as a

whole exhibited a wide range of physical properties and continue to provide a very interesting material system to explore exotic phenomena in condensed matter physics.

Perovskite complex oxides, in particular received an excessive amount of consideration given their vast potential for technological applications and fundamental science. With a relatively simple structure and chemical formula ABO_3, these perovskite oxides long have been known to show a range of properties including large dielectric constant, piezoelectricity, pyroelectricity, ferromagnetism, ferroelectricity, colossal magneto resistance, superconductivity *etc*. [26]. Such diversity in physical behavior is observed primarily because of the different possibilities of ionic radii and (single- or multi-) valency of metal cations occupying the 'A' and 'B' lattice sites. The ability to independently vary 'A' site and 'B' site (or both) occupancy in these perovskite compounds allowed researchers to not only control and enhance their property, but also manipulate them to induce new functionalities. One notable example is Strontium titanate perovskite, $SrTiO_3$ (STO), which is an insulator in stoichiometric form and becomes a quantum paraelectric below 4 K [28]. The STO compound can be changed to show metallic behavior when the 'B'-site (currently occupied by 'Ti') is substituted or doped with a low concentration of 'Nb' atom [33]. Moreover, by substituting 'A' site with 'La' element, superconductivity in doped-STO compounds has also been realized [34]. Thus, using chemical substitution, electronic conductivity can be controlled by orders of magnitude as per requirement. Further, using chemical substitution on 'A' site with 'Ba' atoms, even ferroelectricity can be induced into doped-STO [35]. Another notable example is $LaMnO_3$, which has an antiferromagnetic order and is electrically insulating [36]. Upon doping 'Sr' atoms on A-site, $La_{1-x}Sr_xMnO_3$ changes the magnetic order to ferromagnetic and induces metallicity in the material [37]. These examples demonstrate the potential to achieve remarkable control of a physical property in these perovskite oxides, in addition to inducing new physical behavior not present in their bulk stoichiometric form. Therefore, I have chosen this material system to study the novel physical behavior described in this thesis. In what follows next, I will discuss various aspects of perovskite oxides such as their chemistry, crystal structure, and electronic structure *etc.*

1.2.2 Crystallographic structure

An ideal cubic perovskite crystal structure with a chemical composition of ABO_3 is illustrated in Figure 1.1(a). In the depicted unit cell, 'A' atoms are occupying the corners of the cube, the 'B' atom is occupying the center of the cube and 'O' atoms are located at the face center of the sides of the unit-cell. 'A' atoms are surrounded by the 12 nearest oxygen atoms making its co-ordination number 12, while the 6 nearest oxygen atoms making the co-ordination number 6 surround 'B' atoms. The ionic radii of the metal cations determine the type 'A' atoms occupying the site with coordination number 12 and 'B' atoms occupying the site with coordination no. 6. In this ideal structure, the radius of metal cations is such that the anions (oxygen) touch the metal cations. There can be many scenarios where there is a large difference between the ionic radii of the two atom types, for example $r_A << r_B$ where 'r_A' and 'r_B' are ionic radii of metal cations, and the above

stated condition does not hold. In all such cases, where a disproportionate amount of disparity exists between ionic radii of 'A' and 'B' metals, the crystal structure will deviate from the ideal cubic structure shown in Figure 1.1(a). The deviation in the ionic radii of metal cation from ideal cubic structure is given by the Goldschmidt tolerance factor, t [38]:

$$t = \frac{r_A + r_O}{\sqrt{2}(r_B + r_O)} \tag{1.1}$$

, where 'r_A', 'r_B' and 'r_O' are the ionic radii of cation A^{n+}, cation B^{m+}, and anion O^{2-}. In the ideal cubic case, the tolerance factor is 1. Given the tolerance factor $t < 1$, the A-O bonds are in tension, and B-O bonds are in compression. In order to relieve the stress in the crystal structure, the unit-cell lowers its symmetry from a cubic phase to a tetragonal, rhombohedral, or orthorhombic phase [38; 39]. In the case of $t > 1$, the A-O bonds are in compression and B-O bonds are in tension, and the crystal structures relieves the stress by adopting hexagonal symmetry [38; 39]. The condition of charge neutrality allows A and B cations to have valency of (+1, +2, +3) and (+3, +4, +5) respectively, forming the following possible compounds such as $A^{1+}B^{5+}O_3$, $A^{2+}B^{4+}O_3$, and $A^{3+}B^{3+}O_3$. Thus, in the family of perovskites compounds, 'A' metal can be from alkali/alkaline earth metals or rare earth metal, while 'B' metal can be from transition metals, rare earth metal or group III metals. Some examples from $A^{1+}B^{5+}O_3$ subfamily include $KTaO_3$, $LiNbO_3$ *etc.*, $A^{2+}B^{4+}O_3$ subfamily examples include $CaTiO_3$ (CTO), $SrRuO_3$ (SRO) *etc.*, and $A^{3+}B^{3+}O_3$ example include $DyScO_3$ (DSO), $NdGaO_3$ (NGO), $LaAlO_3$ (LAO) *etc.* Although the bond character in these perovskites is typically ionic, they may exhibit some covalent character.

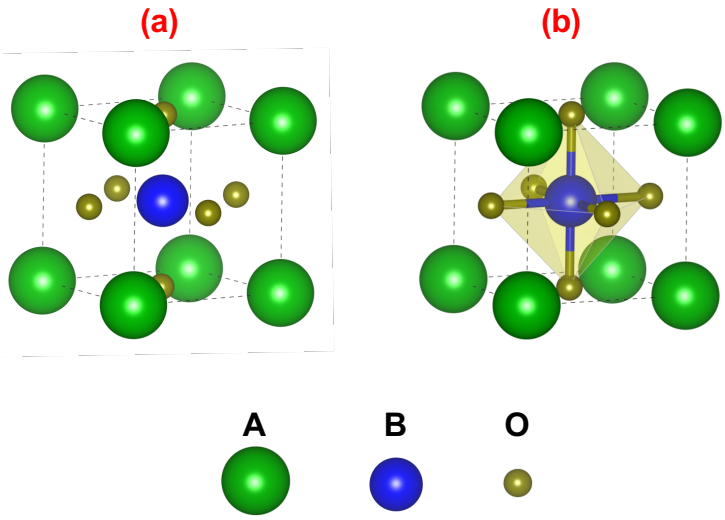

Figure 1.1: Schematic of ideal perovskite unit cell, ABO_3.

As discussed above, the subfamilies of perovskite oxides are likely to exhibit a range of crystal structures. To understand their crystal structure and associated symmetry-

lowering distortion, we will discuss the concept of BO_6 oxygen octahedra [40]. Figure 1.1(b) depicts the oxygen polyhedral formed by joining the corner of the oxygen atoms for an ideal cubic unit cell. Since there are six oxygen atoms, polyhedral formed will have eight sides, hence the name octahedral. In all perovskite compounds, every octahedral from their respective formula unit, will be connected to their adjacent octahedral via oxygen shared by the side of the cubic unit cells, forming a network of oxygen octahedral, as illustrated in Figure 1.2 (a). When the symmetry lowering from a cubic phase occurs due to a decrease in a tolerance factor below 1, oxygen octahedral (BO_6) rotates in a co-operative manner, resulting in a significant change in the spatial arrangement of the oxygen octahedron network. There are, in total, 15 different tilt patterns possible which can provide the necessary distortion to stabilize the crystal structure, resulting in a somewhat lower symmetry for a given ABO_3 composition. They are denoted by Glazer notation, and in shorthand, they describe the rotation of one octahedral with respect to adjacent oxygen, *i.e.* in-phase or out-of-phase, along a certain crystallographic direction [40]. For example, when the rotation occurs about the c-axis (*i.e.* [001]) it gives rise to tetragonal symmetry (Figure 1.2(b)) with two possible (in-phase and out-of-phase) rotational patterns denoted by $a^0a^0c^+$ and $a^0a^0c^-$ (respectively) [40]. Similarly, when rotation occurs about the [111] direction of the cubic reference unit-cell, it gives rise to Rhombohedral symmetry with a rotational pattern such as $a^-a^-a^-$ [40]. The third most common rotation is the one, which occurs along [110] direction of the cubic reference unit cell. The resulting structure assumes orthorhombic symmetry denoted by $a^-a^-c^+$ Glazer notation [40]. Examples of perovskite compounds stabilizing in these common tilt patterns are $PbTiO_3$ (PTO) and $BaTiO_3$ (BTO) in tetragonal symmetry (Figure 1.2(b)), $BiFeO_3$ and $LaNiO_3$ in rhombohedral symmetry (Figure 1.2(c)), and DSO and NGO in orthorhombic symmetry (Figure 1.2(d)). In a similar manner, other lower symmetry structures can be found from the 15 different rotational tilts patterns [40]. Note, throughout this dissertation orthorhombic directions are also referred in the pseudocubic notation. For example orthorhombic directions $[110]_o$, $[\bar{1}10]_o$, and $[001]_o$ (of DSO or NGO) represent $[001]_{pc}$, $[100]_{pc}$, and $[010]_{pc}$ directions in the pseudocubic notation respectively.

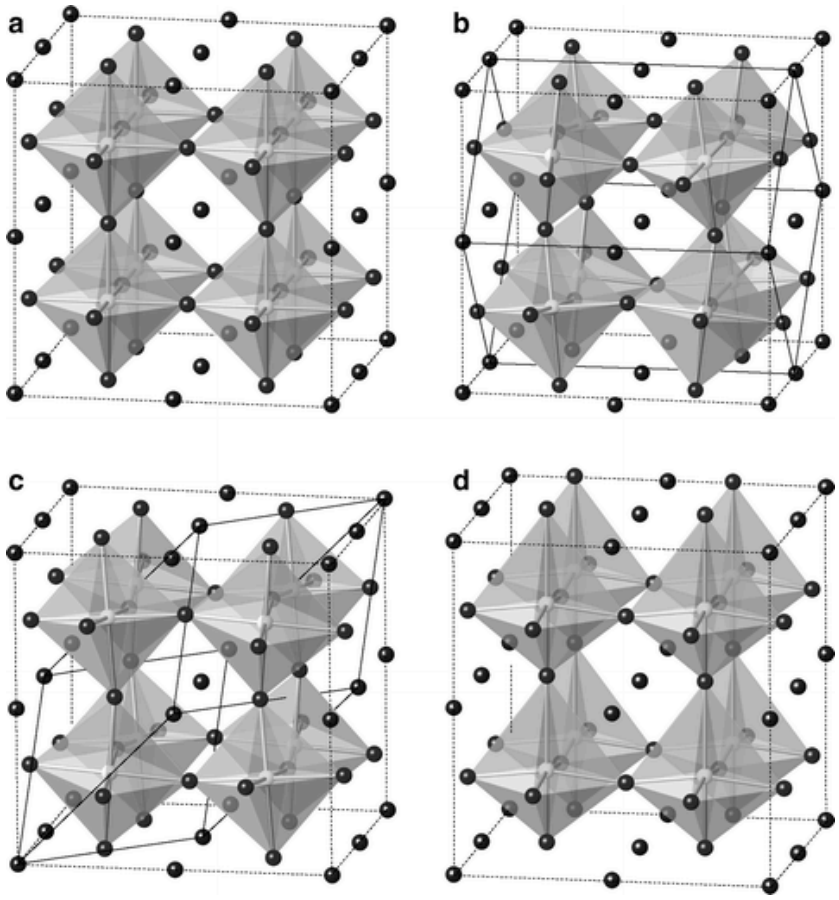

Figure 1.2: Common crystal symmetries found in perovskites: (a) Cubic, (b) Tetragonal, (c) Rhombohedral, and (d) Octahedral symmetry. From [39].

1.2.3 Electronic structure

To explain the electronic structure of perovskite oxides, we consider the STO material again and build the discussion from there. In the following description of the electronic structure of perovskite oxides, we will only consider the strong interaction present between transition metal cations (B^{n+}) and oxygen anions (O^{2-}). This is owed to the fact that the most interesting properties exhibited by these materials stem from this BO_6 oxygen octahedral, *i.e.* the interaction of '*d*' orbitals of transition metal with '*p*' (or '*s*') orbitals of oxygen anion [29; 38]. An exception to this scenario are the group B metals occupying 'A'-site, where the presence of $4f^n$ orbitals at the 'A'-site can overlap with partially filled '*d*' orbitals of 'M'-site metals which will significantly modify the electronic structure. There are a few other special cases such as the presence of lone pairs ($5s^2$ or $6s^2$) on 'A'-site metal cation, which interacts strongly with the partially-filled 'd' orbitals modifying the electronic structure [29; 38]. Having mentioned this, we begin describing

the electronic structure of STO. As noted in the previous section, at room temperature, STO crystallizes in a cubic symmetry with a unit-cell structure shown earlier in Figure 1.1 (a). Bare 'Ti' atomic orbitals have a five-fold degeneracy, which is altered when 'Ti' forms a bond with six oxygen atoms within a TiO_6 octahedral, highlighted in Figure 1.1(b) by a yellow shaded region. For the 180° bond angle between the Ti-O-Ti bond in a cubic STO, the overlap of d_{xy}, d_{yz}, d_{zx} with oxygen 2*p*-Ti orbitals and that of $d_{3z^2-x^2}$ and $d_{x^2-y^2}$ with oxygen, 2*s* or 2*p* orbitals lift the degeneracy of 'Ti' *d*-orbitals [38]. The resulting electronic structure of 'Ti' *d*-orbitals is illustrated in Figure 1.3. Note the cubic symmetry of Ti-site lifts the degeneracy in a way that antibonding π^*-states (d_{xy}, d_{xz}, d_{yz}) are lower in energy as compared to antibonding σ^*-states ($d_{3z^2-x^2}, d_{x^2-y^2}$) [29; 38]. The reason is the expectation value for virtual charge transfer between O^{2-} '*p*' orbitals and an empty Ti '*d*' states is higher for σ^*-states compared to π^*-states [38]. Finally, a split in energy level is observed with three-fold degeneracy (π^*) orbitals and two-fold degeneracy (σ^*) orbitals. This splitting in energy states is sometimes also referred to as crystal field splitting. The magnitude of the crystal field splitting is generally between 1-2 eV and is denoted by Δ_c [29; 38]. The low-energy triplet states are commonly referred to as t_{2g} and high-energy double states as e_g.

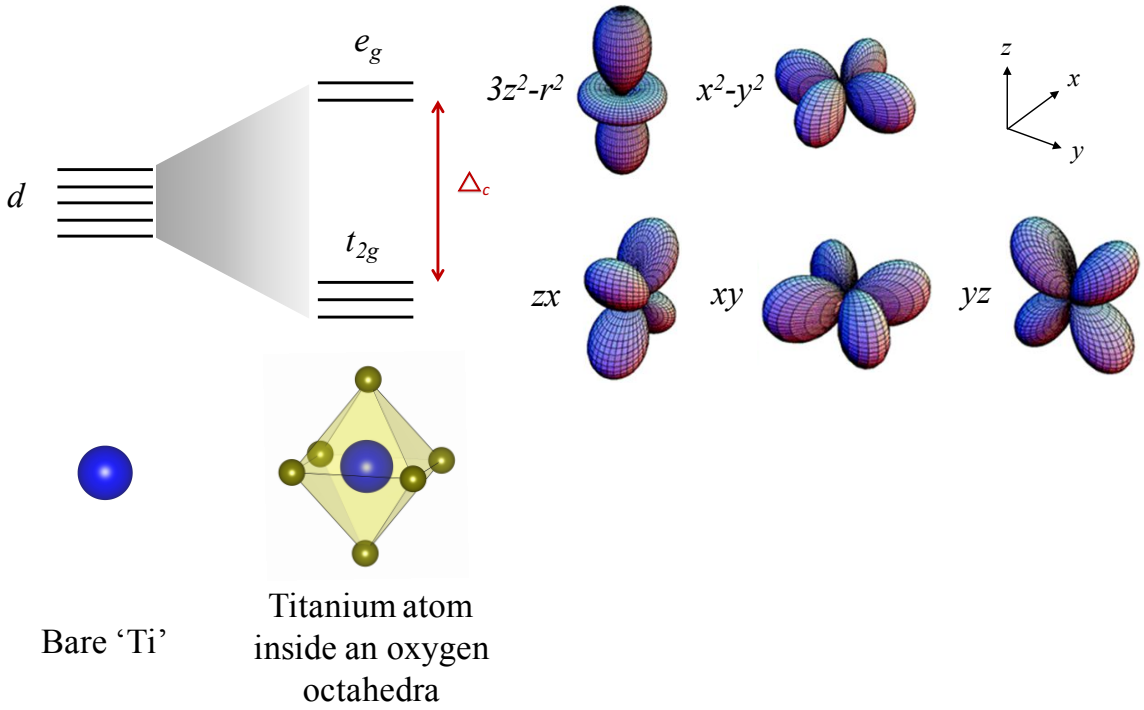

Figure 1.3: Electronic energy levels of 'Ti' *d*-orbital. The figure also depicts the shape of d-orbitals in t_{2g} (d_{xy}, d_{yz}, d_{zx}) and e_g ($d_{3z^2-x^2}, d_{x^2-y^2}$) levels. Figure adapted from [28; 41].

Now, t_{2g} states on adjacent 'Ti' atom in a crystal can couple via oxygen '*p*' orbitals present in between. This bridging between electronic 'Ti'-states via oxygen ('*p*') orbitals collectively lead to the formation of a band structure for this material [28]. Thus, when the material is doped on A-site ('Sr') or B-site ('Ti') the addition of electron will start filling t_{2g} states. The transport of these electronic carriers then takes place via hopping between t_{2g} states of adjacent 'Ti'-atoms. For these t_{2g} orbitals, the hopping matrix is much higher when the hopping takes place in the plane of the lobes of '*d*'-orbitals as compared to perpendicular [28], as illustrated in Figure 1.4. Such dependence of the hopping matrix on a crystallographic direction has a strong influence on the fermi surface in *k*-space, and thus greatly affects the transport behavior of carriers [28]. The ability to manipulate charge in the materials, thereby affecting the electronic structure, gives the charge a degree of freedom in these systems. Finally, there are two important parameters to note: first is the number of '*d*' electrons, which is also called filling number and the hopping matrix, which relates to the kinetic energy term for the transport of carriers [28].

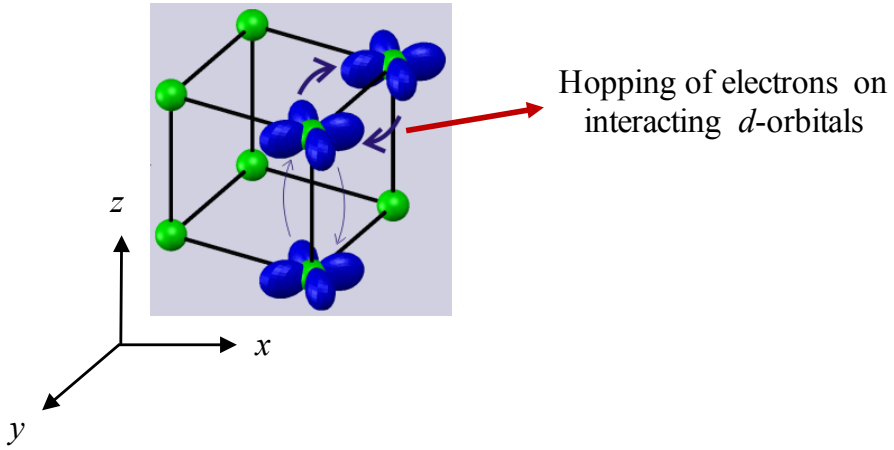

Figure 1.4: Titanium d_{xy} orbitals are depicted on neighboring Ti-sites of a cubic STO structure, illustrating a stronger hopping along *x* and *y* directions (thicker arrows) compared to *z* direction (thin arrow). Figure adapted from [28].

Recall that we considered the case of ideal cubic structure with 180°-bond angle between Ti-O-Ti in the above instance. In all other cases, where the bond angle between Ti-O-Ti is not 180°, not only will it strongly affect the kinetic energy term (hopping matrix), but also it will directly affect the electronic structure [38]. As seen in the previous subsection, a different combination of A-site/B-site metal ions in the ABO_3 perovskite structure leads to symmetry lowering in accordance with the Goldschmidt factor from a high symmetry (cubic) structure. Symmetry lowering is achieved by the co-operative movement of BO_6 oxygen octahedral (along a certain crystallographic direction), which results in the deviation of the B-O-B bond angle from 180°, leading to one of the lower symmetry structures such as tetragonal, orthorhombic, rhombohedral *etc* [38; 40]. Therefore, it is likely to modify the electronic structure and consequently the kinetic energy

for the transport of carriers. In addition, symmetry lowering can trigger other structural distortions which may induce charge ordering in the crystal. One notable example is structural instability due to small ionic radii of 'Ti' in BTO, which lowers the symmetry of BTO to a tetragonal structure. During the process, Ti^{4+} moves away from the center, thus breaking the inversion symmetry of the unit lattice [38]. The off centering of Ti^{4+} atoms with respect to the center of the oxygen octahedral leads to the generation of a dipole moment within the unit-cell. The cooperative movement of Ti^{4+} atoms in the neighboring unit cells leads to the ordering of dipole moments, which results in the creation of ferroelectric ordering in the material. Such ferroelectric distortions will further lift the orbital degeneracy of *d*-states modifying the electronic structure of the perovskite oxide [42]. From the above discussion, it follows that the manipulation of the crystal structure, by changing the composition of the perovskite compound, can significantly affect both the transport characteristics of charge and the electronic structure. It also highlights the coupling between the two degrees of freedom: charge and lattice.

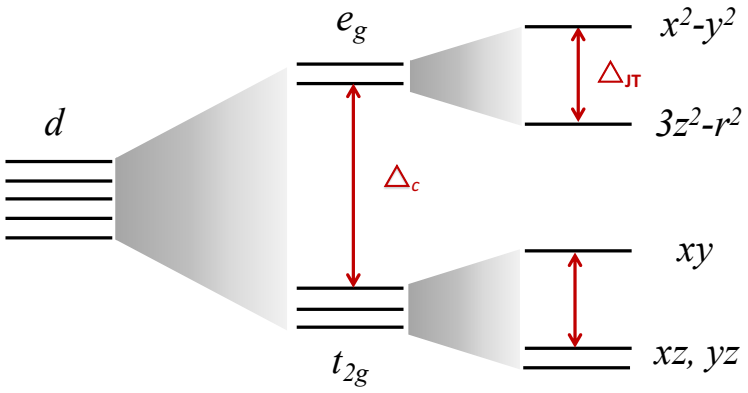

Figure 1.5: The effect of Jahn-Teller distortion on electronic structure of Titanium *d*-orbitals. [42]

The cooperative movement of the BO_6 oxygen octahedral to stabilize a lower symmetry structure is found to have a profound affect on the magnetic (spin) ordering in these perovskite oxides. While the degeneracy in 't_{2g}' and 'e_g' can be lifted by the structural distortions due to a large mismatch in ionic radii of metal ions, they can also be driven by other distortion to stabilize local electronic configuration. For example, in $LaMnO_3$ (LMO), the Mn^{3+} state has '$t_{2g}^3 e^1$' electronic configuration that is in a high spin state, and it tries to lower its energy by removing the degeneracy in *e* orbitals with the help of Jahn-Teller distortion of the MnO_6 oxygen octahedra [43]. The corresponding split in the electronic states due to Jahn-Teller distortion is illustrated in the electronic structure diagram (Figure 1.5). In general, the magnitude of the Jahn-Teller split (Δ_{JT}) is one order lower than compared to crystal field splitting [38]. The cubic symmetry, reducing to orthorhombic symmetry using cooperative movement of oxygen ions, gets superimposed onto the dominant Jahn-Teller distortion, which is the collective displacement of oxygen

ions along two of the M-O-M bond axes in the out-of-phase manner, also resulting in asymmetric bond stretching in the (001) or '*ab*' plane [38]. While the M-O-M bonds along the 'c'-axis remains unstretched, the resulting orbital ordering in the '*ab*' plane of orthorhombic LMO unit cells shows alternate $d_{x^2-r^2}$ and $d_{y^2-r^2}$ orbital occupation on Mn-sites along '*a*' or '*b*' directions as illustrated in Figure 1.6. This example demonstrates the presence of an orbital degree of freedom in perovskite oxides and further shows that the lattice can induce the ordering of ('*d*') orbitals, suggesting a coupling between the two.

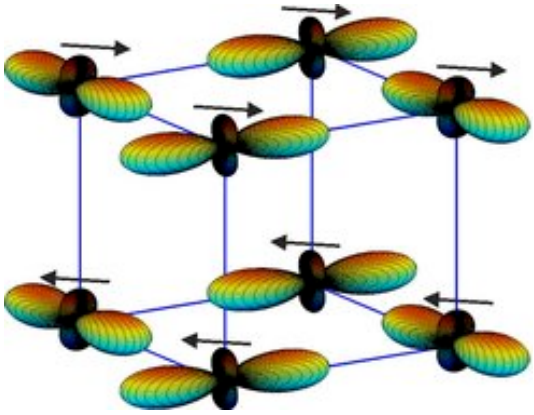

Figure 1.6: Orbital ordering in orthorhombic $LaMnO_3$. From [44].

In LMO, the symmetry lowering from cubic to orthorhombic structure driven by Jahn-Teller distortion is further accompanied by antiferromagnetic (spin) ordering, which is also shown in Figure 1.6 using black arrows at each 'Mn' site. The magnetic moment at adjacent 'Mn^{3+}' cations interact with one another through a mediator anion (O^{2-}), which is also referred to as indirect exchange interaction [30]. In the particular case of Mn^{3+} with four 3*d* electrons leads to a special case of indirect exchange interaction, referred to as super exchange interaction [30]. A schematic super exchange interaction between Mn^{3+} cation in LMO is illustrated in Figure 1.7. The hybridization between the filled oxygen orbital (shown as O^{2-}) and the half-filled '*d*' orbitals will result in the following. First, the opposite spin of electron in oxygen orbital will be donated to the Mn empty *d*-orbitals. Second, the donation of there opposite spin electrons to the two adjacent Mn^{3+} orbitals will ensure the spin of Mn^{3+} atoms is of the opposite sign, satisfying Hund's rule. Thus, through the mediator oxygen anions, the spins in the adjacent Mn^{3+} sites are aligned antiparallel to each other, giving rise to an antiferromagnetic order in the material. The antiferromagnetic ordering of moments on each Mn site is shown in the same Figure 1.6 along with the orbital ordering on Mn-sites. Since the super exchange interaction takes place via the Mn-O-Mn bond, it is apparent that the bond angle will significantly affect the super exchange interaction [30]. Hence, any further tilting of MnO_6 octahedral will not only affect the super exchange interaction but also affect the kinetic energy for the transport of carriers.

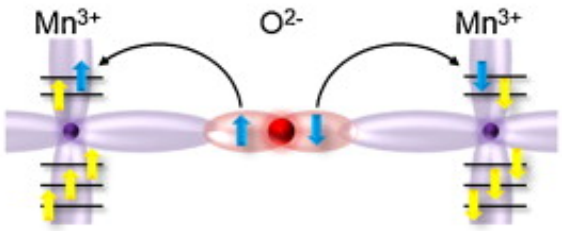

Figure 1.7: A schematic of super exchange interaction in $LaMnO_3$. From [30].

We learned from the above example of LMO that change in crystal structure can strongly affect the ordering of both spin and orbitals, further suggesting a coupling between lattice, spin and orbital degrees of freedom. An even more interesting case arises when LMO is doped with substituent, which results in mixed valence, Mn^{3+} and Mn^{4+}, states in the lattice. Let us take the example of $LaMnO_3$ doped with 'Sr' with the final composition $La_{0.7}Sr_{0.3}MnO_3$ (LSMO). In this case, adjacent manganese atoms interact via oxygen anion, which acts as the mediator. A schematic illustration of the indirect exchange interaction is shown in Figure 1.8. The ground state electronic configuration of both valence states Mn^{3+} and Mn^{4+} states (according to Hund's rule) is drawn in Figure 1.8. Due to the hybridization between oxygen filled orbitals and manganese partially filled orbitals, the oxygen (O^{2-}) '*p*' orbital can donate one electron to the Mn^{4+} site, having the same spin as the electrons on Mn^{4+} to have lower energy configuration according to Hund's rule. The extra electron from the Mn^{3+} site will then fill the vacant oxygen orbital. Therefore, the overall electron transfers from an Mn^{3+} site to an Mn^{4+} site ensures that the spin of the electron does not change during the charge transfer process. As a consequence, it results in the ferromagnetic ordering, *i.e.* parallel alignment of moments on the adjacent Mn-site and the delocalization of electrons over Mn-O-Mn groups make this material metallic [30]. Thus, $La_{0.7}Sr_{0.3}MnO_3$ perovskite oxide becomes a ferromagnetic metal. Note how adding an electron charge in $LaMnO_3$, creating mixed valence states of Mn^{3+} and Mn^{4+}, not only completely changed the magnetic (spin) ordering from antiferromagnetic to ferromagnetic but also changed the electron transport from insulating to metallic. With this example, a strong coupling between charge, spin, orbital and lattice degrees of freedom is noted in these perovskites oxides.

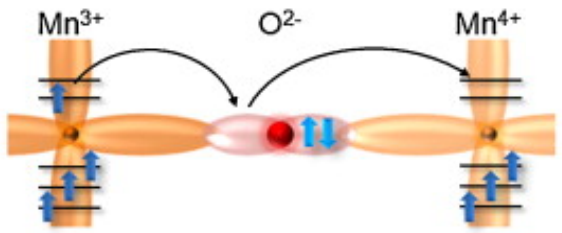

Figure 1.8: A schematic of indirect exchange interaction in $LaMnO_3$. From [30].

In addition to all of the structural changes that alter the symmetry of the lattice, the electronic structure can also be modified by other effects such as the presence of spin-orbit coupling which can further split the energy levels owing to the interaction between the spin of electron and its motion in an orbital. Usually, spin-orbit coupling scales with the atomic number of an atom as Z^4 [45]. For 3*d* transition metals such as 'Ti' and 'Mn', the spin-orbit coupling is weak, but for 4*d* or 5*d* transition metals such as 'Ir', it may result in a significant change of the electronic structure [46]. Finally, we conclude that the orbital degeneracy of B-site cation can be removed by a number of effects including crystal field splitting, spin degeneracy (Hund's rule) and spin-orbit coupling, which can strongly affect the electronic structure and its properties.

In summary, we note that by replacing metal cations at A-site and/or B-site with other metal cations, the mismatch between the ionic radii can significantly modify the symmetry of the crystalline lattice, which will further alter the electronic structure of the compound. The degeneracy in the valence orbitals can also be modified by a number of interactions such as Hund's interaction, spin-orbit interaction and the Jahn-Teller effect. Since the dopant element can further modify these intra- and inter-atomic interactions, they are observed to strongly affect the electronic structure of the compound. As a consequence, the various degrees of freedom such as charge, spin, orbital, and lattice present in perovskite oxides are coupled with one another (illustration in Figure 1.9). In the bulk perovskite oxides, this coupling led to several unique phenomena only found in these materials such as colossal magnetoresistance [47], metal-to-insulator [48], and superconductor-to-insulator transition [49] *etc.* While the bulk perovskite still remains an active route to control the properties, in the past decade or so oxide interfaces showed an entirely new route to exploit the interaction between the four degrees of freedom. The interface between two oxides can enable effects such as inversion symmetry breaking, electrostatic interaction between polar oxides, frustration of spins and charge transfer across the interface. Thus, these interfaces can significantly modify the electronic structure at interfaces, or even create new electronic phases at the interface. For example, the discovery of two-dimensional electron gas at the interface of two insulators, LAO and STO, is found to exhibit both superconductivity and magnetism [50]. When these oxide interfaces, where different order parameters can couple, is utilized in artificial heterostructures such as superlattices, a wealth of new physical phenomena has been discovered. In the next section, I will discuss numerous examples from various subjects of research in complex oxides where artificial superlattices proved worthy as a promising nanostructured system for exploring a new physics that is fundamentally different from their bulk materials.

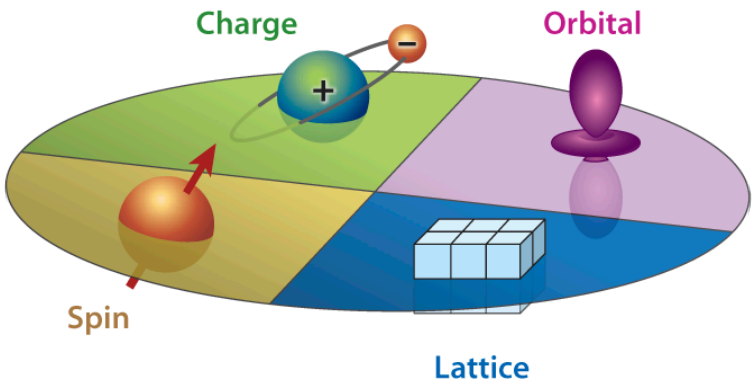

Figure 1.9: A schematic of various degrees of freedom present in complex oxides. Figure adapted from [27].

1.3 Superlattice structures and their Importance

1.3.1 Introduction

As discussed in the previous section, complex oxides, being a strongly correlated material system, are known to exhibit a plethora of fascinating properties. These properties can be largely linked to the characters (ionic radii, valence state) of a specific transition metal ion occupying 'A'- and 'B'-sites in the chemical composition ABO_3 and the crystal structure of the compound. In order to develop the next generation of functional devices based on such radically different electronic and magnetic properties of these complex oxides there is a critical need for an in-depth understanding of their physical phenomenon and for finding routes to control their properties in a systematic fashion. Although both the conventional and solid-state synthesis method and thin-film synthesis methods are perfectly capable of manipulating their properties, and successfully shown to do so, these methods have begun to saturate exhibiting the necessary progress needed in manipulating properties. One of the main reasons is their inability to achieve atomic-scale control. One such example is attaining the desired spatial profile for the chemical substitution in a host lattice. The uncontrolled substitution with only a fraction of volume of the substituent atoms as the controllable parameter leads to the perturbation of local lattice distortion and the related change in electronic states at the undesired lattice sites. Ideally, one would like to control both the spatial profile and the concentration of substituents/dopants to systematically study their role in the property being investigated. In this regard, artificial heterostructures provide a powerful way to achieve the desired spatial arrangement and concentration of an "artificial" single crystal, synthesized by growing different materials stacked on top of each other along a certain crystallographic direction. Perhaps a most suitable example to support this argument is the atomic controlled ordering of Fe^{3+}-O^{2-}-Cr^{2+}, which is needed to enable the observation of theoretically-predicted ferromagnetic

ordering arising due to the super exchange interaction between Fe^{3+} and Cr^{2+} cations via O^{2-} anion. This task of achieving the desired ordering has been particularly challenging in the solid-state synthesis of $LaFe_xCr_{1-x}O_3$ due to the random substitution and/or phase separation of iron and chromium oxides [51]. By synthesizing artificial heterostructures of periodic alternating layers of $LaCrO_3$ and $LaFeO_3$ along [111] crystallographic direction [51], the desired spatial and concentration profile of cations and ions were achieved leading to the theoretically predicted observation of ferromagnetic ordering in the new artificial compound. The other key advantage of artificial heterostructures is to combine materials with completely different properties (such as ferroelectric materials with magnetostrictive material) to achieve multifunctional heterostructures or "new" compounds with desired properties (magnetoelectric coupling, respectively). As will be discussed later, such multifunctionality, as in magneto electric coupling and ferroelectricity, has been achieved experimentally in heterostructures composed of materials with different bulk properties. Lastly, the structural and chemical compatibility present within a family of perovskite oxides further facilitates the stacking of different oxides in a desired manner to synthesize designed artificial heterostructures.

With ever-increasing degrees of maturity in synthesis and characterization of thin-film complex oxides [30; 52], combined with strong coupling between spin, charge, orbital and lattice degrees of freedom, artificial heterostructures of complex oxides emerged as a flourishing field exhibiting a wealth of novel phenomena [27; 53; 54]. In the next section, I will discuss a specific type of heterostructure, *i.e.* superlattice structure, which has been immensely employed across various areas of research and repeatedly proven huge potential in delivering the promises held by such an exotic family of materials.

1.3.2 Superlattice structures

A superlattice is a structure formed when two (or more) different materials are stacked on top of each other in a periodic manner. The resulting structure can be viewed as a single crystal with an effective "super" unit cell, which is composed of two building blocks (unit cells) of two dissimilar materials. An example of a superlattice structure of PTO and STO is shown in Figure 1.10. The figure illustrates a superlattice structure composed of 3 unit cells of STO and 3 unit cells of PTO repeated in periodic fashion, resulting in a super cell having 3-unit cells of PTO plus 3-unit cells of STO as the effective unit along the '*c*' axis lattice parameter of the new crystal. The "new" effective unit cell is highlighted in Figure 1.10 by the dotted red line. From the design of the new effective unit-cell, one can imagine other superlattice structures with different effective super cells. For example, in the previous case, instead of having the same number of unit-cells (three) for both PTO and STO, we can have an unequal number of unit-cells of PTO and STO, for instance 2 unit-cells of PTO and 5 unit-cells of STO, making a super cell of 2 unit-cells of PTO plus 5 unit-cells of STO as the effective '*c*'-axis lattice parameter of the new crystal (see Figure 1.11(a)). Such kinds of superlattice structures are sometimes referred as asymmetric superlattices. The previous example (having the same number of unit-cells of two dissimilar materials) is referred to as symmetric superlattices. Note that one can also

design a complex *effective* unit cell in a similar fashion by having more than one building block of material A and B in the super cell of the superlattice structure. An example is illustrated in Figure 1.11(b), which has 4 unit-cell PTO plus 2 unit-cell STO plus 1 unit-cell PTO plus 3 unit-cell STO as the effective unit cell of the superlattice structure. Based on the number of unit cells of material A and material B chosen to make the *effective* unit-cell, there are a number of symmetric, asymmetric, and complex unit-cell superlattices.

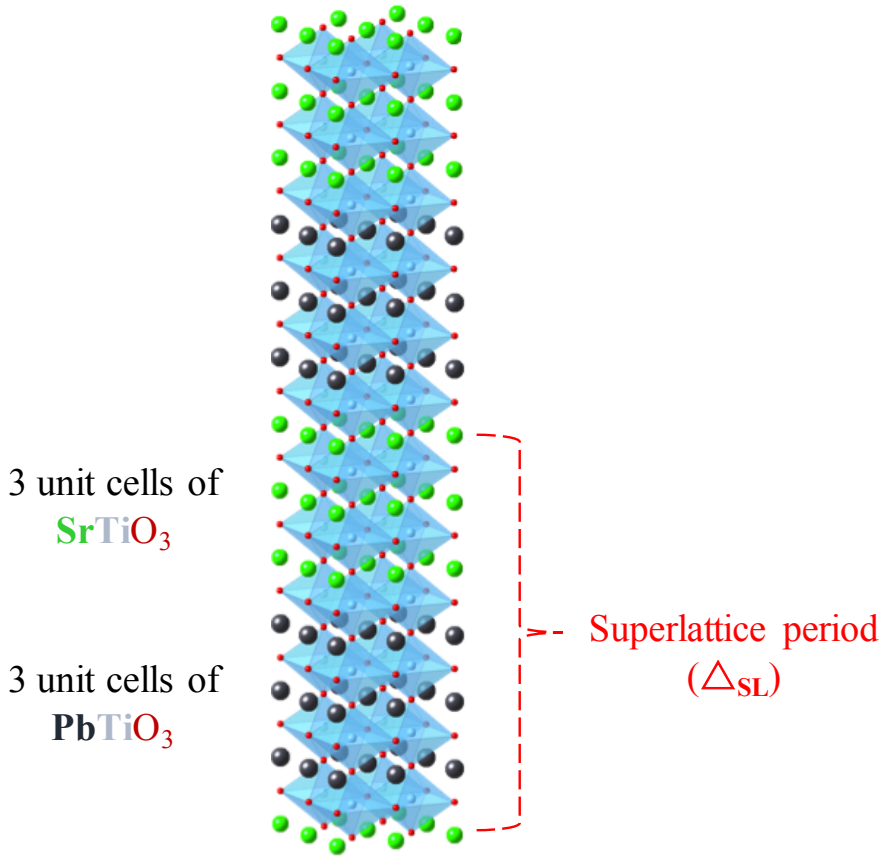

Figure 1.10: A schematic of 3 x 3 PTO-STO superlattice. Figure adapted from [55].

In the above examples of various kinds of superlattice structures, two different materials are combined to build the effective unit cell of the superlattice. They are often designated as bi-color superlattices as two dissimilar materials are used. One can extend the concept to more than two materials, such as superlattices composed of three materials – A / B / C, or four materials – A / B / C / D and so on. Such superlattices are designated as tricolor or multicolor superlattices. In these multicolor superlattices, one can design symmetric, asymmetric, or complex effective unit-cell, generating various kinds of higher-order superlattices. With the number of unit-cells of each material as an–independent variable, there are many possibilities for creating artificial crystals of three-component or

multi-component superlattice structures. Thus, the inherent nature of the superlattice structure allows us to design a large number of effective unit cells with many possibilities.

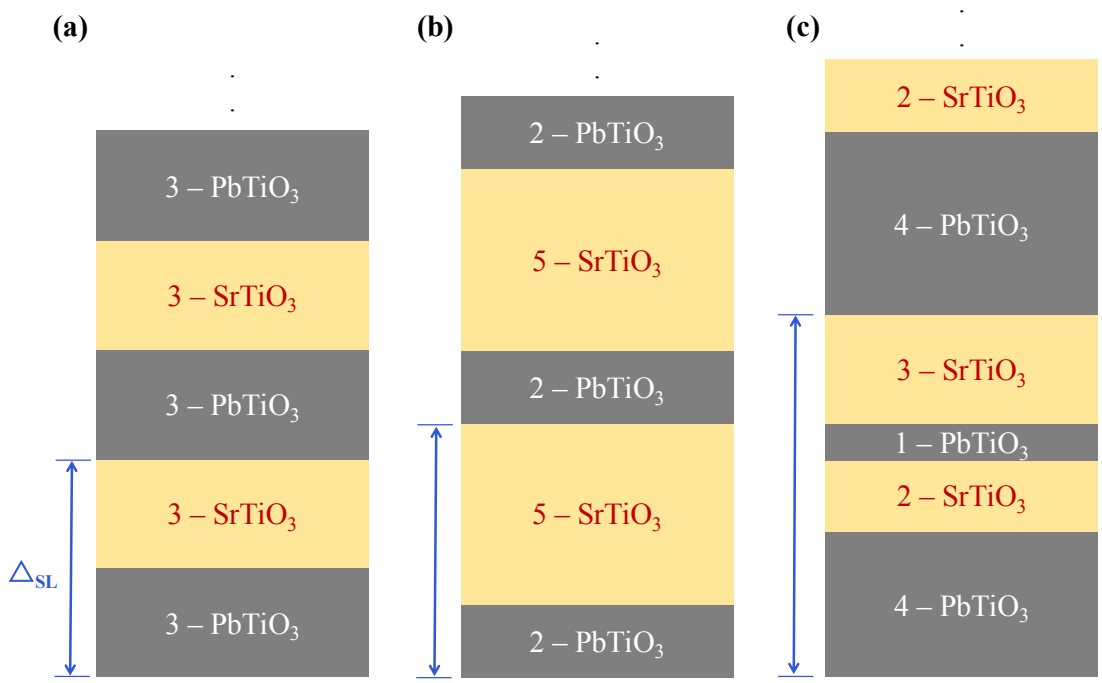

Figure 1.11: A schematic of various possible superlattice structures of PTO-STO, (a) 3 x 3 symmetric superlattice, (b) 2 x 5 asymmetric superlattice and (c) complex unit-cell superlattice. The repeating unit, *i.e.* superlattice period (Δ_{SL}), is also highlighted for all three-superlattice structures.

Interestingly superlattices are found in both naturally occurring phases and artificially synthesized man-made single crystals. One notable example of naturally occurring superlattice is Ruddlesden-Popper phases such as $Sr_{n+1}Ti_nO_{3n+1}$, which are composed of alternating layers of n-unit cells of perovskite oxide (STO) and 1 unit-cell of rock salt (SrO) layers forming a natural superlattice along the [001] direction of the crystal. Figure 1.12 illustrates natural superlattices for a few values of '*n*', which also shows examples of symmetric (*i.e.* $n = 1$), and some asymmetric (*i.e.* $n > 1$) superlattices. Another suitable example of the naturally occurring superlattice phase is Aurivillius compounds [31] with the general formula $(Bi_2O_2)(A_{n-1}B_nO_{3n+1})$, examples of which are $SrBi_2Nb_2O_9$, $Bi_4Ti_3O_{12}$ *etc.* In these Aurivillius compounds, (Bi_2O_2) layers are alternated with *n*-unit cells of perovskite-like $(A_{n-1}B_nO_{3n+1})$ units along [001] direction of the crystal. In these compounds, both symmetric ($n = 1$) and asymmetric ($n > 1$) superlattices can be identified. Similarly, other equilibrium phases such as Dion-Jacobson phases ($A'[A_{n-1}B_nO_{3n+1}]$), can be found in nature where alternating layers of dissimilar elements self-order to form a natural superlattice along a specific crystallographic direction.

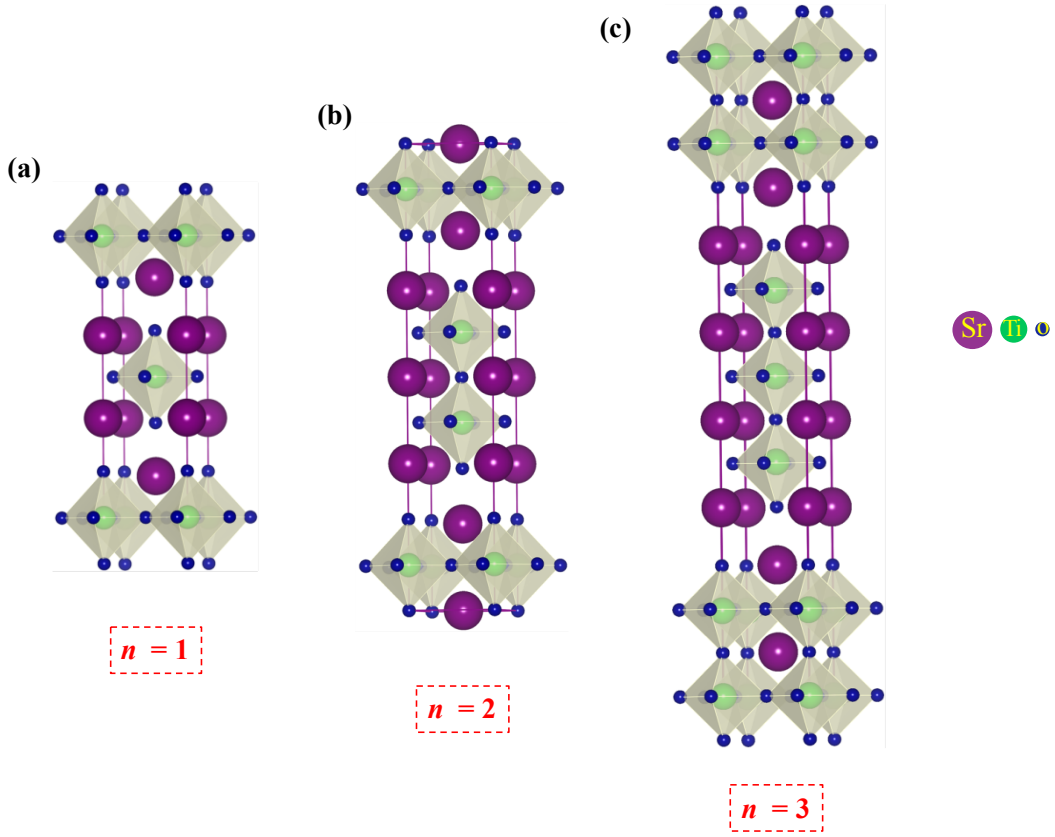

Figure 1.12: The crystal structure of Ruddlesen-Popper phases of $Sr_{n+1}Ti_nO_{3n+1}$ for (a) n = 1, (b) n = 2, and (c) n = 3 is depicted in this diagram. Figure adapted from [56].

In the artificially designed man-made single crystals, superlattice structures have been grown for a wide range of materials from organic to inorganic materials. More specifically, among inorganic materials, superlattices are composed of two different metals, a metal and a semiconductor, two semiconductors, a semiconductor and an insulator, and two insulators, have been successfully synthesized and employed for studies across various areas of research. In this thesis, I have mostly focused on complex oxides as the material system and Figure 1.13 provides a few examples of complex oxide superlattice structures which were employed for various investigations (PTO-STO, BTO-STO, LMO-STO, CTO-BTO-STO *etc.*). Although bicolor superlattices have been most widely used across various fields, tricolor superlattices such as $NdMnO_3$-$SrMnO_3$-$LaMnO_3$ [57], LAO-LSMO-STO [58] *etc.* have also been studied. It is important to note that superlattice structures such as the tricolor superlattice can help to break the inversion symmetry of the structure [58], thus making them suitable for studies such as magneto electric coupling [57].

The above discussion of naturally occurring superlattices and artificially designed superlattices brings us to an important concept of superlattice structures. Notice how choosing one unit-cell blocks of individual components (example: SrO and STO for n = 1

RP phase of $Sr_{n+1}Ti_nO_{3n+1}$) forms a new compound (which in the case of n = 1 RP phase also happens to exist in a natural bulk crystal) with the *interface* between the two components losing its meaning. In other words, the superlattice structures having only a few unit cells as the effective unit cell (also known as the superlattice period) may start to exhibit completely different physical behaviors as compared to their parent constituting materials. This particular concept of superlattices has been used significantly in exploring novel phenomenon in complex oxides and will be discussed in detail later. Moreover, the meaning of interface becomes arbitrary with the transition from a regime of thick effective unit-cells (or thick superlattice period), in which individual materials are thick enough to form an *interface*, to a regime of thin effective unit-cells (or thin superlattice period).

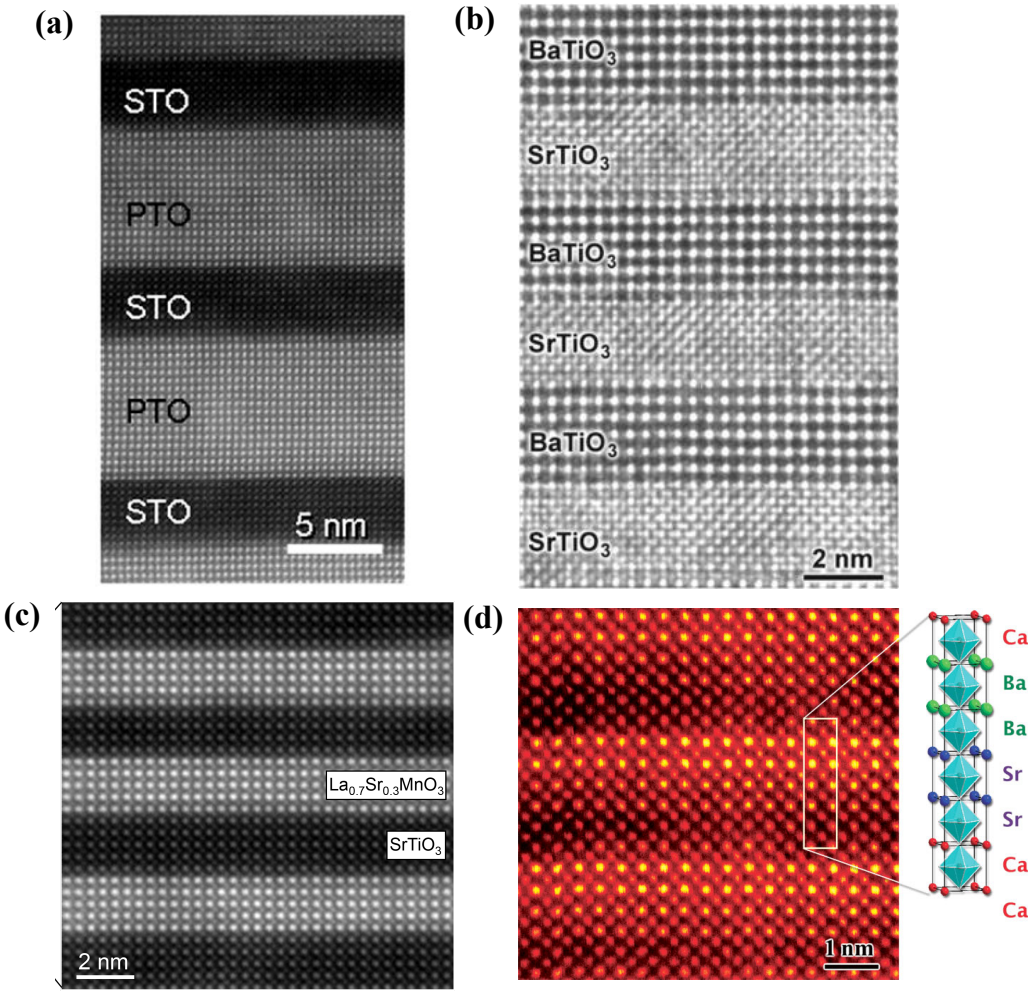

Figure 1.13: Superlattice structures of complex oxide material system are shown. Cross-section TEM of bicolor superlattice (a) PTO-STO, (b) BTO-STO, (c) LSMO-STO, and tricolor superlattice (d) CTO-BTO-STO are depicted. These figures are adapted from [59-62].

The other important concept of superlattices (for examples A and B) is that these artificial structures are representing metastable phases of a system comprised of individual components of the superlattice. This essentially means that the equilibrium phase diagram of a system composed of individual components of the superlattice (in their respective volume fraction) will not exhibit these periodically long-range ordered superlattice phases (of course the naturally-occurring superlattices are exceptions). Thin-film synthesis techniques such as Pulsed Laser Deposition, which are inherently non-equilibrium in nature, stabilizes these metastable structures [31]. The kinetically driven nature of the deposition process ensures a high activation energy barrier for the atoms to diffuse across the superlattice structure, disallowing the achievement of thermodynamic equilibrium and forcing them to freeze in the metastable state. From this, one can imagine a boundless number of possibilities for synthesizing metastable states of various materials with unique degrees of freedom, opening a large phase space to explore novel physics in material systems.

In addition to the fundamental advantages of studying the superlattice structures discussed above, there are more merits to their inherent periodic structure, which makes them one of the most promising candidates for studying nanoscale physics. Foremost of notice is the ability of superlattice structures to study phenomena related to interfacial physics. For instance, interfaces between two complex oxides have shown a multitude of novel phenomena such as the discovery of two-dimensional gas (2DEG) at LAO/STO interface and the associated unique properties such as magnetism and superconductivity in 2DEG at their respective interfaces [50]. Superlattice structures are ideal to study such novel phenomena at the interfaces and at the length scale of the interaction at the interfaces (leading to novel properties). This particular scheme has been applied across various fields to understand new interfacial phenomena exhibited by them. Moreover, the inherent periodic structure of the superlattice allows for multiplying the number of interfaces in a film, thus enhancing the detectability of those phenomena by increasing the signal to noise ratio. Similarly, if the physical phenomenon is central to the thickness of either constituents, an example of which will be discussed in chapters 5 and 6, the superlattice structure can increase the volume fraction of these nanoscale features bringing them closer to detectability limits of the characterization tools used for their study. Lastly, since the superlattice structures can be synthesized in thin-film form using the highly controlled thin-film growth technique currently available, the structure allows us to use standard characterization techniques to perform characterization of the nanoscale phenomena and their effect on macroscopic property.

1.3.3 Significance of Artificial Superlattices

Having discussed the different types of superlattices along with the unique advantages presented by them, we now turn our attention to studies employing superlattices as their primary sample structure for investigations. Since this thesis presents work based on complex oxides as materials system, I will limit our discussion to the advances enabled by the superlattice structures in the field of complex oxide research. In the time span of a

decade or so, superlattice structures composed of complex oxides expanded the prospects for observing unique and unprecedented physical phenomena in various areas of research. Some examples of these subjects of research are superconductivity, ferromagnetism, ferroelectricity, and thermoelectrics. I will begin our discussion with contributions made by superlattices in the area of superconductivity.

In the early works on cuprite superconductors, artificial superlattice structures attracted great attention due to the inherent layered crystal structure of cuprates (such as LBCO, YBCO *etc.*) resembling that of a heterostructure. Some of the High-T_c superconductors discovered in the early 1990s, were essentially artificial *metastable* superlattice structures [63; 64]. An example is the pioneering work of Li *et al.* [63], synthesizing superlattice structure composed of 3-unit cells of $BaCuO_2$ and 1-unit cell of $CaCuO_2$ which formed a new superconducting compound. Note that neither $BaCuO_2$ and $CaCuO_2$ are superconducting by themselves and provide an example of a new metastable compound that can by synthesized using artificial superlattice structures which may exhibit fundamentally different properties compared to its parent constituents. In another instance artificial superlattices of $SrCuO_2$ (SCO) and $BaCuO_2$ were reported to improve the T_c (transition temperature) of the new superconducting phases formed by the superlattice of $BaCuO_2$ and $SrCuO_2$ [64], *i.e.* $Ba_2Sr_{n-1}Cu_{n+1}O_{2n+2+\delta}$, $Ba_4Sr_{n-1}Cu_{n+3}O_{2n+6}$ *etc.* Again, the superlattice constituents $SrCuO_2$ and $BaCuO_2$ do not show superconductive behavior in their individual bulk forms. Similarly, there were many studies on metastable compounds using artificial superlattice structures that provided a great platform to explore superconducting properties in cuprate oxides. In addition, the ability to change the layer spacing in superlattice structures, examples in cuprate oxides such as $Bi_2Sr_2CaCu_2O_8/Bi_2Sr_2CuO_6$ [65], $YBa_2Cu_3O_7$ (YBCO)/$PrBa_2Cu_3O_7$ superlattices [66], provided a great depth for understanding the dimensionality of the superconducting state in these cuprate oxides (YBCO, $Ba_2Sr_2CaCuO_2$ *etc.*). Similarly, varying the layer thickness in the superlattice period was found to strongly affect the superconducting phase transition temperature (T_c) in artificial superlattices such as $(LaSr)_2Cu_4O_4/Sm_2CuO_4$ [67], YBCO/LCMO [68] *etc.*, revealing the presence of interlayer interactions on the electronic ground state of superconducting constituents (LSCO, YBCO respectively). Additionally, superlattice structures were applied for probing the limits of the interaction range of the proximity effect in ferromagnetic/superconductor superlattices such as LCMO/YBCO [69; 70]. Superlattice structures were further utilized for studying the interaction between the order parameters of the superconducting layer and ferromagnetic layer in enabling unusual phenomena such as the metal-insulator transition induced by proximity effects in YBCO/LCMO superlattices [71], magnetism at the interface of YBCO/LCMO superlattices [72] *etc.* Lastly, novel properties were also observed in artificial superlattices, like negative refractive index [73] for light of wavelength in millimeters. Here, the negative permittivity of superconducting layers interacts with the negative permeability of ferromagnetic layers to induce negative refractive index.

This brings us to the field of ferromagnetism, where artificial superlattices have made significant contributions. I will begin our discussion with the most noteworthy example of ferromagnetism observed in the superlattice structures of two antiferromagnetic oxides, *i.e.* $LaFeO_3$ and $LaCrO_3$. Unsuccessful attempts to synthesize ABO_3 compounds,

having Cr^{3+} and Fe^{3+} in a mixed ratio on B site, are due to the phase separation of iron oxide and chromium oxide phases in conventional solid state synthesis (thermodynamic equilibrium process) [74]. This obstacle further impeded the observation of ferromagnetic ordering arising from the super exchange interaction between Cr^{3+} and Fe^{3+} through the oxygen ion as predicted by theory for this system [75]. The epitaxial stabilizing of $LaCrO_3$ and $LaFeO_3$ in an artificial superlattice grown along [111] direction results in the metastable state of the $LaCrO_3$ and $LaFeO_3$ system with a desired metal bridge formed by oxygen anions. Indeed, by synthesizing 1-unit cell of $LaCrO_3$ by 1-unit cell of $LaFeO_3$ artificial superlattice, a ferromagnetic order is introduced into the system through the interaction between the iron layer and chromium layer, having saturation magnetization close to the theoretically predicted value for Cr^{3+} and Fe^{3+} order. Further note that when the period of the superlattice is increased to a 7-unit cell of $LaCrO_3$ by 7-unit cell of $LaFeO_3$, the saturation magnetization was reduced [51]. This provides a unique example of how an artificial superlattice can enable the stabilization of a metastable state, which has not been realized using conventional equilibrium synthesis techniques, and can possess unique properties, which are not found in either of their constituent materials. Further, superlattice periods were shown to tune their unique properties (such as ferromagnetism in the above case). Another notable example of superlattice structures inducing unusual phenomena not present in their parent materials is $LaNiO_3$-$LaAlO_3$ superlattice. This superlattice shows metal-insulator transition and antiferromagnetic order in 2-unit cell of $LaNiO_3$ by 2-unit cell of $LaAlO_3$ superlattice structures upon cooling below certain temperatures [76]. In contrast, the bulk $LaNiO_3$ shows metallic behavior at all temperatures and does not exhibit any magnetic phase transition from paramagnetic to antiferromagnetic order [77]. The bulk of $LaAlO_3$ is a wide band gap insulator and does not show any metal-insulator transition [78]. Furthermore, by changing the superlattice periodicity to a 4-unit cell of $LaNiO_3$ by 4-unit cell of $LaAlO_3$ the bulk behavior of $LaNiO_3$ was restored [76]. This example provides more evidence of metastable phases stabilized by superlattice structures and also the ability to tune their property by changing their superlattice period. There are similar examples of properties of superlattice structures, which are otherwise not observed in its constituents. For example, synthesizing a superlattice of $CaMnO_3$ and $CaRuO_3$ shows magnetic order [79], which is not present in either of the bulk constituents. In bulk, $CaMnO_3$ is antiferromagnetic order and insulating in nature [80], while $CaRuO_3$ is paramagnetic and metallic [81]. Superlattices of $CaMnO_3$-$CaRuO_3$ were observed to exhibit ferromagnetic transition at temperatures below 95 K [79]. Interestingly, in this case when the superlattice period was varied, magnetization normalized with respect to total number of interfaces revealing independence of the ferromagnetic ordering on layering thickness [79]. Thus, suggesting that the phenomenon of ferromagnetism in superlattices of paramagnetic/antiferromagnetic materials is purely interfacial. Another example is the $LaMnO_3$/$LaNiO_3$ superlattice where the presence of interfacial coupling between antiferromagnetic ($LaMnO_3$) and paramagnetic ($LaNiO_3$) material at the superlattice interfaces induced ferromagnetic order in the superlattice structure [82]. In this case also, the property (magnetization in this case) was found to be tunable through the change of the superlattice period. Furthermore, the strength (or length-scale) of interfacial coupling between $LaMnO_3$ and $LaNiO_3$ was similarly determined by independently varying the

thickness of either $LaMnO_3$ or $LaNiO_3$ in the superlattice structure, which showed a maximum of around 5 x 5 superlattice periodicity, confirming the interfacial origin of this phenomenon [82]. Finally, we note that there are many similar examples where using a superlattice structure has shown remarkable success in enabling new electronic ground states. For example, in $(SrMnO_3)_n$-$(LaMnO_3)_{2n}$ superlattices, a ferromagnetic metallic behavior was observed for $n < 3$, while an insulating behavior for $n > 3$ [83] revealing the role of interfacial effects such as oxygen octahedral in dictating ferromagnetic properties of $LaMnO_3$-STO superlattices [84].

The reach of superlattice structures was not limited to the field of superconductivity and ferromagnetism but they have proven to be equally powerful in the field of ferroelectrics [85]. We begin the discussion with an example of a superlattice structure possessing a fundamentally different property compared to its bulk constituents. The superlattice structure of $SrZrO_3$-STO was found to be ferroelectric as a whole, in spite of the fact that its constituents are not ferroelectric in bulk form [59]. These superlattices were further observed to exhibit superlattice-period-dependent dielectric response and ferroelectric behavior, which indicates the tunability of ferroelectric properties in superlattice structures. The second example is the tricolor superlattice of $NdMnO_3$-$SrMnO_3$-$LaMnO_3$, which was reported to be ferroelectric as a whole [57], while the constituents were not ferroelectric in bulk form. Here too, the tunability of ferroelectric characteristics such as spontaneous polarization, phase-transition temperature *etc.* was demonstrated by varying the superlattice periodicity [57]. The presence of antiferromagnetic order in all of the three manganites ($LaMnO_3$, $SrMnO_3$, $NdMnO_3$), in conjunction with ferroelectric behavior, allowed these superlattices to exhibit enhanced magneto electric coupling [57] with more than 100% change in polarization under the influence of a magnetic field. The observed unique behavior was attributed to the space inversion symmetry broken by the inherent tricolor superlattice structure (enabling the asymmetry in A-site cations), and the multivalency of Manganese cations (Mn^{3+}, Mn^{4+}). A third unique example is the emergence of *improper* ferroelectricity [86] in superlattices of a (proper) ferroelectric (PTO) and paraelectric (STO) material. The structural instability resulting in the necessary symmetry lowering operation for the onset of ferroelectricity in superlattices of PTO-STO is the antiferrodistortive (AFD) distortion of oxygen octahedral near the PTO-STO interface [86]. This non-polar AFD distortion in STO layers near the interface was found to be the key element in stabilizing a completely different ferroelectric ground state in superlattices as compared to what is normally expected in polar zone-center distortion-driven ferroelectric instability in bulk PTO. Superlattice-period-dependent investigation revealed that this phenomenon is purely interfacial and was observed to diminish as the layering thickness of STO is increased in the superlattice structure [86]. This phenomenon was further observed to exhibit an unusually large dielectric constant with temperature-independent behavior, which is a characteristically different behavior compared to other improper ferroelectric materials [86]. The fourth example is another unique case where the enhancement in ferroelectric properties of a known-ferroelectric material was achieved by combining it with non-ferroelectric materials in a superlattice structure. When BTO, a very well known ferroelectric material, is grown with two non-ferroelectric oxides such as CTO and STO, the polarization of the whole superlattice

structure was enhanced by 50% [59] to the bulk value of BTO. Further, this enhancement is attributed to a large compressive strain on BTO unit cells favoring *c*-axis polarization in addition to interfacial effects and the influence of space-inversion symmetry breaking in the tricolor superlattice structure [59]. Finally, we note that many studies on tuning the unique ferroelectric properties using superlattice structures such as enhanced tunability of dielectric constant in BTO-STO superlattices [87], PTO-CTO superlattices [88] and improvement in piezoresponse of PTO-CTO superlattices [88] have been reported.

Now, I will discuss a few examples of the contributions made by superlattice structures in the area of thermoelectricity. In this case also, superlattices exhibited great potential in enabling the observation of unique phenomena and tunability of thermoelectric properties. We begin with an example of a superlattice structure exhibiting a fundamentally different property. An example is the Seebeck coefficient or thermopower of a superlattice when compared to its superlattice constituents. Superlattices of metallic $La_{2/3}Ca_{1/3}MnO_3$ and superconductive $YBa_2Cu_3O_7$ were observed to exhibit a positive Seebeck coefficient as a whole [89], in spite of the fact that thin films of LCMO and YBCO grown under the same conditions showed negative Seebeck coefficient. Note that the Seebeck measurement was done above the superconductive phase transition temperature (T_c) of YBCO. While maintaining positive thermopower for all superlattice periodicities, it was noted that thermopower could be further tuned by varying the superlattice periodicity [89]. The reversal of the sign in thermopower was attributed to electronic reconstruction at the superlattice interfaces, whose effect is long-range and may not be limited to interfaces. Another notable example is a five-fold increase in the observed thermopower of $SrNb_{0.2}Ti_{0.8}O_3$-STO superlattices as compared to bulk STO [90]. This tremendous enhancement in thermopower was achieved by the presence of a two-dimensional electron gas (2DEG) at each interface of the superlattice. Note that with the use of the superlattice structure, the effect of the 2DEG layer from each interface on the measured thermopower was amplified. Moreover, it was observed that increasing the number of unit cells of $SrNb_{0.2}Ti_{0.8}O_3$/STO from one to two and two to four drastically decreased the measured thermopower of the superlattice, again suggesting tunability of this property using superlattice periodicity [90]. The giant Seebeck coefficient observed in these superlattices was attributed to the two-dimensional quantum confinement, which supports the theoretically predicted enhancement of thermopower in quantum-well structures [91]. In another report, significant enhancement to the thermoelectric figure of merit ZT was observed by synthesizing superlattice structures of Pr-doped STO and Nb-doped STO [92]. The thermoelectric figure of merit ZT, decides the efficiency of a thermoelectric device (for conversion of heat to electrical energy) and is equal to '$S^2\sigma/\kappa$' where 'κ' is thermal conductivity, 'S' is the Seebeck coefficient, and 'σ' is electronic conductivity. ZT of a specific 8 unit-cell by 8-unit cell superlattice structure of Pr-doped STO and Nb-doped STO is found to be 0.46 K at 1000 K [92], which is the highest amongst STO-based thermoelectric systems [93]. The significant increase in ZT was attributed to a large reduction in the cross-plane thermal conductivity of superlattices achieved by increased phonon scattering at the superlattice interfaces and within each layers of the superlattice layers [92]. Extrinsic dopants Pr^{3+} and Nb^{5+} not only improves the power factor by providing carriers, but it also helps scatter phonons within superlattice layers. Using such

scheme, ZT was observed to be tunable by changing the superlattice periodicity, and it showed a maximum value for a 8 x 8 superlattice [92]. Lastly, we note that similar studies for controlling the thermoelectric properties using superlattice structures were investigated. Remarkable results such as a giant Seebeck coefficient in LMO-LSMO superlattices [94] and improvement in the Seebeck coefficient of amorphous oxide superlattices [95] *etc.* were reported.

The above examples from various areas of research clearly emphasize the importance of superlattice structures in providing unprecedented access to novel physical phenomena, which are rare in their bulk counterparts or otherwise. The capability of artificial superlattices to stabilize metastable structures is the key component in enabling their tremendous potential for the search of new physics and associated unique properties. The other standout features of superlattice structures are controllability, by varying its superlattice periodicity, of the interaction range at interfaces and within a layer. And, it is possible to amplify the effect of interfacial phenomenon by having many interfaces in the superlattice structure. By combining these advantages inherent to the superlattice geometry in strongly correlated materials such as complex oxides, superlattice systems have not only shown a wealth of hidden physical phenomena but also showed exceptional capability in tuning the properties of materials. Thus, these artificial superlattice structures provide a unique route to explore novel physics in material systems with several interacting degrees of freedom.

1.4 Summary

In this chapter, first an overview of fundamentals involved in crystallographic and electronic structure of complex oxides is provided. Later, a brief review of the importance of superlattice structures in various subjects of complex oxide research is discussed. Motivated by the remarkable results shown by superlattices of conventional semiconductors, I have studied superlattices of complex oxides. The presence of various interacting degrees of freedom in these complex oxides, when combined with metastable structures such as superlattices, it is expected to open several phase spaces which are rich in novel physics. Such novelty is observed with respect to showing new phenomenon not observed in bulk and enhancing the properties as compared to parent materials.

Chapter 2

Synthesis and Characterization

2.1 Synthesis

2.1.1 Pulsed Laser Deposition

Complex oxides can be synthesized in both bulk [96; 97] and thin-film geometry [30]. In this dissertation, thin-film geometry is used to study various aspects of different physical phenomenon discussed. Pulsed Laser Deposition (PLD) method was employed to synthesize thin-films of complex oxides. Unless mentioned otherwise, all thin-films studies presented in this dissertation were grown by the PLD method.

Pulsed Laser Deposition is a physical vapor deposition (PVD) method [98], and it is a highly non-equilibrium process compared to other deposition methods such as Molecular Beam Epitaxy [99], Chemical Vapor Deposition [100] *etc.* PLD is the most versatile deposition technique and has been used in the deposition of different classes of materials *e.g.* oxides, nitrides, semiconductors *etc* [98]. The greatest advantage of using PLD is the stoichiometric transfer of target atoms to the substrate under optimal growth conditions [101]. A schematic of conventional PLD deposition chamber is shown in Figure 2.1. In a normal operation of this technique, a very short laser pulse is focused on the target material, which has the same composition as the desired film composition, and it can be either a single crystal or polycrystalline. The high-energy laser pulse leads to instantaneous ablation of the material forming a plasma plume. The ablated material in this plasma plume then propagates in a controlled atmosphere to condense on a substrate. Each step in this deposition process adds another experimental parameter, which is crucial in optimizing the growth of a material. The detailed physics of each step, starting from material ablation to plume formation, and plume propagation, finally condensing onto a substrate is fairly complex and is discussed in detail elsewhere [98; 101]. Here, I will provide a qualitative discussion of the various steps involved in the deposition process.

In a typical PLD deposition process, the wavelength of laser light is used generally in the UV-range. The laser light can be generated via different sources, *e.g.* excimer lasers, solid-state lasers *etc.* In excimer lasers, the gas composition is optimized to produce laser light with different wavelengths, *e.g.* ArF produces 193 nm, KrF produces 248 nm (one used in this thesis), XeF gives 308 nm *etc.* Solid-state lasers can also be used to produce lasers with a wavelength in the UV-range. For example, Nd:YAG laser which first

produces laser radiation of wavelength 1024 nm and later frequency quadrupled to 266 nm using two non-linear optical materials (Lithium Triborate and Cesium Lithium Triborate) from 1024 nm to 532 nm, and finally from 532 nm to 266 nm. Note that ablation of a material depends on both the laser characteristics and the optical properties of the materials, and thus, the choice of laser light can be critical in optimizing growth of certain class of materials.

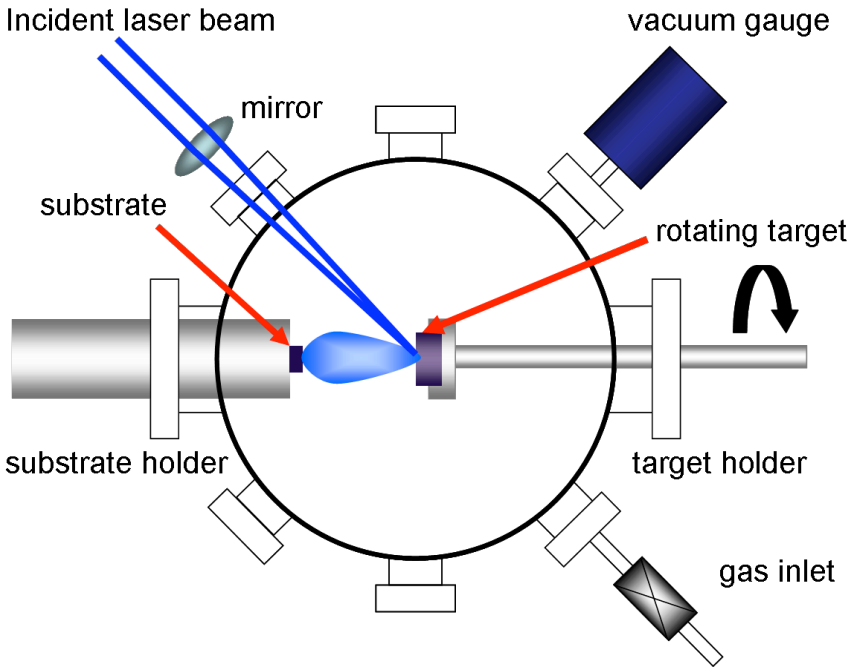

Figure 2.1: A schematic of a typical Pulsed-laser Deposition chamber. From [102].

With an appropriate choice of laser, when the material is subjected to a short-pulsed (10-30 ns) laser, it undergoes several stages before ablating the material into the chamber. Excitation of the material from a solid state to a plasma state involves thermal, mechanical and chemical excitation, whose mechanism is very complex. The short-pulsed nature of the laser ensures uniform ablation of the material. One may want to perform additional rotation and rastering of the target to achieve uniform ablation for longer period of time. Once the material ablates, the shape and size of the plume can be tuned by external pressure (controlled atmosphere achieved by using either mixture of O_2, N_2, Ar *etc.* gases), shape of laser spot on the target and the energy of the laser. The external pressure can change the energy of the atoms/ions in the plume, and hence, the energy spectrum of the plume. Typically, these atoms /ions in the plasma plume assume energy of the order of several eVs, which makes this process highly non-equilibrium. The size, and sometimes the shape of the plume, can be tuned by energy density, also known as Laser Fluence (energy per unit area of the laser spot), either by changing the energy, laser spot or both. Note that the Laser Fluence is one of the critical growth parameters that are optimized to achieve stoichiometric transfer of the target atoms on to the substrate.

Changing the frequency of the laser may control the flux of incoming species (atoms/ions) via plume propagation. Typically, it is varied between 1-20 Hz. This is another parameter, which can be used to do finer tuning of growth optimization. After achieving pulsed flux of atoms/ions, the vapor above the substrates finds itself in the super saturation state leading to the dense nucleation of small two-dimensional islands. Finally, growth parameters such as temperature of the substrate, lattice parameter, and crystal symmetry of the single-crystalline substrate are optimized to obtain the desired thin-film deposition of a specific composition, crystallographic phase, and orientation of the thin-film. As will be discussed later, various characterization techniques were then employed to study the structural, chemical, thermal *etc.* properties of thin-films grown via the PLD method.

There are many advantages of using PLD as the primary thin-film deposition method [98]. For example, it provides tremendous flexibility in adapting different operational modes owing to the fact that vacuum hardware can be decoupled from energy source evaporating the material. This allows the deposition of materials in various controlled gas atmospheres such as O_2, N_2, Ar *etc.* and under pressure ranges from ultra high vacuum (UHV) to ambient pressures. In addition, it further allows for multiple *in situ* characterization techniques in the same PLD chamber such as Time-of-Flight (TOF) Spectroscopy [103] and Reflection High Energy Electron Diffraction (RHEED). Congruent evaporation of target material in this deposition method has made this technique a most popular choice when synthesizing multicomponent phases such as oxides (PTO, CTO), nitrides (TiN, CN), carbides (TiC, SiC), alloys ($La_xSr_{(1-x)}MnO_3$), artificial heterostructures of these multicomponent phases [98] *etc.* More recently, the PLD method was successfully employed for the synthesis of thin-films of *2D materials* such as MoS_2 [104], graphene [102]. Moreover, this method offers a cost-effective method of depositing such a wide variety of materials. Lastly, due to the highly non-equilibrium nature of this deposition technique, PLD can enable the growth of metastable phases as well [105].

2.2 Characterization Methods

2.2.1 *In situ* characterization: Reflection High Energy Electron Diffraction

With respect to *in situ* characterization techniques, PLD becomes another convenient method for synthesizing thin films. Due to the pulsed nature of flux control of incoming atomics species in PLD, this method allows for the control of material growth less than a unit cell [106; 107]. During the PLD process, growth rates as small as 0.01 unit-cell per laser pulse can be achieved [108; 109]. Therefore, if the PLD system is equipped with an *in situ* monitoring of material growth, in principle, one can synthesize artificial structures such as superlattices, multilayers *etc.*, with desired periodicity or layering sequence. Here, I've employed one such *in situ* characterization techniques, known as

Reflection High Energy Electron Diffraction (RHEED), which is greatly used in a variety of thin-film deposition techniques [110; 111].

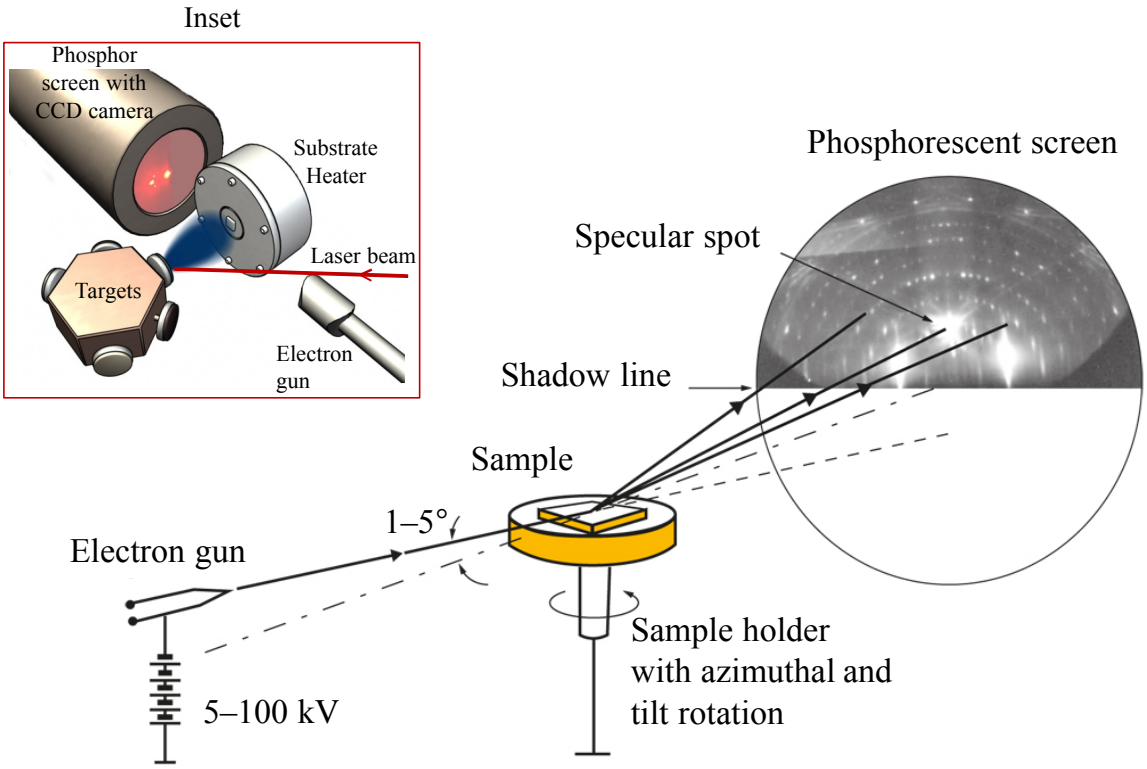

Figure 2.2: A schematic of *in situ* RHEED experimental set up (adapted from [112]). Inset shows a schematic of combined assembly of RHEED with PLD chamber (Courtesy of Jeroen Huijben).

A typical RHEED setup includes a high-energy electron gun, a phosphor screen, and a CCD camera to record the relative change in the position and intensity of scattered electron on the phosphor screen. A schematic of a RHEED setup is drawn in Figure 2.2. As the name suggests, when the high-energy electrons are incident at a specific angle, they are diffracted from the crystalline surface lattice forming a RHEED pattern. The reciprocal lattice decides the formation of this RHEED pattern [112], which is similar to other diffraction techniques such as TEM, XRD *etc.* The high-energy electron source provides electrons with energies of the order tens of keVs (5-100 keV). And, a phosphor screen is used to convert the scattered electrons from the sample to photons, which is then imaged using CCD camera. In our RHEED-assisted PLD chamber, a P43 phosphor screen is used because of the high conversion efficiency and spatial resolution in combination with a K200D CCD camera. The electron gun and the phosphor screen are aligned to the substrate in a way that the geometry of the incident electrons is grazing with the incident angle typically between 1-5°. The grazing incidence, along with the high energy of electrons, ensures RHEED sensitivity to only a few monolayers of the surface, and probing width

that is the same as the width of the sample (diameter of the electron beam decides the area of the sample probed by the RHEED). The RHEED pattern is formed by the intersection of Ewald's sphere [112] with the plane of phosphor screen (Figure 2.3). An actual RHEED diffraction pattern from atomically flat singly terminated (TiO_2) STO (001) substrate is also shown in Figure 2.4. As will be discussed later, different surface structure leads to characteristic RHEED pattern. Thus, RHEED can be used to monitor growth dynamics of thin films, *e.g.* growth mode from the diffracted electrons, thickness from the modulation of specular reflection *etc* [113].

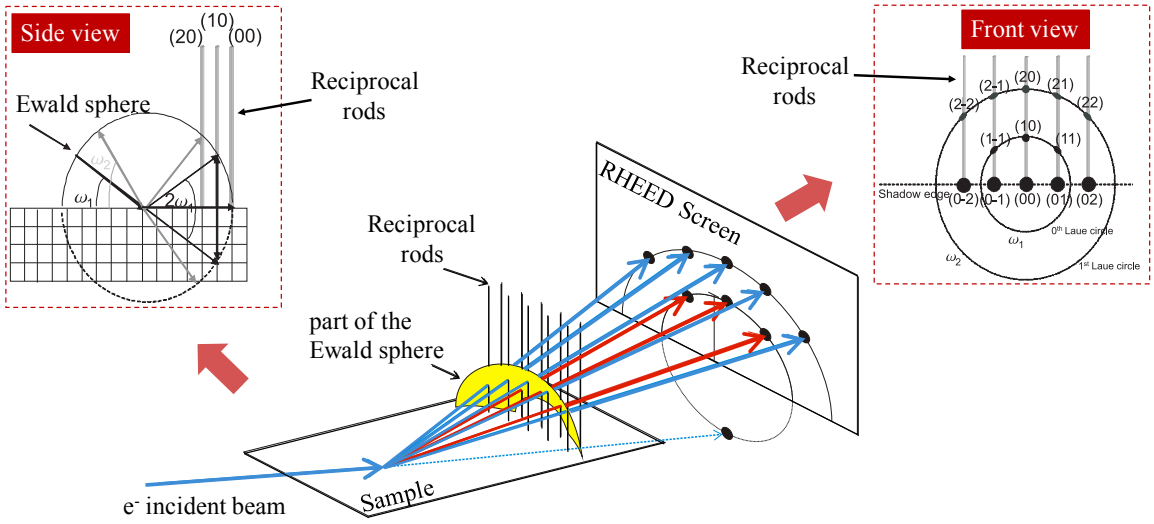

Figure 2.3: A schematic of formation of RHEED diffraction using Ewald's sphere construction is illustrated. Along with a 3D view, a side and front view are also drawn for better illustration. Figure is adapted from [114] and [115].

In situ controlled growth of materials using RHEED provides a powerful way to optimize the PLD growth parameters to achieve the desired growth mode, and hence, controlled synthesis of the desired heterostructures. To understand the growth dynamics, one has to consider different free energy terms involved in the formation of a film from supersaturated vapor. The change in the free energy in the process of formation of single layer of film material ('A') on a substrate material ('B') involves free energy of formation of film material ('A'), free energy of formation of interface between film and the substrate materials, and the strain energy associated with film formation due to the difference in lattice parameter of the film and substrate. The change in the interfacial energy decides the wetting of film material on the substrate material. The kinetic terms, which may influence growth of film on a substrate, are surface mobility of adatoms which may depend on temperature of the substrate, nature of substrate surface, and flux of incoming atoms [113]. The nucleation and growth of film material greatly depends on parameters discussed above. Here, we will discuss thin-film growth modes, which are most commonly observed, *i.e.* island growth mode (3D), layer-by-layer plus island growth mode (2D to 3D), and layer-by-layer growth mode (2D).

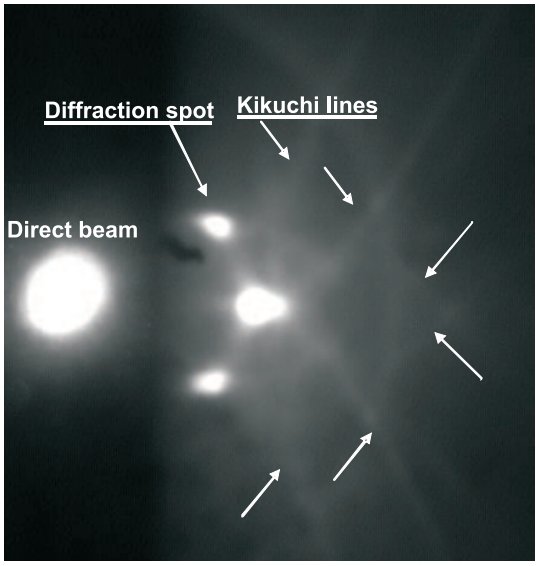

Figure 2.4: RHEED diffraction pattern from a TiO_2-terminated STO (001) substrate. From [114].

In island growth mode, also called *Volmer-Weber* growth [114], adatoms starts forming island clusters on the substrate, which acts as a nucleation site for the growth of the film. The 3D growth usually leads to large surface roughness of the film grown under this mode. Island growth mode is generally observed in the case where the film is not able to wet the substrate. It may also be observed in the cases where surface mobility of adatom is very low which may result from either or combination of factors including low substrate temperature, low energy density for target ablation, nature of substrate surface. The characteristic RHEED pattern quickly turns to the one shown in Figure 2.5 from a 2D pattern of the crystalline substrate.

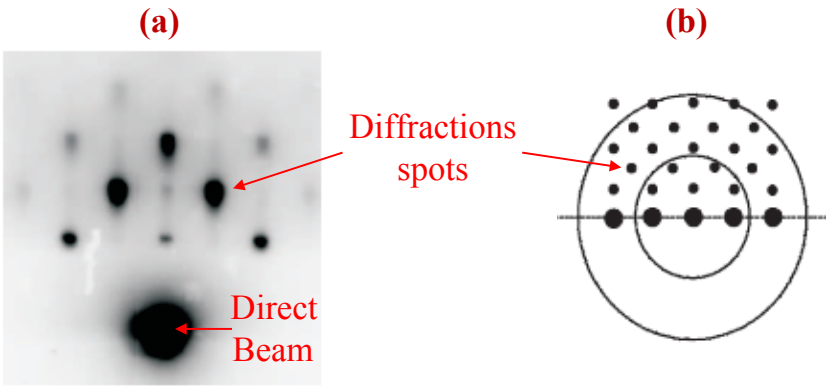

Figure 2.5: RHEED diffraction pattern for *Volmer-Weber* growth mode (a), along with a schematic (b) is shown. Figure adapted from [114].

In the second growth mode, the film first starts with layer-by-layer growth mode and then transitions to island growth, also known as *Stranski Krastanov* [114], is commonly observed in the case where a large lattice mismatch is present between the in-plane lattice parameters of the film and substrate. After certain critical thickness, decided by the lattice mismatch and young's modulus of film material, growth mode changes to island growth to minimize large strain energy. The characteristic RHEED pattern after changing to island mode looks very similar to the one shown in Figure 2.5.

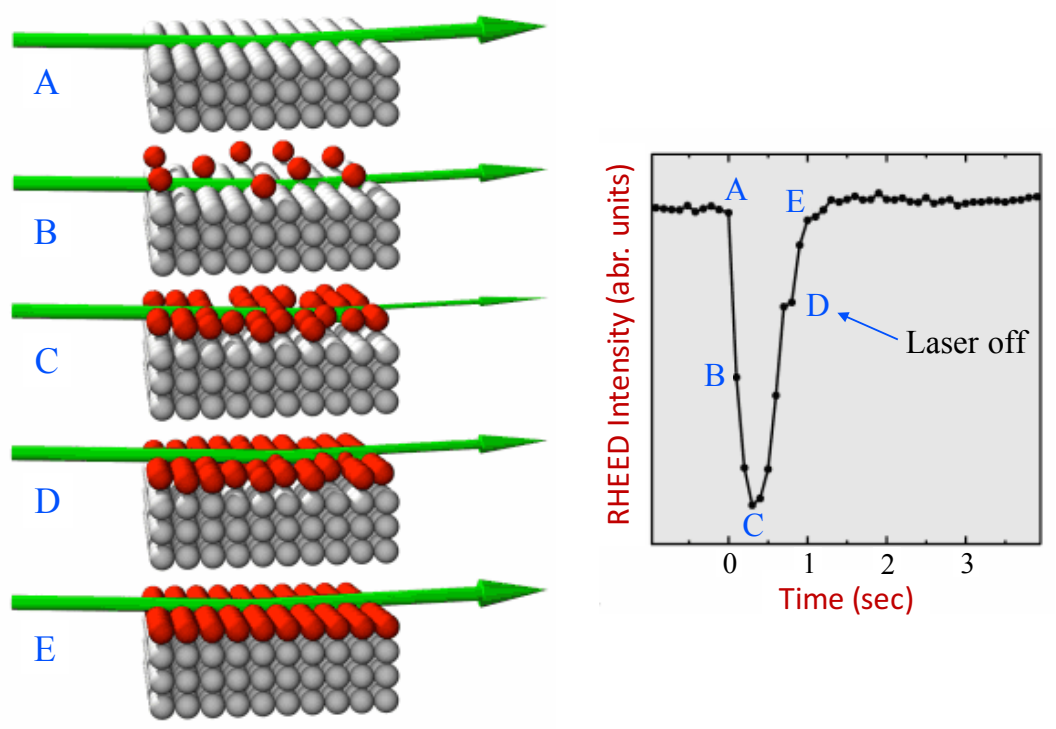

Figure 2.6: Different stages of layer-by-layer growth monitored via RHEED. Figure adapted from [116].

The third most common, perhaps the most important, growth mode is layer-by-layer, also known as *Frank Van der Merwe mode* [114]. In this mode, the film material completely wets the substrate surface and leads to film growth via formation of planar sheet of atoms, hence the name 2D growth mode. Using this growth mode, the surface of the substrate undergoes a cycle of smooth to rough and back to smooth surface. This type of growth mode allows us to employ RHEED in monitoring growth of materials *in situ*, and hence, enables synthesis of artificial heterostructures. The intensity of specular spot on the RHEED pattern is monitored to study the evolution of film growth via 2D growth mode. Figure 2.6 illustrates different stages of layer-by-layer growth monitored via recording the modulation in the intensity of specular spot. The sinusoidal variation of intensity represents the coverage of atoms on the surface due to the change in the surface roughness as it

progresses to form one layer of atoms. Note that one such oscillation observed during a 2D growth only suggests the formation of one layer of atoms. Depending on the material being grown, one oscillation may not necessarily indicate formation of one unit-cell. For example, the growth of Sr_2IrO_4 on STO (001) substrate under optimized conditions leads to layer-by-layer growth with four oscillations making one unit-cell [117]. This results from the layered structure of the material having perovskite and rock salt units. Thus, one has to perform *ex situ* characterization such as X-ray Reflectivity (XRR), Transmission Electron Microscopy (TEM) *etc.*, to find the precise growth characteristics of the material.

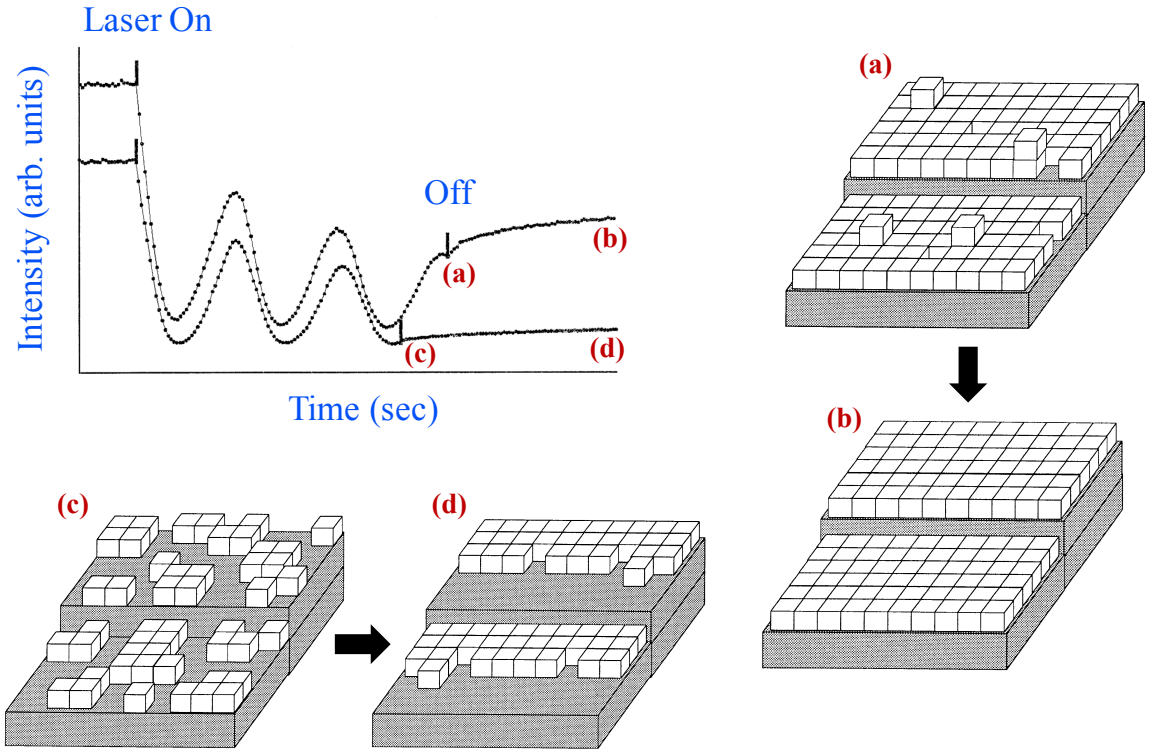

Figure 2.7: RHEED oscillations for homoepitaxial growth of STO on a treated-STO (001) substrate and associated schematic of surface coverage. Figure adapted from [118].

Owing to the importance of layer-by-layer growth, I will discuss few more characteristics of this growth mode. Figure 2.6 shows the RHEED oscillations for homoepitaxial growth of STO interrupted at 3 monolayers (three complete oscillations) and 2.5 monolayer (two complete and one half oscillation) on a treated STO substrate (*i.e.*, substrate surface has steps with terrace width of 200 nm and step height of 1 unit-cell of STO). The corresponding cartoon picture of adatoms coverage on the surface is shown in Figure 2.7 at difference stages (a)-(d). The first observation is that after turning off laser or flux of atoms at position '(a)', intensity of specular spot continues to increase. And, after certain recovery time, the RHEED intensity saturates. This increase in intensity of specular spot suggests that all adatoms hasn't occupied all empty sites on the surface. When enough

time is given, they diffuse on the surface to fill all empty sites, which are also illustrated schematically in (a)-(d). Note that one can use this characteristic of pulsed flux of incoming atoms for growing alloy thin films with varying degree of alloying disorder. In PLD growth, the time constant for the exponential recovery [119] of RHEED intensity is a good indicator of one of the important growth optimization parameters, *i.e.* laser fluence. For laser fluence lower than optimum value, the recovery will be very slow, and thus, this characteristic of RHEED can be used as a feedback mechanism to optimize laser fluence on the target. Another important point to note from the Figure 2.7 is that completion of one oscillation does not fill all atomic sites present on the surface and this generally leads to continued decrease in strength of RHEED oscillation for uninterrupted growth [120]. One may notice that if a film is grown via 2D growth mode frequent interruptions during the growth to make the surface smoother allows better sustainability of RHEED oscillations. This characteristic has been particularly useful, as will be shown later chapters, in enabling layer-by-layer growth of single layer thin-film (ex. CTO on NGO (110)) or superlattices (STO-CTO or PTO-STO superlattice) up to 200 nm thickness with good RHEED oscillations present through the growth process.

Another important characteristic of layer-by-layer growth mode is that it allows for the monitoring crystal structure of the grown layer from the RHEED pattern, especially when they are different for film and substrate. For instance, RHEED pattern will show different diffraction pattern for an orthorhombic structure compared to a cubic structure, *i.e.* additional diffraction spots will appear in between the two diffraction spots as shown in Figure 2.8 (a) (by white arrows). So, when an orthorhombic material is grown on a cubic substrate or vice-versa, RHEED pattern before and after the growth can be used to characterize the film, and sometimes, can provide another feedback mechanism to optimize growth parameter such as lattice parameter, crystal symmetry of the substrate [113]. Thus, layer-by-layer growth mode provides a powerful way to *in situ* control the growth of a film while simultaneously characterizing the artificial structures being grown using materials with different lattice parameter and crystal symmetry.

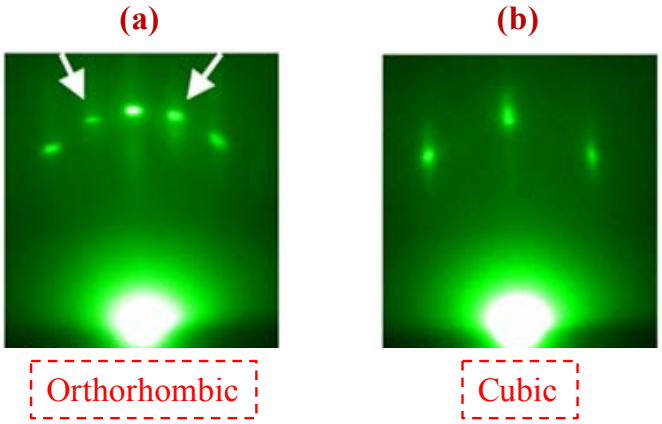

Figure 2.8: A schematic of RHEED diffraction pattern for (a) orthorhombic vs. (b) cubic crystal. Figure adapted from [121].

Enabled by the *in situ* characterized growth of complex oxides using RHEED-assisted Pulsed Lased Deposition, superlattices and heterostructures of STO, CTO, PTO were synthesized with accurate control of unit-cell by unit-cell deposition of these materials. After synthesis, a number of *ex situ* characterizations were performed to fully characterize thin films of superlattices and heterostructures. Various *ex situ* characterization techniques, which are used in this dissertation, are discussed next.

2.2.2 Laboratory-based X-ray Diffraction

X-ray diffraction is one of the most common *ex situ* characterization techniques used routinely by material scientist working in bulk single crystals, powder polycrystalline samples, thin-films *etc.* [122]. This technique is primarily used to identify the phase of crystalline materials along with the identification of their unit-cell lattice parameters. The X-ray diffraction technique is based on the principle of constructive interference of monochromatic X-rays diffracted from a crystalline specimen. In a laboratory-based X-ray diffraction machine, X-rays are generated using a cathode ray tube, which is then filtered to get monochromatic X-rays. When monochromatic X-rays are incident on a crystalline specimen, they get scattered from different location within the sample and interfere constructively to form diffraction pattern satisfying equation, $n\lambda = 2d \sin\theta$, also known as Bragg's law [123]. This law relates the wavelength of the monochromatic X-rays to the lattice spacing of the crystalline sample and angle 'θ' of the diffraction geometry. One can perform such diffraction experiments to identify the crystal structure or phase of the material of interest [122]. Since this thesis focuses on thin-films, I will limit our discussion to various aspects of this technique in characterizing thin-films of superlattices and heterostructures.

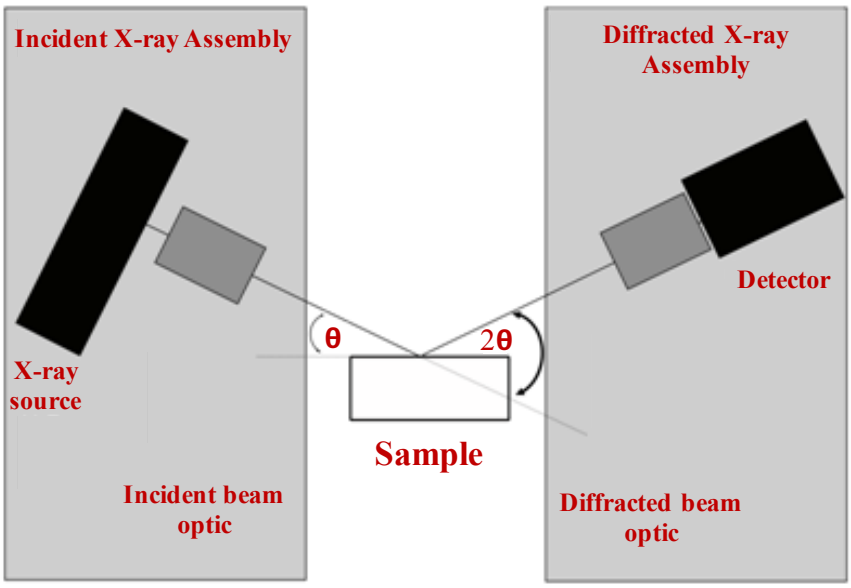

Figure 2.9: A schematic of XRD experimental set up. Adapted from [124].

X-ray Diffraction (XRD) machine used in this dissertation was X'Pert Pro manufactured by PANalytical Inc. It produces monochromatic X-rays of wavelength 1.5408 Å from a Cu – Kα source. The machine was equipped with a high-resolution line detector to collect diffracted beams from the sample. In a typical XRD measurement, forward scattering geometry was used to collect diffracted X-rays on the detector as shown in schematic Figure 2.9. In a standard 'θ - 2θ' scan, the sample and the detector are moved simultaneously maintaining 'θ - 2θ' geometry between incident angle (of the X-rays on the sample) and diffracted angle (aligned with the detector position) to collect Bragg peaks from the sample. This diffraction geometry is sometimes also referred as Symmetric Scan, whose schematic is shown in Figure 2.10. This schematic is an illustration of scattering geometry for all symmetric scans with gray arrows showing '2θ - Ω' scans and 'Ω' scans. This Ewald sphere construction also shows the reciprocal points accessible in this scattering geometry. It is in general desired to have high resolution in the angle 'θ' of the incident (or '2θ' of the detector angle) from the goniometer for characterizing thin-films, as will be discussed later. As an example, Figure 2.11, is showing symmetric X-ray diffraction of 126 unit-cells of CTO grown via *in situ* RHEED controlled layer-by-layer growth on NGO (110) substrate. The y-axis shows the intensity of diffracted X-rays measured in arbitrary units (counts per second) and for laboratory based X-ray machines this number is typically of the order of 10^5. The X-axis for this graph represents '2θ' value of the detector position (or 'θ' value of sample) in 'θ - 2θ' symmetric scan. The two peaks observed in this graph (Figure 2.11) represent the Bragg peaks arising form the (002) planes of the <001>–pseudocubic oriented CTO film and NGO substrate. Since film thickness is typically less than 200 nm, the strongest peak generally corresponds to substrate peak. Due epitaxial nature of the thin-film growth, CTO film grows with same crystallographic

orientation as that of NGO substrate, *i.e.* <001>–pseudocubic oriented. Note that this graph shows only a subsection of 'θ - 2θ' symmetric scan where only one Bragg peak of film and substrate is seen, which is indexed by atomic planes responsible for giving rise to those peaks. The intensity of these Bragg peaks are decided by the structure factor of the unit-cell and it is strongest for the (002) planes of <001>–pseudocubic oriented CTO or NGO crystal. The '2θ' position corresponding to the film peak can be used to calculate the *d*-spacing of (002) planes of CTO film. This simple symmetric scan is immensely used in studying effect of in-plane strain on the out-of-plane lattice parameter [125; 126] and their effect on physical properties of complex oxide thin films [127; 128]. The presence of additional peaks around 002 peak of CTO films is called *Pendellösung* fringes or *Kiessig* (thickness) fringes. Their presence generally suggests smooth interface between both film/substrate and film/air. As they contain information regarding the thickness of the film, they can be used to analyze the total thickness of single layer [129] or multilayer thin-films [130; 131].

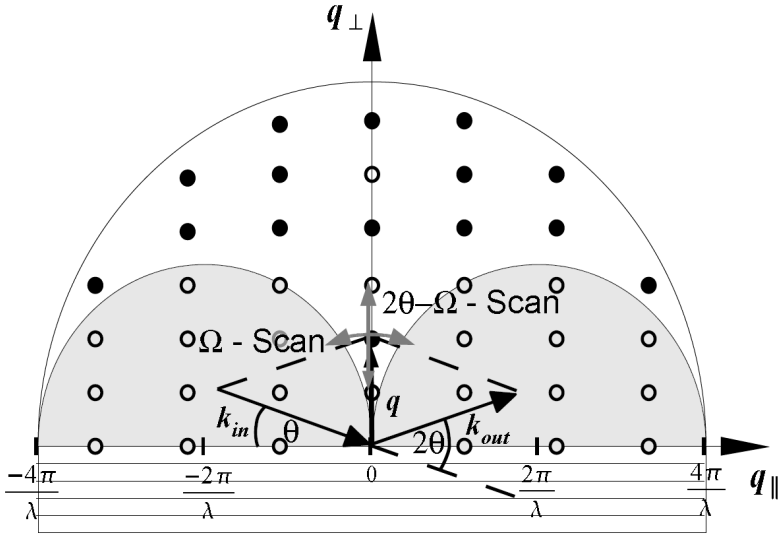

Figure 2.10: A schematic of symmetric XRD scan is shown in the Ewald sphere construction. The region shaded in grey encompasses reciprocal lattice points which are not accessible in the normal reflection geometry, for the given incoming wave vector $\boldsymbol{k_{in}}$. From [132].

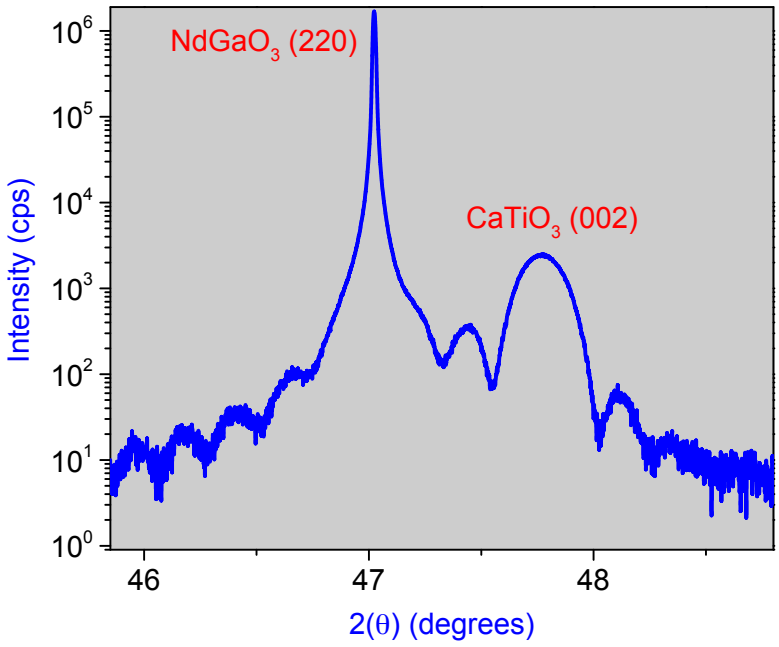

Figure 2.11: Symmetric XRD scan of 126 unit cells of CTO grown on NGO (110) substrate.

Most laboratory based XRD systems have a goniometer capable of rotating the sample around an axis perpendicular to its plane (also called as 'Φ' or 'Phi' scan). 'Φ' scans are frequently performed on thin films to ensure that film maintains certain desired crystal orientation with respect to the substrate. In case of heteroepitaxial growths, these scans are readily performed to ensure intended epitaxial relation is present between with the film and the substrate, for ex. cubic STO grown on orthorhombic NGO or vice-versa. Before we turn our attention to other modes of X-ray Diffraction measurements, I will discuss a few more examples of symmetric scans, which can help characterize additional structure order present in thin-film structure. Thus, making this characterization technique extremely useful for studying thin-film heterostructures.

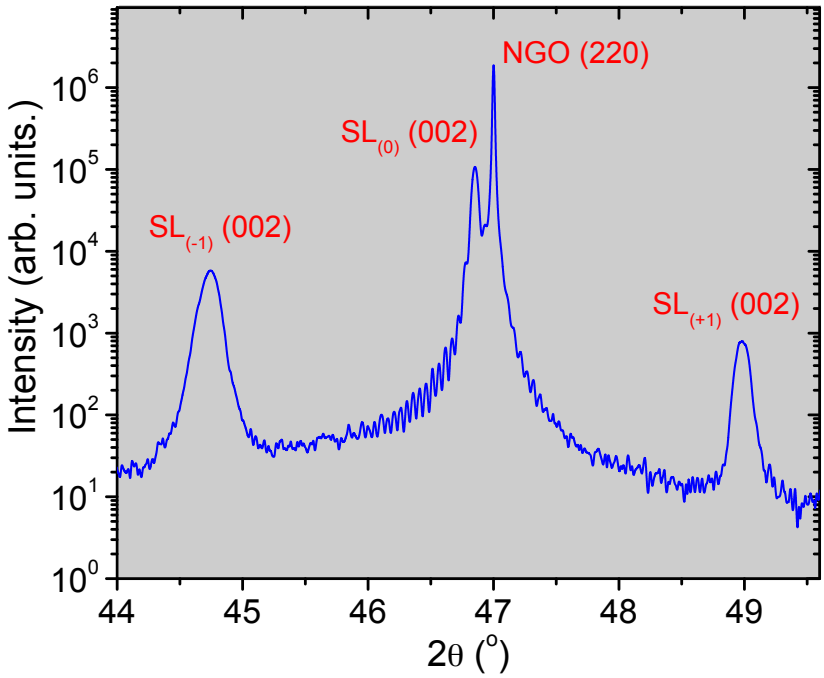

Figure 2.12: Symmetric XRD scan of 200 nm thick 6 x 6 STO-CTO superlattice film grown on treated-NGO (110) substrate.

First, we will consider a periodic superlattice of STO and CTO made up 6 unit-cell of STO and 6 unit-cell of CTO repeated 44 times to constitute a total of 200 nm thick superlattice film. XRD scan of such a superlattice grown via RHEED-controlled layer-by-layer growth on a NGO (110) substrate is depicted in Figure 2.12, where the presence of multiple peaks from the film is observed. The strongest peak from the film is the Bragg peak corresponding to (002) planes, whose '2θ' peak position when translated to d spacing, it corresponds to average spacing between TiO_2 planes and SrO (or CaO) planes. In this case, it is also referred to as peak corresponding to 50:50 alloy peaks corresponding to 50:50 volume ratio of STO-CTO. The other two peaks on either sides, labeled as $SL_{(-1)}$ 002 and $SL_{(+1)}$ 002 ('SL' is abbreviation for superlattice), arises from the additional periodicity registered in the lattice translational symmetry caused by repeating 6 unit-cells of STO stacked on top of 6 unit-cells of CTO. The '2θ' position of these superlattice peaks can be used to extract the periodicity of the superstructure grown by stacking 6 unit-cell of STO on 6 unit-cell of CTO on 6 unit-cell of STO on 6 unit-cell of CTO, and so on. Thus, the superlattice structure characterized *in situ* via RHEED can be confirmed after growth by performing *ex situ* XRD characterization.

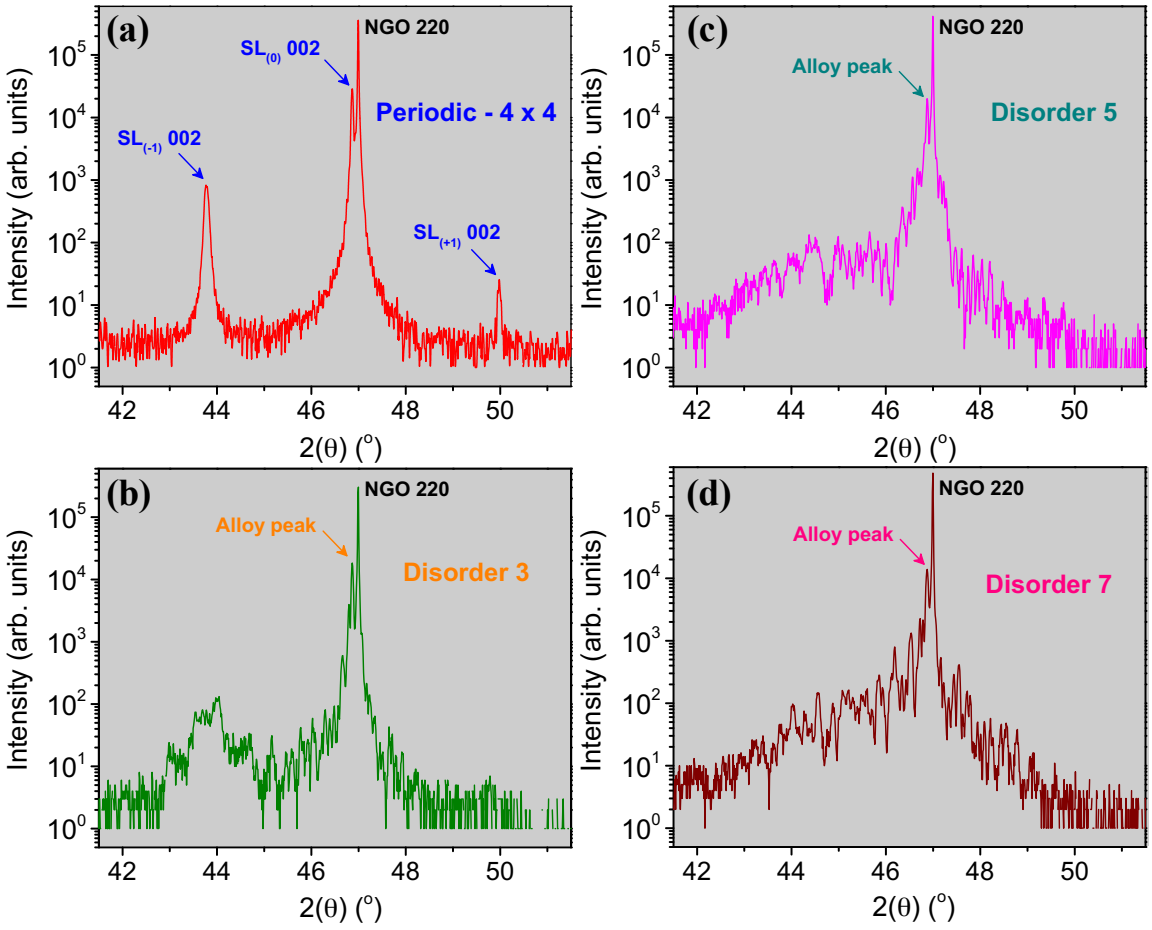

Figure 2.13: Evolution of structural ordering in aperiodic superlattice films of STO and CTO as characterized from symmetric XRD scans.

Second, since the X-ray diffraction is very sensitive to the additional structural order present in the thin-film structure, one can use that characteristics of this technique to study Quasi-periodic structures or even completely aperiodic (random) structures. For example, Figure 2.13 shows the evolution of degree of structural disorders in random multilayers, *i.e.*, random stacking, of STO and CTO. By carefully designing the stacking sequence of these random multilayers, *i.e.* keeping the volume fraction, total thickness and average interface density of the superlattice structure constant and equal to a reference periodic superlattice, heterostructures of STO and CTO has been grown with varying degree of structural order. Starting from a completely periodic sequence, *i.e.* periodic superlattice as discussed above, to a completely aperiodic sequence with no translational symmetry present in the layering sequence. The XRD of such designed heterostructures with increased degree of disorder is illustrated in Figure 2.13, which shows the evolution of XRD when degree of order is varied from completely periodic (4 x 4) to completely random sequence with no periodicity in the structure. As the disorder is increased in the grown sequence, the intensity of superlattice peaks ($SL_{(-1)}$ 002 and $SL_{(+1)}$ 002) starts

diminishing and additional peaks near the alloy peak starts appearing. When the layering sequence makes the structure completely disordered all the superlattice peaks around (00*l*) peaks disappear almost completely. Thus, one can simply do a symmetric scan of superlattice-like structures to study and understand great deal of evolution of structural order in the system.

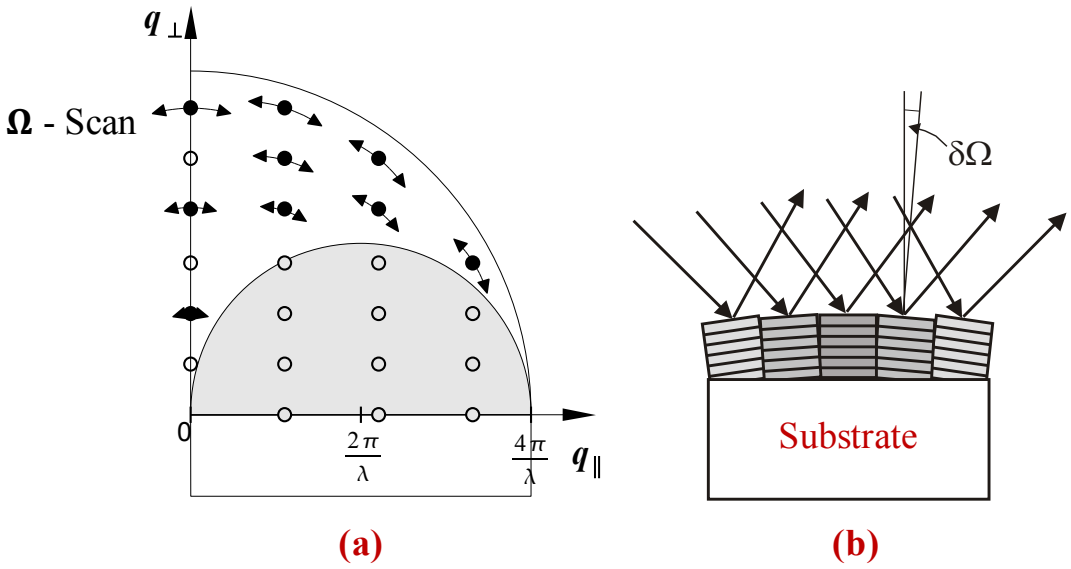

Figure 2.14: A schematic of rocking curve scan is shown in (a) under Ewald sphere construction, while (b) depicts a possible scenario, which can give rise to finite broadening in the rocking curve. Figure adapted from [132].

Now, we turn our attention to another scan mode with symmetric scan geometry, which is widely used to assess the quality of thin-films. This scan mode is depicted in Figure 2.14(a) as 'Ω' scan, commonly referred to as Rocking curve. In this particular scan, '2θ' position of the detector is fixed to a Bragg peak and the sample is rocked using 'Ω' scan with all other variables fixed. As the 'Ω' begins to deviate from the Bragg position, intensity of the diffracted beam at the detector starts going down rapidly. This characteristics of intensity falling down rapidly with increase in difference 'Ω' scan value from the Bragg position tells great deal about the texturing of the thin-film. To explain this schematically, Figure 2.14(b) shows broadening of the peak in rocking curve caused by the tilting of crystallites in the sample about an axis present in the in-plane direction. Thus, Full-Width-at-Half-Maximum (FWHM) of rocking curve from a thin-film is frequently used as a parameter to indicate the degree of film texturing along certain direction. When the growth condition in PLD is optimized carefully, one can obtain FWHM of thin-films comparable to that of oriented single crystal substrate in rocking curve. For example, rocking curve of 200 nm thick 6 x 6 STO-CTO superlattice grown on NGO (110) substrate along with the substrate rocking curve around 002 peak is shown in Figure 2.15. FWHM of film (Figure 2.15(a)) is found to be 0.028°, which is comparable to 0.016° value of the

substrate (Figure 2.15(b)) suggesting high degree of texturing in these superlattices grown via RHEED-assisted PLD. Thus, this particular mode of XRD characterization can provide useful feedback for the optimization of growth parameters. This also emphasizes the need for having high resolution in goniometer, *i.e.* position of the detector or sample rotation ('θ'), in order to avoid limitations caused by the machine broadening.

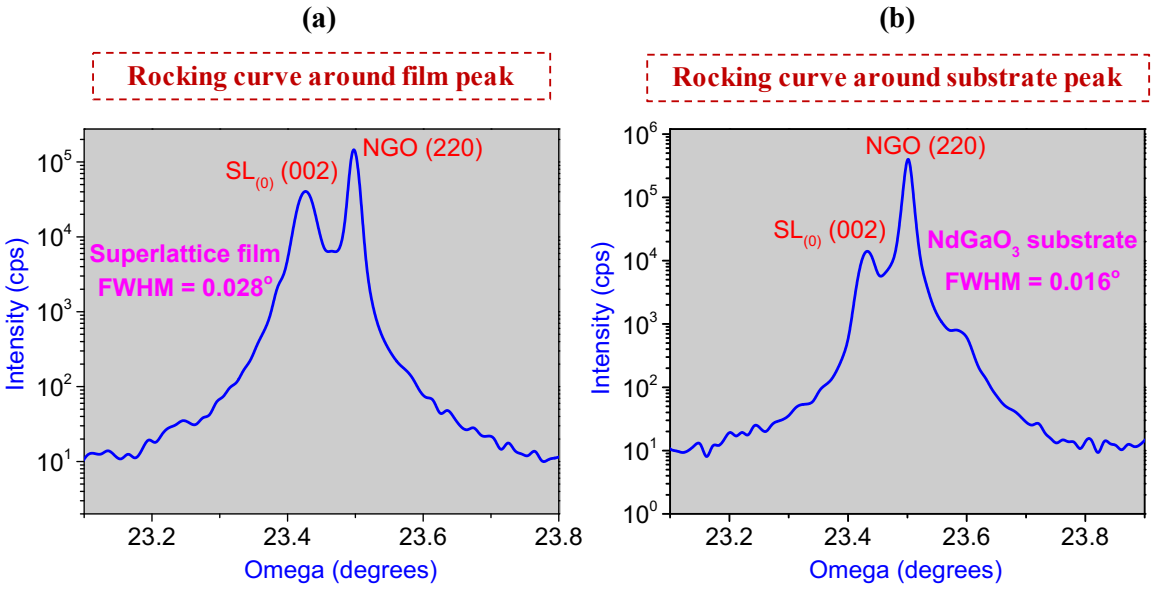

Figure 2.15: Full-width-half-maximum (FWHM) of (a) superlattice film around (002) Bragg peak, and of (b) NGO (220) substrate peak.

Another important mode of XRD is Asymmetric scan geometry, commonly referred to as Reciprocal Space Map (RSM). A schematic of asymmetric scan is depicted in Figure 2.16. In this mode, series of '2θ - Ω' (or line scans) are performed at a fixed values of 'Ω' or '2θ' and results into a 2D map of reciprocal space instead of line scans discussed in previous modes. Reciprocal space maps are widely used for characterizing the strain state of thin-films [133]. In most cases with the lattice parameter being different from the substrate, it is desired to know the maximum thickness (or critical thickness) of the film before it strain relaxes by forming defects such as misfit dislocations [134]. Since strain engineering is widely employed method to tune the properties of thin films [127; 128], the thickness up to which a film can be grown without introducing such defects becomes an important parameter. It is usually desirable to know the critical thickness of a given material grown on a known substrate [135-137]. For such studies, RSMs are frequently employed to characterize the strain state of the thin-film. As an example, Figure 2.17 shows RSM of a 9 x 9 STO-CTO superlattice grown on NGO (110) substrate. The Q_x value, in units of reciprocal lattice units (*i.e.* r.l.u.), of the alloy peak of the superlattice film aligning with the substrate peak (NGO 332) indicates that 200 nm thick superlattice films is strained to the substrate. Also note the additional peaks along Q_z direction at Q_x value of the substrate/film. These reflections arise due to the presence of superlattice ordering along

$[001]_{pc}$ direction resulting into additional ordering present on the (103) planes. In addition to obtaining strain state of thin film, reciprocal space maps can also be used to find exact unit-cell lattice parameters, *i.e.*, *a*, *b*, *c*, α, β, γ, by performing RSM around different reciprocal lattice points or (*hkl*) co-ordinates. Many thin-film studies have extensively used RSM's to obtain unit-cell parameters [133].

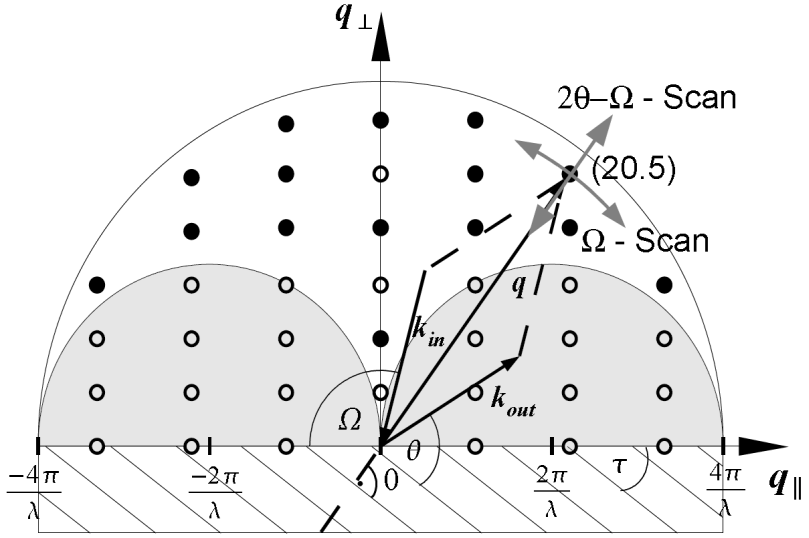

Figure 2.16: Schematic of Asymmetric XRD scan is shown in the Ewald sphere construction. The arrows in grey show the scan direction for '**Ω**'-scan or '2θ - **Ω**' scans for a given reciprocal lattice point (205). From [132].

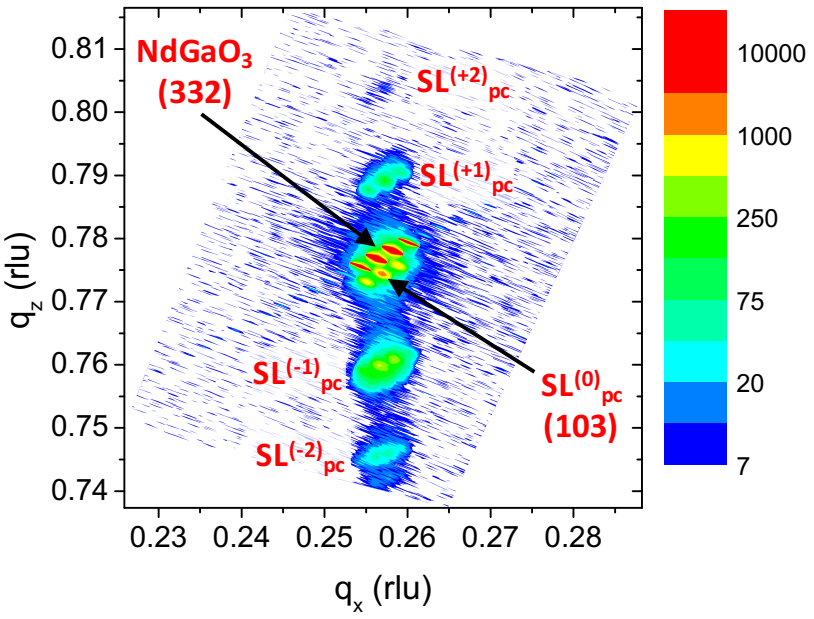

Figure 2.17: Asymmetric scan or reciprocal space maps of 200 nm thick 9 x 9 STO-CTO superlattice grown on NGO (110) substrate around 332 reciprocal lattice peak.

The last mode of X-ray diffraction technique, which is also widely used to characterize thin films, is X-ray Reflectivity (XRR) [138]. In this mode, X-rays are incident almost at grazing angle and specular reflection is recorded at the detector. Based on the difference in the density of film and substrate material, interference between X-rays reflected from the film/substrate interface and film/air interface leads to constructive or destructive interference as a function of incident angle 'θ'. Note that if the thin-film structure is bilayer or multilayer comprised of materials with different density, X-ray Reflectivity spectra will accordingly change, and thus, the analysis to extract film properties such as thickness, density and roughness of the film. This technique is widely used to measure thickness of thin-films up to few nanometers. In addition, since reflectivity spectra also depend strongly on the interface roughness (film/air and film/substrate), this method can also give the information regarding the film roughness. Figure 2.18 shows the reflectivity spectra of 25 unit-cells of STO grown on NGO (110) substrate via RHEED-assisted PLD. For a material like STO with known atom constituents and unit-cell structure, one can simulate the X-ray reflectivity curve for a film grown on a given substrate such as NGO. And, this simulated spectrum can be fitted to the experimental curve (Figure 2.18) to extract film thickness, roughness, and density of the film.

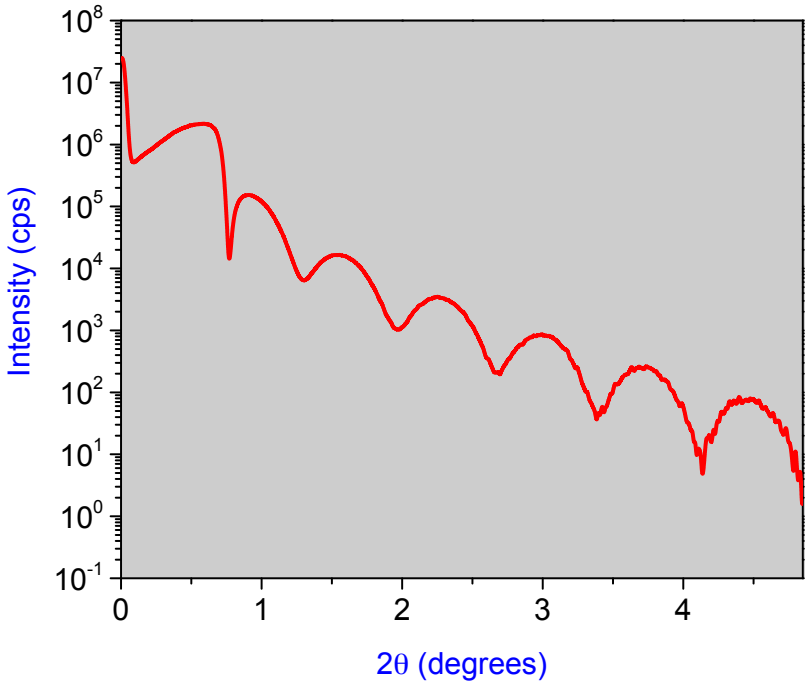

Figure 2.18: Experimental X-ray Reflectivity measurement of 25 unit cells of STO grown on NGO (110) substrate.

For multilayers or superlattices, which are comprised of two or more than two materials with many interfaces present in between, XRR is employed heavily to study the quality of interfaces in superlattice-like structures [131]. Note that for superlattice films, XRR can show Bragg reflections, which can further be used to characterize both the out-of-plane superlattice periodicity and quality of superlattice interfaces [131]. Lastly, XRR can be very useful in complementing *in situ* RHEED characterization for synthesizing materials like Sr_2IrO_4 for which one RHEED oscillation does not mean deposition of one-unit cell. In such cases, *ex situ* XRR can be performed to aid *in situ* growth characterization of complex oxides. Thus, XRD in combination with XRR provides the ultimate tool to fully characterize the structure of thin-films. Moreover, it also provides feedback mechanisms to help optimize growth parameters to achieve desired crystalline phases with intended physical properties.

2.2.3 Synchrotron-based X-ray Diffraction

Synchrotron X-ray diffraction [139] is essentially based on the same X-ray diffraction principle discussed above except for the fact that Synchrotron Light Source generates the monochromatic X-rays used for diffraction. Synchrotron radiation is obtained by first accelerating charged particles, typically electrons, in a particle accelerator called *synchrotron*. These high-energy electrons are then injected into a magnetic storage ring,

which is kept at ultra-high vacuum, and where electrons circulate in a large ring (with circumference of kilometers or so) for a large number of rotations (~10^9) in that ring. The change in the direction of electron velocity moving in such circular paths gives rise to acceleration, which results in emission of photons (tangentially to their circular trajectory). The wide range of photon energies available from a synchrotron light source allows research from various disciplines to take advantage of such unique light sources. Broadly, there are three categories of experiments performed using synchrotron light source, Spectroscopy, Imaging, and Scattering [140]. In this section, I will discuss the application of synchrotron light source in performing scattering (diffraction) experiments needed to probe nanoscale features in thin-film superlattices, which would otherwise be very difficult to study through laboratory-based X-ray diffraction machines. In the last section of this chapter, I will discuss a spectroscopy measurement based on a synchrotron light source to probe optical properties of features which can only be studies using such special light sources.

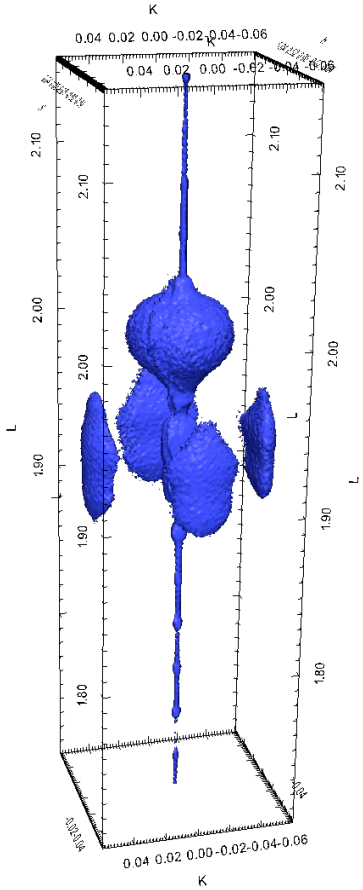

Figure 2.19: Three dimensional (3D) Reciprocal space map around (002) reciprocal point of STO (001) substrate, for a 16 x 16 PTO-STO superlattice film grown on STO (001) substrate. Courtesy of Dr. Christian Schlepütz.

Using a synchrotron source has many advantages over laboratory-based X-ray source. The biggest advantage is the intensity of incoming x-ray light which are many orders of magnitude (~ 10^{12} counts) higher than a laboratory source (~ 10^{6} counts). This high flux of light source is extremely useful in detecting weak diffracted peaks, for example, the superstructure originating from ferroelectric ordering in thin-films [141; 142], superlattices [62; 143], and from structural ordering arising from oxygen octahedral tilting in thin-films of complex oxides [144]. Although there are other advantages of using a synchrotron source, for example, the availability of continuous spectrum, high brightness, high coherence *etc.*, their importance becomes apparent in other synchrotron-based spectroscopic and imaging experiments. The secondary advantage of having such high flux of incoming photons is that one can have a diffraction set-up installed where a three-dimensional (3D) reciprocal space map around a reciprocal lattice point can be acquired with high accuracy [145]. In addition to performing 3D RSMs around a reciprocal lattice point present in the out-of-plane direction (such as Figure 2.17 from RSM section of previous section), high flux of X-rays also allows to acquire 3D RSMs around reciprocal lattice points present along the two in-plane directions of the thin-film. The latter is extremely difficult in laboratory-based X-ray diffractometers given the fact that thin-films are only few hundred nanometers thick at most.

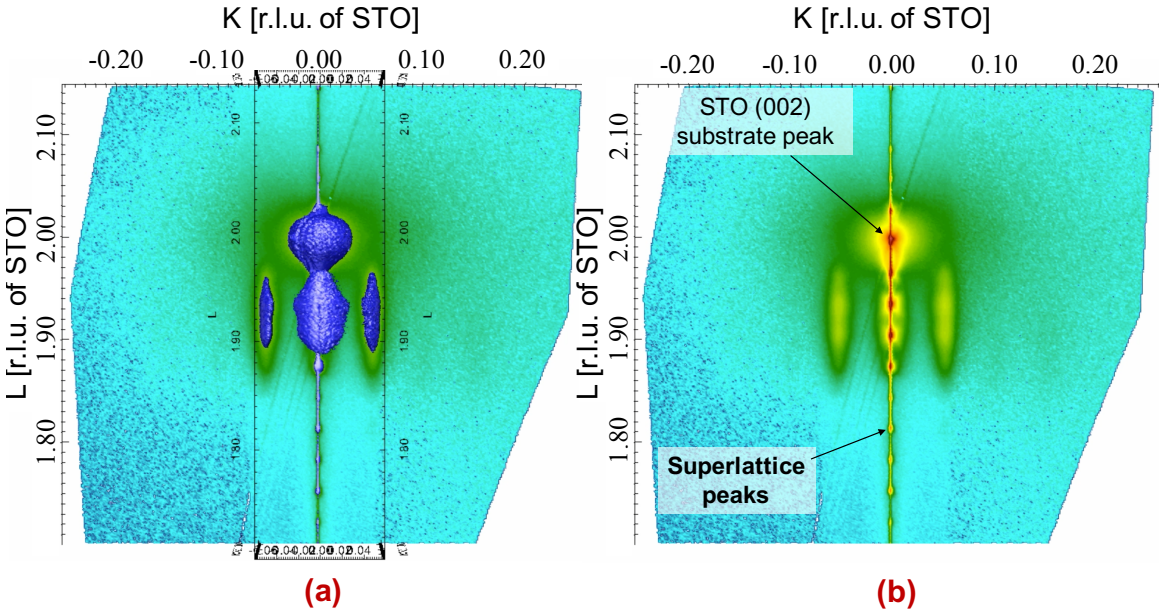

Figure 2.20: An LK-cut taken at H = 0 overlaid on 3D RSM (a) yielding a two-dimensional map shown in (b).

One such diffraction set up is available at Sector 33-BM-C beamline of Advanced Photon Source (APS) at Argonne National Laboratory. The set up is equipped with 4-circle Huber diffractometer, which has excellent angular accuracy and allows to determine orientation of crystallographic peaks very reliably. In addition, the availability of area

detector (recall in laboratory-based uses a line detector), *i.e.* PILATUS 100K pixel detector [146] at that station further allows acquisition of high resolution and efficient 3D reciprocal space maps. Moreover, the beamline has two double crystal monochromator, which in combination with two mirror delivers highly monochromatic beam (of wavelength 0.8 Å) with negligible second harmonic contamination. When acquiring 3D RSM on superlattice films, beam of size 0.8 x 0.5 mm^2 was used on the sample and focused on to the detector for best resolution [145]. In standard set-up, sample is mounted 859.1 mm away from the detector. Superlattice thin-films grown on various substrates were measured at this beamline for detailed investigation of ferroelectric domains and superstructures arising from novel polarization distributions. And, their results are discussed in chapter 5 and chapter 6. Here, I will briefly discuss different aspects of 3D RSMs, which can be used to perform detailed structural characterization of superlattice thin-films.

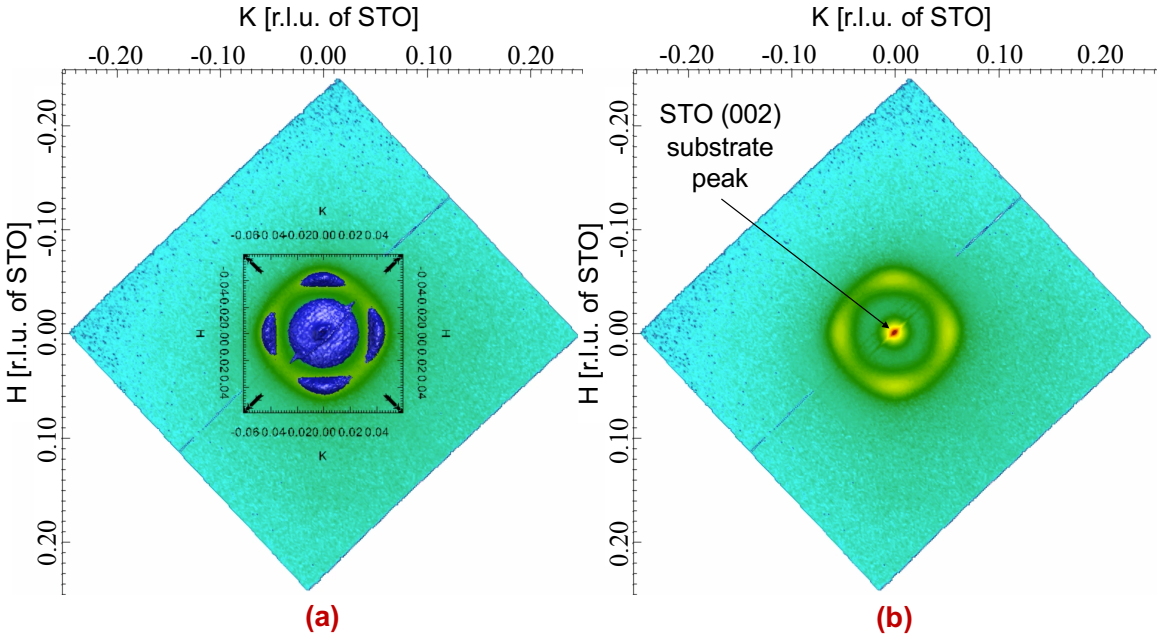

Figure 2.21: A HK-cut taken at L = 0.965 overlaid on 3D RSM (a) yielding a two-dimensional map shown in (b).

We will take an example of superlattice film of STO/PTO with superlattice periodicity of 12.4 nm, *i.e.* 16 x 16, and total thickness of 100 nm grown on STO (001) substrate (details of growth are discussed in chapter 5). The 3D RSMs of this superlattice film is acquired at Sector 33-BM-C beamline of APS. A 3D view of reciprocal space map around 002 reciprocal lattice point of STO substrate is shown in Figure 2.19. The three orthogonal axes represent 'H', 'K' and 'L' direction of reciprocal lattice space for STO. The features in this plot represents all positions in a three dimensional space defined by the reciprocal lattice vectors where diffracted beams are recorded. Previously discussed diffraction experiments such as standard symmetric 'θ - 2θ' scan and 2D reciprocal space

map are a line profile and 2D planar cut respectively in these 3D Reciprocal Space Map (RSM). Thus, one 3D RSM contain all information of diffracted beams around a specific reciprocal lattice point. To illustrate this better, we start from same 3D reciprocal space map (shown in Figure 2.19), now viewed along a direction in which H-direction points inside the plane of the paper. A 2D planar cut through this three-dimensional RSM is taken at H = 0 position, also known as 'L-K' cut, and overlay of that with 3D figure is shown in Figure 2.20(a). The two-dimensional reciprocal space map is colored according to the intensity profile recorded on that plane. Finally, we get a two-dimensional space map (Figure 2.20 (b)) which shows the position of intense peaks corresponding to those features observed in 3D. Now, we can use the peak positions on this map to analyze various periodic features present along 'L' and 'K' direction (shown in Figure 2.20(b)). For example, periodic bright red peaks present along L-direction at K = 0 corresponds to superlattice periodicity, which comes out to be 12.4 nm consistent with that measured from laboratory-based XRD. The periodicity along K-direction can similarly be calculated and comes out to be about 7.2 nm (accurately determined from the line (intensity) profile taken along K-direction for a given value of 'H' on this map). The superstructure responsible for giving rise to this periodicity is discussed in later chapters and is of great importance to this dissertation.

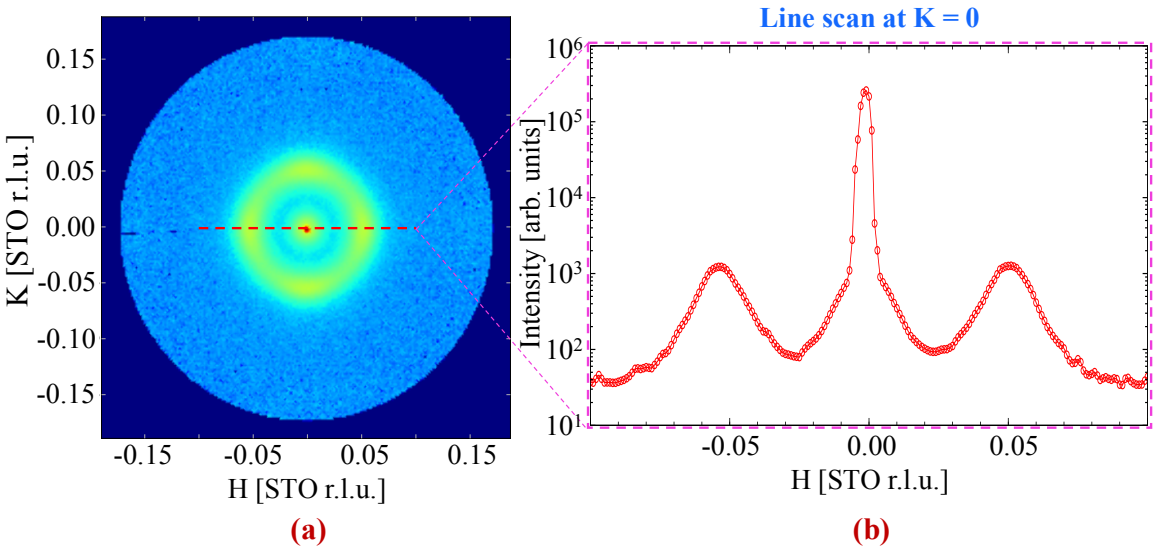

Figure 2.22: Using a HK-cut (a) obtained from a 3D RSM around (001) peak of STO (001) substrate, a line scan taken along H at K = 0 and L = 0.965 is shown intensity profile in (b).

Similarly, we can obtain other planar cut through the 3D RSM by choosing an appropriate position of reciprocal lattice point. Figure 2.21 presents another example of 2D planar cut at L = 0.965 giving rise to HK-cut. Note the value of 'L' for HK-cut is chosen in a way that the cut passes through the alloy peak (50:50) of the superlattice film. The peaks observed on the HK-cut RSM represents superstructure present along both H- and

K-directions. A line scan (intensity profile) taken along H-direction at K = 0 is shown in Figure 2.22 from which 7.2 nm periodicity associated with those features is extracted. As mentioned earlier, one can also obtain simple line scans from these 3D RSMs. To explain this more, we consider a LH-cut of 3D RSM of the same superlattice sample discussed above (Figure 2.23). Note that, in this case, 3D RSM data was acquired in a way, which collected two reciprocal lattice points, *i.e.* 001 and 002, of STO substrate. The reason for choosing two reciprocal lattice points is to bring out the similarity between this and the regularly performed 'θ - 2θ' symmetric scan showing both 001 and 002 peaks of the STO substrate. Now, the 'θ - 2θ' scan regularly performed in laboratory-based XRD, is simply the intensity profile taken along L-direction at H = 0 on this RSM map. Figure 2.24 shows the Intensity vs. L value for the line scan along L-direction or standard out-of-plane direction of the substrate. The superlattice peaks (SL $^{(n)}$ 002) present along L-direction corresponds to the same 12.4 nm periodicity of the superlattice structure, *i.e.* 16 x 16.

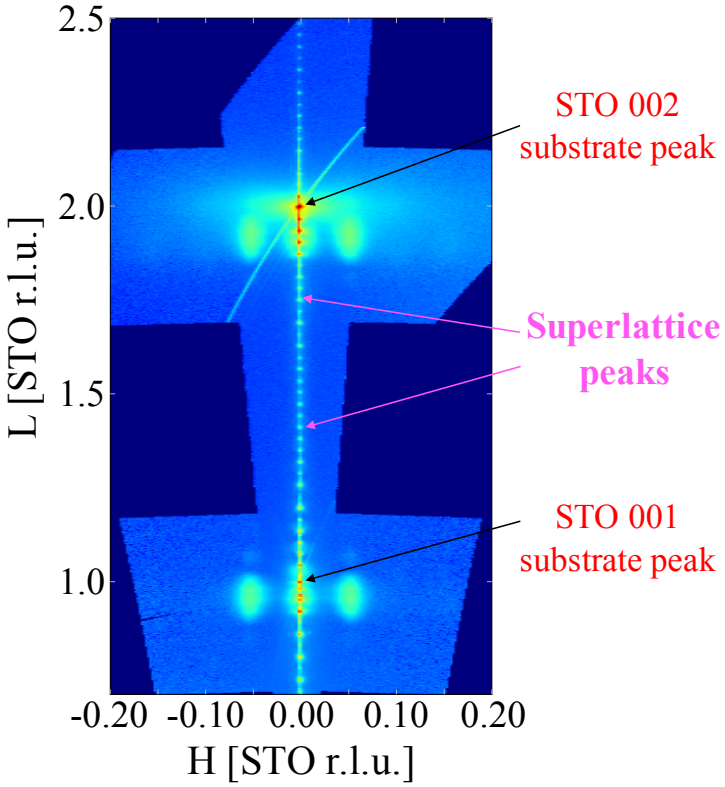

Figure 2.23: An LH-cut from a 3D RSM encompassing both (001) and (002) Bragg peak of 16 x 16 PTO-STO superlattice grown on STO (001) substrate is shown.

Synchrotron X-ray diffraction, thus, enables us to characterize structure features present in thin-film, which are very difficult to study using laboratory-based X-ray diffractometers. In addition, it allows to acquire full three-dimensional reciprocal space around a given reciprocal lattice point efficiently and with high accuracy. *In situ*

temperature dependent X-ray diffraction (3D RSMs) of superstructures can also be performed at this beamline, which further emphasizes the importance of these measurements in achieving full physical understanding of nanoscale features. Moreover, one can also perform other *in situ* experiments such as Electric-field dependent X-ray diffraction [143] of ferroelectric domains using such high-flux photon sources. In summary, Synchrotron X-ray diffraction provides a powerful method to perform full structural characterization of thin-films and superlattices.

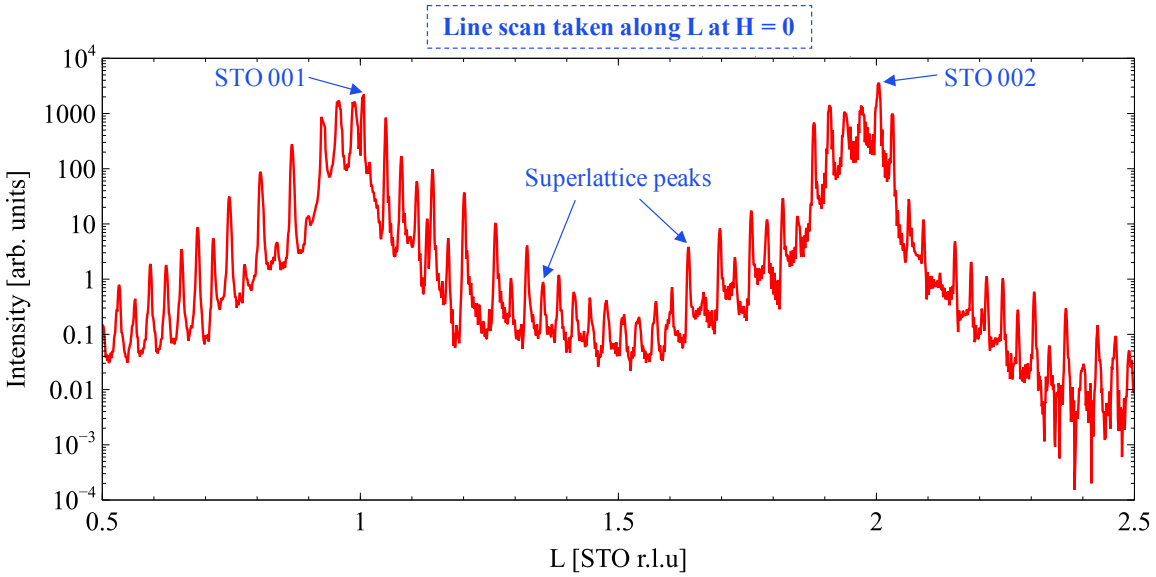

Figure 2.24: A line scan taken along L direction in the LH-cut obtained from 3D RSM having both (001) and (002) peak is shown as intensity profile vs. L values.

2.2.4 Scanning Probe Microscopy

Scanning probe microscopy (SPM) [147] is a widely used technique for imaging and measuring surface characteristics down to atomic level. Unlike optical microscopes where the user can directly *see* the surface, scanning probe microscopes *feels* the surface and creates a representative image of the surface. The working principle of scanning probe microscopes is depicted in Figure 2.25. Various components of an SPM include an extremely sharp tip, typically has radius of curvature of 3 – 50 nm [147] but it could be as sharp as single atom [148], mounted on a flexible cantilever which allows the tip to have motion in 'z' and also in the in-plane direction of the sample. When the tip is brought near the sample surface, the interaction between tip and sample causes the cantilever to deflect. The laser detects this deflection, which is getting reflected off from the top of the cantilever and recorded into an array of photodiodes. As the tip scans the sample surface, data gets recorded into a computer, which then creates a representative image of the sample surface.

Now based on the tip-sample interaction or feedback mechanism, scanning probe techniques can be divided into three main categories: First, when the feedback mechanism is based on weak electric current passing between tip and the sample held at a distance, commonly known as Scanning Tunneling Microscopy [149]. Second, when the feedback mechanism is based on detection of light energy from a very small light source located very close to the sample surface, also known as Near-field Scanning optical microscopy (NSOM) [150]. Third is, when the feedback mechanism is based on the interaction force between the tip and the sample, also known as Atomic Force Microscopy (AFM) [151]. Since AFM is mostly used SPM technique in the studies presented in this thesis, we will limit our discussion to AFM and its most widely used variation for characterizing ferroelectric thin films, *i.e.* PiezoForce Microscopy.

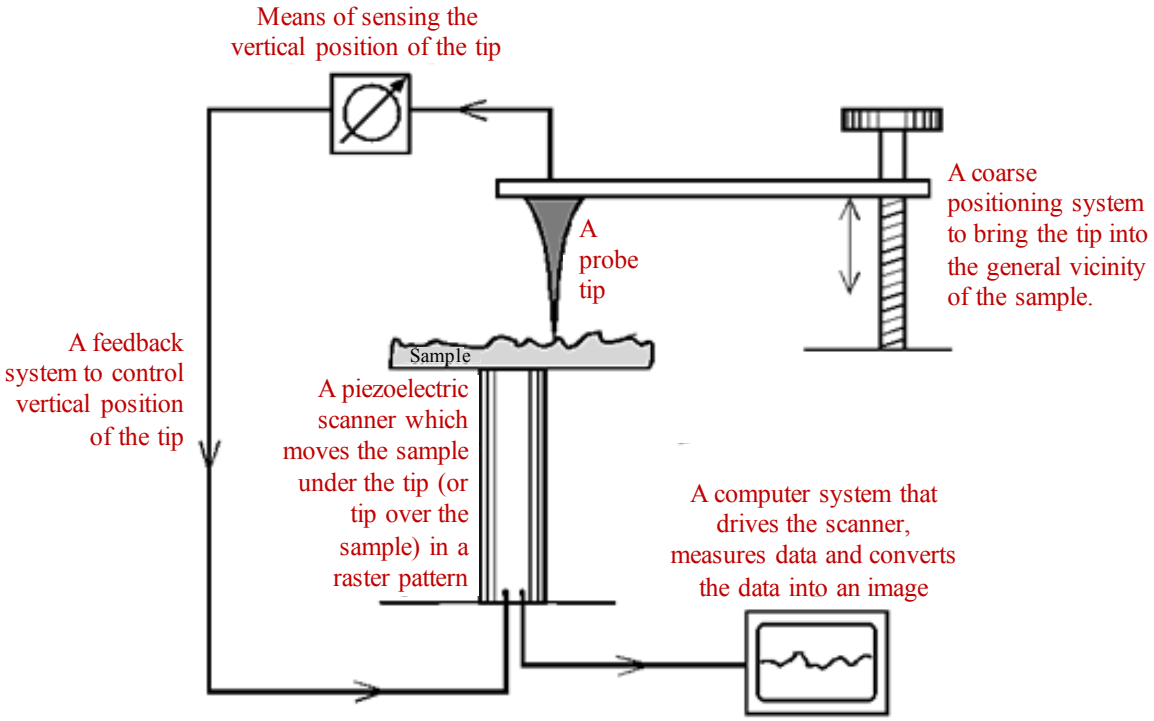

Figure 2.25: A schematic of typical scanning probe microscope. Figure adapted from [152].

Atomic Force Microscope as discussed above uses the interaction force between the tip and the sample as the feedback mechanism to image the sample surface. Amongst various modes of operation, two most common modes used in imaging regular surface topography are Contact mode and Non-contact mode or tapping mode. In contact mode AFM, as the tip scans the sample surface it maintains constant (short-range repulsive) force between the sample and tip by moving the cantilever up or down as needed. Recording the deflection of cantilever as tip maps the topography of the sample surface forms the image. In non-contact or tapping mode AFM, the cantilever is vibrated at a frequency near to its

resonance frequency. When the oscillating tip is brought closer to the surface, the interaction with the sample changes its amplitude and phase. Thus, when the oscillating tip scans the sample surface, changes in the amplitude and phase provides information about the distance between the sample and tip which is then used to form an image of the surface topography of the sample. As an example, Figure 2.26 is drawn which provides AFM image of treated STO substrate.

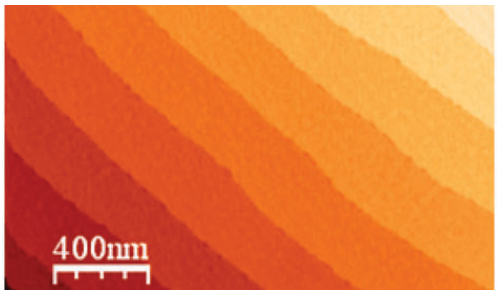

Figure 2.26: AFM image of a treated-STO (001) substrate. Figure adapted from [153].

AFM is very frequently employed SPM technique in characterizing surface characteristics of crystalline substrates [154; 155] and thin-films [106; 118]. The ability of this technique to provide surface topography with 0.1 nm resolution in height makes it ideal for characterizing surfaces having atomic steps/terraces [153]. When optimizing growth conditions for a given material, AFM may become extremely crucial in providing feedback for the need of further optimization of growth parameters. For example, optimizing growth parameters for synthesizing thin-film of SRO critically depends on the surface topography of the as-grown films [106]. In other materials, for example, $BiFeO_3$, the presence of second phase particles in thin-film, especially for small volume fraction of these second phases which may be difficult to characterize with laboratory based XRD, AFM can identify those secondary phases owing to the difference in the crystallographic structure, and hence, their surface topography [156]. This further emphasizes the importance of AFM being a crucial characterization tool for optimizing growth parameters of various materials.

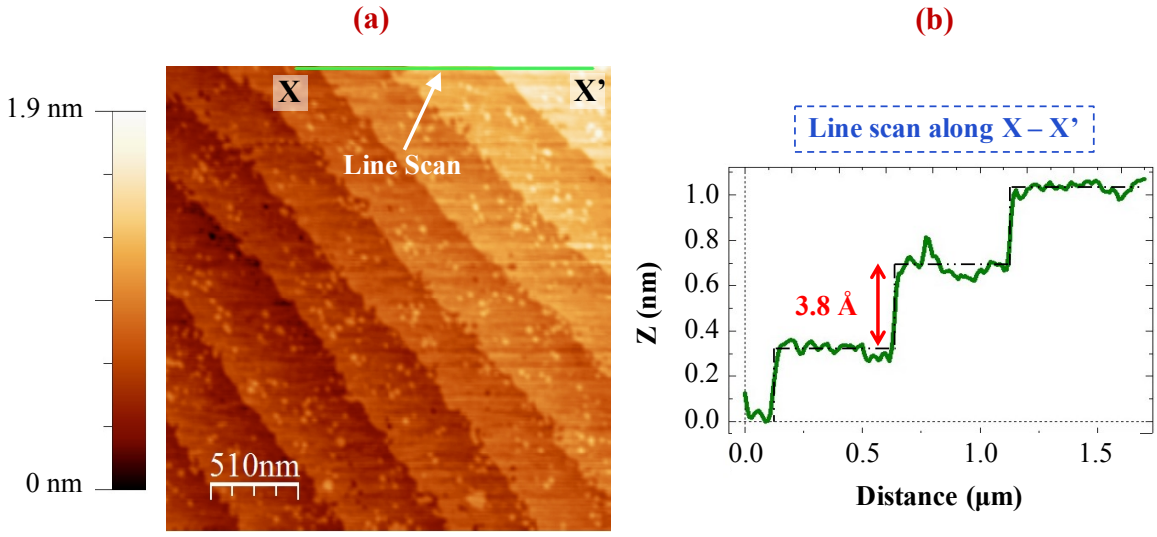

Figure 2.27: AFM image (a) of a 200 nm thick 2 x 2 STO-CTO superlattice grown on a STO (001) substrate imaged under non-contact mode is shown along with a line scan along the atomic steps in (b) to extract the step height for these films.

After achieving right growth conditions, AFM can be further employed to characterize surface characteristics of thin-films. For example, AFM of a 200 nm thick 2 x 2 STO-CTO superlattice film grown on STO (001) substrate is shown in Figure 2.27. The presence of atomic steps confirms the *in situ* RHEED characterized layer-by-layer growth of 200 nm thick superlattice thin-film. The line scan shown in Figure 2.27(b) reveal step height of 3.8 Å, which is approximately equal to the unit-cell of STO. The roughness of thin-films is other important parameter frequently probed by AFM. For example, the roughness of the superlattice film shown in Figure 2.27 is approximately 3 Å, which attest to the smooth surface topography of these films. Thus, AFM technique proves to be an important surface characterization method for synthesis and characterization of thin-films of superlattices and heterostructures.

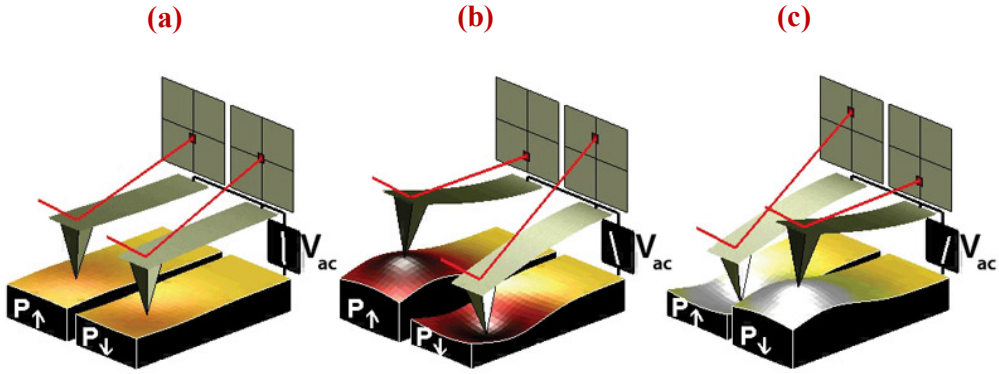

Figure 2.28: A schematic of tip-sample interaction for the case when the sample has polar domains aligned parallel or antiparallel to out-of-plane direction, with an external voltage applied across using a conductive tip. From [157].

Based on the same working principle as AFM, another SPM technique widely used in characterizing thin-films of ferroelectric materials is Piezoforce Microscopy (abbreviated as PFM) [158]. PFM technique is based on the electromechanical coupling present in functional materials such as piezoelectric, ferroelectric materials. In PFM mode, sample surface is scanned in contact mode using a conductive AFM tip. During the scan, a voltage between the tip and the sample is applied which establishes an electric field within the sample. If the sample is ferroelectric/piezoelectric in nature then due to inverse-piezoelectric effect or electrostriction, the sample will locally contract or expand depending on the direction of applied electric field and polarization state (local electrical domain structure) of the sample (illustrated in Figure 2.28). When the polarization is pointing out-of-the-plane sample and is parallel to the applied electric field, it will cause domains to expand at that region. Similarly, if the polarization is anti-parallel to the applied electric field, it will cause the domains to contract. Since the AFM tip is in contact mode, expansion or contraction of that region will cause cantilever to bend upwards or downwards respectively. The amount of cantilever deflected is directly related to the amount of expansion or contraction of domain, which is further proportional to the applied electric field. So, essentially, the electrostriction coefficient of the piezoelectric or ferroelectric material provides feedback mechanism for the PFM image formation mapping the domain structure of the sample.

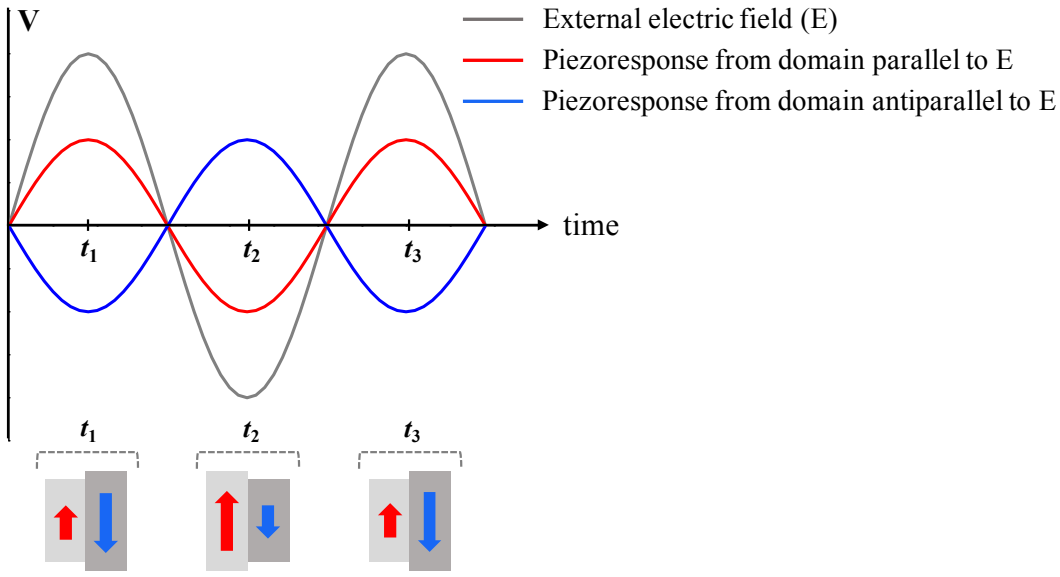

Figure 2.29: A schematic of piezoresponse signal as a function of time when bias voltage has small AC signal embedded in it. Figure also shows schematic of domains aligned parallel or antiparallel to electric field, at different intervals of time. Figure adapted from [159].

Now, if the applied voltage also contains a small AC voltage then due to same inverse piezoelectric effect the sample surface will start oscillating at a certain frequency in response to the applied ac signal. For an ideal case, the following relation gives polarization associated with such applied mechanical stress:

$$P_i = d_{ijk}\,\sigma_{jk} \tag{2.1}$$

, where 'd_{ijk}' is rank-3 tensor of the material. For a tetragonal structure, the tensor simplifies [158; 159] to:

$$d_{ijk} = \begin{pmatrix} 0 & 0 & 0 & 0 & d_{15} & 0 \\ 0 & 0 & 0 & d_{15} & 0 & 0 \\ d_{31} & d_{31} & d_{33} & 0 & 0 & 0 \end{pmatrix} \tag{2.2}$$

When an ac voltage $V = V_O \cos(\omega t)$ is applied across the sample, the surface vibrates with $\Delta Z = \Delta Z_O \cos(\omega t + \varphi)$. In a simple case of polarization pointing parallel or antiparallel to electric field as discussed above, amplitude (ΔZ_O) would be $d_{33}V_O$ with phase (φ) be 0° or 180° respectively as shown in Figure 2.29. In a typical PFM experiment, the applied voltage is much smaller than the coercive bias and therefore does not alter the local domain structure. Under those conditions, a PFM image can be generated which will have phase contrast at different positions on the sample along with the amplitude of local piezoelectric coefficient in the vertical direction (also called as Vertical PFM or out-of-

plane PFM). In general, we would encounter the AFM tip deflecting not only in the 'Z' direction but also in 'X' or 'Y' direction *i.e.* in the in-plane direction of the sample. One needs to similarly measure the lateral components of deflection of AFM tip to generate an PFM image which will have phase contrast and local piezoresponse in the in-plane direction (also called as Lateral PFM or in-plane PFM). As an example, Figure 2.30(a, b) shows the amplitude and phase contrast PFM image of a ceramic PZT. In a typical PFM measurement, a vector PFM is done which provides information for both vertical and lateral deflections of the tip giving rise to out-of-plane (OOP) and in-plane (IP) PFM image of the sample [158], illustrated in Figure 2.31. In the case of PFM also, the resolution is limited by the conductive AFM tip used for applying voltage and is typically about 30 nm. Lastly, note that I have only discussed the basic principle behind the working of PFM, more details about the optimization of measurement parameters to reduce experimental noise such as cross-talk between in-plane and out-of-plane signal is discussed elsewhere [158].

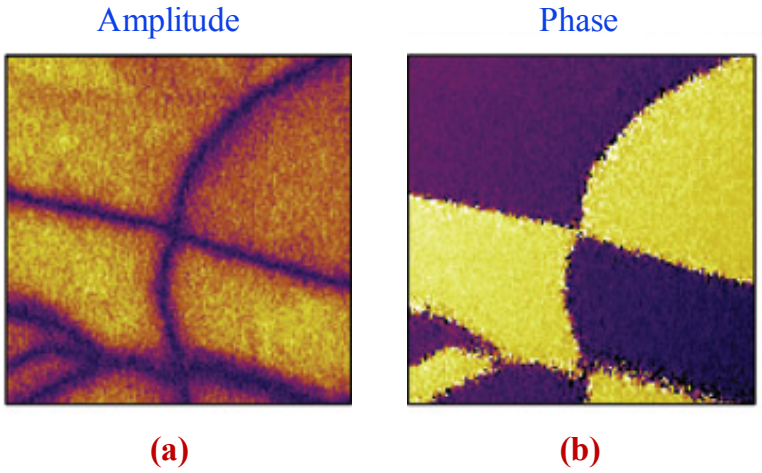

Figure 2.30: Amplitude (a) and phase (b) image of ceramic PZT sample. From [157].

Thus, using PiezoForce Microscopy one can characterize various domain structures present in thin-films of ferroelectric/piezoelectric materials. Moreover, one can also perform detailed switching dynamics of various domain structures [160] by applying voltages more than coercive bias. PFM can also be used in conjunction with other structural characterization methods such as XRD and RSM to identify exact unit-cell distortion associated with the ferroelectric phase [161]. As will be discussed in chapter 6, PFM when used in conjunction with other characterization techniques such Transmission Electron Microscopy and XRD, can help identify the regions of interest along with their associated piezoresponse present along certain crystallographic directions. In addition, PFM can also be used to perform *ex situ* electrical field-dependence study of other physical properties such as optical properties (example: X-ray Circular Dichroism). Similarly, one can perform *ex situ* temperature dependent study to investigate phase transitions of ferroelectric domains present in thin-films. Lastly, using PFM one can also obtain local hysteresis response of various ferroelectric phases present in a thin-film sample, by measuring

piezoresponse as a function of applied dc voltage and/or frequency of the ac-component in the voltage bias. This is also called as PFM spectroscopy and it complements the imaging mode of PFM technique. Above examples emphasizes the importance and versatility of PFM technique in characterizing of ferroelectric properties of thin-films.

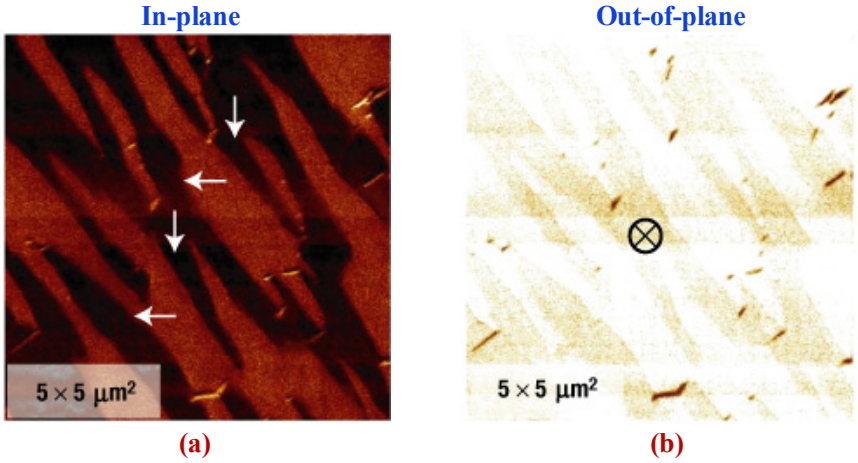

Figure 2.31: In-plane (a) and Out-of-plane (b) PFM image of 600 nm thick (as-grown) $BiFeO_3$ on SRO (001) buffered with conducting SRO bottom electrode. From [162].

2.2.5 Transmission Electron Microscopy

Transmission electron microscopy (abbreviated as TEM) is another microscopy technique that is employed for material characterization across various disciplines. While its similar to optical microscope in the sense of "seeing" the sample directly, the resolution of Electron Microscopes can be as small as 0.5 Å [163], which is at least three orders of magnitude lower than achieved via optical microscopes. The other major advantage of using TEM is its capability to allow imaging of samples with magnifications as high as 10^6 [163]. In addition, TEM provides both the image of the sample and the electron diffraction pattern of the sample, which makes this technique one of the most powerful method to do structural characterization of materials. Moreover, TEM is also capable of doing chemical analysis for ex. via Electron Energy Loss Spectroscopy (EELS) [163], making this method truly versatile. Since this thesis focuses on applying TEM for structural characterization, I will limit our discussion to principle and operating modes of imaging and diffraction only.

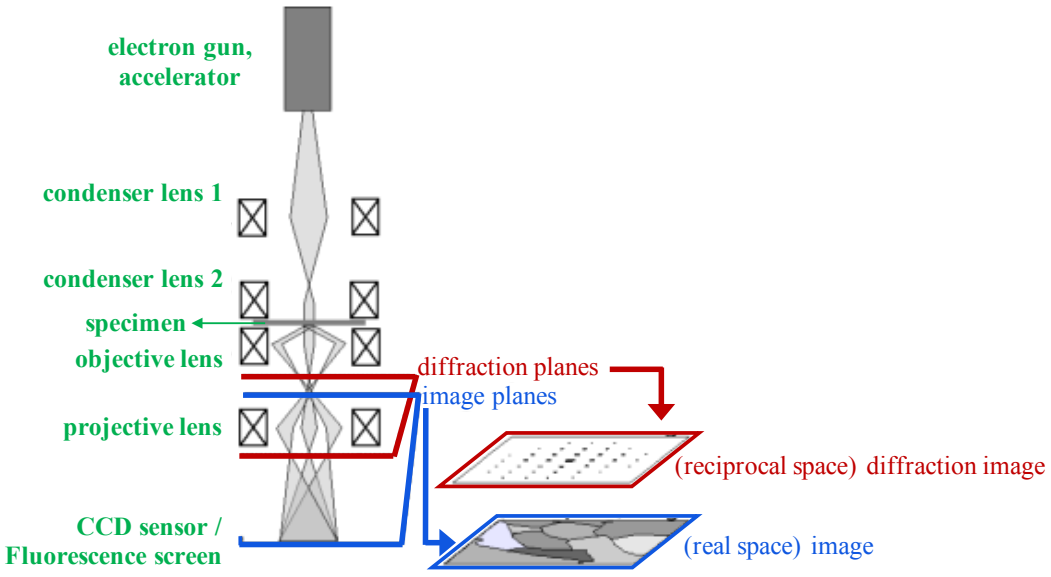

Figure 2.32: A schematic of a conventional transmission electron microscope. Figure adapted from [164].

The basic working principle of conventional transmission electron microscopes is illustrated in Figure 2.32. First, electrons are generated either by thermionic emission or field emission with a help of high voltage source (100 – 300 kV). Preliminary focus to these emitted electrons is achieved by applying voltage and using aperture of appropriate size making them ready to be introduced in the lensing system. The first set of lenses (condenser lenses) then focuses the electron beam of a desired size (usually is in micrometers) on the sample. Typically, the specimen thickness is about 20-30 nm and considerable amount of time is spent in preparing these TEM samples to ensure that they are electron transparent. When these highly energy electrons pass through the specimen, an objective lens is used to form an image from the interaction of electrons with the specimen. This image is then further magnified using intermediate lens positioned further down on microscope and finally focused on to a fluorescent screen. This fluorescent screen is either has a CCD camera or a photographic film to record the image. If the specimen is crystalline, one can record the electron diffraction pattern of the specimen by readjusting the back focal plane to the position where diffraction image forms as illustrated in the schematic (Figure 2.32). Thus, one can use these electron diffraction patterns to perform detailed analysis of the phase, crystal structure and lattice parameters of the unit-cells [163]. While the direct imaging of the crystalline lattice allows us to delineate the defects in the sample [163], analyze the local structural distortions in the bulk [165], at the interfaces [166] *etc.*

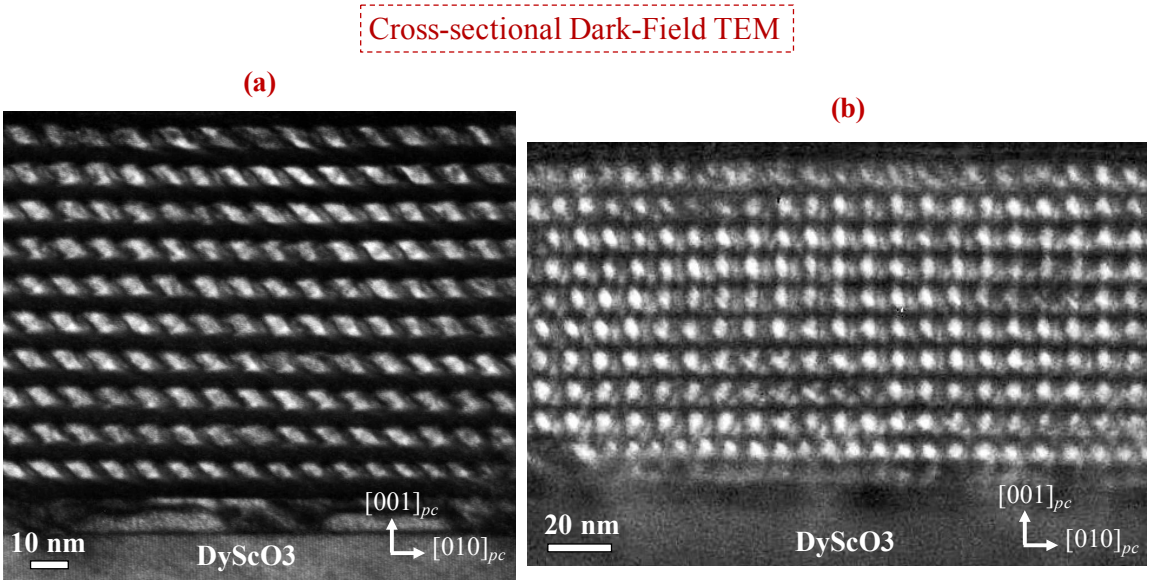

Figure 2.33: Cross-sectional dark-field TEM images of a 12 x 12 PTO-STO superlattice film grown on a 5 nm SRO on DSO substrate is shown for two different tilt angles (a) and (b). Courtesy of Dr. Christopher Nelson.

Now, there are many imaging modes possible in a conventional TEM such as diffraction contrast, phase contrast *etc.*, depending upon which transmitted electron beams (deflected or non-deflected) were used to form the image. In diffraction contrast image, an "objective" aperture is inserted into the back focal plane of the objective lens to block most of the diffraction spots and allow only one diffraction spot to form the final image. When the aperture is positioned in a way to allow only the directly transmitted electrons it forms what is called Bright-Field image of the sample. Conversely, if the aperture allows one of the diffracted spots to form the image it is called Dark-Field image of the sample. In case of crystalline materials, good diffraction contrast image can be obtained from what is called two-beam condition, where the sample is normally tilted so that only one diffracted beam corresponding to a Bragg angle is excited. An example of dark-field TEM image obtained under 2-beam condition depicted in Figure 2.33(a), which shows contrast in PTO layers of 12 x 12 PTO-STO superlattice thin film grown on DSO (110) substrate. Note that the contrast observed in a 2-beam condition strongly depends on the chosen diffracted peak to form the image. For example, Figure 2.33(b) shows the dark-field image of the same sample, but the contrast shows more like bright "spots" occurring periodically, as compared to previous image, which showed more, like "screw-like" pattern again occurring periodically in each PTO layers. More detailed discussion of these features will be discussed later in Chapter 5. In a phase contrast image, however, more than one beam, *i.e.* directly transmitted and diffracted beam(s) is used to form the image. Note that the image formation in this mode will constitute both amplitude and phase of electron waves scattered from the sample, and thus, will form high-resolution image of the sample.

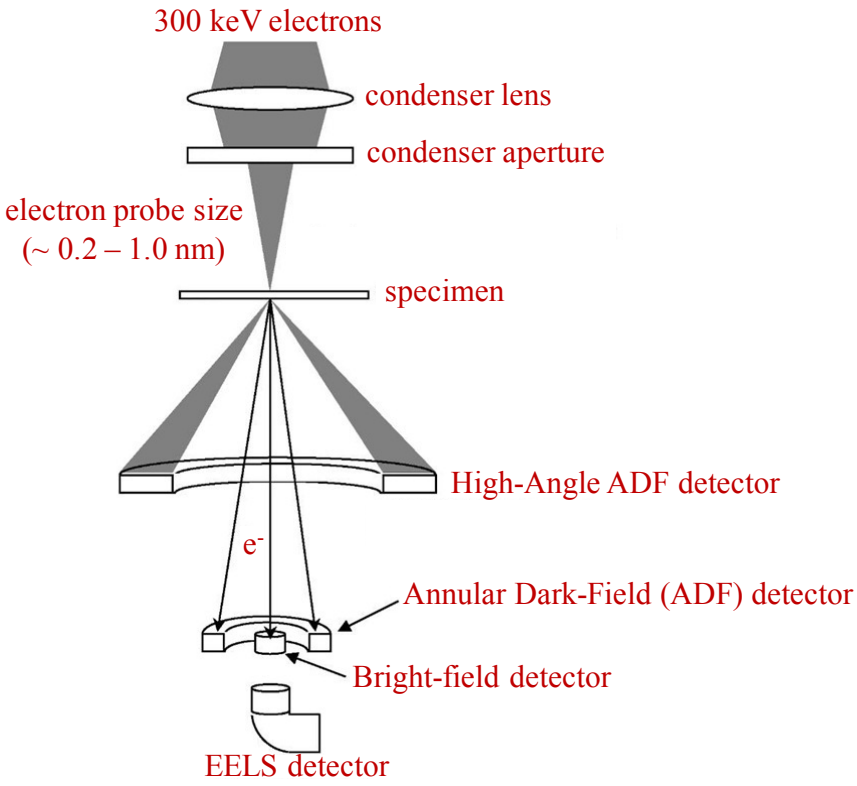

Figure 2.34: A schematic of a scanning transmission electron microscope. Figure adapted from [167].

There is another important mode of TEM, which is immensely used in characterizing thin-films called as Scanning Transmission Electron Microscope (STEM). In STEM mode, lenses of the microscope are adjusted to converge the electron beam to a probe size of 0.1 – 0.5 nm, which destroys the electron beam coherence. This is in contrast to conventional TEM mode where parallel beam of electrons of size few micrometers is focused on the sample. The focused electron probe is scanned across the sample point-by-point making a 2D map of the sample, as compared to an area illuminated in normal TEM. The STEM image is formed by mapping the intensity of electrons scattered at certain angles, which are collected by either High-Angle Annular Dark-Field detector (HAADF), or Annular Dark-Field detector, or a Circular Bright-Field detector (as shown in Figure 2.34). An incoherent image is formed when the high-angle scattered electrons are used for image formation, which is chemically sensitive, *i.e.* it forms a Z-contrast image. And, these Z-contrast STEM images shows better contrast than High-resolution TEM (which form coherent image). Essentially, a Z-contrast STEM image represents an atomic resolution 2D map of scattering power ($I \propto Z^2$) of the sample. More importantly, ADF-STEM images are directly interpretable since there is no phase information in the incoherent image, thus does not require any contrast reversal like in HR-TEM. An example of Z-contrast high-resolution STEM is given in Figure 2.35 which shows a cross-sectional TEM of a 16 x 16

PTO-STO superlattice film grown on 5 nm SRO on DSO (110) imaged along $[001]_o$ or $[010]_{pc}$ zone axis of the DSO substrate.

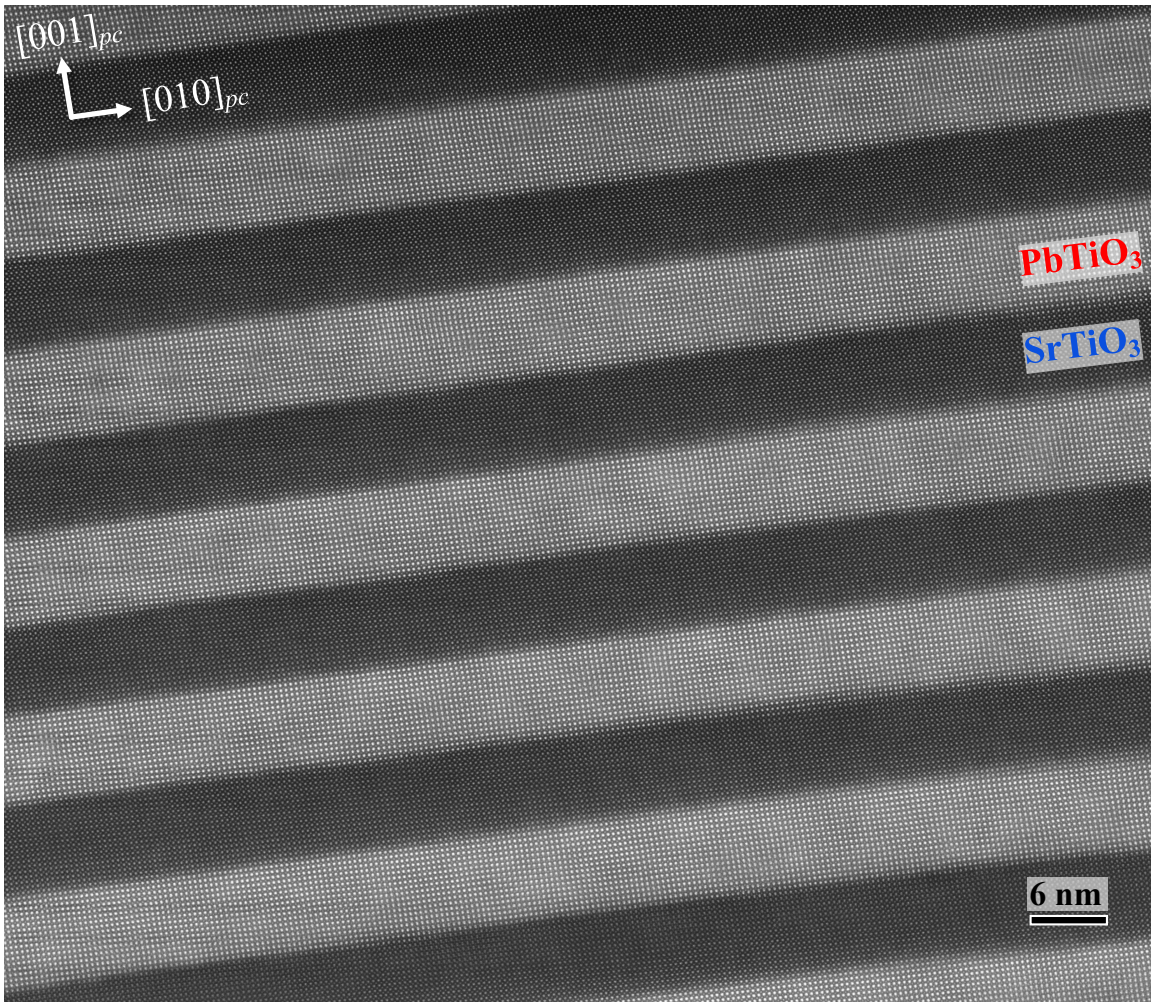

Figure 2.35: A cross-sectional atomic-resolution HAADF Z-contrast TEM image of sub region of a 16 x 16 PTO-STO superlattice film grown on 5 nm SRO on DSO (110) substrate. Courtesy of Dr. Christopher Nelson.

We note that most of these superlattice films were studies under cross-sectional view, implying XZ cross-section where 'Z' points in the out-of-plane direction of the thin-film sample. In certain cases, one may want to look at the planar section of the thin-film sample, *i.e.* XY section, also known as planar TEM. Although the sample preparation is slightly different for planar TEM, the working principle is the same. Figure 2.36 provides an example of a planar dark-field TEM of a 6 x 6 PTO-STO superlattice film grown on 5 nm SRO on DSO (110) substrate, obtained under STEM mode, showing long-range

ordered ferroelastic a_1/a_2-type domains present in these superlattice films (see chapter 6 for more details).

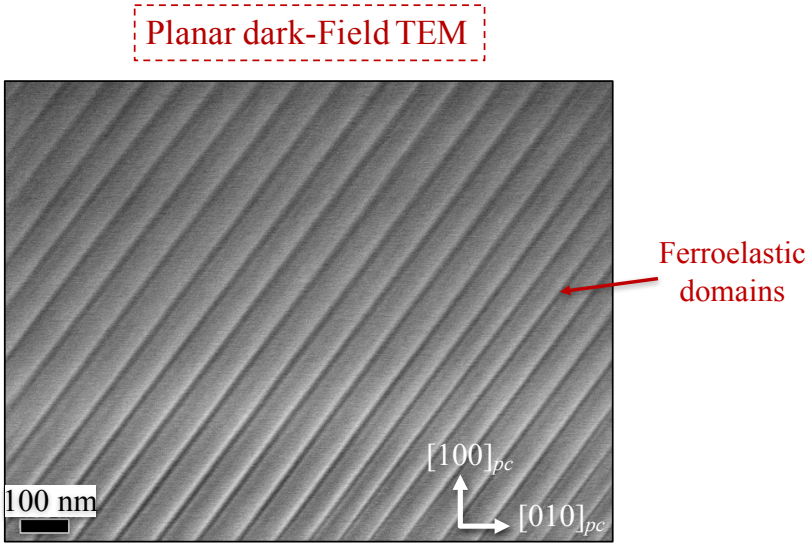

Figure 2.36: A planar view dark-field TEM of 6 x 6 PTO-STO superlattice film grown on 5 nm SRO on DSO (110) substrate. Courtesy of ShangLin Hsu.

Superlattice thin-films discussed in this thesis were characterized by TEM operated in various different modes as discussed above. The most crucial mode was HR-STEM given its capability to achieve atomic resolution Z-contrast images of crystalline samples. The availability of such atomic-resolution STEM images allows one to preform simulations, which can help extract different information about the crystalline sample. As will be discussed later, the layering sequence of aperiodic superlattices, which were *in situ*, characterized via RHEED, were later confirmed with the help of simulation performed on the atomic-resolution STEM images (Figure 4.20). Moreover, these high-resolution Z-contrast STEM images were also used in conjunction with simulations to measure the local atomic displacements with picometer resolution in ferroelectric materials [166; 168]. From such measurements of local atomic displacements in a crystalline sample can be further analyzed to extract more insights about the sample. For example, Figure 2.37(a) shows the polar displacement map of a sub region of 16 x 16 superlattice along with analysis (Figure 2.37(b-e)) that can be done on atomic-resolution STEM image. Thus, this particular technique of electron microscope proved extremely crucial in characterizing the quality of interfaces in superlattice films and identifying nanoscale features discussed in this thesis.

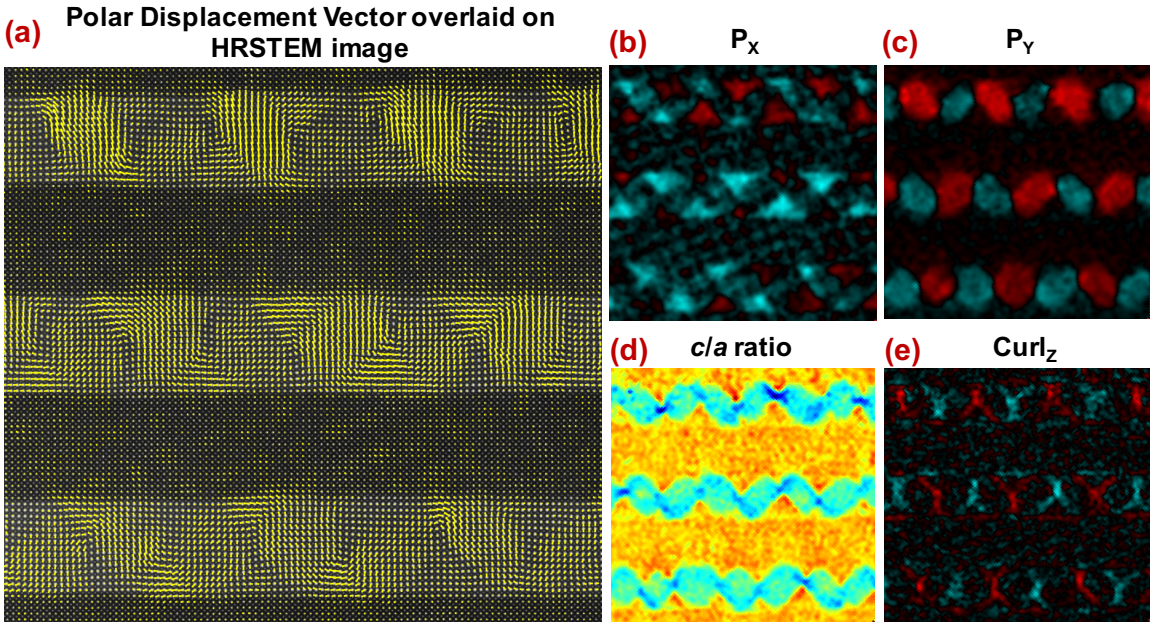

Figure 2.37: Polar displacements of A-site (Pb, Sr) atoms in a 16 x 16 PTO-STO superlattice film grown on a DSO substrate, extracted from atomic-resolution Z-contract STEM image is shown in (a), whereas the components of polar displacements along *x*- and *y*-direction is shown in (b) and (c) respectively. More analysis such as mapping c/a ratio (d) of unit cell lattice constant, and curl of polar displacement (e) based on the atomic resolution STEM image can be obtained. Courtesy of Dr. Christopher Nelson.

2.2.6 Rutherford Backscattering Spectrometry

Rutherford backscattering is a technique which allows determination of chemical composition of materials. The technique works on a simple principle that when low atomic number atoms (example: He) are bombarded on the target, due to head-on collision of these incident atoms with the target atoms, significant portion of incoming atoms gets backscattered. These backscattered atoms were collected using a detector, which analyzes their respective energies giving rise to a RBS spectrum. The backscattering cross-section strongly depends on the atomic number of the nuclei present in the sample. Hence, this technique is capable of detecting heavy atoms only few nanometers thick [169; 170]. Moreover, the energy spectrum also reveals the depth profile of the target atoms. Thus, one can use this RBS spectrum to obtain information regarding the thickness of the films [169; 170]. Another major advantage of this technique is that no standards are needed to determine the composition of the material, only an RBS spectrum and a software package to simulate the spectrum is needed [171]. We also note that no sample preparation is required to perform this measurement and it is a non-destructive characterization technique [169]. One can also use this technique to characterize crystalline perfection of single

crystals and thin-films [172; 173]. In this thesis, this technique was mostly employed to measure the composition and its depth profile in thin-films and bulk PLD targets.

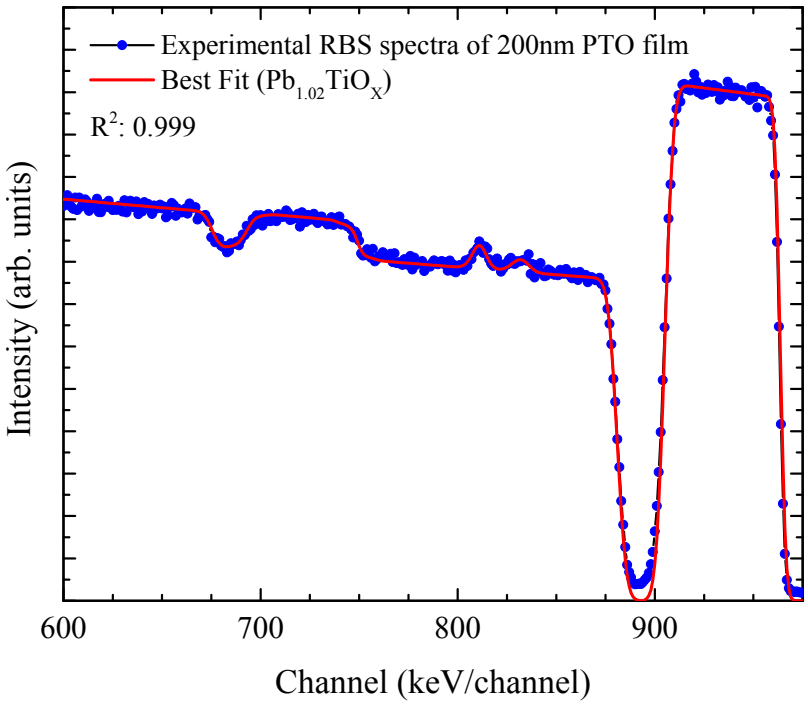

Figure 2.38: Experimental RBS spectra of a 200 nm PTO film grown on a $GdScO_3$ (110) substrate is shown, along with a simulated spectrum from which the stoichiometry of the film is extracted [168].

The optimization of growth parameters for various materials discussed in later chapters was finally checked with RBS to confirm the stoichiometry of ABO_3 with a desired A:B ratio as close to 1 as possible. Figure 2.38 provides an example of 200 nm PTO films grown on a $GdScO_3$ (110) substrate, which also shows a simulated RBS spectrum revealing Pb:Ti composition equal to 1.05:1. Note that in measuring the composition of thin-films substrate material should be chosen in a way to minimize the overlap of elements present in film and substrate (example: Figure 2.38). In the inset of Figure 2.38, R^2 known as coefficient of determination, a number, which represents how well the simulated graph fits to the experimental spectrum, is also given. As R^2 values approaches to 1 the quality of fit to the experimental data improves and equal to 1 suggests perfect fit. Further note that since depth profile of chemical constituents is also revealed in RBS, this method becomes very useful in characterizing thin-films which are comprised of volatile atoms such as lead (Pb) in PTO films. Similarly, target compositions were also checked to ensure desired composition of the target is chosen for growth, especially when polycrystalline targets were used. As it will become apparent in chapter 5, optimizing the composition of a polycrystalline PTO target played a crucial role in achieving layer-by-layer growth of PTO. In determination of chemical composition using RBS, an

experimental error of about 5% generally occurs. Lastly, a large probe size of He ion beam, *i.e.* about 2 mm in diameter, provides an average composition of the film or bulk sample, making this technique ideal for characterizing chemical composition.

2.3 Thermal Conductivity measurement

Thermal conductivity is one of the fundamental properties of materials and is widely used for characterizing materials of different classes, including new class of materials which are discovered regularly such as 2D materials (graphene) with the current advanced synthesis and characterization techniques available. Thus, measuring thermal conductivity plays a crucial role in performing full characterization of artificially-synthesized [174] or naturally-occurring [175] materials.

Thermal conductivity is defined as the ratio of heat-flux (heat per unit area, Q/A) and temperature gradient (temperature difference per unit length, ΔT/L). When a certain amount of heat (A) passes through a given area (A), it causes certain temperature difference (ΔT) to develop over a length (L) of the material. Thus, for a given material with known geometry, one needs to measure the heat along with the temperature difference developed to calculate the thermal conductivity of the material.

Now, there are different techniques [176-182] to measure thermal conductivity of materials based on the type of heating source used for the measurement. Broadly, these techniques can be characterized into two classes, steady-state technique and non-steady state technique (or transient) technique. In steady-state techniques, a time-independent heat-flux is used to induce temperature gradient across the material. With known geometry of the sample, temperature difference is measured and with measured heat flux thermal conductivity is calculated. Examples of steady-state measurements include hot-wire method [181], axial-flow measurements [176], radial flow-method [180], hot-plate method [178]. In non-steady state or transient method, a time-dependent heat flux is applied and temperature as a function of time is measured. The measured temperature variation with time is then compared to the solution of time-dependent heat equation and thermal conductivity of the material is calculated. In contrast to previous techniqu, this method measures thermal diffusivity of the material instead of thermal conductivity, due to inherent nature of time-dependent heating of the material. Since thermal diffusivity is related to thermal conductivity through the following relation: $\alpha = \frac{k}{\rho C}$, where '$\alpha$' is thermal diffusivity, 'k' is thermal conductivity, 'ρ' is density and 'C' is heat capacity, and, with known density and heat capacity, thermal conductivity is extracted using this relation. Examples of transient techniques include 3omega (3ω) method [177], Time-domain Thermoreflectance (TDTR) method [182].

For the measurement of thermal conductivity of bulk samples, steady-state techniques are readily applied for being relatively simple to use and straightforward in analysis due to steady-state heat equations. However, they suffer from challenges in accurately measuring the heat flux because of Blackbody radiation losses, which could

result in large amount of errors in measuring thermal conductivity, especially for low-thermal conductivity materials. In addition, the requirement of being in steady state may result in acquisition time of 30 mins or more for each measurement. More importantly, steady-state techniques are extremely difficult to employ in measuring thermal conductivity of thin-films. This is primarily due to the fact that temperature difference across a thin-film is extremely small and measuring such small temperature difference can influence actual temperature itself. Also, using steady state method will require placing temperature sensors at both bottom and top of the thin-film, and hence, will add the need for extensive fabrication processing. Thus, the use of steady-state techniques has been mostly limited to bulk-samples only.

For thin-films, on the other hand, transient techniques such as 3omega, TDTR *etc.* are heavily applied to measure thermal conductivity. Usually in these transient methods, a pulsed or periodic heat source is used. Due to the transient nature of these techniques, they offer great advantage of measuring thermal diffusivity of thin-films with relative ease, which would otherwise be very difficult to measure using previously described steady-state techniques. For instance, being large surface to volume ratio of thin-film, the radiation losses will be significantly higher let alone the difficulty in fabricating temperature sensors at both ends of thin-films. Moreover, the ability of these techniques to reliably measure the thermal conductivity of thin-films reflect on their importance in expanding the reach of characterization methods because thin-films can enable synthesis of artificial multilayer structure [183] or metastable phases [31], which are not available in bulk form. The assessment of crystalline quality of thin-films from these transient thermal conductivity measurement techniques have also been reported [184], further highlighting their usefulness in characterization of materials. Lastly, the transient techniques are much faster, typically takes few seconds to minutes to acquire data for each measurement compared to previous steady-state techniques.

Since this dissertation mainly focuses on thin-films, I will limit our discussion to transient techniques only. There are mainly two techniques, which are employed readily to measure the thermal conductivity of thin-films: 3omega (3ω) [177] and pump-probe technique [179; 182]. In 3ω method, a metal line is evaporated on the surface of the film, which is either electrically insulating or has electrically insulating top surface. The metal line acts as both the heater and thermometer for the thermal conductivity measurement. A current is passed through metal at a frequency ‘ω’, causing Joule heating (I^2R) of the metal which results in temperature rise of the metal oscillating at ‘2ω’ frequency. Since resistance of the metal increases with temperature, this causes resistance to oscillate at ‘2ω’ frequency also. Thus, when voltage ($I \bullet R$) is measured across the metal, it is observed to oscillate at frequency of ‘3ω’. The rise in temperature of the metal line (ΔT) is related to ‘3ω’ component of the voltage. Now, the expression for the temperature rise of the thin-film sample at certain distance can be calculated under appropriate assumptions for a known geometry of the metal line, containing terms such as thermal diffusivity/conductivity. By measuring ‘3ω’ component of voltage as a function of current frequency ‘ω’ temperature rise in the sample as a function of frequency is measured and compared against the analytical or numerical expression to extract the thermal conductivity of thin-film. In most

thin films of interest, the thickness of the film is much smaller than thermal penetration depth, *i.e.* the distance heat diffuses in the sample for one heating cycle, resulting into a measured signal which has contribution of frequency-independent temperature rise of both thin-film and substrate (on which film is synthesized). In that case, the bare substrate is separately measured to extract the signal from the film. In general, 3ω method provides higher accuracy for measurement of low thermal conductivity electrically insulating materials compared to other transient techniques such as TDTR. It can also be used to perform temperature-dependent thermal conductivity measurement from 30 K up to 1000 K. But, this method also poses some limitations to the materials it can characterize. For example, the accuracy of the 3ω measurement reduces when measuring semiconductor thin-films and becomes comparable to other techniques [185]. The biggest drawback of this method is its inability to measure thermal conductivity of thin-films whose values are comparable to the substrate on which the film is synthesized. For example, thermal conductivity of an isotopically pure Silicon film grown epitaxial on a Silicon substrate cannot be measured using 3omega method [186]. Thus, a high mismatch in thermal conductivity between the substrate and film material is needed (at least an order of magnitude higher) for 3ω methods to be able to characterize those class of thin-films. One more class of thin-films is complex oxides grown epitaxially on other complex oxide substrates (for ex. STO on NGO (110)). Precisely because of this reason, 3ω method was not used in characterizing superlattice films discussed in this dissertation.

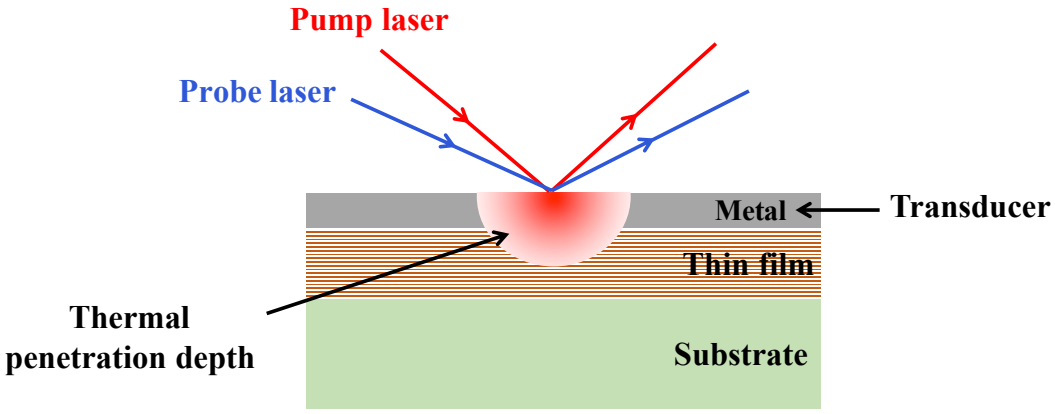

Figure 2.39: A schematic of a typical transient pump-probe technique.

Pump-probe transient method is another widely used method for measuring thermal conductivity of thin-films. The basic working principle in all these optical pump-probe techniques is the same, a schematic of which is depicted in Figure 2.39. In a transient pump-probe thermoreflectance technique, a metal transducer is deposited on top of the film, which is used to provide heat flux to the sample using an optical *pump* light source. The change in the temperature of the metal transducer is measured by the change in reflectivity of *probe* light reflected from the metal surface, owing to the thermoreflectance property of the metal. The thermal properties of underlying thin-film correlate strongly with the

measured change in reflectivity of the metal transducer. And, thermal models with free parameters were later used to fit the experimentally measured response to extract film properties such as thermal conductivity (in-plane [187] and out-of-plane [188] direction of film), thermal conductance of film/metal interface [189], heat capacity of thin-film [188]. There are two major implementations of pump-probe transient thermoreflectance (TTR) technique which are used to characterize thin-films: Frequency-domain Thermoreflectance (FDTR) [179] and Time-domain Thermoreflectance (TDTR) [182]. The basic difference between the two variations lies in the free experimental parameter used in the measurement, but the solution to diffusion equation to build the thermal model for extracting thermal properties of thin-film is essentially the same. In FDTR, the modulation frequency of the pump-probe is varied as the experimental parameter, which allows measurement of thermal properties such as thermal conductivity and heat capacity extracted from a single measurement [179]. In TDTR, however, time-delay of the probe pulse using a mechanical delay stage is used as the experimental parameter. TDTR being the most popular between the two techniques, I have employed this technique to measure the thermal conductivity of superlattice films discussed in chapter 4. The description of TDTR technique is presented next with an example of extracting thermal conductivity of single layer STO thin-film grown on NGO (110) substrate from a TDTR measurement.

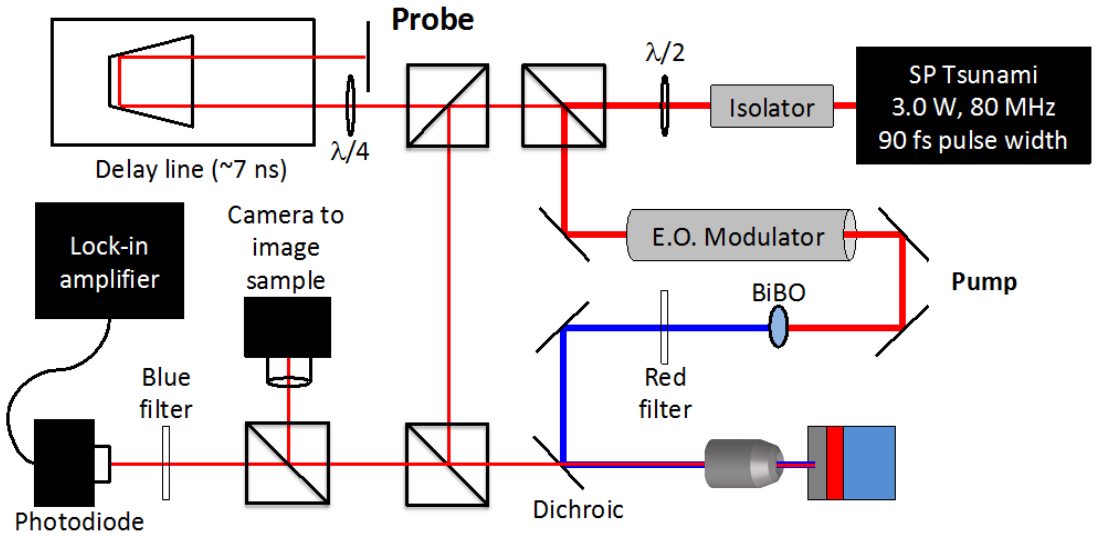

Figure 2.40: Schematic of main components of a standard TDTR equipment. Courtesy of Prof. Patrick Hopkins, UVa.

A schematic of TDTR experiment set-up used in this thesis is depicted in Figure 2.40 (courtesy of Prof. Patrick Hopkins, University of Virgina (UVa)). A Ti: Sapphire laser light source generating 90 femtoseconds pulse width of optical pulses with repetition rate of 80 MHz is used. Note the reason for choosing ultra short pulses as compared to time scale of measurement (typically ns) and repetition period (12.5 ns in this case) is to validate the assumption of considering these optical pulses (Figure 2.41(a)) essentially a delta-

function when building equivalent heat diffusion model for the measurement as detailed in literature [182]. The output of light from the laser is centered on 800 nm wavelength and this light source is split into a pump beam and a probe beam, which is further separated in time using mechanical delay stage (used for the probe beam). Pump beam having a train of femtosecond pulses repeated at 12.5 ns passes through an electric-optic modulator (EOM), shown in Figure 2.41(a), which imposes a square modulation chopping the beam with a reference frequency ω_o (Figure 2.40(b)), which in our case was ω_o = 11.4 MHz. Since we will be using only fundamental component of the modulation frequency (ω_o) in lock-in amplifier to reject both dc offsets and higher harmonics, sinusoidal modulation waveform comes out (Figure 2.41(c)). This sinusoidal modulated pump beam further undergoes a conversion from 800 nm wavelength to 400 nm using a Bismuth Borate crystal (BiB_3O_6 or BIBO). This is necessary to suppress the reflected pump beam from the sample contributing to the detection optics and is further subjected to optical filters to completely separate the pump beam from the probe beam. This greatly increases the signal-to-noise ratio of the measurement and also simplifies the beam alignment. Then the pump beam is focused on the sample using an objective lens yielding a pump beam radii of 24.5 μm on the sample. The probe beam, on the other hand, keeping the original output of the Ti: Sapphire light source is delayed using a mechanical delay stage, which can provide delay times up to few nanoseconds (5-7 ns). Using the same objective lens the probe beam is coaxially focused on the sample with beam radii of about 10 μm on the sample. The coaxial focusing of pump and probe beam allows removing any in-plane heat transfer contributing to the reflected signal of the probe beam [182]. In our case, Aluminum metal is used as temperature transducer with typical thickness of about 80 nm deposited using e-beam evaporation (at UVa). The reason for choosing aluminum metal lies in the fact that it has exceptionally high thermoreflectance coefficient (*i.e.* dR/dT) of about 10^{-4} K^{-1} at room temperature for light of 800 nm wavelength [190]. In addition, the reflectivity of aluminum is highly sensitive to strain making it ideal for picosecond acoustics (which give accurate transducer film thickness at the location of measurement). As will be mentioned later, the accuracy of TDTR measurement critically depends on the accurate measurement of thickness of metal. Moreover, because of this characteristics, Ti: sapphire laser is used in general for TDTR measurements instead of other lasers such as Er: Fiber (1.55 μm wavelength [191]) or Yb: Fiber (1.03 μm wavelength [192]), where the absence of picosecond acoustics puts them at significant disadvantage for their use in TDTR measurements.

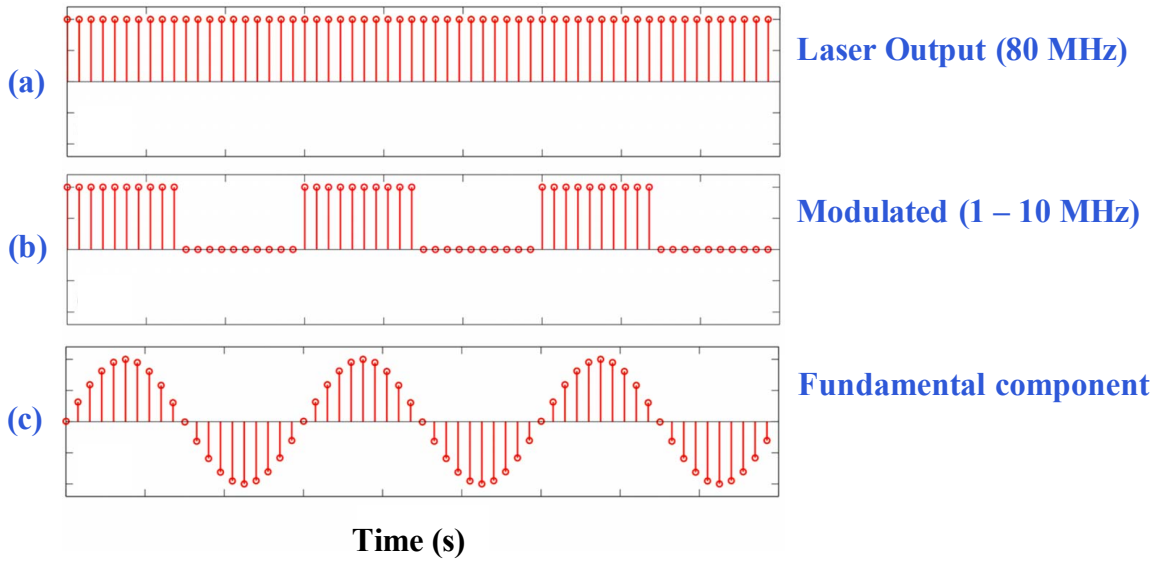

Figure 2.41: A schematic of laser output is shown as a train of delta functions in (a), while that of (b) shows the pump beam after going through a EO modulator, and finally choosing only the fundamental component results in beam profile shown in (c). Figure adapted from [182].

The reflected beam pulses from the sample surface are collected at the Silicon photodiode detector, which is connected to RF lock-in amplifier. The lock-in amplifier is supplied with the same reference frequency to measure the probe signal at frequencies within the lock-in pass band (~ 10Hz) of the modulation frequency (ω_o = 11.4 MHz). Figure 2.42 illustrates the measurement process of probe signal as detected by RF lock-in amplifier [182]. To measure the thermal response of the sample, probe pulses after different delay times (τ) are incident on the sample area exactly where pump beam was heating the sample. Figure 2.42 depicts the measured signal for one delay time (τ_1) other delay times are similarly measured. The temperature response of the sample due to the pump pulses has the contribution form the last pump pulse (single heat pulse), also called as impulse response, and the modulated train of pump pulses leading to what is called as *pump accumulation*. Figure 2.42(b) shows the temperature profile of the metal surface superimposed (indicated by the blue lines) on the modulated train of pump pulses. It is imperative to state the assumption that the thermal response from the sample to pulsed heating is linear and doesn't vary with time. This essentially means that temperature changes of the sample in this measurement process is small enough to assume that physical properties are constant which ensures that temperature of the sample follows superposition principle as shown in Figure 2.42(b). The linearity of the system ensures that the thermoreflectance coefficient is linear over the range of temperature increase of the sample due to both single heat pulse and heat accumulated from modulated pump beam. This increase in temperature is of the order of few kelvins making the assumption of linearity reasonably good. The probe pulses arriving after time delay (τ_1) from each pump pulse is

shown Figure 2.42(c) (indicated by black vertical lines). The intensity of these reflected probe pulses is recorded at the detector and is proportional to the temperature of the metal surface. The measured signal by the lock-in amplifier from the probe pulses arriving at the photo detector is shown in Figure 2.42(d). Note that the lock-in amplifier only measures the probe signal at the fundamental modulated frequency (ω_o = 11.4 MHz) and rejects all other high harmonics. Thus, the output of the measurement is the amplitude (A) and the phase (φ) of the fundamental component of probe signal (recall that the probe pulses were not modulated). This measured signal having amplitude and phase is also represented as X and Y or in-phase and out-of-phase components. Same measurement repeated for different delay times yields in-plane and out-of-plane components as function of probe delay times. In general, TDTR measurement is presented as the ratio of in plane to the out-of-plane components as function of delay times (Figure 2.44(a)).

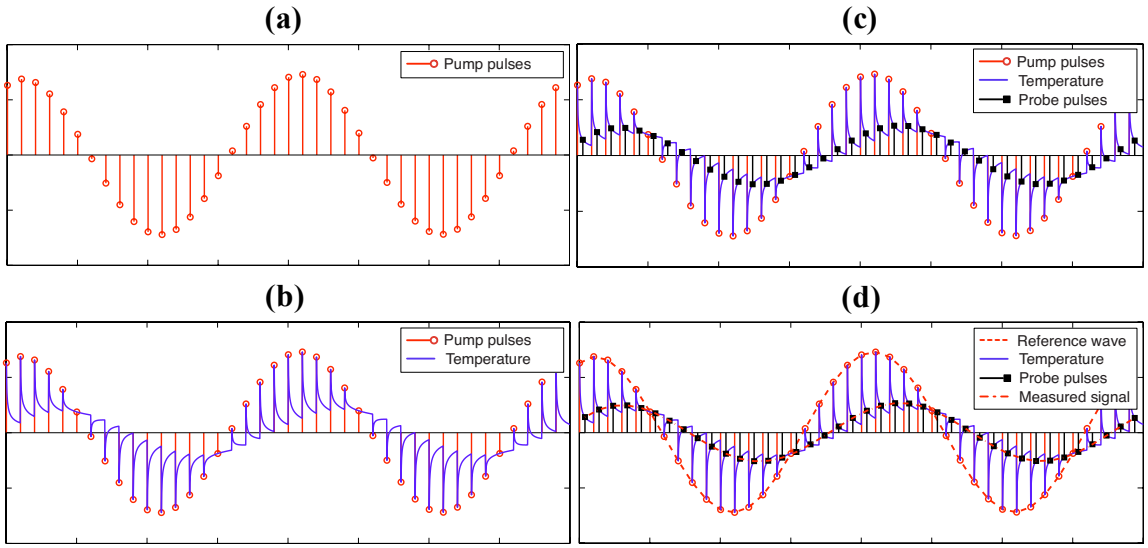

Figure 2.42: A schematic of information revealed about the sample by the measured probe signal. Figure adapted from [182].

From analysis point of view, this measurement can be viewed as the output being $Ae^{i(\omega_o t+\varphi)}$ for the input reference wave of $Ae^{i(\omega_o t)}$ (see Figure 2.43). In other words, $Ae^{i\varphi}$ or $Z(\omega)$ represents the "impedance" of the sample, which can also be written as $Z(\omega_o)e^{i\varphi}$. Now, a heat diffusion model can be constructed based on the sample structure which is composed of Al metal film, thin-film structure, and the substrate using their thermal parameters such as heat capacity, thermal conductivity, thermal conductance at each interface and thickness of metal, thin-film [182]. Amongst these, some quantities are taken from literature and in general there are three unknown parameters left to fit the experimental data to the thermal model, which are thermal conductance between metal and film, thermal conductivity of thin-film and the substrate [182]. Note that in some cases separate TDTR measurement of the substrate may be required to eliminate the number of variable in thermal model to fit the experimental data. The thickness of Al metal is

measured by picosecond acoustics; strain echoes present in the TDTR signal enables the accurate measurement of metal thickness [182]. While the thickness of the thin-film is measured either using *in situ* (RHEED) or *ex situ* technique such as X-ray reflectivity. An example of thermal conductivity measurement of a 200 nm STO film grown epitaxially on NGO (110) substrate is shown in Figure 2.44. The extracted thermal conductivity of STO from this TDTR measurement was found to be 7.02 $Wm^{-1}K^{-1}$, *i.e.* within 10% of the reported value in literature [184], which is also the accuracy of a typical TDTR measurement. When performing curve fitting using a theoretical model delay times greater than 100 picosecond (ps) is used because after 100 ps the diffusion of phonons becomes dominant. Before 100 ps, the system is in highly non-equilibrium state and it evolves in the following way. First, energy from the photon gets deposited on the metal and gets transferred to electrons within pulse width of the laser, *i.e.* 150 femtoseconds. The, electrons exchange energy within themselves and thermalize within 500 femtoseconds. In the next 10 ps or so, hot electrons transfer their energy to phonons, which take additional 10-100 ps to thermalize. Thus, only after phonons thermalize diffusion model begins to apply and one can use those models to do the curve fitting and extract thermal parameters of the sample.

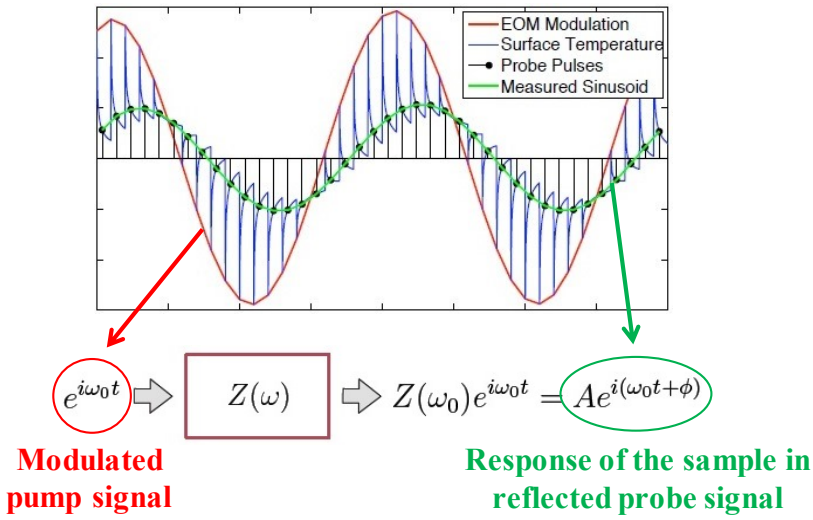

Figure 2.43: A schematic of information revealed about the sample by the measured probe signal.

There are many advantages of TDTR technique, which makes it a robust and routine method for characterizing thermal properties of materials. TDTR has tremendous advantage with respect to convenience in carrying out the measurement. Although the initial set-up cost is high, the non-contact method, which needs only optical access, enables this method to measure samples in conditions such as low [193] or high temperatures [194], high pressures [195], or high magnetic fields [196]. TDTR is also capable of measuring thermal conductivity in various samples geometries such as bulk single crystals [197], 2D geometry such as thin-films, few monolayers of graphene [198], even one-dimensional

(1D) geometries such as nanowires [199], making this technique truly versatile in characterizing materials in nanostructures to bulk form. The other advantage of this technique is high spatial resolution, as compared to other methods, which combined with high signal-to-noise ratio has enabled thermal conductivity mapping of metallurgical phase diagrams [200], thermal barrier coating [201] with high throughput and micrometer resolution [202]. Finally, with the ability of this technique to measure the thermal conductivity of almost anything, which has a smooth surface of roughness less than 15 μm [190], this method has been employed to measure thermal conductivity of almost entire range of materials, *i.e.* from very high thermal conductivity materials such as diamond [203], to ultralow thermal conductivity materials such as fullerene derivatives [204] and disordered layered structures [205].

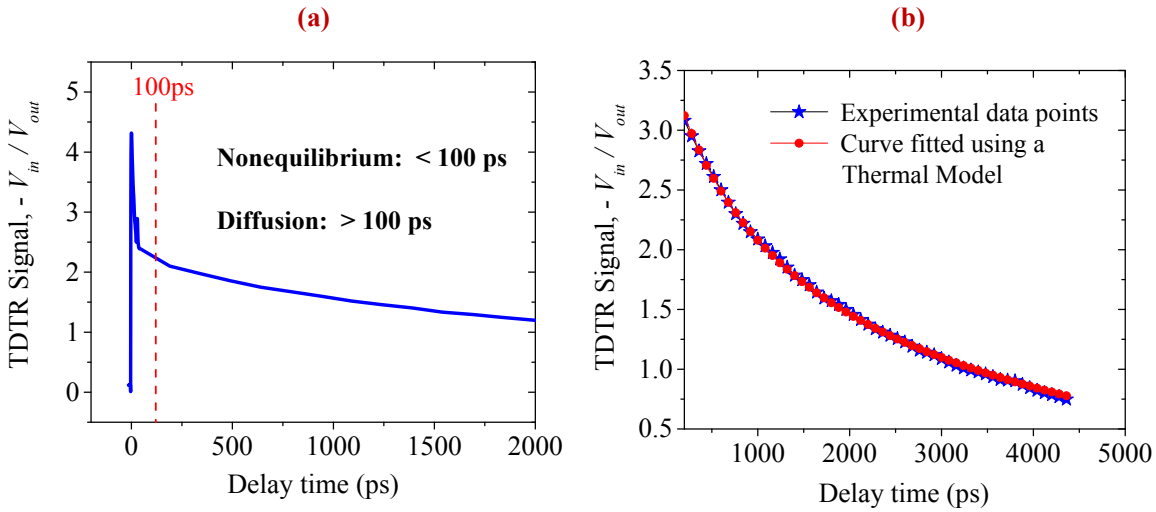

Figure 2.44: A typical TDTR signal is shown in (a) along with a critical time scale beyond which diffusive regime starts and thermal model can be used to extract the thermal conductivity of the thin film (b).

2.4 Spectroscopic measurement

Spectroscopic methods are frequently employed to characterize materials of interest. They are based on absorption, emission and scattering of either electromagnetic radiation such as visible, ultraviolet, infrared, X-rays, radio waves, microwaves *etc.*, or high energy particles such as neutrons, electrons or ions. In this thesis, I have employed soft x-rays, which has wavelength in the range of few nanometers (~ 1-3 nm) generated by a synchrotron source at Advanced Light Source, Lawrence Berkeley National Laboratory [206], to perform what is called as Resonant Soft X-ray spectroscopy (RSXS) [207-209]. In RSXS, X-ray scattering is combined with X-ray absorption spectroscopy (XAS) to investigate electronic structure of atom of interest. This technique takes advantage of high

flux of X-rays provided by synchrotron source in performing electronic structure characterization of bulk materials [210], thin-films [211; 212], and interfaces [213; 214] in artificial heterostructures. X-ray scattering provides spatial modulation of scattering entities while the X-ray Absorption spectroscopy reveals information regarding the electronic structure of scattering centers of interest. This particular characteristic of RSXS allows one to probe spatial modulations of scattering entities specific to a unique element occupying a particular atomic site (in a crystal) in a given valence state. Thus, offering a powerful way to study charge, spin and orbital degrees of freedom in a solid with nanometer resolution. A schematic of Resonant X-ray spectroscopy is illustrated in Figure 2.45, which differentiates it from the non-resonant scattering experiments. RSXS offers a great advantage of being bulk sensitive, *i.e.* can probe 1000 Å within the sample surface, compared to commonly used spectroscopic techniques such as X-ray Photoemission Spectroscopy [215], Angle-resolved Photoemission Spectroscopy [216] *etc.*, which are highly surface sensitive (~ 5–50 Å). Furthermore, RSXS can enable electronic structure characterization studies under applied external fields such as electrical and magnetic fields [217]. RSXS has proved extremely powerful technique in characterizing complex oxides with properties such as magnetism [209], ferroelectricity [211], magnetoelectric effect [212] *etc.* In what follows next, I will cover the basic principle behind Resonant Soft X-ray Spectroscopy technique. Detailed description of this technique is discussed elsewhere [207-209; 217].

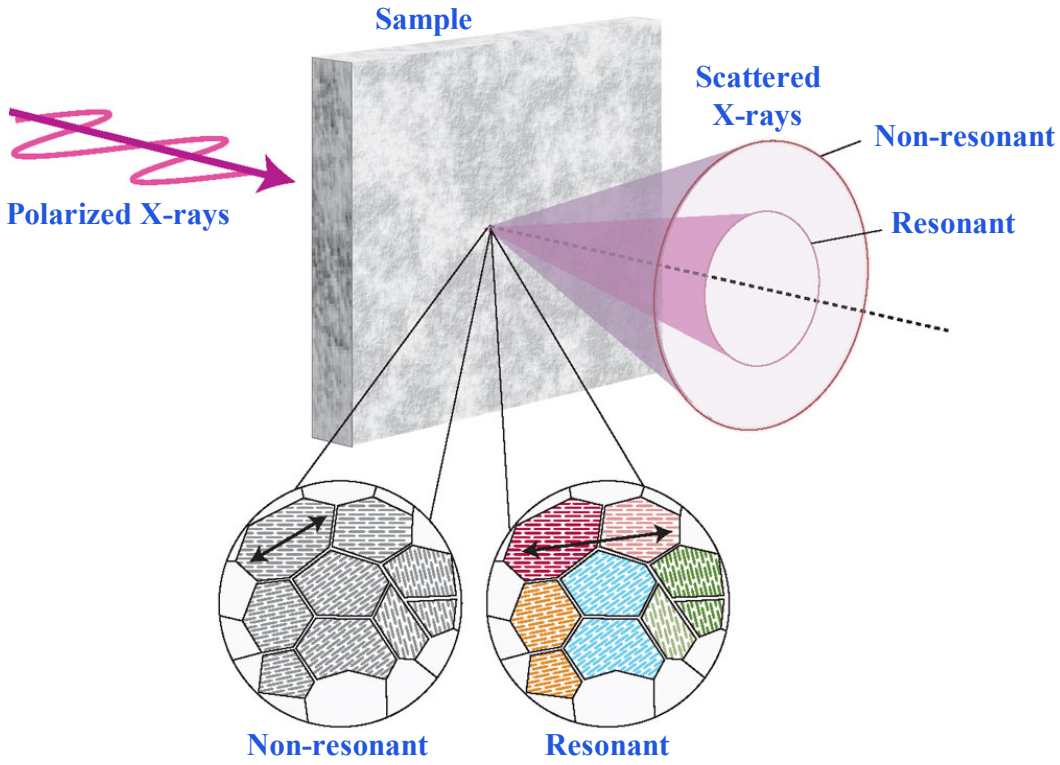

Figure 2.45: A schematic of resonant vs. non-resonant scattering of polarized X-rays (in transmission mode). From [218].

In a non-resonant X-ray scattering process, an atom elastically scatters light with a atomic form factor, $f(\vec{k})$, given by the following expression [217]:

$$f(\vec{k}) = \int r_o \, \rho(\vec{r}) e^{i\vec{k}\cdot\vec{r}} d\vec{r} \tag{2.3}$$

, where $\rho(\vec{r})$ is electron density of an atom (assumed to have spherical symmetry for sake of simplicity) and $(\vec{k})$ is momentum transfer (*i.e.* difference in incoming wave front and scattered wave front). For atoms arranged in a periodic lattice, contribution from each atom (or scattering entity) is summed over whole crystal lattice yielding structure factor for the crystal given by [217]:

$$F(\vec{k}) = \sum_{\vec{k}} f(\vec{k}) \, e^{i\vec{k}\cdot\vec{R}} \tag{2.4}$$

, where $\vec{R}$ is lattice vector. The scattering intensity shows a peak when all atom scatters the incoming light in phase, *i.e.* $\vec{k} \cdot \vec{R} = 2\pi m$ ($m \in$ Integer). While this X-ray diffraction from

crystalline lattice is greatly used for determination of symmetry of the lattice (as discussed previously in section 2.2.1 and 2.2.2), non-resonant scattering has been limited in enabling studies involving ordering of electronic features such as charge, orbital or spin. The primary reason for their low applicability in probing such ordering phenomenon is the weak scattering cross-section when non-resonant scattering processes are used. This is where resonant scattering becomes extremely useful in probing ordering associated with charge [219], orbital [220], and spin [221] in solids. Resonant scattering uses the fact the scattering of light by an atom not only depends on the wave vector of the incoming photon but also on the energy of the incoming photon [217], *i.e.*,

$$f_{total}\left(\vec{k}, \hbar\omega\right) = f\left(\vec{k}\right) + f'(\hbar\omega) + i\, f''(\hbar\omega) \tag{2.5}$$

, where $\hbar\omega$ is photon energy, $f^{'}(\hbar\omega)$ is related to the response of electrons with different binding energies to the incoming field, whereas $f^{''}(\hbar\omega)$ relates to the damping of electrons arising from the associated binding energy. The above expression will transform the structure factor of a crystal in the following way:

$$F\left(\vec{k}\right) = \sum_{\vec{k}} f_{total}\left(\vec{k}, \hbar\omega\right) e^{i\vec{k}\cdot\vec{R}} \tag{2.6}$$

Thus, the scattered intensity, $\left|F\left(\vec{k}\right)\right|^2$, will show peak values not only for those waves scattered in-phase from the structural features of the lattice, but also when the incoming photon energy is tuned to match the energy gap between a electron occupied in an inner core shell to unoccupied (valence) states, *i.e.*, the absorption edge of the atom of interest. The resulting peaks correspond to what is called as Resonant Scattering (see Figure 2.46). One can use quantum mechanical approach under the assumption that system's response to incoming field is linear, to derive the following expression for X-ray Absorption (XAS) intensity and elastically scattered intensity [217]:

$$I_{XAS}\left(\hbar\omega\right) = \frac{1}{2}\,\mathrm{Im}[\hat{\epsilon}^{*}\cdot\sigma(\hbar\omega)\cdot\hat{\epsilon}] \tag{2.7}$$

where, $\hat{\epsilon}$ is a unit vector along with the polarization direction of the incoming light wave, 'ω' is the frequency of the photon and 'σ' is the conductivity tensor whose real and imaginary part are related through Kramer-Kronig relation [217]:

$$I_{RSXS}\left(\hbar\omega\right) = \frac{\left|\vec{E}_{out}\right|^2}{\left|\vec{E}_{in}\right|^2} \;\alpha\; \left|\hat{\epsilon}^{*}_{out}\cdot\sigma(\hbar\omega)\cdot\hat{\epsilon}_{in}\right|^2 \tag{2.8}$$

where, $|\vec{E}_{out}|$ and $|\vec{E}_{in}|$ are the radiated field and incoming field, and $\hat{\in}$ is the unit vector along the polarization direction of electric field.

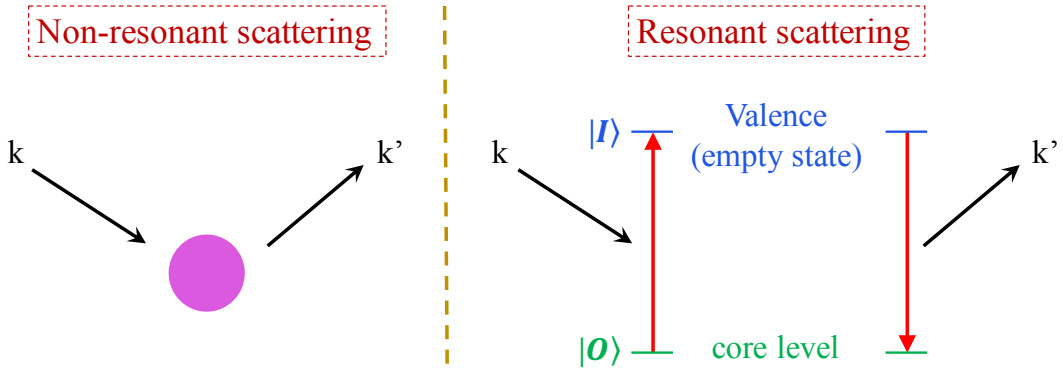

Figure 2.46: A schematic of non-resonant vs. resonant scattering, where the latter can tell us the spatial distribution of |I>. [217]

Note that the conductivity tensor is related to the energy-dependent scattering factors introduced in equation (2.5) by the following relation:

$$\sigma(\hbar\omega) \;\alpha\; [f'(\hbar\omega) + i\, f''(\hbar\omega)] \tag{2.9}$$

This implies that $f''(\hbar\omega)$ is related to the X-ray absorption process described earlier and the conductivity tensor is key to both the scattering and absorption process involved in the RSXS process. Thus, the conductivity tensor is largely used for the analysis and interpretation of XAS spectra obtained in a RSXS process [217] as it holds relevant information about the material system.

The enhancement in scattering cross-section due to resonant nature of scattering process can be understood by the expression for the conductivity tensor derived for the case when photon's energy matches a transition from a core level to valence state. Using quantum-mechanical first-perturbation theory, one can derive the following expression of conductivity tensor for a simplest case of two-level system under resonant condition (details of the derivation can found in [217]:

$$\sigma = \frac{e}{2\pi m^2}\left(\frac{1}{\omega_1 + \omega_o + i\frac{\Gamma}{2}} + \frac{1}{\omega_1 - \omega_o + i\frac{\Gamma}{2}}\right) \tag{2.10}$$

where, 'ω_o' corresponds to the energy difference between the initial and final states and 'ω_1' is the energy corresponding to the incoming photon, 'Γ' is extremely small term compared to 'ω_1' or ω_o and generally refers to the broadening of the incoming energy peak

at $\omega_1 = \omega_o$. The divergence of the denominators of the conductivity tensor at $\omega_1 = \omega_o$ or at the absorption (transition) edge leads to several orders of magnitude increase in scattering cross-section. Note that the tuning of incoming photon energy to any absorption edge may not sufficiently increase the scattering cross-section in the detectable range. Only those dipole-allowed transitions which excite inner core-shell electrons to valence state near the Fermi-level leads to sufficient increase in the scattering cross-section allowing us to probe spatial modulation of valence states. For example, the optimum dipole-allowed transitions in '3*d*' transition metal oxide (the ones studies in this thesis) is from occupied '2*p*' states to '3*d*' valence states where several orders of magnitude increase in scattering cross-section is observed when energy of incoming photon is tuned to this absorption edge. Since the absorption edge corresponding to '2*p*' → '3*d*' states falls into 200-2000 eV (1-6 nm), *i.e.* within the range of soft X-rays, I have used soft X-ray synchrotron source to perform Resonant Soft X-ray Spectroscopy. The relatively large wavelength (1-6 nm) of X-rays used for resonant X-ray scattering limits the amount of momentum that can be transferred and hence accessibility of reciprocal space. However, RSXS becomes extremely powerful in studying superstructures with periodicity larger than few nanometers, which will be the case for the ferroelectric ordering, presented in chapter 5.

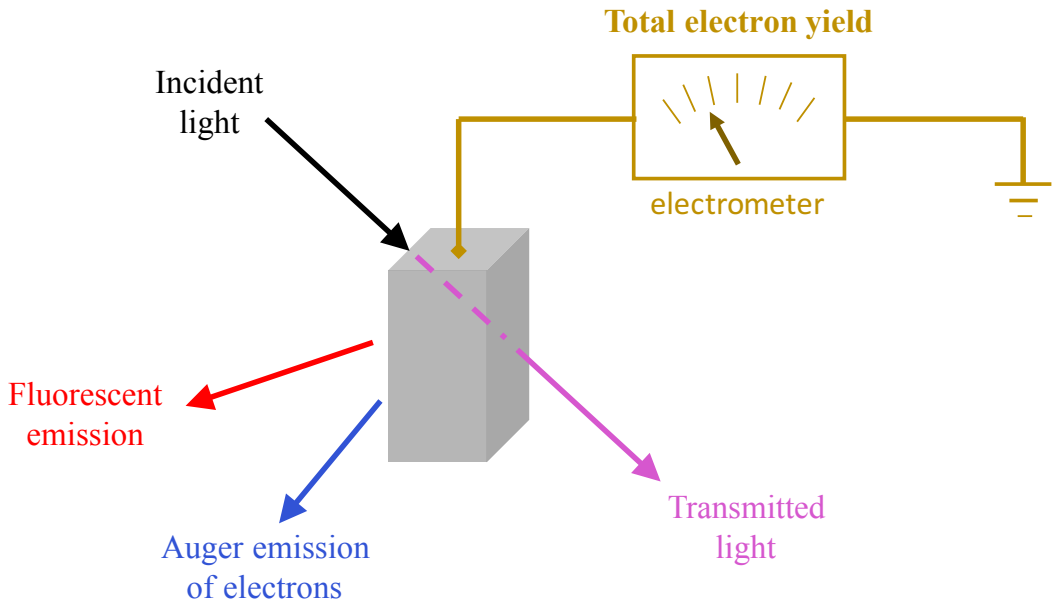

Figure 2.47: A schematic X-ray Absorption spectroscopy is drawn, which illustrates various modes under which a XAS can be performed at resonant scattering condition. [222]

There are three-measurement mode for doing X-ray absorption (XAS) in RSXS, *i.e.* Transmission mode, Fluorescence Yield mode, and Total Electron-Yield mode. A schematic of XAS measurement is illustrated in Figure 2.47. When the XAS measurement is done in the transmission mode (shown earlier in Figure 2.45 also), the ratio of the X-ray

intensity measured before and after transmission is recorded to interpret the absorption coefficient of the sample. This mode is generally applied with hard x-rays because soft x-rays interact very strongly with the matter leaving very weak intensity of transmitted x-rays. In the total electron yield mode, sample surface is grounded with an electrometer connected in between to measure the drain current or the Total electron yield (TEY) signal when the sample is incident with X-rays. This drain current results from the fact that when an electron is excited to a valence state the relaxation process involves generation of Auger electrons through inelastic scattering. The no. of emitted electrons is directly proportional to the probability of creating Auger electrons, which is further proportional to absorption probability. Thus, TEY signal provides information regarding the absorption coefficient of the sample. From the method, it is obvious that the depth of sample, which can be probed using TEY mode, is going to be rather small (typically about 5 nm) and hence it is mostly applied in studying interfaces [207; 209; 217]. A typical XAS spectra obtained in TEY mode is shown in Figure 2.48(b) (adapted from [214]). In the Fluorescence yield (FY) mode, when the electron is excited to a valence state the relaxation of these excited electrons occurs via fluorescent emission of photons and the intensity of emitted X-rays is recorded as a function of photon energy. A typical XAS spectra obtained under the FY mode is shown in Figure 2.48(a). In contrast to TEY mode, FY mode allows us to probe sample within 1000 Å of the surface enabling bulk measurement of X-ray absorption. Thus, FY mode is frequently employed to do RSXS for bulk and thin-films [210].

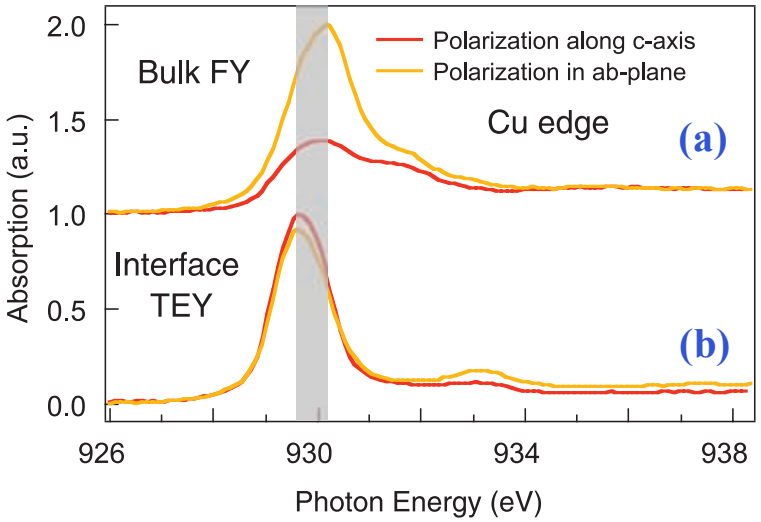

Figure 2.48: X-ray Absorption spectra obtained under Fluorescence Yield (FY) (a) and Total electron yield (TEY) (b), at the Cu-L_3 absorption edge for a LCMO/YBCO heterostructure is shown. Figure adapted from [214].

One of the most common application of RSXS is doing polarization-dependent X-ray absorption studies where the polarization of the incoming photon is chosen in a way to be of certain type, *i.e.* linear or circular, and pointing along certain direction. Since the

absorption of electrons strongly depends on the electric field of incoming photons, polarized X-rays can selectively induce transitions of specific kind. For example, a circularly polarized light needs to be used to transfer angular momentum to the excited photoelectrons for the X-ray absorption to become spin-dependent and hence provide insights about the magnetic order in the system. Thus, the dependence of XAS spectra on the polarization direction of incoming photon, say for example between left- or right-circularly polarized photons proves to be useful in studying electronic structure of the atom of interest. In general, this is accomplished by taking difference in the absorption spectra for incoming photon polarized in different directions, commonly known as X-ray Dichroism. If the incoming photons are linearly polarized or circularly polarized it is referred to as X-ray Linear Dichroism (XLD) or X-ray Circular Dichroism (XCD) respectively. Depending on the material being studied, the origin of X-ray dichroism can be the anisotropy in either charge or spin in the system. If its spin, the X-ray dichroism reveals information regarding the magnetic order in the system and thus it has led to numerous investigations based on what is called as X-ray Magnetic Dichroism, *e.g.* XMCD (X-ray magnetic circular dichroism) (Figure 2.49) or XMLD (X-ray magnetic linear dichroism). Similarly, if the anisotropy is caused by charge only, we refer to them as X-ray Linear Dichroism (XLD) or X-ray Magnetic Dichroism (XMCD). In this thesis, XCD were used to study ferroelectric ordering in a superlattice system and will be discussed in chapter 6.

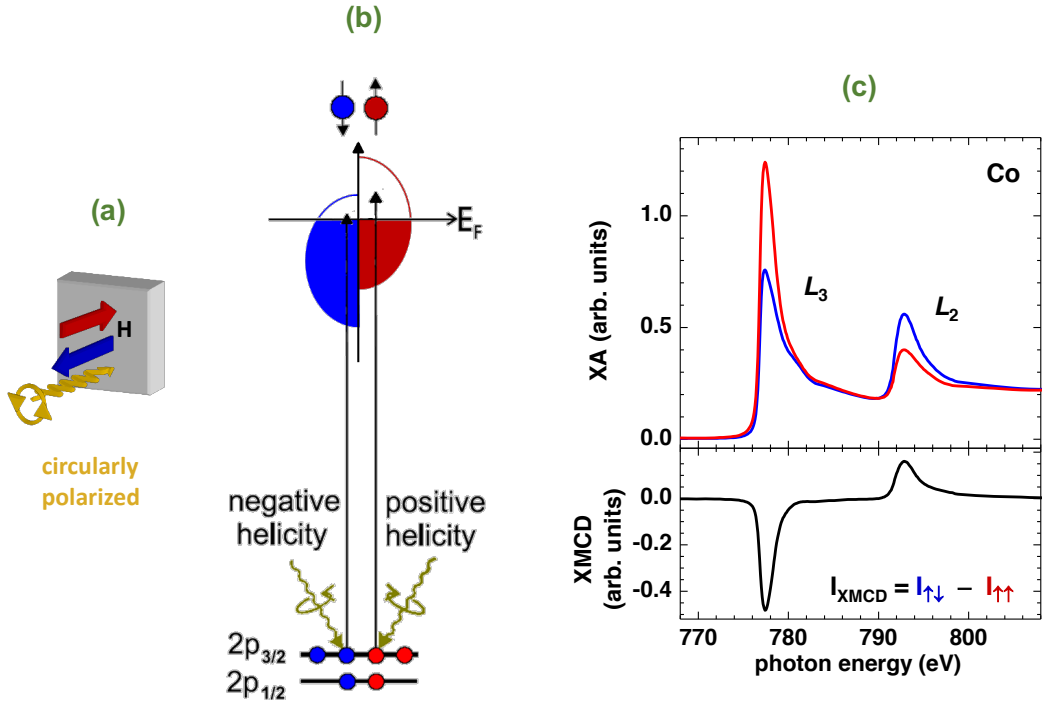

Figure 2.49: Principle of X-ray circular magnetic dichroism is illustrated: (a) shows a schematic of sample incident with a circularly-polarized light with two possible opposite Helicity (H), where (b) depicts the dependence of light absorption on Helicity of circularly

polarized light with a corresponding absorption spectra and circular dichroism shown in (c). Courtesy of Prof. Elke Arenholz.

To summarize, Resonant Soft X-ray Spectroscopy has found its application in wide areas of materials research from organic materials [223] to inorganic material [210]. Within the inorganic materials, complex oxides have been studied immensely to understand various exotic phenomenon exhibited by this class materials where there is strong correlation between charge, spring, orbital and lattice degrees of freedom. For example, antiferromagnetic order in complex oxides such as $BiFeO_3$ has been extensively studies using XMCD and XMLD [224; 225]. Furthermore, since this technique is element specific it has been used to study magneto electric coupling at BFO/LCMO interface by independently doing XMCD at Mn and Fe L-edges [212]. Additionally, valence-specific or oxidation-state sensitive nature of this spectroscopic technique has enabled studies such as magnetic order in LSMO thin-films (grown epitaxial on STO substrate) where the contributions of Mn^{3+} and Mn^{4+} states to the observed magnetic configuration have been investigated using XMCD [212]. Since the occupation of an atom to a particular symmetric-site in a unit cell can affect its electronic structure, for example, octahedral symmetry vs tetrahedral symmetry of Ti-site strongly affects the absorption spectra as the tetragonal symmetry further splits the e_g and t_{2g} states to a_{1g}, b_{1g}, e_g, b_{2g} states [42; 45]. Moreover, X-ray dichroism studies have also been applied to investigate structural changes before and after switching ferroelectric polarization of PZT [211]. Thus, the ability of RSXS technique to probe various electronic ordering phenomenon in materials have made this non-destructive technique of great importance for condensed matter research.

2.5 Summary

The aim of this chapter was to give introduction and basic working principle behind various experimental techniques employed in various studies presented in this thesis. For detailed description of these techniques, the reader is encouraged to read the references listed therein. While some of the *in situ* and *ex situ* characterization techniques assisted in providing positive feedback for the optimization of synthesis parameters, some techniques were judiciously chosen to understand the characteristic features found in their respective studies. The relevance of each is also mentioned alongside to highlight their role in designing the experiments presented in this dissertation. In sum, the experimental techniques discussed in this chapter allowed us to perform various types of characterization needed for a particular subject of investigation.

Chapter 3

An overture to the Dissertation

3.1 Introduction

As discussed in chapter 1, superlattice structures of complex oxides have been applied across various subjects of research and the results of those studies were undoubtedly remarkable. The inherent ability of superlattice structures to alter the length scale of interaction present between two (or more) superlattice constituents by changing the superlattice periodicity, along with increasing the volume fraction by repeating superlattice unit (period) to a desired thickness of the film where the nanoscale features can be characterized by thin-film characterization techniques, puts them at a significant advantage over other nanostructures. Moreover, the relative ease with which superlattice structures can be synthesized with accurate deposition of unit-cell precision via advanced thin-film deposition technique, allows us to apply thin-film deposition technique in synthesizing desired superlattice structures (symmetric vs asymmetric) with two or more constituents which are chosen in accordance with the objective of the research.

Given the immense potential of superlattice geometry, I judiciously choose research objectives, which are ideal to pursue with complex oxides as the material system. With the advantages of superlattice geometry combined with strongly correlated material such as complex oxides, one would expect observation of novel phenomena central to the superlattice geometry and are rarely observed in bulk-like systems. With various studies presented in this dissertation, it is claimed that superlattice structures offers a promising nanostructured system where unique and hidden phenomenon can be discovered, and in some cases can lead to enhancement in physical properties compared to bulk materials. Several experimental studies presented in this dissertation corroborates this assertion, and provides further discussion on other equally interesting avenues, which are opened-up by the research findings, and, are ideal to pursue through this route of combining superlattice-like structures with an appropriate choice of superlattice constituents from complex oxides family.

Complex oxides offer a suitable material system to be combined with superlattice structure given the availability of various degrees of freedom such crystal lattice, electronic charge, orbital and spin degrees of freedom, and the presence of strong coupling between them. In the studies presented in this dissertation, I have mostly utilized the first three degrees of freedom, *i.e.* crystal lattice, electronic charge, and orbital degrees of freedom. First, utilizing only lattice degree of freedom, *i.e.* crystal structure, unit-cell parameter, a

novel heat transport phenomenon in short-period superlattice films was discovered, which has been theoretically predicted in superlattice systems. This unique phonon transport phenomenon was further investigated in detail by synthesizing more designed superlattice-like (aperiodic) structures. In the second major discussion, charge and orbital degree was incorporated, which are intrinsically coupled to lattice degree of freedom, *i.e.* in a ferroelectric material, as one of the superlattice constituent to pursue another novel phenomenon which has been theoretically-predicted in various ferroelectric nanostructures (including superlattice systems). Other characteristically different ferroelectric behavior associated with novel ferroelectric features observed in superlattices were identified and studied. Due to the existence of this novel ferroelectric phenomenon, various ferroelectric ground states was stabilized as a function of superlattice period, thereby forming a phase diagram dependent on the periodicity of the superlattice structure. Lastly, unusual phenomenon associated with such novel ferroelectric ground states were noted and found to be fundamentally different than those exhibited by bulk ferroelectric materials.

3.2 Combinatorial Approach: Complex Oxides in Superlattice geometry

3.2.1 Employing only one degree of freedom: Lattice

Complex perovskite oxides with formula, ABO_3, allows one to independently vary A-site cations vs B-site cations thereby gaining a variety of crystals structures such as cubic, tetragonal, orthorhombic, rhombohedral *etc.*, with wide range of unit cell lattice parameters available in perovskite oxides (Figure 3.1). Such availability of various complex oxides enables one to choose an appropriate choice of superlattice constituents needed for the investigation. For instance, in the search for unique phonon transport phenomenon predicted in superlattice systems, the most apt choice for superlattice constituents would be electrically-insulating perovskite because the measured thermal conductivity will not have any contribution from the heat conduction by electrons. Within the family of electrically insulating perovskites, the list will be further narrowed by other considerations critical to the observation of phenomenon. Examples of which could be thermal properties of materials used in superlattice structure such as bulk thermal conductivity, phonon mean free path and coherence length *etc.*, misfit strain between the two superlattice constituents, ability to achieve controlled synthesis with unit-cell precision of superlattice constituents *etc.*

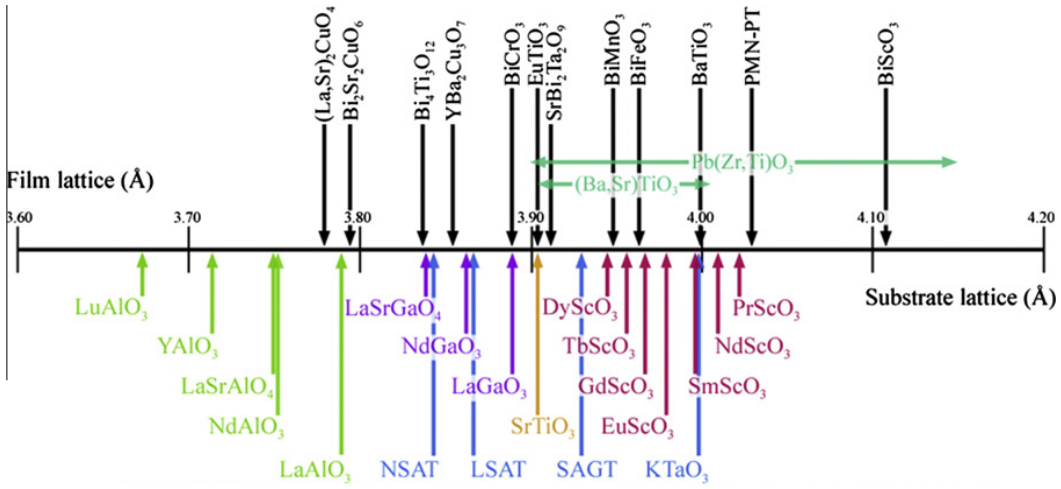

Figure 3.1: Variety of complex oxides substrates commercially available are listed on an axis of their pseudo-cubic or pseudo tetragonal '*a*'-axis lattice parameter, along with few sample of thin-film complex oxides materials synthesized on selected substrates. From [52].

Superlattices based on $SrTiO_3$, which possesses favorable thermal properties along with the relative ease of achieving controlled thin-film synthesis, presents one suitable choice of superlattice constituent. It was found that the compatibility of growth conditions with the other constituent leaves only few other insulating perovskites, ex. $CaTiO_3$, $BaTiO_3$, $PbTiO_3$. A schematic of superlattice structures based on $SrTiO_3$ - $CaTiO_3$ (Figure 3.2 (a)) and $SrTiO_3$ - $BaTiO_3$ (Figure 3.2 (b)) chosen for this investigation is drawn. Following synthesis of high-quality superlattices of both these superlattice systems, thermal conductivity of superlattice films as a function of superlattice periodicity was measured. With theoretical studies predicted a unique phonon transport phenomenon in short-period superlattice structures, experimental results followed suit. Below certain critical periodicity, thermal conductivity showed an unexpected trend, which is a result of coherent phonon transport phenomenon.

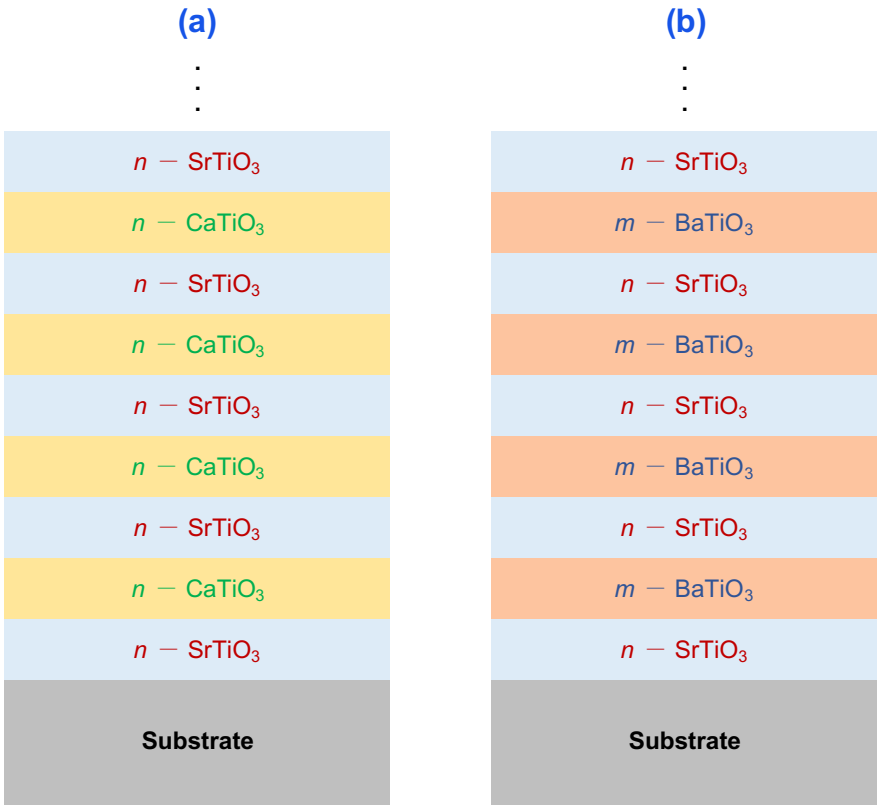

Figure 3.2: A schematic of (a) '*n* x *n*' periodic $SrTiO_3$ - $CaTiO_3$ superlattice structure and (b) '*n* x *m*' periodic $SrTiO_3$ - $BaTiO_3$, where '*n*' and '*m*' represents no. of unit-cells.

The importance of superlattice structure becomes apparent in this case as this novel phenomenon can only be observed when wave nature of phonons is dominating their transport. The ability of superlattice structure to vary the length scale from 1 unit-cell (few Angstroms) to tens of unit cells (nanometers) becomes crucial and is central to the observation of this phenomenon. It is because most heat-carrying phonons have wavelengths less than few nanometers, which makes it extremely difficult to realize the wave effects in conventional bulk thermal conductivity measurements. Thus, making superlattice structures ideal candidate to realize this phenomenon. In this case when the superlattice periodicity is varied from short-period to large period, a transition from coherent phonon transport dominated by wave-nature of phonons, to traditional incoherent phonon transport dominated by particle-nature of phonons respectively, was observed. This result highlights the other important characteristics of superlattice structures, which is its ability to tune physical properties by varying periodicity, in this case thermal conductivity. Eventually, this leads to generation of a phase diagram (Figure 3.3) which differentiates novel coherent transport phenomenon in short-period limit from conventional incoherent transport observed in large periods where bulk-like behavior is recovered.

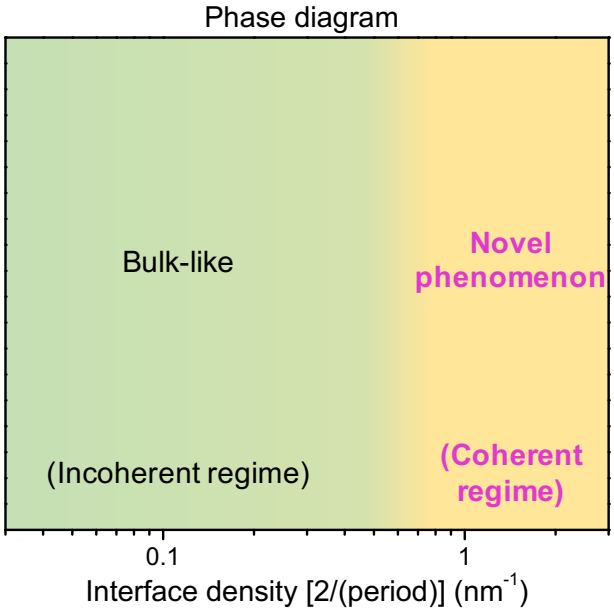

Figure 3.3: Superlattice period dependent phase diagram differentiating coherent phonon transport in short-period superlattices to conventional incoherent phonon transport in thick-period superlattices.

3.2.2 Utilizing more than one degrees of freedom: *Charge*, *Orbital* and *Lattice*

In addition to lattice degree of freedom, complex oxides offer other degrees of freedom such as charge and orbital, which in some cases have shown coupling between one another. Ferroelectric perovskites are one example where there is strong coupling between these degrees of freedom. In nanostructured systems such as superlattices composed of ferroelectric materials, theoretical studies have suggested that the interplay between charge, orbital and lattice leads to stabilization of non-uniform polarization states forming structures such as vortices, waves, dipolar skyrmions *etc.* Specifically, in superlattice structures composed of paraelectric-ferroelectric perovskite oxides such as $SrTiO_3$-$PbTiO_3$ (Figure 3.4), predictions suggest stabilization of polarization distribution in the form of vortex structures in ferroelectric layers of the superlattice structure. Synthesis conditions of $PbTiO_3$ was optimized to attain similar level of controlled deposition with unit-cell precision as that of $SrTiO_3$ obtained previously, to fabricate thin-film superlattice of $SrTiO_3$-$PbTiO_3$ with varying periodicity. For a critical range of superlattice periodicity, $PbTiO_3$ layers exhibited non-uniform polarization distribution forming vortex-antivortex arrays agreeing well with theoretical predictions. These polarization vortices were further characterized and found to possess chirality, which also has been predicted for these non-uniform polarization structures.

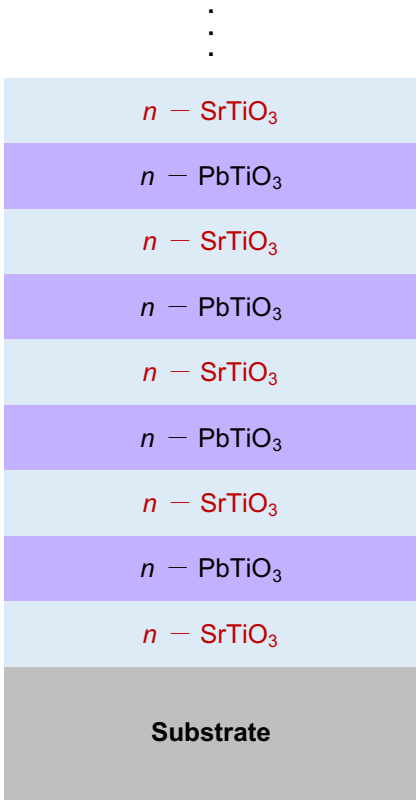

Figure 3.4: A schematic of a '*n* x *n*' periodic superlattice of $SrTiO_3$-$PbTiO_3$, where 'n' represents no. of unit cells.

Similar to previous case, when the periodicity is varied from short period to large period, superlattice films showed a period-dependent phase diagram. In the phase diagram, various novel ferroelectric ground states were found to exist, which exhibited a rich spectrum of ferroelectric domain structure. This phase diagram provided another example where a certain property, in this case ferroelectric behavior, can be tuned by changing the superlattice periodicity. Within specific regimes of this phase diagram, *i.e.* from 4 x 4 to 12 x 12, unusual domain size evolution was observed and characterized. Domain size variation with ferroelectric thickness in superlattice structure (or superlattice periodicity) showed inverse scaling behavior, which is fundamentally different from Landau-Lifshitz-Kittel domains found in traditional ferroelectric systems. As expected when the periodicity is increased to thick-period regime, polarization distributions within ferroelectric layers begins to form uniform domains similar to those observed in bulk ferroelectric systems, suggesting recovery of bulk-like behavior.

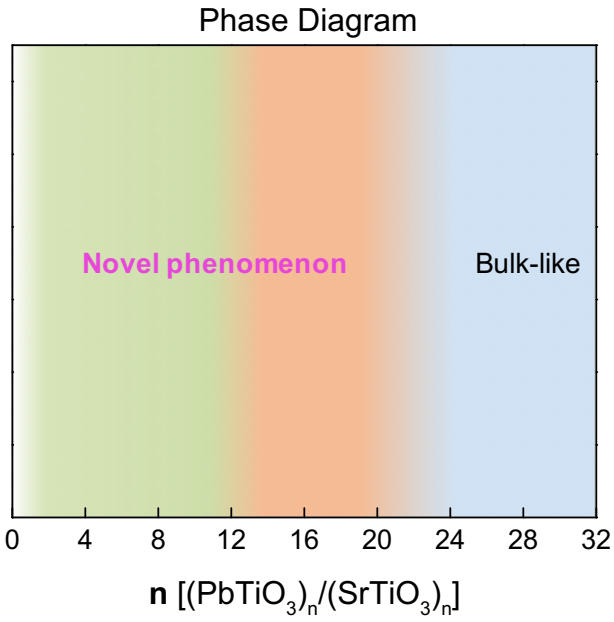

Figure 3.5: Phase diagram of PTO-STO superlattices, exhibiting novel ferroelectric ground states.

3.3 Organization of the dissertation

In this dissertation, I will discuss several experimental studies on superlattice thin films of complex oxides in search of novel physical phenomena and associated properties. First, in chapter 4, I will present results on the heat transfer across superlattice structures, which provided evidence of coherent heat transport, a phenomenon rarely observed in the bulk materials. Essentially, in chapter 4, I have utilized the lattice degree of freedom available in complex oxide materials to enable the observation of this unique heat transport phenomena in solids. In the next section, chapter 5, I have incorporated charge and orbital degrees of freedom to show another novel phenomenon, which has been only discussed in theoretical studies. Specifically, I will show the experimental observation of vortex structures of electrical polarization in ferroelectric (PTO) layers of paraelectric/ferroelectric (STO/PTO) superlattice, which shows resemblance to spin topologies known in magnetic systems such as skyrmions, merons *etc.* In the last chapter, novel phenomena associated with STO/PTO superlattices having polarization vortex structures in PTO layers is discussed. Finally, I will conclude with the experimental findings presented in this thesis and suggest future directions based on those results.

Chapter 4

Demonstration of Coherent Phonon transport in Superlattice structures

This chapter will provide first example of how an artificially designed structure can enable observation of a phenomenon, which is extremely rare to observe in bulk samples. More specifically, I will discuss experimental results on thermal transport across superlattice structures composed of two insulating oxides. Motivated by number of theoretical predictions made more than a decade ago, I have demonstrated experimental evidence of coherent phonon transport in superlattices of two different oxide systems *i.e.* STO-CTO and BTO-STO. The presence of wave-effects in phonon transport across superlattice structures has the potential, and been anticipated, to enable other transport phenomenon (such as phonon localization) which are still remaining to be found in crystalline systems. Thus, the study presented in this chapter supports the claim that superlattice structures are promising candidates to search for exotic phenomenon in materials systems.

4.1 Introduction

Heat conduction in solids has been a subject of research for decades [226-228]. In spite of such long history, the control of thermal conductivity in material at room temperature is limited to only six orders of magnitude [229]. In contrast, electronic conductivity, at room temperature, has shown controllability of twenty or more orders of magnitude [230] enabling remarkable advances in electronics (see Figure 4.1 for comparison). The lack of control in thermal conductivity has created obstacles in advancement of many technologies [231]. To emphasize the technological importance of thermal transport, we consider the following two examples; First, thermal management in current microelectronic chips poses serious issues due to miniaturization of devices. A survey of failure of integrated chips shows that the overheating of the device, *i.e.* poor thermal management, causes more than 50% of the failure events [232]. The increasing trend of further reducing the dimensions of devices, *e.g.* channel length of Field-effect transistors (FETs), leading to increasing demand of high power density [233-235], and hence a desperate need on the expansion of higher limits of thermal conductivity.

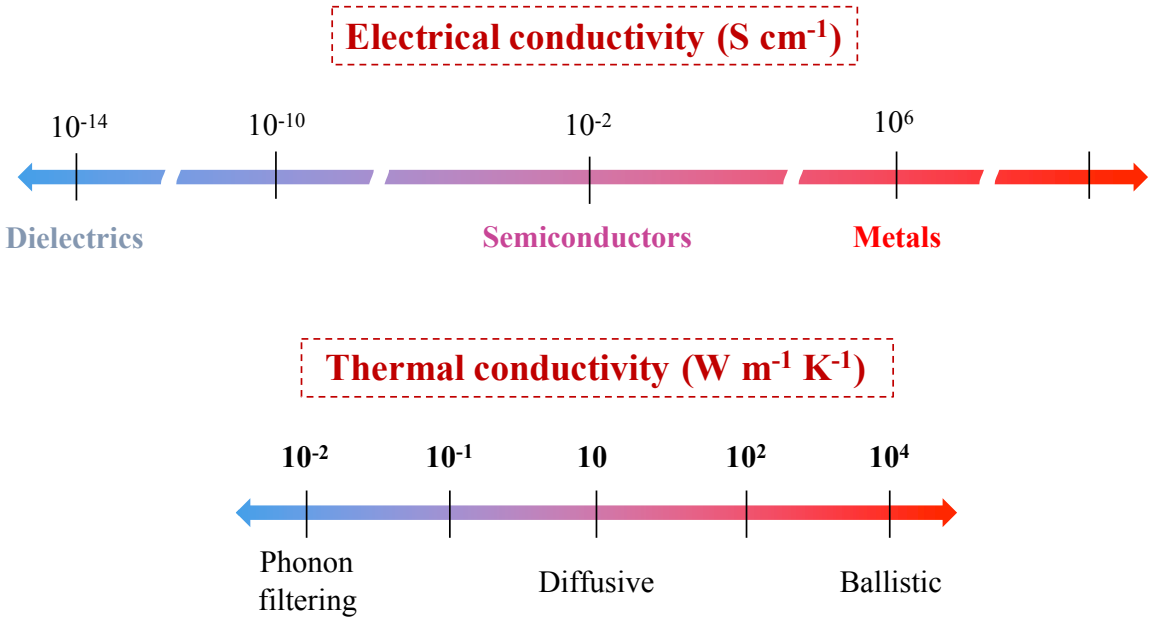

Figure 4.1: A schematic of range of electronic conductivity and thermal conductivity observed in material systems.

Second, the challenges for thermal transport further increases when one considers the energy conversion, transmission and storage. A recent survey of United States energy supply and demand in 2009 [236], shows that more than 50% of the energy supplied is rejected as waste heat. Recovery of such huge amount of heat losses through for example thermoelectric energy conversion, *i.e.* direct thermal to electrical energy conversion where there are no moving parts, has been a strong motivation for research in improving the efficiency of solid state thermoelectric devices [237-240]. One of the major focuses in improving efficiency of thermoelectric devices has been reducing the thermal conductivity of bulk or nanostructured systems [241-244]. The figure of merit (ZT) for thermoelectric performance is given by: $S^2\sigma/\kappa$, where 'S' is Seebeck coefficient, 'σ' is electronic conductivity and 'κ' is thermal conductivity. The interdependence of these three variable has been main obstacle in enhancing the efficiency of thermoelectric devices [242]. Hence, there has been a tremendous amount of research in search for ways to independently optimize either of these variables [241]. One area of efforts was aimed at reducing thermal conductivity without significantly affecting electron transport (*i.e.* S or σ). Thus, expanding the limits on lower end of thermal conductivity spectrum is desired for many applications.

To give one more example on the need to expand the lower limits of thermal conductivity, the case of Thermal Barrier coatings (TBC) in gas turbine engines is considered [245; 246]. The efficiency of a gas turbine engine is directly related to gas temperature entering into the turbine, *i.e.* higher the temperature of this gas more will be the efficiency of the engine. Now, in order to protect the metallic parts in the hottest region of the gas turbine engine, thermal barrier coatings, which have extremely low values of

thermal conductivity, are applied on these metallic parts to protect them raising their temperature. Since the mechanical properties can degrade significantly because of large increase in their temperatures, the operation temperature of these gas turbine critically depends on these TBCs. Thus, the performance and efficiency of gas turbine engines greatly relies on the improvements of low thermal conductivity materials used for thermal barrier coating. Above examples clearly emphasizes the fact that if thermal conductivity can be manipulated to further expand the limits of both low and high ends, its technological impact would be humongous.

To explore the limits of thermal conductivity, we need to further improve our understanding of heat transport at different length- [247] and time- [248] scales in material systems. Nanostructured systems, in particular, have shown a tremendous potential in search of novel phenomenon in thermal transport [174; 243; 249-251], including those exploring limits of thermal conductivity [252-256]. For example, the thermal conductivity of suspended graphene, *i.e.* a two-dimensional nanostructure, at room temperature have been reported to be 4000-5000 W/mK, which exceeds the value of best known thermal conductivity materials such as diamond. Similarly, one-dimensional nanostructures such as carbon nanotube (*e.g.* multiwalled carbon nanotube) has also been reported to show a thermal conductivity of ~ 3128 W/mK at room temperature [255] which exceeds the limits posed by naturally occurring diamond. One the lower limit of thermal conductivity, silicon nanowires of diameter ~ 52 nm have been shown to have thermal conductivity of 1.6 W/mK which is as low as that of amorphous glass [253]. Similarly, multilayer thin-film structures of W/Al_2O_3 have been shown to exhibit extremely low thermal conductivity, *i.e.* 0.6 W/mK [252]. Given the promise held by these nanostructured systems, heat transport at the nanoscale have been the subject of intense investigation for the last two decades [190; 247; 257]. And, they continue to be the most promising candidate for exploring the limits of thermal conduction in materials [258].

Both electrons and phonons (which are quantized lattice vibrations [259]) can transport heat in solids. The discussion of this chapter will be focused on the non-metallic systems where the heat is transported only by phonons (there is no contribution of electrons to the total thermal conductivity). Using an appropriate choice of insulating material system, I will demonstrate a novel phonon transport phenomenon, namely coherent phonon transport, which has the potential to address the goal of achieving lower limits of thermal conductivity [258; 260; 261]. In the following sections of this chapter, first a brief introduction of fundamentals of thermal conduction in solids is given, followed by a discussion on number of theoretical predictions of coherent phonon transport in superlattice systems. Second, a detailed discussion of experimental observation of crossover from incoherent regime of phonon transport to a coherent regime of phonon transport in superlattice structures is provided. Last, the implications of these results on phonon transport across thin films and heterostructures, along with their broader impacts, are discussed.

4.2 Theoretical predictions of Coherent Phonon Transport in Superlattices

4.2.1 Fundamentals of Thermal Conductivity

Heat flow in a medium can occur via conduction, convection and radiation. Since this chapter is centered on thermal conductivity in solids, we will restrict ourselves to heat flow via conduction mechanism only. In a solid, heat can be transported by both electrons and lattice vibrations (specifically by *phonons* which are quantized lattice vibrations). In systems where electron concentration is high, for example metals, significant contribution to thermal conductivity is by transport of energy by electrons. The electronic part of thermal conductivity is related to its electronic conductivity given by Wiedmann-Franz law [226], *i.e.*

$$k_{electronic} = L\,\sigma\,T \tag{4.1}$$

, where 'L' is Lorentz no., 'σ' is electronic conductivity, and T is temperature. The contribution to thermal conductivity by electrons is directly proportional to its electronic conductivity for constant value of temperature (L being in general constant). On the other hand, the material systems, which have very low concentration of electrons, for example insulators, heat, are mostly transported by *phonons* or quantized lattice vibrations [259]. With more details on heat transport by phonons provided later, we will start with the most general framework used to introduce lattice part of thermal conductivity. Most simplistic picture of phonon transport in solids is given by assuming phonons as energy-carrying particles in a medium analogous to gas molecules travelling in a confined space. Under these assumptions, thermal conductivity of a solid is given by:

$$k = \frac{1}{3}\,C\,v\,l \tag{4.2}$$

, where 'C' is heat capacity of the material, 'v' is average phonon group velocity, and 'l' is mean free path of phonons. This simple theory provides a great way to qualitatively understand lattice thermal conductivity in solids. For example, if one aims to manipulate thermal conductivity of a materials, parameters, which could allow for the same are heat capacity, phonon group velocity and phonon mean free path. As will be discussed later, parameter most frequently deployed to tune the thermal conductivity is average phonon mean free path (*mfp*). In a material where *mfp* is limited by the size of the system (for ex. at very low temperatures), *i.e. mfp* ~ constant, the thermal conductivity follows the heat capacity for constant average group velocity. Similarly, in the case of constant heat capacity and group velocity (ex. at high temperatures), thermal conductivity follows the

variation of population of phonons, suggesting one more way of manipulating thermal conductivity in a material system.

Now, we will begin with detailed discussion of heat conduction by phonons. In what follows, first phonon dispersion curve will be discussed for 1D chain of atoms with two atoms in the unit cell, followed by a discussion on heat capacity. Second, phonon thermal conductivity will be derived under given assumptions, followed by various phonon scattering mechanisms whose understanding provides a great platform to manipulate thermal conductivity in solids.

4.2.1.1 Phonons

In a crystalline solid, atoms are chemically bonded to other atoms, which are vibrating near their equilibrium position at a given temperature. The array of atoms in a lattice can be modeled as an array of balls with masses 'M' connected by a spring [259]. For crystal having 'N' atoms, there are total of 3N normal modes whose characteristic frequencies can be calculated by using harmonic approximation. For example, in a linear (1-dimensional) chain of atoms with one atom in a unit-cell, the equation of motion of nth atom is given by [259]:

$$M\frac{d^2u_n}{dt^2} = K\,(u_{n+1} + u_{n-1} - 2u_n) \tag{4.3}$$

, where, 'M' is the mass of the atom, 'K' is spring constant, and 'u_n' is the displacement of nth atom. The generic form of the solution for this equation (4.3) is a travelling wave, which carries energy as it travels through the solid medium. The expression for the travelling wave is given as:

$$\psi(\vec{r}) = U\left(\vec{k}\right) e^{(\vec{k}\cdot\vec{r} - \omega t)} \tag{4.4}$$

, where '$U\left(\vec{k}\right)$' is the amplitude of the wave, '$\vec{k}$' is wave vector, '$\vec{r}$' is position vector, 'ω' is the characteristic frequency of the vibration, 't' is time. When equation (4.4) is used in equation (4.3), a relation between characteristic frequency 'ω' and wave vector '$\vec{k}$' is obtained, which is called as dispersion relation [259]. Similar approach can be adopted for a two-atom unit-cell in linear chain of atoms to obtain the dispersion relation shown in Figure 4.2 for the first Brillouin zone defined by $(-\pi/a_0) < k < (\pi/a_0)$, where a_0 is the lattice constant. The lower branch in the dispersion relation is called as acoustic branch where atoms are vibrating in-phase to its neighboring atoms. In contrast, the upper branch has atoms vibrating in out-of-phase to its neighboring atoms which is called as an Optical branch. The slope of the dispersion curve, *i.e.* $\frac{d\omega}{dk}$, is the group velocity of the wave traveling through the linear chain of atoms. The group velocity is another important parameter in

heat transport as it decides which modes will carry significant amount heat, and hence will mostly contribute to thermal conductivity. For example, group velocity for an optical branch is almost zero and thus optical modes do not contribute much to the heat conduction. Acoustic branch, on the contrary, contributes a lot to the heat conduction owing to large group velocities from long- to mid-wavelength modes. Note that in the limit of extremely large wavelengths, group velocity reaches the continuum limit, at which group velocity approaches the speed of sound in the crystal. Another interesting aspect of the dispersion curve is the gap in the characteristic frequencies between the acoustic branch and optical branch, which will become extremely crucial in deciding the characteristics of superlattice dispersion curve, and hence their thermal conductivity trends.

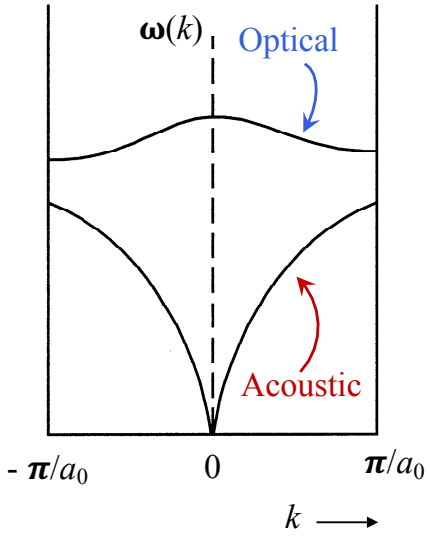

Figure 4.2: Phonon dispersion relation is shown for linear chain of atoms having two atoms in the unit cell. [259]

The other important aspect of solving the equation of motion of an atom using harmonic approximation is to obtain the energy associated with characteristic frequencies. The energy of all normal modes of a crystal is quantized, *i.e.*

$$E = \hbar\omega(\vec{k})\left(N_0 + \frac{1}{2}\right) \tag{4.5}$$

, where 'N_0' = 0, 1, 2, '$\hbar$' is Planck constant, '$\omega(\vec{k})$' is the characteristic frequency of the normal mode. This quantum of energy, $\hbar\omega(\vec{k})$, is associated with an elementary excitation called as phonon, and thus, a phonon is a quantum of vibrational energy of a crystal. For a normal mode with characteristic frequency '$\omega(\vec{k})$', 'N_0' represents no. of phonons occupying that characteristic frequency (or state in dispersion relation). At thermal

equilibrium, Bose-Einstein relation gives the no. of phonons 'N_0' occupying state '$\omega(\vec{k})$' at a given temperature T:

$$N_0 = \left(\frac{1}{(e^{\hbar\omega/k_BT} - 1)}\right) \tag{4.6}$$

It is noteworthy that number of phonons occupying a normal mode is also a strong function of temperature, in addition to being dependent on characteristic frequency. As will be discussed later, this characteristics of phonon greatly affects phonon transport as a function of temperature.

4.2.1.2 Heat Capacity

Once the phonon dispersion curve has been calculated, heat capacity of the system can be calculated under certain assumptions. The most accurate model used in literature for discussing heat capacity is Debye model, where the dispersion relation is assumed to be linear, *i.e.*,

$$\omega(\vec{k}) = v\,|\vec{k}| \tag{4.7}$$

, where 'v' is velocity of sound. This model predicts low temperature behavior of T^3 dependence of heat capacity, which matches well with experimental observation. In contrast, Einstein model for calculating heat capacity, where all atoms are assumed to be oscillating with same frequency, predicted an exponential decrease of heat capacity with temperature. Thus, we will discuss the heat capacity under Debye model and calculate quantities such as Debye frequency and Debye temperature, which are widely used in understanding thermal transport in various material systems.

Heat capacity is simply the derivative of total energy (E) with respect to temperature under constant volume, and can be written as:

$$C_v = \left(\frac{\partial E}{\partial T}\right)_v \tag{4.8}$$

, where 'C_v' is heat capacity at constant volume. The total energy of a system can be calculated by summing energies corresponding to all respective normal modes which are occupied with known number of phonons (at a given temperature), *i.e.*,

$$E = \sum_{k,p}\left(\langle n\rangle_{k,p} + \frac{1}{2}\right)\hbar\omega(\vec{k},p) \tag{4.9}$$

, where 'p' is band index. In the limit when the size of the crystal is very large, wave vectors ($\vec{k}$) becomes extremely dense, and in that case, summation can be replaced by an integral, *i.e.*,

$$E = \sum_{p} \int \left(\langle n \rangle_{k,p} + \frac{1}{2} \right) \hbar\omega(\vec{k}, p)\, dk \tag{4.10}$$

For a system with a known phonon dispersion relation, one can compute the density of states, D(ω), which is defined as number of phonon modes per unit frequency, *i.e.* D(ω) $d\omega$ is the total no. of phonon modes in the range 'ω' to '$\omega + d\omega$' of frequency.

$$D(\omega) = \frac{dN}{d\omega} \tag{4.11}$$

$$E = \sum_{p} \int \left(\langle n \rangle_{p} + \frac{1}{2} \right) \hbar\omega(p)\, D_p(\omega)\, d\omega \tag{4.12}$$

, where '$D_p(\omega)$' is phonon density of states for a given polarization 'p' of the respective phonon branch. Density of states can be calculated from the total no. of phonon modes present in the crystal. Assuming L as the length of each side of a 3D crystal and it is large enough for allowed wave vectors 'k' to assume almost continuous values in reciprocal space, total no. of phonon modes, N, is:

$$N = \frac{4\pi k^3/3}{(2\pi/3)^3} \tag{4.13}$$

, where '$(2\pi/3)^3$' is the volume occupied by one mode. Using the definition of $D(\omega) = \frac{dN}{d\omega}$, we get:

$$D(\omega) = 4\pi k^2 \left(\frac{L^3}{8\pi^3} \right) \left(\frac{dk}{d\omega} \right) \tag{4.14}$$

$$D(\omega) = \left(\frac{k^2 L^3}{2\pi^2} \right) \left(\frac{dk}{d\omega} \right) \tag{4.15}$$

Now, heat capacity under constant volume can be calculated by:

$$C_v = \left(\frac{\partial E}{\partial T}\right)_v \tag{4.16}$$

$$C_v = \sum_p \int \frac{\partial n_p}{\partial T}\, \hbar\omega(p)\, D_p(\omega)\, d\omega \tag{4.17}$$

In Debye model, the dispersion relation gives: $\omega(\vec{k}) = v\,|\vec{k}|$. Thus, density of states becomes:

$$D(\omega) = \left(\frac{V\omega^2}{2\pi^2 v^3}\right) \tag{4.18}$$

, where 'V' is volume of the crystal (L^3). Using phonon density of states and Bose-Einstein relation, equation (4.17) can be simplified to:

$$C_v = \frac{3V\hbar^2}{2\pi^2 v^3 k_B T^2} \int_0^{\omega_D} \frac{\omega^4 e^{\hbar\omega/k_B T}}{[e^{\hbar\omega/k_B T} - 1]^2}\, d\omega \tag{4.19}$$

, under the assumption 'ω' is independent of polarization. 'ω_D' is Debye frequency which is the cut-off frequency at which corresponding wavevector reaches the edge of first Brillouin Zone (BZ). In the limit of very low temperature, the equation (4.19) can be further simplified to:

$$C_v = \frac{12}{5}\pi^2 N k_B \left(\frac{T}{\theta_D}\right)^3 \tag{4.20}$$

, where 'θ_D' is Debye temperature and equals to:

$$\theta_D = \left(\frac{\hbar v}{k_B}\right)\left(\frac{6\pi^2 N}{V}\right)^{1/3} \tag{4.21}$$

The equation (4.20) is also known as Debye T^3 law for heat capacity that is also found to hold true in experiments with temperature below 0.02 θ_D, *i.e.* $T \ll \theta_D$. In the other limit of extremely high temperature, *i.e.* $T \gg \theta_D$, equation (4.20) reduces to:

$$C_v = 3Nk_B \tag{4.22}$$

, which is also known as Dulong-Petit limit. It is worthwhile to discuss the importance of Debye Temperature in studying thermal transport in solids. When the temperature of the system is raised to θ_D or above, all normal modes are populated with phonons (with their total no. depending on BE statistics) and is found to strongly affect phonon transport at higher temperatures. When temperature is low ($T \ll \theta_D$), only those normal modes gets filled which have very low energy, *i.e.* low frequency (or high-wavelength) acoustic phonons, which are responsible for characteristic trends observed in low-temperature phonon transport. Thus, Debye temperature provides a good reference temperature to qualitatively understand phonon transport as a function of temperature, and to compare against different materials (as will be discussed later for choosing particular material system to study coherent phonon transport).

4.2.1.3 Lattice Thermal Conductivity

Previously, we have been discussing phonons, and their effect on heat capacity, assumed to be at thermal equilibrium. To study transport of phonons, we need to consider localized wave packets that are formed due to superposition of normal modes as compared to just the normal modes (which are extended throughout the crystal). The localized wave packets are essentially local concentration of phonons or vibrational energy. Thus, they can be regarded as pseudo-classical energy-carrying particles and their transport can be studied under the framework of Boltzmann Transport Equation [226]. The general theory of Boltzmann transport equation is given as:

$$\frac{\partial N}{\partial t} + \vec{v} \cdot \nabla N + \vec{F} \cdot \frac{\partial N}{\partial \vec{p}} = \left[\frac{\partial N}{\partial t}\right]_{scattering} \tag{4.23}$$

, where '$N\ (\vec{r}, \vec{p}, t)$' is statistical distribution function of an ensemble of those pseudo-classical particles which vary with position ($\vec{p}$), momentum ($\vec{r}$), and time (t). $\vec{F}$ and $\vec{v}$ is force applied to the particle and group velocity of the particles respectively. To further simplify this equation (4.23), relaxation time approximation is taken on the scattering, *i.e.* right-hand side of the equation (4.23) becomes:

$$\left[\frac{\partial N}{\partial t}\right]_{scattering} = \left(\frac{N - N_0}{\tau}\right) \tag{4.24}$$

, where 'N_0' is equilibrium concentration at the given local temperature and 'τ' is the relaxation time for the scattered particles.

Now, the heat flux due to the transport of these energy-carrying pseudo-classical particles can be calculated from simply summing the number of particles (N) multiplied by energy they carry ($\hbar\omega$), and their group velocity, over the allowed momentum space, *i.e.*,

$$Q' = \sum_{k} \vec{v}\, N(\vec{r}, \vec{p}, t)\, \hbar\omega \tag{4.25}$$

, where 'Q'' is heat flux. Using the phonon dispersion curve, we can rewrite the equation (4.25) as:

$$Q' = \int \vec{v}\, N(\vec{r}, \vec{p}, t)\, \hbar\omega\, D(\omega) d\omega \tag{4.26}$$

The Fourier law states that heat flux is proportional to the temperature gradient the solid is subject to, with thermal conductivity as the proportionality constant. One of the main assumptions of Fourier law is that there is local thermal equilibrium, which implies that:

$$\frac{dN}{dx} = \frac{dN_0}{dx} \tag{4.27}$$

Under the given assumptions, BTE can be solved to get 'N' and hence the heat flux. In almost all of the cases, there is no external force acting on the phonons, and time scales of the system are much larger than phonon relaxation time. For sake of discussion, we will consider one-dimensional case, for which equation (4.20) simplifies to:

$$(\vec{v} \cdot \nabla T)\, \frac{dN_0}{dT} = \left(\frac{N - N_0}{\tau}\right) \tag{4.28}$$

$$N = N_0 - \tau\, (\vec{v} \cdot \nabla T)\, \frac{dN_0}{dT} \tag{4.29}$$

Then, the heat flux becomes:

$$Q' = \int \vec{v} \left(N_0 - \tau\, (\vec{v} \cdot \nabla T)\, \frac{dN_0}{dT}\right) \hbar\omega\, D(\omega) d\omega \tag{4.30}$$

$$Q' = \int \vec{v}\, N_0\, \hbar\omega\, D(\omega) d\omega - \int \vec{v} \left(\tau\, (\vec{v} \cdot \nabla T)\, \frac{dN_0}{dT} \right) \hbar\omega\, D(\omega) d\omega \tag{4.31}$$

The first term will sum to zero because heat transport is isotropic at equilibrium. In other words, without a finite temperature gradient net heat flux should be zero.

Heat flow in 'x' direction:

$$Q' = - \int v'_x\, \tau\, v_x \left(\frac{dN_0}{dT} \right) \hbar\omega\, D(\omega) d\omega\, \frac{\partial T}{\partial x} \tag{4.32}$$

By comparing with Fourier law, *i.e.*, $Q' = - k \frac{\partial T}{\partial x}$, we can obtain the expression for thermal conductivity, 'k':

$$k = \int v'_x\, \tau\, v_x \left(\frac{dN_0}{dT} \right) \hbar\omega\, D(\omega) d\omega \tag{4.33}$$

The expression of thermal conductivity can be further simplified by averaging '$v'_x \cdot v_x$' over all frequencies which will turn out to be $\frac{1}{3} v^2$. And, the expression for thermal conductivity (equation 4.33) can be rewritten as:

$$k = \frac{1}{3} \left(\int v^2 \tau \left(\frac{dN_0}{dT} \right) \hbar\omega\, D(\omega) d\omega \right) \tag{4.34}$$

Now, using the expression for 'C_v' derived earlier (equation (4.17)) and assuming group velocity and relaxation time are independent of frequency (same assumption was used in kinetic theory model), expression for thermal conductivity reduces:

$$k = \frac{1}{3}\, C_v\, (v^2 \tau) \tag{4.35}$$

or,

$$k = \frac{1}{3}\, C_v\, v\, l \tag{4.36}$$

, where $l = v \cdot \tau$ is mean free path of phonons. This is the same expression of thermal conductivity we started our discussion about thermal conductivity in crystalline solids under the assumption that transport of phonons is behaving the similar way as energetic gas molecules traveling in a confined space.

We note that with the knowledge of phonon dispersion relation and phonon relaxation times, the thermal conductivity of a solid can be calculated from equation (4.33). Moreover, it becomes apparent that in order to manipulate thermal conductivity of a solid, the parameters that can be tuned are heat capacity, phonon group velocity, and phonon relaxation time. Heat capacity is the least studied parameter to tune thermal conductivity because in general the size of the system is orders of magnitude higher than what is needed to modify the phonon dispersion curve. Phonon group velocity in a solid cannot exceed the range, with maximum value of sound velocity, which depends on strength of chemical bond between atoms and mass of atoms, and minimum value of zero at the zone edges. Thus, either changing the bond strength (for example, *Van der Waal* bonding in polymers) or mass of atoms, one can manipulate thermal conductivity. Third, and the most widely used parameter to tune thermal conductivity is phonon relaxation time, which can be significantly varied by changing the scattering process of phonons, *i.e.* by materials engineering such as embedding second phase particles, alloying (adding impurity scattering) *etc.* The manipulation of thermal conductivity by controlling the scattering of phonons has been studied extensively [262-265], and thus, needs a detailed discussion. In what follows, I will discuss various scattering mechanisms followed by the effect of external conditions such as temperatures on those scattering processes.

4.2.1.4 Phonon Scattering Mechanisms

Phonons can be scattered by any lattice imperfections such as point defects (dopants, alloying elements), line defects (dislocations), volume defects (second phase nanoparticles embedded in the lattice), by crystal boundary scattering, and also by interacting with other phonons [226; 238]. These scattering mechanisms can be broadly categorized into two types: elastic and inelastic phonon scattering processes. In elastic scattering processes, ex. phonons scattered by lattice imperfections, the frequency or energy of the incident phonon does not change. While, in the inelastic scattering processes, frequency of the incident phonon does changes. Phonon relaxation time strongly depends on the scattering process involved, and scattering processes further depend on the material, frequency of incident phonon and temperature *etc.*

As discussed before, lattice vibrations can be studied using spring and mass model. Any defect in a lattice can be thought of as change in spring and/or mass locally, which alters the local vibrational characteristics of the crystal. Thus, the defect results in local change of the acoustic impedance, which leads to scattering of phonons incident at those sites. For example, an impurity atom, which has different spring constant and mass than the host atom, therefore leads to scattering of phonons when they are incident at those impurity sites. The relaxation time for phonons getting scattered from a lattice imperfection can be calculated using the assumption that phonons can be regarded as pseudo-classical energy-carrying particles under which kinetic theory can be applied. The average time (or relaxation time) between successive collisions of phonons with a lattice imperfection can be written as:

$$\frac{1}{\tau} = \alpha\, \sigma_{scatt}(\chi)\, \rho\, v \tag{4.37}$$

, where '$\sigma_{scatt}(\chi)$' is scattering cross-section which depends on size parameter (χ), 'ρ' is density of scattering centers, 'v' is group velocity of incident phonon. The scattering cross-section depends on the wavelength of phonon and size (radius) of lattice imperfection. Thus, size parameter can be written as:

$$\chi = \frac{2\pi R}{\lambda} \tag{4.38}$$

, where 'R' is radius and 'λ' is phonon wavelength. For the case when the size parameter approaches zero (ex. in impurity scattering), scattering cross-section follows Rayleigh's law, which states that:

$$\sigma_{scatt}(\chi) \propto (\chi^4) \tag{4.39}$$

$$\sigma_{scatt}(\chi) \propto \left(\frac{R^4}{\lambda^4}\right) \tag{4.40}$$

In the other limit of $\chi \gg 1$, scattering cross section becomes independent of the size parameter of scattering center and equals the projected area of imperfection, *i.e.* πR^2. For the cases, which lie in between these two limits, scattering cross-section can be calculated from following expression:

$$\sigma_{scatt}(\chi) = \pi R^2 \left(\frac{\chi^4}{\chi^4 + 1}\right) \tag{4.41}$$

Thus, only short-wavelength phonons or phonons near Brillouin Zone edge get scattered effectively by impurity atoms and other point defects (of the order of atomistic scale).

Boundary scattering is another mechanism by which phonons gets scattered, for example, at the crystal boundaries. Such scattering processes process is dominant for long wavelength phonons or in the case where size of the system is of the order of few lattice constants (such as nanowires, nanotubes). There is another scattering mechanism, which is crucial in deciding the effective mean free path of phonons in materials, called as phonon-phonon scattering, *i.e.* a phonon getting scattering by a different phonon. This mechanism can be understood using the same spring and mass model. If the interatomic potential between two atoms is purely harmonic, the spring constant will not change when the spring is deformed. In real crystals, the interatomic potential is anharmonic, which results into spring stiffness being dependent on the amount of spring deformation. Thus, if a phonon

wave is incident on a strain field, caused by occupation of other phonons at that local site, it experiences a change in spring stiffness or local change in acoustic impedance resulting into scattering of incident phonon.

There are two types of phonon-phonon scattering processes: Normal processes (N) and Umklapp processes. In a phonon-phonon scattering there are two possibilities either one phonon will break into two phonons, or two phonons will combine to form a single phonon. In normal (N) processes, both energy and momentum are conserved before and after the scattering event. On the other hand, in Umklapp (U) processes, energy is conserved but the momentum is not conserved. The basic difference between Normal processes and Umklapp processes is that the sum of the incident phonon wave vectors lies inside the first Brillouin Zone (BZ) or exceeds the limits set by edges of first BZ. In later case, when the sum lies outside first BZ, adding a reciprocal lattice vector to bring back the resultant vector into first BZ again conserves the momentum. This results into final propagating vector of phonon pointing in the opposite direction (compared to incident direction), thus the name *Umklapp* (a German word whose English translation is *flipped-over*). Therefore, Umklapp processes produce a resistance to heat flow. In contrast, N processes do not change the propagation direction of phonons, thus do not pose any resistance to heat flow. Further note that, because of this characteristics, Umklapp processes play a crucial role in establishing thermodynamic equilibrium locally. Using such phonon-phonon scattering processes, phonons of different frequencies can exchange energy with them. Although N processes do not contribute to thermal resistance, they assist in redistributing phonon energies over wide range of frequencies in dispersion curve, which are later subjected to Umklapp processes.

As mentioned earlier, temperature of the material plays a significant role in determining which phonon scattering is going to dominate over other mechanisms. This is primarily because phonon wavelengths, which carry most of the heat at a given temperature, are decided by Wein's displacement law (for phonon), *i.e.*

$$\lambda_{\text{eff}}\, T = constant \tag{4.42}$$

As the temperature is increased (or decreased), the dominant phonon wavelength (λ_{eff}) decreases (or increases) and thus the dominating phonon scattering mechanism is expected to depend on temperature of the material. It is imperative to bring Debye Temperature as the reference to discuss temperature-dependent phonon transport behavior. A typical temperature-dependent thermal conductivity graph is shown in Figure 4.3, where three regimes of different scattering mechanisms can be identified. At low temperatures ($T \ll \theta_D$), phonon wavelengths are very long thus their likelihood of getting scattering from the impurity or defects is low. In addition, long wavelength corresponds to small wave vector, which means that possibility of Umklapp process is also very low. Boundary scattering is the dominating scattering mechanism, which decides the mean free path of phonons. Since mean free path is fixed by the size of the crystal and phonon group velocity as be approximated as sound velocity, thermal conductivity in that case becomes directly

proportional to heat capacity which follows T^3 dependence. Thus, thermal conductivity has T^3 dependence at very low temperatures.

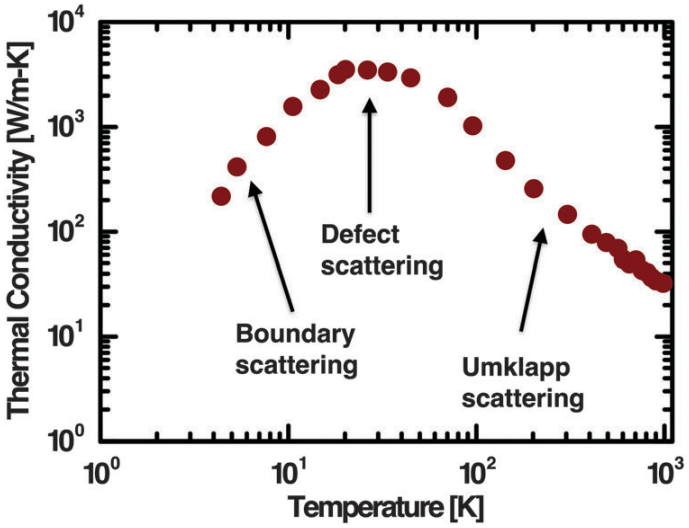

Figure 4.3: The generic trend of thermal conductivity as a function of temperature is illustrated by taking the example of bulk silicon. From [266].

When the temperature increases, dominant phonon wavelength decreases and scattering from defects (such as impurity, secondary phase) becomes significant. The thermal conductivity reaches a peak (at $T \sim (\theta_D/10)$) where the impurity scattering is the dominant scattering mechanism. Note that impurity scattering directly depends on the phonon frequency and indirectly depends on the temperature. Further, N processes, which becomes dominant with enough population of phonons, also plays a role in impurity scattering by redistributing phonon frequencies. Thus, the characteristics of thermal conductivity peak as a function of temperature is decided by both the dominant impurity scattering mechanism and the presence of N processes.

As the temperature is continued to increase the dominant phonon wavelength continues to decrease and eventually approaches a stage where wave vectors become large enough for Umklapp processes to start dominating. In this third regime, where Umklapp processes become dominating mechanism, thermal conductivity decreases with $1/T$ temperature dependence. This can be explained by approximating, N_0,

$$N_0 = \left(\frac{1}{(e^{\hbar\omega/k_BT} - 1)}\right) \approx \frac{k_BT}{\hbar\omega} \tag{4.43}$$

, at temperatures much higher than Debye temperature (*i.e.* $T \gg \theta_D$). This suggest that number of phonons in a mode increases linearly with temperature. Since the Umklapp processes depend strongly on the number of phonons available, the mean free path of

phonon becomes inversely proportional to temperature. With heat capacity saturated at $T \gg \theta_D$ and weak effect of higher temperatures on phonon group velocity, thermal conductivity starts decaying with $1/T$ dependence.

There is another length scale of phonons, which becomes crucial in thermal transport studies, called as phonon 'coherence' length. The phonon coherence length can be estimated using the following expression [267]:

$$L = v \int_0^{\vartheta_m} |g(\vartheta)|^2 d\vartheta \tag{4.44}$$

, where 'v' is average phonon group velocity, 'ϑ' is frequency of phonon ($\omega/2\pi$), and ' $g(\vartheta)$' is phonon density spectrum which satisfies:

$$\int_0^{\vartheta_m} g(\vartheta)\, d\vartheta = 1 \tag{4.45}$$

In nanostructures, whose size is of the order of coherence length, phonon dispersion curve gets modified and thus the mean free path of phonons can be changed significantly. The coherence length essentially means the average length phonon wave packets travel without losing its phase information [226]. For the observation of interference effects in phonons, coherence length plays a key role. If the size of the system is much larger than coherence length, phonon can be treated as energy-carrying particles (which is in general the case for bulk thermal transport studies). From the discussion of temperature dependent scattering processes, it is obvious that change in temperature will also affect phonon coherent length. As an example, the change in coherent length as a function of temperature is theoretically calculated for bulk GaAs [268] and is shown in Figure 4.4. When the temperature is much higher than Debye temperatures where Umklapp process starts dominating, coherence length is expected to become very small and saturate on further increasing the temperature. At temperatures much lower than Debye temperature where elastic scattering processes are dominating, coherence length is expected to be much more sensitive to changes in temperature, an example of which can be seen in sharp increase at T < 30 K in case of bulk GaAs. Moreover, the coherence length being much shorter (typically few lattice constants [267]) in normal temperature range further corroborates the absence of coherent effects in heat transport studies in micro- or macrostructures.

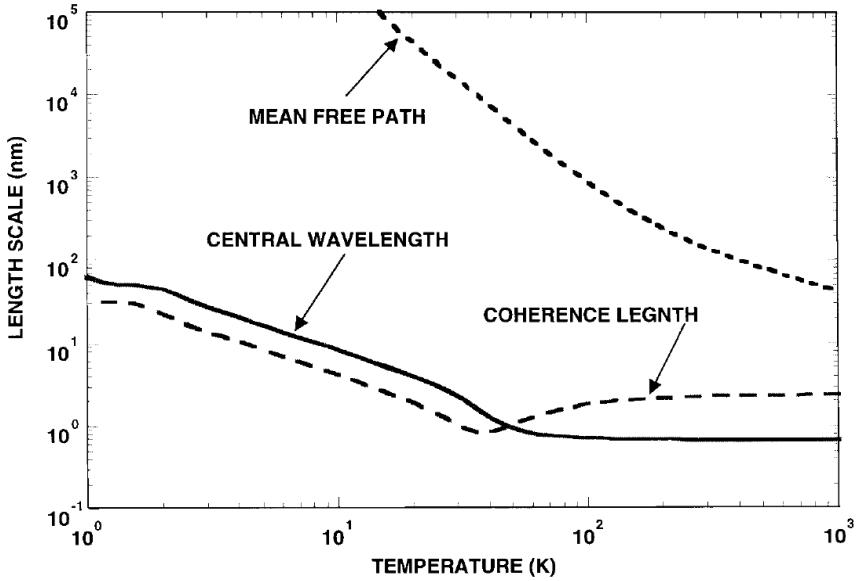

Figure 4.4: Phonon coherence length in bulk GaAs calculated as a function of temperature. From [268].

4.2.2 Theoretical models predicting Coherent Phonon transport

A number of theoretical studies have been employed to study phonon transport in superlattice structures. Due to the inherent layered structure of superlattices, phonon transport along both parallel [267; 269; 270] and perpendicular [226; 271; 272] to superlattice interfaces becomes interest of study. Since this chapter focuses on results on thermal conductivity across superlattice interfaces, I will limit our discussion to only those theoretical studies done across the superlattice structures. From the many theoretical approaches [273-276] used to calculate thermal conductivity across superlattice interfaces, lattice dynamics [274], molecular dynamic simulations [275], first-principles based approach [276], have been applied to study coherent phonon transport in superlattice structures. The main result of both these theoretical models essentially predicts the same physical phenomenon [274-276] (Figure 4.5), supporting the universality of the prediction. Here, we will discuss the model based on lattice dynamics as later it will discussed with regards to modifications made to the model to adapt it for experimental settings.

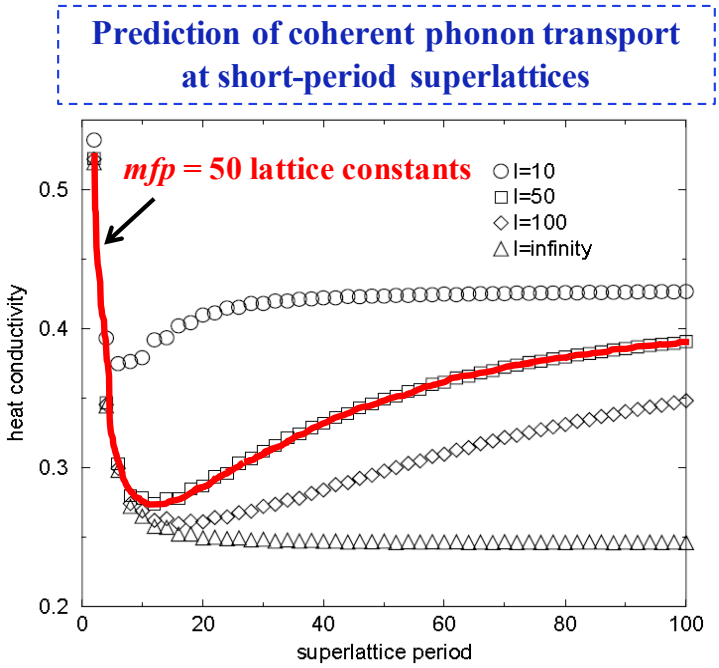

Figure 4.5: Theoretical prediction of coherent phonon transport in superlattice systems. Figure adapted from [274].

In the conventional Boltzmann Transport Equation (BTE) approaches [273; 277] applied to study phonon transport across superlattice structures, phonon transport is treated as energy carrying particles propagating through the superlattice. Such theories neglect the presence of phonon wave interference at superlattice interfaces and its effect on the phonon dispersion curve. In one of the first theoretical models Simkin and Mahan using lattice dynamics proposed taking account of phonon interference effects on cross-plane thermal conductivity of superlattices. In this model, phonon states of the superlattice structure are used as the input to the scattering of phonons to calculate the thermal conductivity of superlattice with varying periodicity. Previously, when wave nature of phonons was neglected and only particle nature was used to predict the thermal conductivity of superlattices, a general trend of decreasing thermal conductivity with decreasing superlattice period was observed. As will be shown later, when the wave nature of phonons is considered, the thermal conductivity shows a complete opposite trend, *i.e.* it increases with decrease in superlattice period. The dual nature of phonons in computing thermal conductivity across superlattices is resolved by including the mean free path of phonons as the critical input parameters. For the superlattices whose layer thickness is smaller than *mfp*, wave nature of phonon dominates, while for layer thicknesses larger than *mfp* the particle nature becomes dominant. This phenomenological model developed by Simkin-Mahan, takes account of the mean free path of phonons by adding an imaginary term to the phonon wave vector ('$\vec{k}$'), which is inversely proportional to *mfp*, *i.e. i/l*, when computing

properties of a given superlattice. A summary of their phenomenological model is provided here and more details about this model can be found elsewhere [274].

Phonon modes, $\omega_\lambda(k)$, in a superlattice structure can be calculated using wave theory, which then can be used in the standard formula for calculating thermal conductivity in 'm' dimensions [274], *i.e.*,

$$k(T) = \sum_{\lambda} \int \frac{d^m k}{(2\pi)^m} \, \hbar\omega_\lambda(k) |v_z(k)| \ell_\lambda(k) \, \frac{\partial n(\omega, T)}{\partial T} \tag{4.46}$$

, where 'k' is phonon wave vector, 'v_z' is group velocity, 'ℓ_λ' is phonon mean free path, and '$n(\omega, T)$' is Bose-Einstein distribution function. To simplify the model, a high temperature approximation is made:

$$n(\omega, T) \sim \frac{k_B T}{\hbar\omega_\lambda(k)} \tag{4.47}$$

In that case, equation (4.46) reduces to:

$$k(T) = k_B \sum_{\lambda} \int \frac{d^m k}{(2\pi)^m} \, |v_z(k)| \ell_\lambda(k) \tag{4.48}$$

In order to further simplify the model for the sake of developing a phenomenological model, one special case is considered where mean free path is kept constant. Under this approximation, equation (4.48) reduces to 'k_l',

$$k_l(T) = k_B l \sum_{\lambda} \int \frac{d^m k}{(2\pi)^m} \, |v_z(k)| \tag{4.49}$$

For the case of one dimensions, *i.e.* m = 1, the equation (4.49) further reduces to:

$$k_l(T) = k_B l \sum_{\lambda} \int dk \, \left| \frac{\partial \omega}{\partial k} \right| \tag{4.50}$$

$$k_l(T) = \frac{k_B l}{2\pi} \sum_{\lambda} [\, \omega_\lambda^{max} - \omega_\lambda^{min} \,] \tag{4.51}$$

, where 'λ' is band index.

$$k_l(T) = \frac{k_B l}{2\pi} \left[\omega^{max} - (\text{energy gaps}) \right] \tag{4.52}$$

Under the above given approximations, equation (4.52) suggest that increasing the energy gaps in the phonon band structure leads to decrease in thermal conductivity.

Now, to estimate 'k', one has to solve the dynamical matrix for phonons to find the allowed phonon modes. For one dimensional case, *i.e.* atomic chain of two different atoms assuming same spring constant, a 3 x 3 one dimensional superlattice will have the matrix:

$$\mathbf{M} = \begin{vmatrix} 2 & -1 & 0 & 0 & 0 & -e^{-ikN} \\ -1 & 2 & -1 & 0 & 0 & 0 \\ 0 & -1 & 2 & -1 & 0 & 0 \\ 0 & 0 & -\alpha & 2\alpha & -\alpha & 0 \\ 0 & 0 & 0 & -\alpha & 2\alpha & -\alpha \\ -\alpha e^{ikN} & 0 & 0 & 0 & -\alpha & 2\alpha \end{vmatrix} \tag{4.53}$$

, where 'α' is mass ratio, 'k' is phonon wave vector, 'N' (in this case) is 6.

The characteristic equation can be obtained by setting:

$$\|\mathrm{M} - \omega^2 1\| = 0 \tag{4.54}$$

which on further solving gives:

$$\cos(kN) = \cos(k_1 N/2)\cos(k_2 N/2) - \left(\frac{1 - \cos(k_1)\cos(k_2)}{\sin(k_1)\sin(k_2)}\right) \times sin(k_1 N/2)\sin(k_2 N/2) \tag{4.55}$$

, where $\cos k_1 = 1 - \omega^2/2$, $\cos k_2 = 1 - \omega^2/2\alpha$, and '$k_1$', '$k_2$' are dimensionless wavevectors in material 1 and material 2.

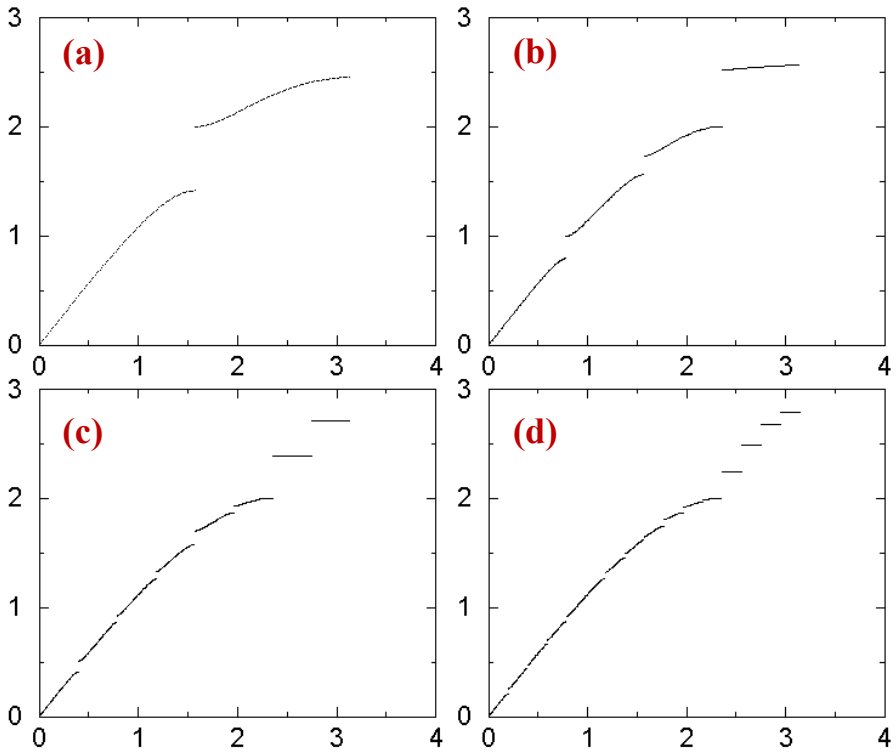

Figure 4.6: In the extended zone scheme, the effect of band folding effect on phonon dispersion curve is shown for the case of N equal to (a) 2, (b) 4, (c) 8, and (d) 16. From [274].

Band folding effect can now be seen in Figure 4.6, where N is systematically varied from N = 2 to 16 and 'α' is chosen to be 2. Increasing the superlattice period increase the number of minibands due to band folding effect, which is a well-documented phenomenon [226]. Mean free path of phonon can be taken into account by solving equation (4.53) with all wave vectors 'k' replaced by '$k + i/l$' to recalculate the dispersion relation. This can be further used in equation (4.51) to calculate the effective thermal conductivity across the superlattice structure. The normalized thermal conductivity as a function of superlattice period is calculated for different constant values of *mfp* (l) and is summarized in Figure 4.7.

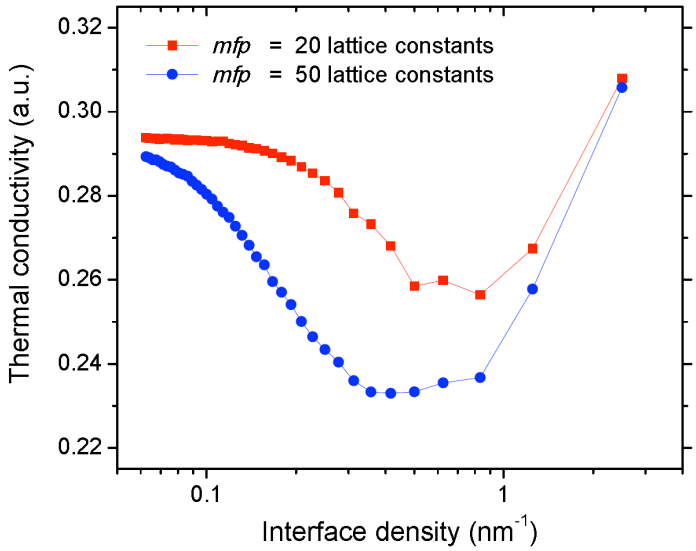

Figure 4.7: Normalized thermal conductivity of STO-CTO superlattices calculated as a function of superlattice period. Courtesy of Prof. Joel Moore.

In summary, the results of this prediction suggest that due to the wave interference of phonons (which are getting scattered at the superlattice interface), the phonon band structure is being modified. The cause of superlattice phonon dispersion modification is the band folding effect when superlattice period is changed for example from 2 x 2 to 16 x 16 (Figure 4.6). In general, as band folding increases the average phonon group velocity decreases [278] which leads to reduction in thermal conductivity. Hence, the increase in mini-band formation with increase in superlattice period, due to band folding effect, leads to decrease in thermal conductivity. Such a trend is completely opposite to the expected result of continuous decrease in thermal conductivity as the superlattice period is decreased. Phonon transports being particle-like, increasing the no. of interfaces increases the overall thermal resistance and hence decrease in effective thermal conductivity. Thus, when the superlattice period is continuously decreased from a very thick-period limit to a short-period limit, a transition in thermal conductivity across the superlattice interfaces is observed, going from incoherent scattering of phonons to coherent scattering of phonons, respectively. This crossover is phonon transport is manifested as minimum in thermal conductivity as a function of superlattice period. Furthermore, such a crossover is predicted to be a strongly dependent on the phonon mean free path in the superlattice structure. Since phonon mean free path is a strong function of temperature, coherent regime is predicted to turn on at higher superlattice periods (or lower interface densities) when the temperature is lowered (Figure 4.8(a)).

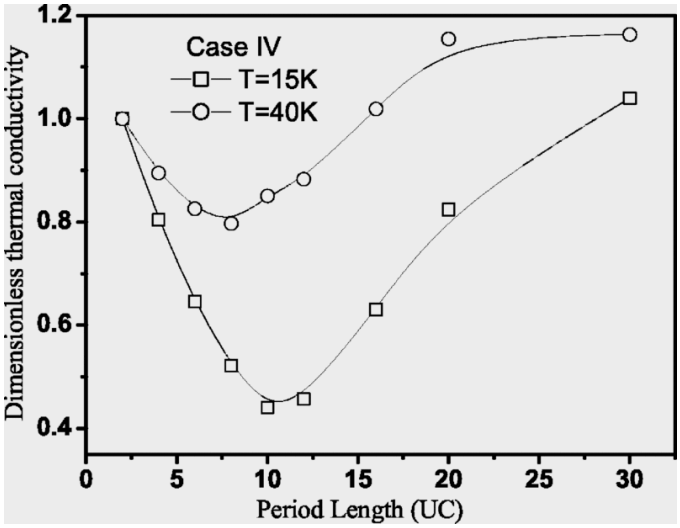

Figure 4.8: Effect of temperature on coherent phonon transport is calculated using molecular dynamics simulations for superlattice structures. From [275].

Before embarking on the experimental observation of this phenomenon, it is imperative to discuss the other parameters, which were not given enough consideration theoretically, but are important from experimental standpoint. For instance, the roughness at the superlattice interfaces, a very sensitive parameter in the experimental synthesis of superlattice structure, has not been considered while predicting the thermal conductivity. It will be discussed later in the experimental section, where the importance of interface roughness will become apparent. Another important parameter is the strength of phonon scattering at the interface formed between two constituents of the superlattice, *i.e.* acoustic impedance mismatch (AIM). Acoustic impedance is defined as the product of density and average phonon group velocity. Now, the phonon reflection coefficient is strongly dependent on AIM, larger the mismatch higher will be reflection of phonon waves at the interface. Lastly, the calculations in this model did not consider the effect of phonon coherence length on the crossover, which intuitively seems to be even more critical parameter than mean free path, in affecting the crossover from coherent regime to incoherent regime. Despite lack of discussion with regard to these parameters, the phenomenological model provided by Simkin-Mahan is reasonably good in capturing phonon interference effects on overall cross-plane thermal conductivity of superlattices.

4.3 Experimental Demonstration of Coherent Phonon Transport in Periodic Superlattices

4.3.1 Background

Many experimental studies of thermal transport in superlattices have been performed in various material systems such as GaAs-AlAs [279; 280], Si/Ge [281], Bi_2Te_3/Sb_2Te_3 [282], and AlN/GaN [283]. Most of these studies have been inconclusive with regard to showing crossover in phonon transport from particle-like to wave-like, either because of electronic contribution (Bi_2Te_3/Sb_2Te_3, AlN/GaN) [282; 283] and/or imperfect interface or defects (dislocations) (Si/Ge) [277; 281] in the superlattice films. Among these material systems so far GaAs-AlAs has shown to be most promising system to observe coherent crossover owing to good lattice mismatch and years of perfecting their growth using MBE [284-288]. However, the thermal conductivity of GaAs-AlAs superlattices as a function of superlattice period did not show the trend where a crossover can be highlighted [279; 280]. In this study, I have employed perovskites oxides such as STO, CTO and BTO as the material system, which offers an alternative, and perhaps a more suitable system to study this crossover in phonon transport regimes. While AIM of these oxide systems (STO-CTO and BTO-STO ~ 1.2) is comparable to previously studied systems (Si/Ge ~ 1.37, GaAs-AlAs ~ 1.13), the higher Umklapp peak in pervoskites (~ 100 K) [184] compared to Si and GaAs (~ 30-50 K) [266] favors observation of wave interference at room temperature. This is attributed to decreased anharmonic phonon-phonon scattering leading to less decoherence of phonons Umklapp peak shift towards room temperature. In addition, the phonon coherence length in a material could significantly affect the observation of such coherent effects. An estimate of phonon coherence length of LA and TA modes in GaAs is about 2 nm and 1 nm respectively [267], while that of STO is estimated to be 4.5 nm and 3 nm respectively [289]. Moreover, recent progress in identifying rich variety complex oxides [52] offers more possibilities in optimizing the desired acoustic mismatch for such thermal transport studies. In addition, most of these complex oxide systems such as titanates, ferrites, gallates, scandates *etc.*, being insulating lets us study only phonon contributions to thermal conductivity making the investigations more substantial/conclusive. Lastly, with recent advancements in synthesis of complex oxides via RHEED-assisted PLD [30; 113] and Molecular Beam Epitaxy [99; 290] enabled by wide range of substrate lattice parameters available (Figure 3.1) along with surface treatment processes leading to single-termination substrates, high-quality of oxide superlattices and heterostructures have been fabricated with atomically sharp interfaces, comparable to those achieved in conventional semiconductor superlattices [128].

Before we begin discussing experimental observations, it is important to clarify the basic differences between the often-reported coherent generation and detection of phonons in superlattice and heterostructures [291-293] and above-discussed coherent transport of phonons. In the former case, the experiments are mostly centered on generation and detection of mostly monochromatic phonons (acoustic or optical) possessing short-lifetimes using various optical pump-probe techniques [294]. However, the latter is about studying the transport of phonons, which is broadband in nature, meaning phonons of different wavelengths in a wave packet propagating through the superlattice structure, and in this particular case getting scattered coherently from the superlattice interfaces.

Typically, at room temperature, phonons which carry most of the heat in a solid have wavelength in between 1-5 nm [248], the effect of coherent scattering of phonons at various scattering centers present within that solid, would largely be absent on macroscopic thermal measurement. Thus, nanostructures such as superlattices (which allows controllability of structure down to one unit-cell) provides an excellent candidate to search for coherent scattering of phonons on a macroscopic quantity such as thermal conductivity.

4.3.2 Experimental Methods

Superlattices of $(STO)_m/(CTO)_n$ (short notation: '*m* x *n*') were synthesized via RHEED-assisted PLD, where '*m*' and '*n*' refers to the thickness in unit cells of respective materials oriented in the $[001]_{pc}$ (psuedocubic) direction. Superlattices with periodicities ranging from 1 x 1 to 87 x 89, or in terms of interface density (which is equal to 2/(superlattice period)) from 0.025 nm^{-1} to 2.59 nm^{-1}, were grown on a $(001)_{pc}$-oriented NGO (NGO) and (001)-oriented STO substrates. NGO substrates were heat-treated at 1000°C for 3 hrs to obtain singly terminated *i.e.* NdO-terminated NGO substrate [155]. STO substrates were first chemically treated with buffered HF and then heat treated at 1000°C for 3 hrs in flowing O_2 to obtain TiO_2-terminated STO substrate [154; 295]. On both STO and NGO substrates, 200 nm thick superlattice films were grown at the chamber pressure of 50 mTorr and growth temperature of 700°C. PLD growth of STO layers were achieved using stoichiometric single crystal STO target, while that of CTO layers was done using both stoichiometric polycrystalline and stoichiometric single crystal target. The laser fluence for both STO and CTO was set to 1.5 J/cm^2. After the growth at 700°C, films were cooled down to room temperature at an oxygen pressure of 50 Torr to ensure full oxidation of oxide layers in superlattice structure. These superlattice film were characterized by both *in situ* and *ex situ* characterization techniques. RHEED was used as the *in situ* characterization method to monitor the layer-by-layer growth mode and thickness of individual layers. The RHEED oscillations were monitored for specular spots along $[\bar{1}10]$ (in-plane) direction of NGO and $[100]$ direction of STO substrate. In the *ex situ* characterization, XRD, AFM, TEM were later employed to fully characterize superlattice thin films. For thermal conductivity measurement, TDTR was used with Aluminum as the metal transducer, having a thickness of 75-100 nm, and it was deposited using *e*-beam evaporation method (at UVa).

Superlattices of $(STO)_m/(BTO)_n$ (short notation: '*m* x *n*') were grown on $(001)_{pc}$-oriented $TbScO_3$ and (001)-oriented STO using reactive molecular beam epitaxy at Cornell University (for details about the growth parameters, see [296]) again with the use of *in situ* RHEED characterization. Superlattices of BTO-STO were deposited onto the substrate by providing single layer doses of SrO, TiO_2, BaO, TiO_2 for a desired superlattice period at a substrate temperature of 650°C and a background molecular oxygen pressure of 5 x 10^{-7} Torr [296]. As will be discussed later, further characterization using XRD, AFM, and TEM were performed to ensure high quality of superlattice films.

4.3.3 Results and Discussion

Prior to the synthesis of superlattices of STO-CTO with varying periodicities, growth parameters of individual constituents of the superlattice structure was carefully optimized to obtain highly-controlled superlattice growth process. The choice of substrate with a given lattice parameter plays a crucial role in obtaining controlled synthesis of these materials. For instance, the in-plane lattice parameter of STO is 3.905 Å and CTO is 3.81 Å (pseudocubic) and for the superlattice growth along (001)-oriented perovskite layers, one has to choose a substrate with in-plane pseudocubic lattice parameter equal to or close to the average of 3.905 Å and 3.81 Å, ex. NGO or LSAT. This will allow individual materials (*i.e.* components of superlattice system) to be strained only to an extent, which is needed to grow a superlattice with good control via *in situ* RHEED [297; 298]. Now, for a desired substrate in-plane lattice parameter, a substrate whose surface can be pre-treated (chemical and/or heat treatment) to have precise atomically flat surface prior to growth [154; 155; 299], would further improve the *in situ* controlled growth of superlattice constituents. NGO (110) is one example of a perfect substrate choice for growing superlattices of STO-CTO owing to close substrate in-plane lattice parameter (3.868 Å) vs. average of STO-CTO (~ 3.87 Å) and being able to heat treat the substrate to get atomically smooth surface having atomic steps [155]. After choosing the appropriate substrate, individual growth parameters were optimized on NGO substrate to find growth window (which give right stoichiometric phase) for both materials. From the overlap of the growth parameters, the condition that allowed best *in situ* RHEED control (meaning sustainable RHEED oscillations) for both materials is chosen. For example, under the optimized condition detailed in experimental methods, Figure 4.9 shows the RHEED oscillations, which was sustained to grow single layer of CTO up to 200 nm thick in layer-by-layer growth mode on a treated NGO (110) substrate.

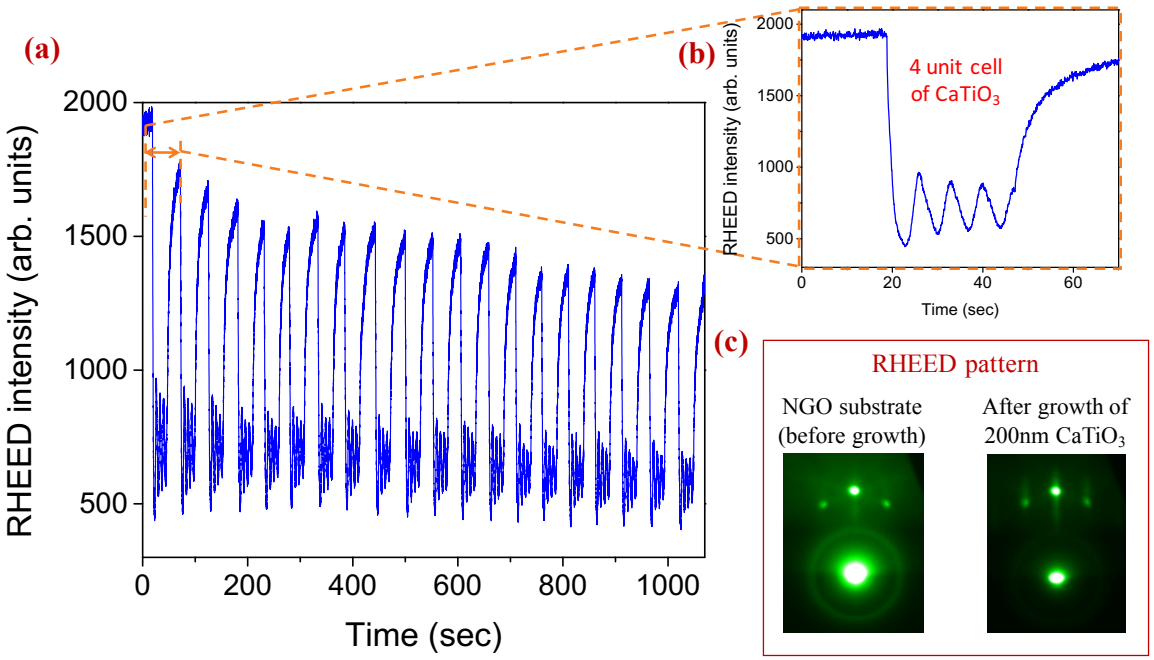

Figure 4.9: (a) RHEED oscillations for the growth of CTO on NGO (110) substrate is shown, where the sustainability of oscillations was achieved by growing 4 unit cells (inset (b)) and giving sufficient time in between for surface recovery. RHEED diffraction pattern is also shown in (c) before and after the growth of 200 nm CTO film.

Enabled by the capability to grow each constituent of the superlattice with *in situ* RHEED control, *n* x *n* superlattices of STO-CTO were synthesized. It is important to realize that layer-by-layer growth of CTO on previously grown-STO (or vice-versa), is possible because surface energy of grown-STO (or grown-CTO) allows wetting of next CTO layer (or STO layer). Thus, enabling the RHEED-controlled growth of superlattices. Note that the growth optimization of STO or CTO was done initially on the NGO substrate, not on each other. We may encounter cases where superlattice of 'A' and 'B' is not feasible because 'A' might not wet 'B' or vice-versa. Moreover, the surface termination of a substrate becomes crucial in stabilizing layer-by-layer of a material an example of which will be discussed in chapter 5. Thus, choice of superlattice system needs to be considered from the synthesis perspective when searching of a novel phenomenon.

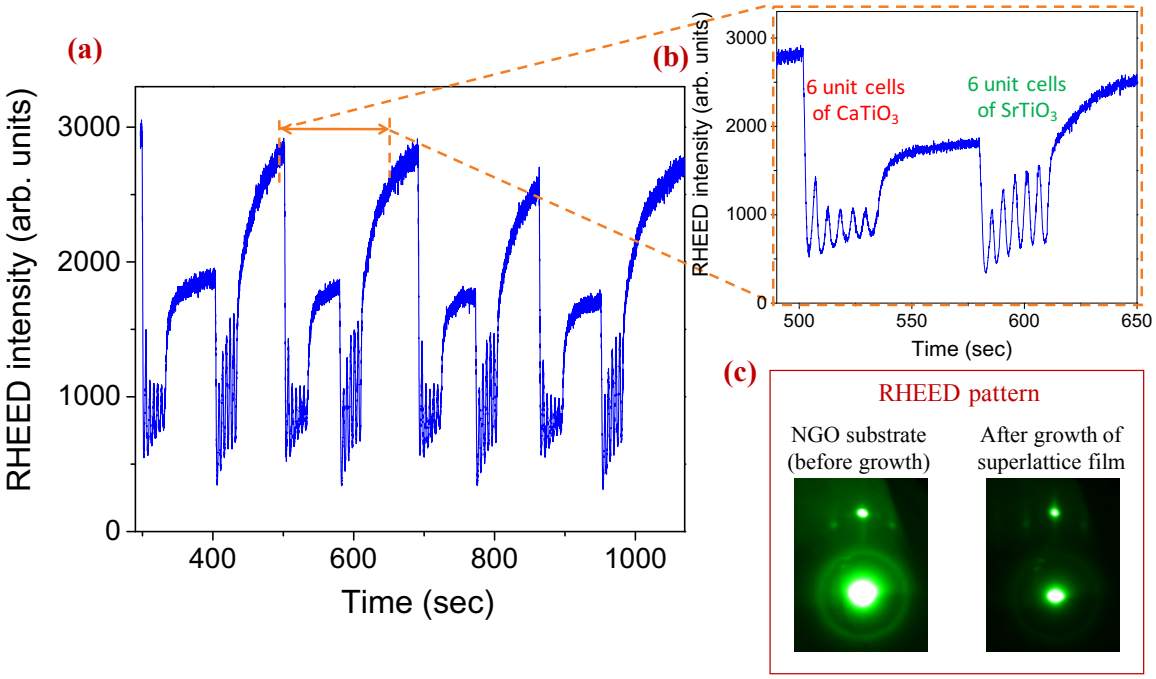

Figure 4.10: RHEED oscillations for four periods of 6 x 6 STO-CTO superlattice film grown on NGO (110) substrate are shown in (a), while Inset (b) shows the oscillations for one period. RHEED diffraction pattern is also shown before growth (*i.e.* of NGO substrate) and after the growth of 200 nm Superlattice film.

In situ RHEED monitoring of a representative 6 x 6 STO-CTO superlattice for four periods is shown in Figure 4.10, when monitored along [$\bar{1}10$] direction of NGO (110) substrate. The recovery of RHEED intensity after the growth of one superlattice period enables use to synthesize superlattice structures of thickness as large as 200 nm. The RHEED pattern of the substrate surface before the start of superlattice growth and after growing 200 nm thick film is shown in Figure 4.10. As can be seen by the presence of both specular spots and diffraction spots, after growing 200 nm film further attests to the surface smoothness of the films. This coupled with advantage of STO growing layer-by-layer on CTO and vice-versa, further allows us to grow symmetric (*n* x *n*), asymmetric (*m* x *n*), quasi-periodic superlattice as well as completely random sequence (aperiodic superlattice, see figure 4.18 in next section) as per requirement. For this study, I have focused only on the symmetric structures keeping 50:50 volume ratio of STO and CTO. Superlattice films of varying periodicities was also synthesized on treated STO substrate under the same growth conditions as on NGO substrate. Similar to NGO substrate, RHEED-controlled synthesis of individual STO and CTO layers allowed us to grow superlattices of periodicities ranging from 1 x 1 to 87 x 89. RHEED pattern before and after growth of 200 nm film showed both specular and diffraction spots.

X-ray diffraction studies were performed to do the structural characterization of the films. Symmetric Bragg scans (a representative scan is shown in Figure 2.11) were used to

check the structural quality of the films. For example, for the 6 x 6 superlattice shown in Figure 2.11, superlattice period calculated using (+1) (or (-1)) superlattice reflection and the Bragg peak (labeled as $SL_{(0)}$ 002), corroborates well with the *in situ* RHEED characterization. The position of (002) Bragg peak of the film corresponds to the 50:50 STO-CTO alloy composition, *i.e.* the desired symmetric structure. In addition, the presence of *Pendellösung* fringes around (002) Bragg peak suggests films are smooth, again supporting the RHEED diffraction pattern from the film. Further analysis of the rocking curve of (002) Bragg peak of 6 x 6 superlattice film shows that Full-width-at-Half-Maximum (FWHM) of the film was 0.028° while that of (002) NGO substrate Bragg peak was 0.018° (Figure 2.13), which suggests that superlattice films are of high-quality.

Reciprocal space maps (RSMs), *i.e.* Asymmetric XRD scans, were also performed to check the strain state of the superlattice films. Two representative RSM of a 1 x 1 and 2 x 2 superlattice films around NGO (332) (or $(103)_{pc}$) is depicted in Figure 4.11, where the same in-plane lattice constant of film as that of substrate suggests that films are coherently strained to the substrate with the absence of misfit dislocations. Similarly, all superlattice films grown on both NGO and STO substrate were characterized by RSM and were confirmed to be strained on the substrate.

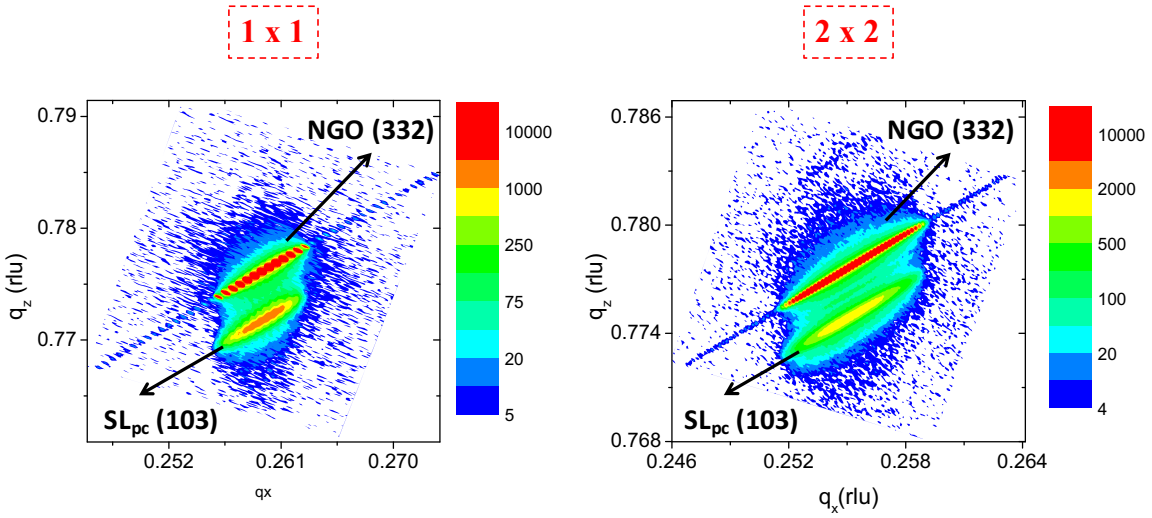

Figure 4.11: Reciprocal space map of 200 nm thick (a) 1 x 1 and (b) 2 x 2 STO-CTO superlattice film grown on NGO (110) substrate.

Surface topography of superlattice films was characterized by AFM. A representative image of surface topography of 2 x 2 superlattice grown on a treated STO (001) substrate and a 1 x 1 superlattice grown on NGO substrate is depicted in Figure 4.12. The presence of atomic steps on 200 nm thick superlattice films grown on both STO and NGO substrates indicate that films were smooth, with step height corresponding to unit-cell of last layer of superlattice structure which in these superlattices was STO (see Figure 2.26 for the line profile along the steps). These results from AFM further corroborate the

evidence of 2D growth mode as characterized from *in situ* RHEED, and the presence of *Pendellösung* fringes in symmetric Bragg scans.

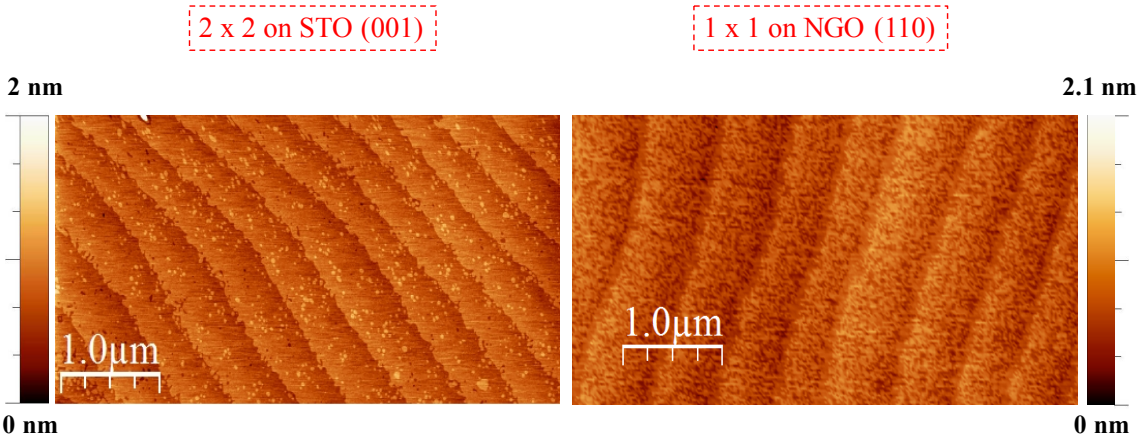

Figure 4.12: AFM (flattened) image of 200 nm thick superlattice films of (a) periodicity 2 x 2 grown on STO (001) and (b) periodicity 1 x 1 grown on NGO (110).

Lastly, TEM was employed to characterize the STO-CTO interface quality in superlattice films. Since phonon scattering is extremely sensitive to interface quality, *i.e.* specular vs diffuse scattering [226; 300], superlattice interfaces plays a crucial in observing the effect of coherent scattering on the thermal conductivity (Figure 4.15). Figure 4.13 shows a high-resolution STEM image of a representative 2 x 2 superlattice revealing atomically sharp-interfaces in superlattices grown using RHEED-assisted PLD. TEM analysis also corroborates well with the *in situ* RHEED characterization.

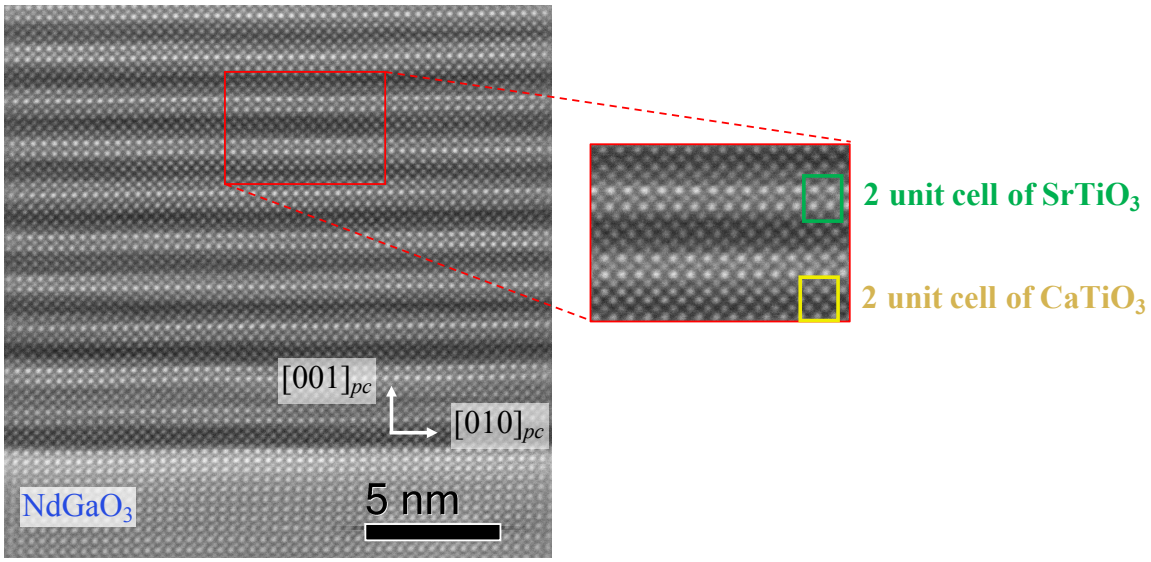

Figure 4.13: STEM image of a sub region of 200 nm thick 2 x 2 STO-CTO superlattice film grown on a NGO (110) substrate.

Similarly, BTO-STO superlattices grown from reactive MBE were fully characterized using *in situ* RHEED and *ex situ* characterization techniques such as TEM, XRD, and AFM. The presence of many order of superlattice reflections along with narrow FWHM of (002) Bragg peak (0.023°) compared to that of substrate (0.018°), indicates long-range ordering of superlattice structure and good crystallinity [296]. In addition, STEM was also done to confirm the high quality of interfaces, which is essential for these investigations. The detailed account of film characterization grown via MBE is discussed elsewhere [296].

After ensuring the high quality of STO-CTO superlattices grown via both RHEED-assisted PLD and BTO-STO grown via MBE, we went ahead to measure the thermal conductivity of superlattices as a function of superlattice period (or superlattice interface density). Thermal conductivity measurements of STO-CTO superlattice were carried at UVa, which that of BTO-STO were measured at both UIUC and UVa. The detailed account of extracting thermal conductivity of superlattice thin film from TDTR measurement is discussed elsewhere [289; 301; 302]. The repeatability of thermal conductivity measurements was checked from sample to sample. The error bar in thermal conductivity measurements takes account of error arising from both measurement technique and the deviation of measured values at different locations on a given sample [289].

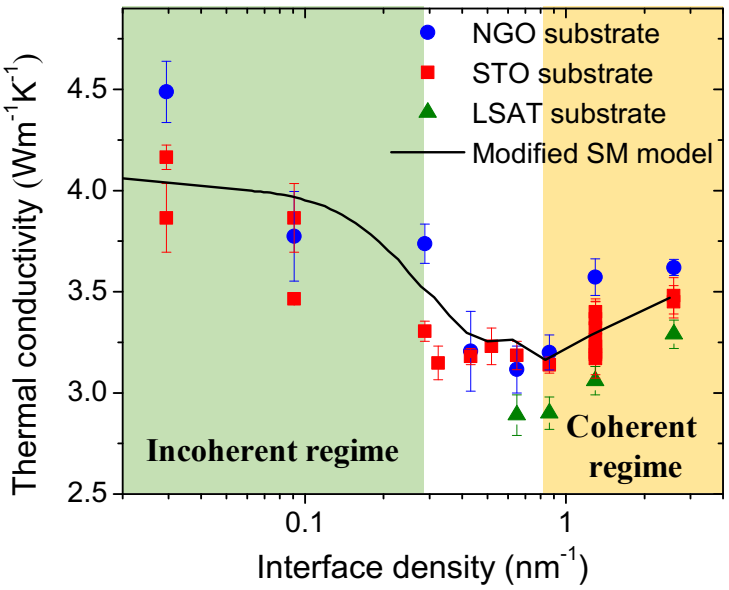

Figure 4.14: Thermal conductivity of STO-CTO superlattice films measured using TDTR at room temperature is shown. From [289].

Thermal conductivity of STO-CTO superlattices as a function of superlattice period or superlattice interface density is shown in Figure 4.14 (measured at room temperature). The graph shows thermal conductivity of superlattices grown on both NGO and STO substrates. The phonon transport in STO-CTO superlattices grown on both substrates can be divided into two regimes, incoherent regime vs. coherent regime, based on whether thermal conductivity decreases or increases with increase in interface density (highlighted green or yellow background color) respectively. In the regime of thick-period superlattice or low interface density, effective thermal resistance of the superlattice structure can be modeled as series summation of individual thermal resistance from each interface of the superlattice sequence. Hence, the thermal resistance increases as the number of superlattice interfaces increases leading to decrease in thermal conductivity with increase in superlattice interface density. This regime is characteristic of incoherent transport of phonons, which is well-discussed phonon transport mechanism in literature [226; 238; 303]. In the regime of short-period superlattice or high-interface density, thermal conductivity is observed to show a trend, where increasing the interface density leads to increase in thermal conductivity, which is a completely opposite trend as compared to the low interface density regime. This regime is characteristic of coherent transport of phonons where scattering of phonons at the superlattice is correlated [226]. Such correlated scattering is a result of phonon wave interference at the superlattice interfaces when the superlattice period becomes comparable to phonon coherence length in superlattice constituents. Under these conditions, superlattice phonon dispersion curve starts to form mini-bands due to band folding effect, which decreases overall average group velocity of phonons. In the high interface density regime, as the superlattice period decreases band folding along the cross-plane axis leads to decrease in number of minibands, hence increase

in overall average phonon group velocity. Thus, in coherent regime, thermal conductivity increases with increase in interface density (or decrease in superlattice period). This crossover from incoherent regime to coherent regime as a function of superlattice period is clearly visible in thermal transport measured at room temperature [Figure 4.14].

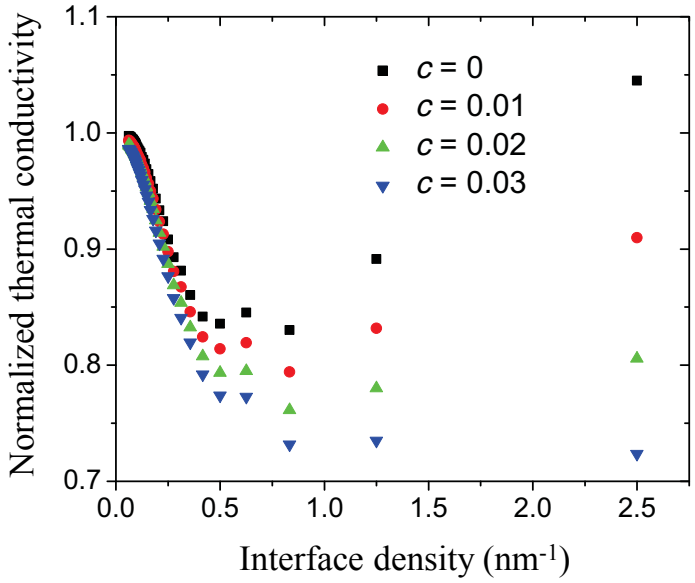

Figure 4.15: Normalized thermal conductivity calculated using modified Simkin-Mahan model to analyze the effect of interface disorder on coherent regime of thermal transport. Courtesy of Prof. Joel Moore.

Analysis of thermal conductivity of STO-CTO superlattice in the coherent regime provides more understanding of coherent scattering of phonon at superlattice interfaces. Interface disorder at the superlattice interfaces could result into mode of conversion of phonons [226], leading to their decoherence and hence reduction in coherence length. Simkin-Mahan model was adapted for STO-CTO superlattices to theoretically study the effect of interface disorder on the thermal conductivity of superlattices in the coherent regime. The modification of the Simkin-Mahan model to incorporate disorder at the interface, is taken into account by adding extra contribution to the mean free path via Mathiessen's rule, *i.e.*,

$$\frac{1}{\lambda(L)} = \frac{c}{L} + \frac{1}{l} \tag{4.56}$$

, where 'c' is constant determining effectiveness of additional interface scattering due to disorder at the interface. The value of 'c' indicates the strength of additional interface scattering due to the presence of disorder at the superlattice interfaces. Figure 4.15 shows the effect of increasing the value of 'c' (with given l = 30 lattice constants) on the coherent

scattering of phonon in determining the thermal conductivity across the short-period superlattices. This graph shows how crucial is the quality of superlattice interfaces in determining the coherent scattering of phonons, and hence observing the effect of coherent scattering of phonons on thermal conductivity.

After looking at the microscopic description of interface disorder on thermal conductivity in the coherent regime, we can explain the experimental data by using Simkin-Mahan model with modification on the interface thermal conductance, which is another parameter used in the original SM model. The calculated thermal conductivity of STO-CTO superlattices, using atomic mass ratio and group velocity reported in literature [304-307], was rescaled to actual thermal conductivity by a factor determined by the thermal conductivity of lowest interface density superlattice. A small-disorder induced thermal boundary resistance, which is assumed to scale linearly with interface density, was introduced to fit the experimental data. Using the series model for thermal resistance, we find:

$$\frac{1}{K_{exp}} = \frac{1}{K_{SM}} + \frac{ID}{G} \tag{4.57}$$

, where 'K_{SM}' is rescaled thermal conductivity, 'K_{exp}' measured thermal conductivity, 'ID' is interface density, 'G' is disorder thermal conductance. For the best fit to the experimental data, disorder thermal conductance at STO-CTO interface was found to be 48 $GWm^{-2}K^{-1}$, which translates to equivalent oxide thickness of 0.21 Å. This further emphasizes the fact that presence of even a small disorder at the interface is detrimental to the observation of coherent effects in SLs. The fitted curve is shown in the main result as 'Modified SM model' (Figure 4.14).

Further observations on thermal conductivity values of superlattices grown on NGO vs on STO, suggests that in general superlattice on NGO substrate have higher thermal conductivity compared to equivalent superlattices on STO substrate. And, the thermal conductivity of STO-CTO superlattices grown on LSAT (001) substrate using MBE (at Cornell University) is also plotted (only for coherent regime). There are number of parameters which could play a role in varying thermal conductivity of superlattices grown on substrates with different in-plane lattice parameter and crystal symmetry. Foremost parameter is the often-reported variation in thermal conductivity due to thickness effects [308; 309]. Since the thickness of all superlattice grown on both NGO and STO, was kept constant at 200 nm, the discrepancy cannot be attributed to size-effects. Second is the volume fraction of superlattice constituents, which could a significant factor, but was kept constant at 50:50 for superlattices grown on both substrates. Strain state of the film could play a role in observed differences in thermal conductivity of superlattice grown on different substrates, for which systematic study is needed to understand the behavior in detail.

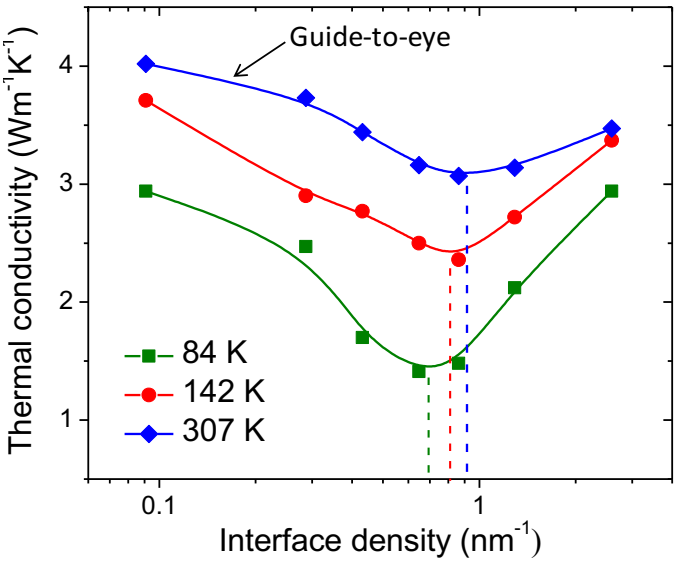

Figure 4.16: Temperature-dependent thermal conductivity of STO-CTO superlattice films grown on NGO (110) substrate. From [289].

Above results are discussed for thermal conductivity measured at room temperature. Since the mean free path of phonons increases when decrease in temperature, coherent scattering of phonons is expected to be more pronounced due to larger mean free paths, as predicted by molecular dynamics and lattice dynamics simulations (Figure 4.5, Figure 4.7 and Figure 4.8 shown earlier), and it can easily be tested by measuring thermal conductivity of superlattice films at lower temperatures. Motivated by this, I measured thermal conductivity at 84 K, 142 K, and 307 K and the results are illustrated in Figure 4.16. As expected at lower temperatures, *i.e.* at 142 K and 84 K, the transition point from coherent to incoherent transport has shifted to thicker superlattice periods supporting theoretical predictions. A qualitative explanation could be derived from the fact that the phonon wave packets propagating through the superlattice structure can retain their phase information for larger lengths [226] leading to more pronounced effect of band folding on the coherent scattering of phonons. This emphasizes the fact that in order to observe coherent effects on thermal conductivity of superlattice structures, temperature has to be optimum. At very high temperatures, Umklapp scattering will dominate which will significantly reduce *mfp*, and at very low temperatures population of phonons will be limited to only low-frequency phonons, which may not carry sufficient heat to enable the effect of coherent scattering of phonons on thermal conductivity. The observation is centered on the transition of scattering regime from being incoherent at low interface densities to being coherent at high interface densities.

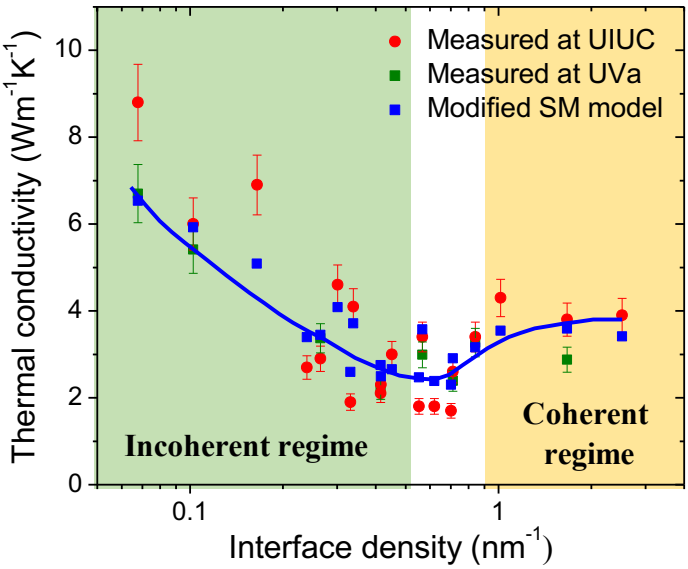

Figure 4.17: Thermal conductivity of BTO-STO superlattice films, grown via MBE and measured using TDTR at room temperature. From [289].

Synthesizing different superlattice system using different synthesis technique checked the robustness of this phenomenon. Thermal conductivity of STO-BTO superlattices grown by MBE with interface density ranging from 0.06 nm^{-1} to 2.59 nm^{-1} was measured using TDTR and results for room temperature measurement is shown in Figure 4.17. In this superlattice system also, one can clearly distinguish two different regimes of phonon transport based on whether thermal conductivity decreases (incoherent) or increase (coherent) with interface density, as indicated by highlighted green or yellow background color. A close inspection on the thermal conductivity of STO-BTO superlattices with varying interface density shows significant degree of deviation in measured data points from S-M model (indicated by solid line as guide to eye). Since in the case STO-BTO superlattices volume fraction was not kept constant when the interface density was being varied, in the modified SM model this variation in volume fraction was incorporated using series thermal resistance model. The final values obtained for STO-BTO superlattices with volume fraction correction is shown in blue square dots, which is capturing well, the deviation observation in measured data points. It is also important to note that total thickness of all superlattice of STO-BTO was not kept constant, which could result in size-effect on the measured thermal conductivity. Role of such size-effects on alloy films have already been reported [302]. Also note that the variation in volume fraction and total thickness of superlattice film was also present in previously studies superlattice systems such as GaAs-AlAs [279; 280] and could explain the absence of coherent effects in those superlattice systems. This emphasizes the fact that systematic variation of interface density with all other parameters (total thickness, volume fraction) fixed is crucial to observe such phenomenon in superlattices. In spite of variations in volume fraction and total thickness of superlattice films, a transition in phonon transport can be observed in

Figure 4.17 (highlighted by solid blue line). Thus, with the help of two superlattice systems I have presented unambiguous observation of crossover from traditional incoherent regime of phonon transport to coherent regime of phonon transport with increase in superlattice interface density (or decrease in superlattice period).

4.4 Role of Coherent Phonon scattering in Aperiodic Superlattices

In the previous section, I showed that changing the interface density in superlattices produces a transition from traditional incoherent phonon transport at low interface densities to coherent phonon transport at higher interface densities. In order to further understand and explore the coherent scattering of phonons at the interfaces, I designed superlattice-like structures, called as Aperiodic Superlattices (ASLs), where the structural order is controlled to vary from a periodic structure to a completely aperiodic structure, where there is no long-range order. Thermal conductivity of ASLs of STO and CTO, with average interface density corresponding to both regimes of phonon transport, coherent and incoherent, were studied. In general, I found that effect of increasing disorder on the thermal conductivity of ASLs appears to depend on the average interface density of the aperiodic structure. In particular, those ASLs, which show lower thermal conductivity than the minimum achieved in periodic superlattices, may indicate that coherent scattering is dominant in deciding the thermal conductivity of ASLs.

4.4.1 Background

In order to fully utilize the coherent scattering of phonons in pushing the lower limits of thermal conductivity, it is imperative to understand the effect of hierarchical order on the coherent scattering of phonons. Several theoretical attempts have been made in the past to study the effect of both short-range and long-range order in superlattice-like systems, not only on the thermal conductivity [310], but also on the phonon transmission and reflection and its relation to wave localization [311-313]. For instance, Landry *et al.* used Green-Kubo method [314] to predict the thermal conductivity of a superlattice with a complex unit cell, and reported thermal conductivity 17% lower than the minimum thermal conductivity achievable through the superlattices of two-layer unit cell [310]. The observed decrease in thermal conductivity of these superlattices occurred only when the short-range order of the sub cells in the complex unit-cell is of the order of phonon mean free path, suggesting significant decrease in the contribution of coherent phonons due to complex unit-cell design. Wang *et al.* performed similar non-equilibrium molecular dynamics simulations (NEMD), to predict the behavior of Random Multilayer (RML) as compared to Periodic Superlattices [315]. Their calculation predicted that the RML has a lower thermal conductivity than a periodic superlattice for the same total thickness of the sample.

In addition, the RML structures show saturation in thermal conductivity as a function of sample thickness, indicating localization of coherent phonons due to random thicknesses of constituting layers, as compared to the periodic superlattice where the thermal conductivity increased with sample thickness due to significant contribution of coherent phonons [315]. Such theoretical and computational approaches to understand the effect of this hierarchical structural order on phonon thermal transport requires validation from experimental studies, which also facilitates the design of optimized structures with enhanced correlated scattering to realize extremely low-thermal conductivity materials. However, experimental efforts in fabricating these superlattice-like structures with different structural order and measuring the thermal conductivity have been largely lacking.

In an attempt to study thermal transport in these superlattice-like structures, I have designed aperiodic structures whose degree of structural order can be systematically varied from a normal periodic superlattice to a completely aperiodic structure, which will have no lattice translational symmetry in the growth direction (or perpendicular to superlattice interfaces). An aperiodic superlattice (ASL) is a non-periodic structure of material 'A' and material 'B,' where random unit cells of material 'A' and material 'B' are stacked together in such a way that there is no lattice translational symmetry. From this definition, one can imagine many different ways to create an aperiodic structure with different average interface densities, *i.e.* the total number of interfaces formed between 'A' and 'B' in the randomly stacked aperiodic sequence per total thickness of the structure, and different volume fractions of two materials 'A' and 'B.'

In order to employ these aperiodic structures for studying thermal transport, I've created aperiodic sequences with certain constraints to compare against a reference structure, which in this case is the periodic superlattice structure. Aperiodic sequences of STO and CTO were generated with same volume fraction and average interface density as that of a reference periodic superlattice. To generate an aperiodic sequence with 50:50 volume fraction and average interface density equal to the corresponding 'n x n' periodic superlattice (where 'n' is the number of unit cells of STO and CTO), one must use a pool of random unit cells of STO and CTO, from layer thicknesses of 'n - m' to 'n + m' unit cells, as the random building blocks of these ASLs. These layers must be stacked in such a way that will ensure the total number of unit cells used be same for both STO and CTO through the thickness of the film. In addition, the number of interfaces formed by these random building blocks of STO and CTO should be the same as that of periodic superlattice for the same total thickness, and hence, it will correspondingly have the same average interface density. The program that we wrote to create an aperiodic sequence by randomly selecting the building blocks of STO and CTO ensuring both of the above mentioned constraints are satisfied. An example of an Aperiodic Superlattice is shown in Figure 4.18(a), where the schematic shows a part of aperiodic sequence generated using such a program following all the abovementioned constraints, for the case of average interface density equivalent to a 3 x 3 periodic superlattice. For comparison, a periodic 3 x 3 superlattice is also drawn in Figure 4.18(b).

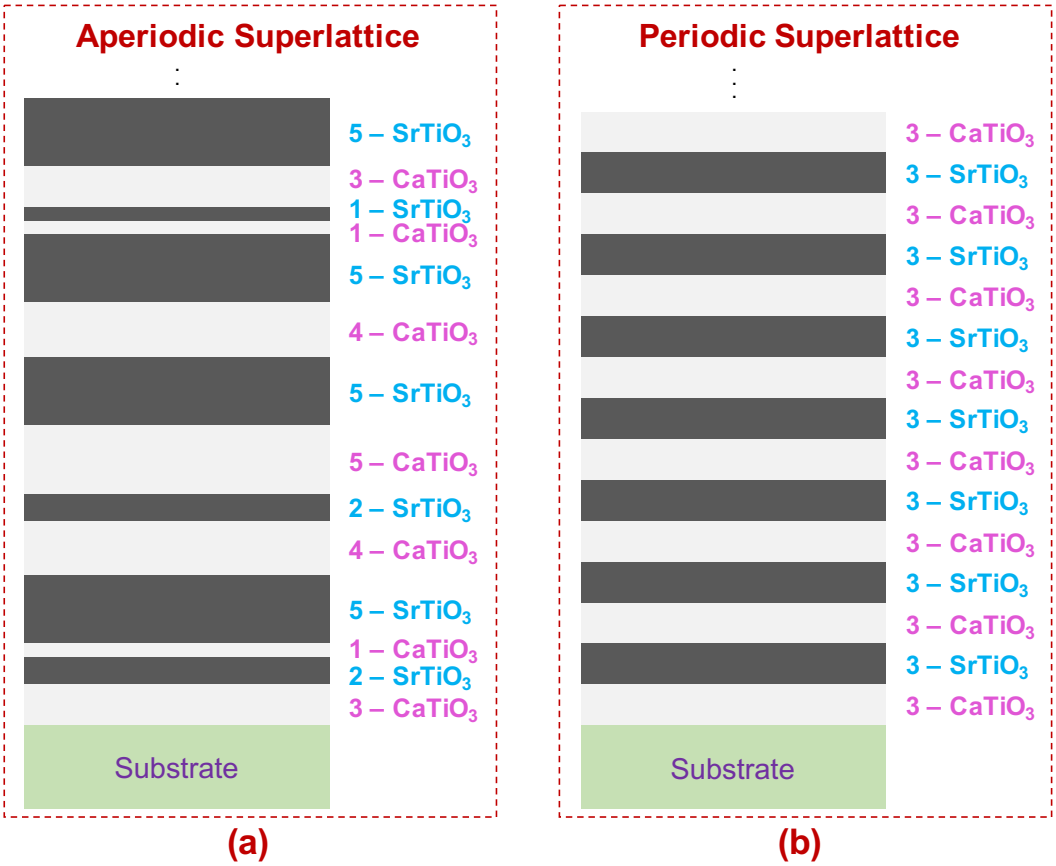

Figure 4.18: A schematic of an Aperiodic superlattice with average interface density equal to 0.86 nm^{-1}, *i.e.* average interface density equivalent to that of a periodic 3 x 3 superlattice, is shown in (a), along with a schematic for the reference 3 x 3 periodic structure.

Using our above-mentioned growth algorithm, we vary the average interface density in our ASLs from 0.1 – 1.29 nm^{-1}, which provides a range of interface densities to study the effects of increasing disorder on coherent and incoherent phonon transport; this range was selected based on the coherent phonon transport regime in periodic STO-CTO superlattices discussed in previous section. Depending on the superlattice interface density, phonon transport can be dominated either by incoherent or coherent scattering of phonons, giving rise to well-established trends in the thermal conductivity as a function of interface density. Aperiodic sequences with varying degrees of disorder were generated to correspond to equivalent periodic superlattices either in the incoherent regime (*i.e.* '27 x 27', '6 x 6', '5 x 5', '4 x 4'), or in the coherent regime (*i.e.* '3 x 3' and '2 x 2'). With the design of these aperiodic superlattices, I have manipulated the hierarchical interfacial structure in such a way that the disorder in the system is controlled by careful repositioning of the STO-CTO interface from a periodic position to a non-periodic position decided by the random block (thicknesses) of STO or CTO layers.

In the following section, I will discuss thermal transport in aperiodic superlattices of STO and CTO with controlled degree of disorder, ranging from completely periodic superlattices to completely aperiodic superlattices, with an average interface density of varying from 0.1 nm^{-1} to 1.29 nm^{-1} and volume fractions of STO and CTO equal to 50:50. Combining the degree of disorder with average interface density enabled us to vary both short-range and long-range disorder to study hierarchical interface effects on the interplay between incoherent and coherent scattering of phonons in superlattices. I'll show that coherent effects can be important in both incoherent and coherent regimes of phonon transport as characterized by average interface density of periodic superlattices.

4.4.2 Experimental Methods

RHEED-assisted Pulsed Laser Deposition (PLD) was again used for the synthesis of the Aperiodic Superlattices of STO and CTO with the same growth optimized parameters as used for the growth of periodic superlattices. ASLs of STO and CTO, with average interface density corresponding to 1.29 nm^{-1}, 0.86 nm^{-1}, 0.65 nm^{-1}, 0.52 nm^{-1}, 0.43 nm^{-1}, and 0.1 nm^{-1} were synthesized. All ASLs films were grown on both NGO and STO substrates for a total film thickness of 200 nm. The rest of the PLD growth parameters were kept same as those used for synthesis of periodic superlattices discussed in the previous section. Transmission Electron Microscopy (TEM) and XRD were used to characterize, and confirm the evolution of structural order in thin-films of ASLs. Thermal conductivity of ASLs, with varying degree of disorder, was measured using Time-domain Thermoreflectance (TDTR) technique (at UVa). The TDTR parameters were also the same as the one used for measuring thermal conductivity of periodic superlattices as discussed in the previous section. Using TDTR, thermal conductivity measurements were performed over a temperature range from 175-300 K.

4.4.3 Results and Discussion

Reflection High Energy Electron Diffraction (RHEED) was again employed as the *in situ* characterization method to monitor growth of the individual building blocks of the aperiodic sequence. *In situ* monitoring of the unit-cell-by-unit-cell growth of individual '*n* + *m*' unit-cells layer of STO (or CTO), enabled by the *Frank-der-Merwe* (layer-by-layer) growth mode of these materials, ensured the realization of theoretical aperiodic sequence generated from the program. Each layer (random block) of the aperiodic sequence was monitored individually, starting from the beginning of the sequence to the end totaling to 200 nm thickness of the aperiodic superlattice, to accurately replicate the theoretical sequence with the materials STO and CTO as the constituent building blocks of the aperiodic superlattice. A representative example of RHEED-monitored growth of an aperiodic sequence is shown in Figure 4.19(a), where counting the number of RHEED oscillations during their growth and growing the whole sequence in a similar fashion grew

random blocks of desired unit-cells of STO or CTO. Other aperiodic sequences were similarly synthesized on both NGO (110) and STO (001) substrates using RHEED-assisted pulsed laser deposition.

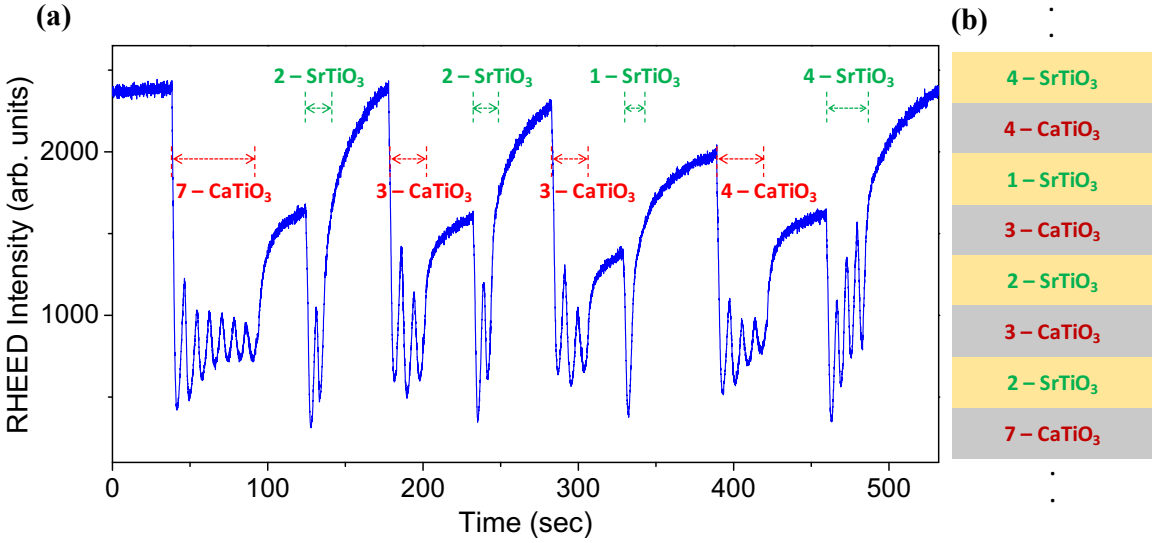

Figure 4.19: (a) RHEED oscillations are shown for a part of an aperiodic sequence with average interface density of 0.65 nm^{-1} and Split 7. (b) shows the schematic of thin-film structure corresponding to the RHEED oscillations depicted in (a).

Transmission Electron Microscopy (TEM) was used to analyze and verify the sequence after synthesis. Figure 4.20 provides analysis based on Transmission Electron Microscopy (TEM) on a representative aperiodic superlattice, which reports the replication of theoretical sequence onto a substrate via RHEED-assisted PLD within an accuracy of 1-unit cell. An ASL with an average interface density of 0.43 nm^{-1} and Split 7 was analyzed in HRSTEM to identify the growth-sequence, and the result is shown in Table 4.1 which compares the theoretical sequence against that measured from TEM analysis (shown in Figure 4.20). Tables shows that grown-sequence matches closely with theoretical one within an accuracy of unit-cell. Since there is little interdiffusion of 'Sr' and 'Ca' across the STO-CTO interface, the resolution of determining the actual number of unit cells in a random block of STO (or CTO) is 1-unit cell. This method of employing RHEED-assisted PLD for synthesizing aperiodic structures is robust, in terms of both allowing the aperiodic sequences to be manipulated in accordance with various constraints and replicating a theoretical sequence in a repeatable fashion.

Table 4.1: Comparison of theoretical (aperiodic) sequence and as-grown aperiodic structure using RHEED-assisted Pulsed Laser Deposition as measured from TEM-based analysis is presented.

Layer	Theoretical	Measured using TEM	Difference	Layer (continued)	Theoretical	Measured using TEM	Difference
CTO	5	5	0	CTO	7	6	1
STO	6	5	1	STO	7	7	0
CTO	8	9	-1	CTO	8	8	0
STO	5	5	0	STO	8	8	0
CTO	7	7	0	CTO	8	7	1
STO	3	4	-1	STO	6	7	-1
CTO	5	4	1	CTO	6	5	1
STO	9	10	-1	STO	9	10	-1
CTO	7	6	1	CTO	9	8	1
STO	9	10	-1	STO	8	9	-1
CTO	9	9	0	CTO	5	4	1
STO	7	7	0	STO	7	8	-1
CTO	9	8	1	CTO	7	6	1
STO	4	5	-1	STO	5	6	-1
CTO	9	8	1	CTO	5	4	1
STO	5	5	0	STO	6	7	-1
CTO	4	4	0	CTO	9	8	1
STO	4	5	-1	STO	9	10	-1

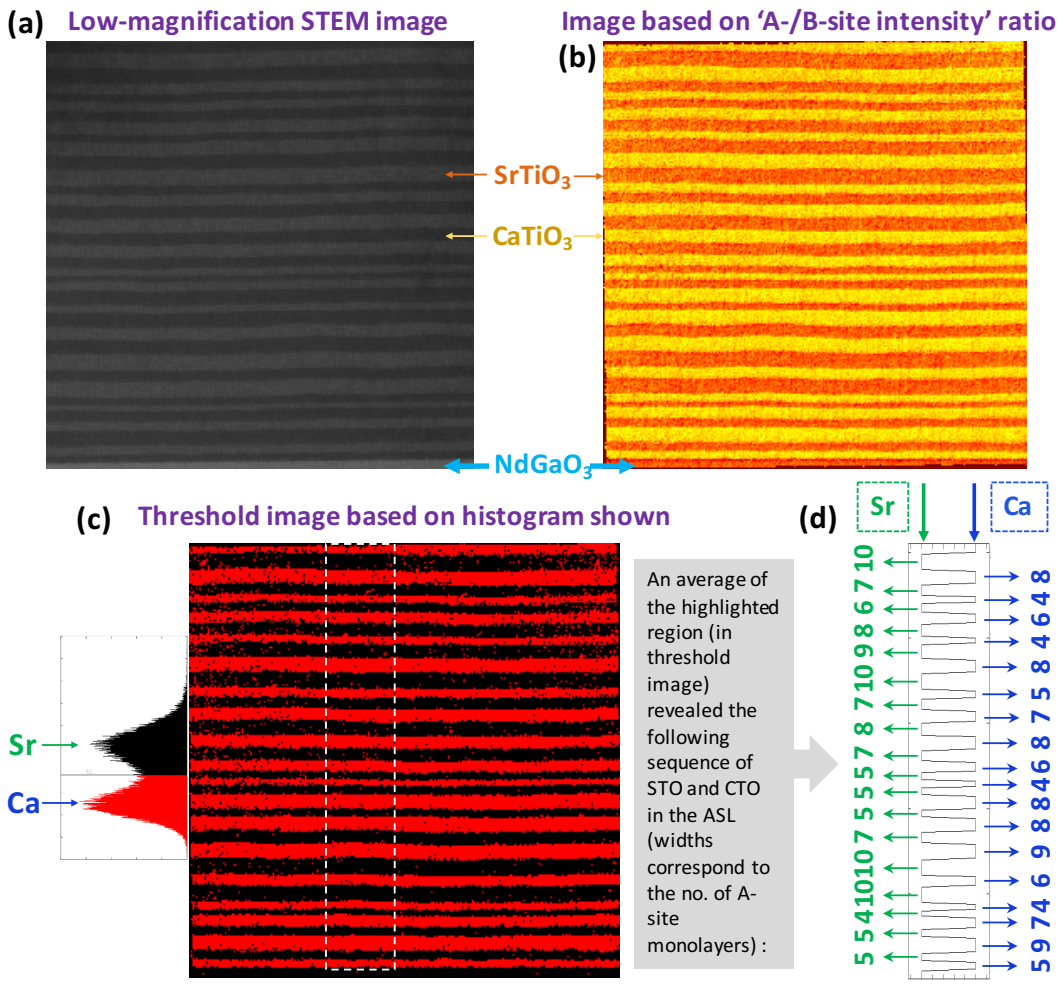

Figure 4.20: (a) shows low-magnification STEM image of sub region of an aperiodic superlattice film with average interface density 0.43 nm^{-1} and Split 7. (b) shows colored STEM image based on A-site/B-site intensity ratio. (c) shows the same image recolored based on the histogram (inset) of overall intensity distribution of the image. A sub region is chosen within this image to analyze the variation of A-site atoms across the thickness of the thin-film, which is shown in (d) along with intensity profile across the highlighted region. TEM analysis courtesy of Dr. Christopher Nelson.

Similarly, other ASLs with varying degree of disorder at a given average interface density was synthesized via *in situ* RHEED characterized pulsed laser deposition. Figure 4.21 shows another example of an aperiodic superlattice with average interface density 0.86 nm^{-1} and Split 5, where low magnification STEM image of an aperiodic superlattice is shown. From this STEM image, one can observe the random variation in the thickness of STO (bright contrast) and CTO (dark contrast) across the thickness of the heterostructure, which is following the desired aperiodic sequence in the thin-film.

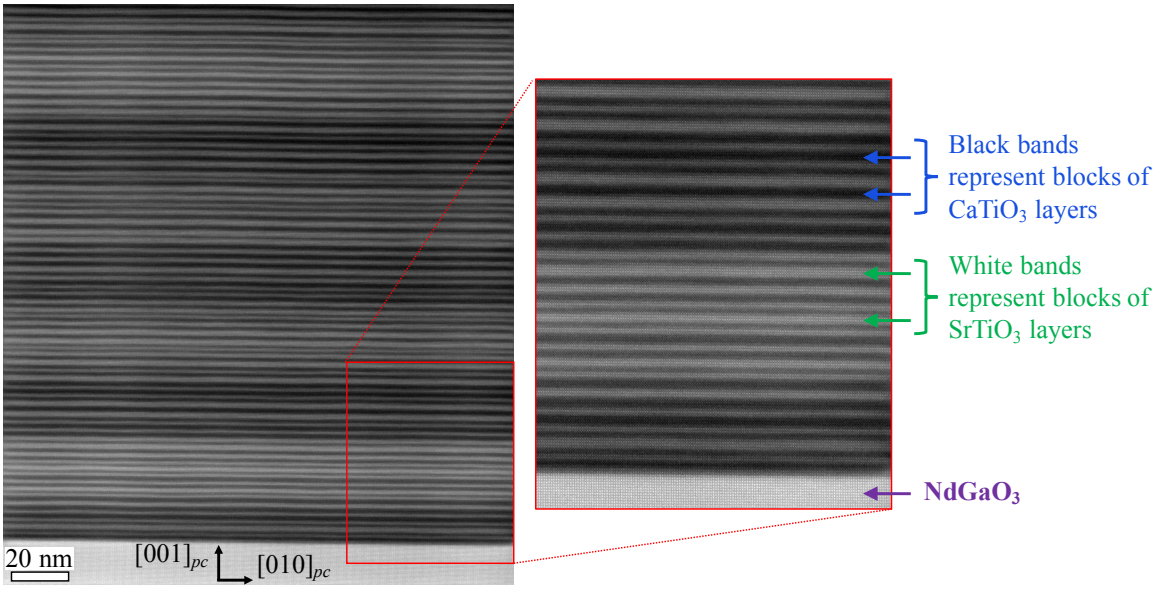

Figure 4.21: STEM image of an aperiodic superlattice film with an average interface density of 0.86 nm^{-1} and Split 5 is shown.

Aperiodic Superlattices with varying average interface density and disorder were synthesized on two substrates NGO (110) and STO (001). After synthesizing a split series for a given average interface density, XRD was performed to confirm the expected decrease in long-range periodicity with increasing split (or disorder), as indicated by the change in the intensity of superlattice peaks. As an example and representative for other aperiodic superlattices, Figure 4.22 shows the evolution of Aperiodic Superlattice grown on NGO (110) with increasing spit for average interface density of 0.43 nm^{-1} (equivalent to '6 x 6' periodic superlattice). At Split 3 – *i.e.*, with the introduction of little disorder – the intensity of first order superlattice peaks, $SL_{(-1)}$ (002) and $SL_{(1)}$ (002), reduces significantly compared to periodic superlattice. In addition, higher order superlattice peaks such as $SL_{(-3)}$, $SL_{(-2)}$, $SL_{(2)}$ *etc.*, disappear at the introduction of little disorder, highlighting the effect of disorder on the periodicity of the aperiodic structure. As the split of sequence is further increased, the superlattice peaks diminish, where at the highest Split, no superlattice peaks are observed, implying the complete removal of long-range periodicity from the structure. It is interesting to note that as the Split is increased from 0 (periodic) to '2m + 1', the density of diffracted peaks near the Bragg peak, $SL_{(0)}$ (002), increases significantly, with the intensity of $SL_{(0)}$ (002) Bragg peak in aperiodic superlattices lower than the corresponding periodic superlattice. Similar XRD trends were observed for aperiodic superlattices with different average interface densities (for example, ASLs for average interface density of 0.65 nm^{-1} is shown earlier Figure 2.12), confirming the similar effect of disorder on the structural periodicity of the aperiodic sequence, which is independent of the average interface density. This indicates the versatility of this method in controllably changing the degree of disorder in an aperiodic structure.

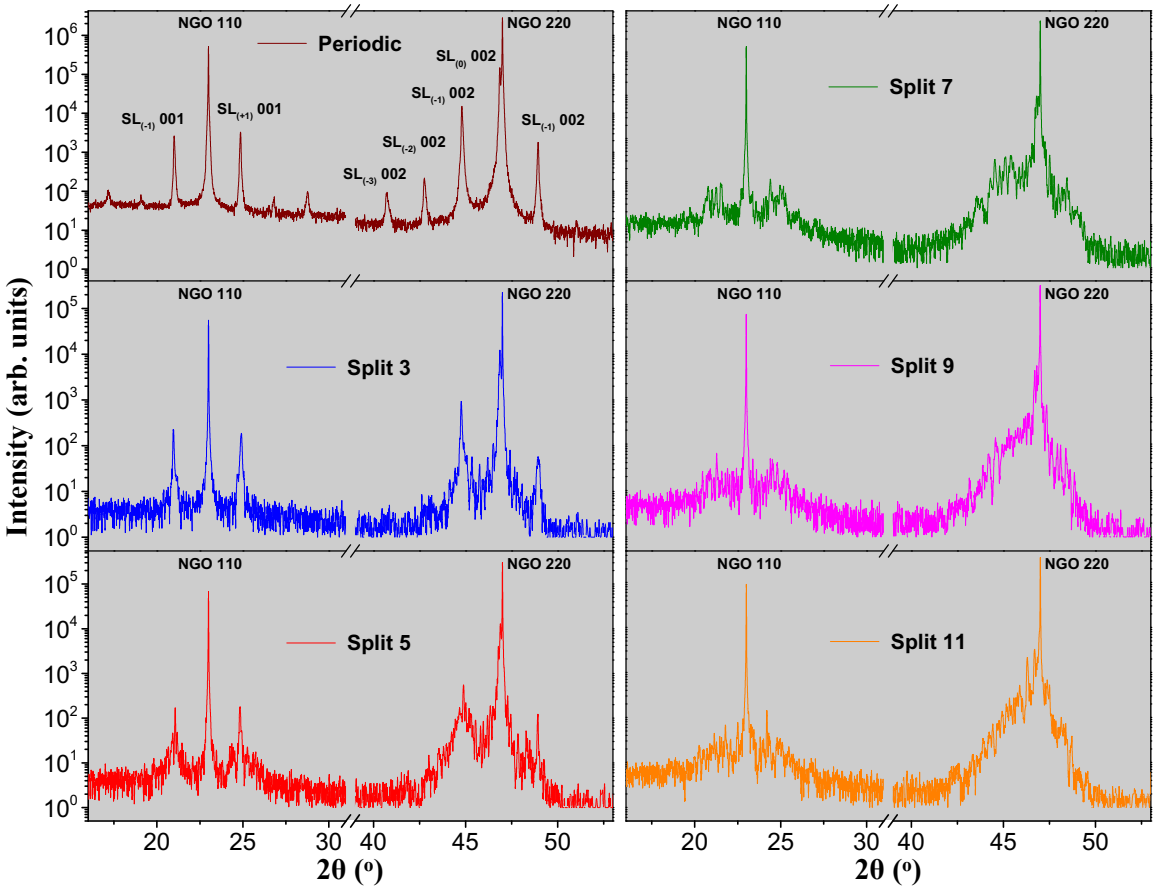

Figure 4.22: Evolution of structural order in aperiodic superlattice films with average interface density equal to 0.43 nm^{-1}.

Reciprocal space maps (RSMs) ensure that the change in the structural order has minimal impact on the strain state of the aperiodic superlattices. Figure 4.23 shows the RSM of an aperiodic superlattice with an average interface density of 0.43 nm^{-1} for Split 7. As apparent from this reciprocal space map, the 200 nm aperiodic superlattice film is strained to the NGO substrate. Note that RSMs of ASLs showed a spread of peaks as opposed to periodic superlattices where in the latter clear superlattice peaks can be identified in their RSMs (Figure 2.17). This spread is related to the additional peaks observed around the Bragg peaks (002 or 001) corresponding to 50:50 alloy composition of STO and CTO present in aperiodic superlattices. All other aperiodic superlattices were also found to be strained to the substrates, eliminating any spurious effects of strain relaxation on the thermal conductivity measurement of these aperiodic superlattices.

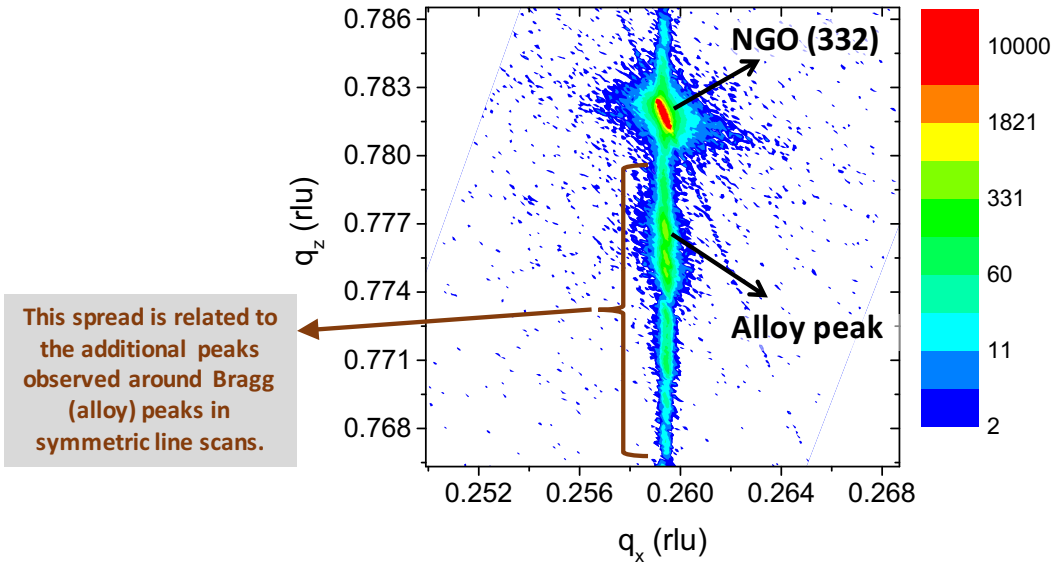

Figure 4.23: Reciprocal space map of an aperiodic superlattice film with an average interface density of 0.43 nm^{-1} and Split 7.

Atomic Force Microscopy (AFM) was also performed on these aperiodic superlattices to confirm the smoothness and layer-by-layer growth of STO and CTO. Figure 4.24 shows a representative surface topography of 200 nm thick aperiodic superlattice grown on STO (001) substrate, where atomic steps are clearly visible. This further supports the accurate layer-by-layer deposition of random layers of STO and CTO, achieved via *in situ* monitoring using RHEED up to films of 200 nm thickness.

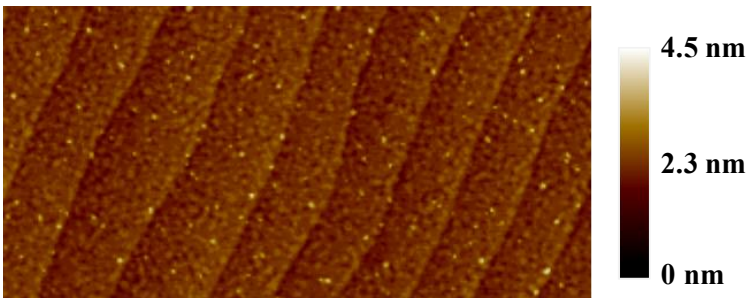

Figure 4.24: AFM (flattened) image of aperiodic superlattice film with an average interface density of 1.29 nm^{-1} and Split 3 grown on STO (001) substrate is shown.

The thermal conductivities of aperiodic superlattices, measured at 175K, with varying average interface density from 1.29 nm^{-1} to 0.1 nm^{-1} and varying splits from '3' to '$2m + 1$' are shown in Figure 4.25. On the other hand, Figure 4.26 illustrates the effect of increasing disorder on the thermal conductivity of aperiodic superlattices for a given value of average interface density. The thermal conductivities of the periodic superlattices,

shown most clearly in Figure 4.25, are as shown in previous section, where I've examined the minimum in the thermal conductivity trends as a function of period thickness using a modified version of the theory of Simkin and Mahan (SM model). The rough qualitative conclusion of the SM model is that there is a crossover from a coherent regime for high interface density to an incoherent regime for low interface density based on the coherence length scale compared to the interface spacing. According to the SM model, in the coherent regime, increasing spacing between interfaces lowers the thermal conductivity due to mini-bad formation in the phonon dispersion curve, whereas in the incoherent regime, increasing spacing between interfaces simply lowers the number of scattering events, therefore increasing the thermal conductivity. The claimed crossover from coherent to incoherent phonon transport then explains the observed minimum of thermal conductivity in the periodic superlattices.

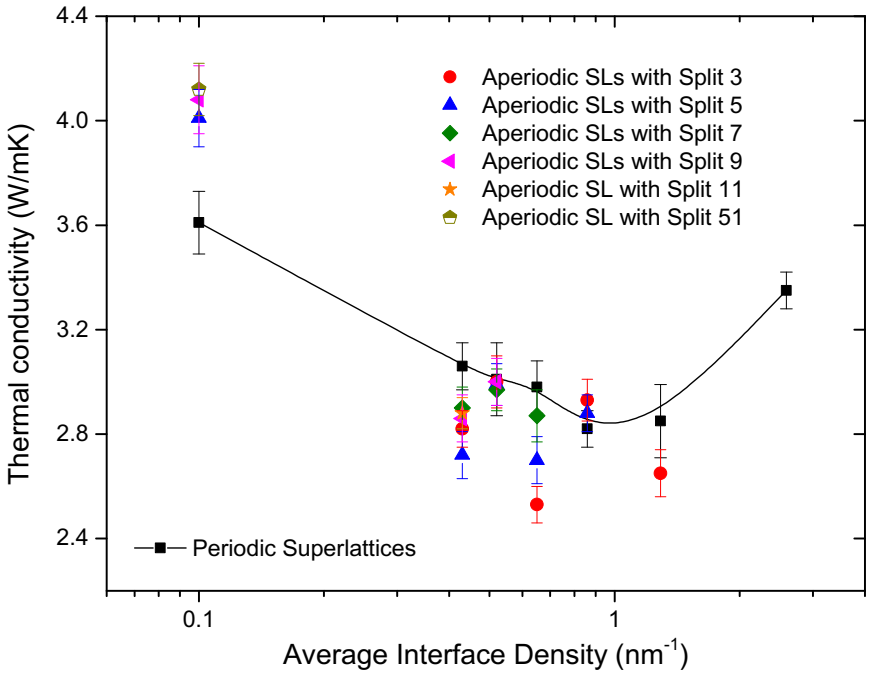

Figure 4.25: Thermal conductivity of aperiodic superlattice as a function of average interface density for different Splits.

Periodic superlattice with interface density of 1.29 nm^{-1} lies in the regime of phonon transport where the behavior of phonons across the STO-CTO interfaces is coherent in nature. When the disorder is added at this average interface density, one would expect coherence in phonon scattering to be destroyed, caused by randomization of the position of interfaces, and hence, will result in reduction in thermal conductivity of the structure. This is exactly what I've observed experimentally in the aperiodic superlattice with average interface density of 1.29 nm^{-1}, which showed lower value than corresponding reference periodic superlattice (Figure 4.25). However, for average interfaces densities, which lie in the incoherent regime of phonon transport, it is not apparent as to how the addition of

disorder and further increase of disorder (at fixed value of average interface density) would affect the phonon propagation through the structure and hence will affect the thermal conductivity. As will be discussed next, I'll show that coherent transport is of critical importance even in the supposedly *incoherent* regime, characterized by the interface density of the periodic superlattice.

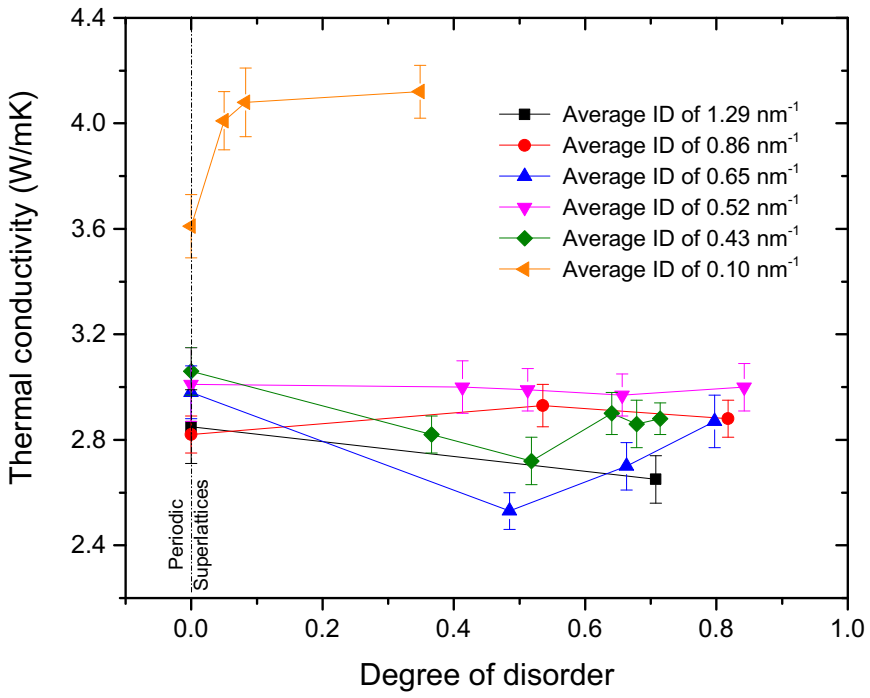

Figure 4.26: Thermal conductivity of aperiodic superlattices as a function of degree of disorder (local ID distribution width) at a given average interface density.

In the case of purely incoherent transport, the two major sources of scattering are interface scattering and intrinsic phonon scattering mechanisms in the CTO or STO layers, neither of which will change, on average, if we change the locations of the interfaces without changing the average interface density. Based on this, one would expect that purely incoherent transport would lead to no dependence on disorder in our measurements. Our measurements, however, indicate a dependence of thermal conductivity on disorder in the regime corresponding to the incoherent regime in the periodic superlattices, and show that the thermal conductivity of a ASL can be lower than its corresponding periodic superlattice, which is consistent with molecular dynamics-based trends indicating the existence of localized coherent phonon modes [315]. Along these lines, Figure 4.26 reveals several surprising results that requires explanation: (a) the thermal conductivity of aperiodic superlattice corresponding to 0.86 nm^{-1} interface density increases when disorder is added, (b) in the aperiodic superlattice corresponding to 0.65 nm^{-1} and 0.43 nm^{-1}, thermal conductivity first decreases and then increases again with increasing disorder, and (c) in the aperiodic superlattice corresponding to 0.52 nm^{-1}, thermal conductivity does not depend

on disorder beyond the experimental error bar. These results are sufficiently surprising that it is tempting to think they may depend on specific realizations of disorder; however, I have measured thermal conductivity of four different aperiodic sequences with interface density of 1.29 nm^{-1}, each of which has the same disorder according to our measure of disorder described below, and thermal conductivities were found to be same within experimental uncertainties. It is thus likely that surprising behavior of thermal conductivity is an effect of disorder strength or the presence of coherent effects in the supposedly incoherent regime rather than the particular manifestation of the disorder.

Next, our goal is to explain this behavior, qualitatively and with some quantitative support. First, I will define what is meant by "disorder," and then a quasi-incoherent model will be presented that captures some features of the data and further highlights the importance of coherent effects. To understand these effects better, I will present another model and finally, summarize our conclusions.

4.4.3.1 Measure of Disorder

The amount of disorder present in an aperiodic superlattice is related to the Split, which depends on the given average interface density. As discussed in the previous section, Split '*s*' of '*n* x *n*' means each layer of the aperiodic sequence has an equal probability of having each integer thickness (in unit cells) in the range '$n - (s-1)/2$' to '$n + (s-1)/2$', giving '*s*' different layering thicknesses in total. It seems intuitively reasonable that increasing splitting, '*s*', is equivalent to an increase in disorder since the thickness of a given layer becomes less predictable. In other words, we can define several notions of disorder and see how the splitting number corresponds to each one.

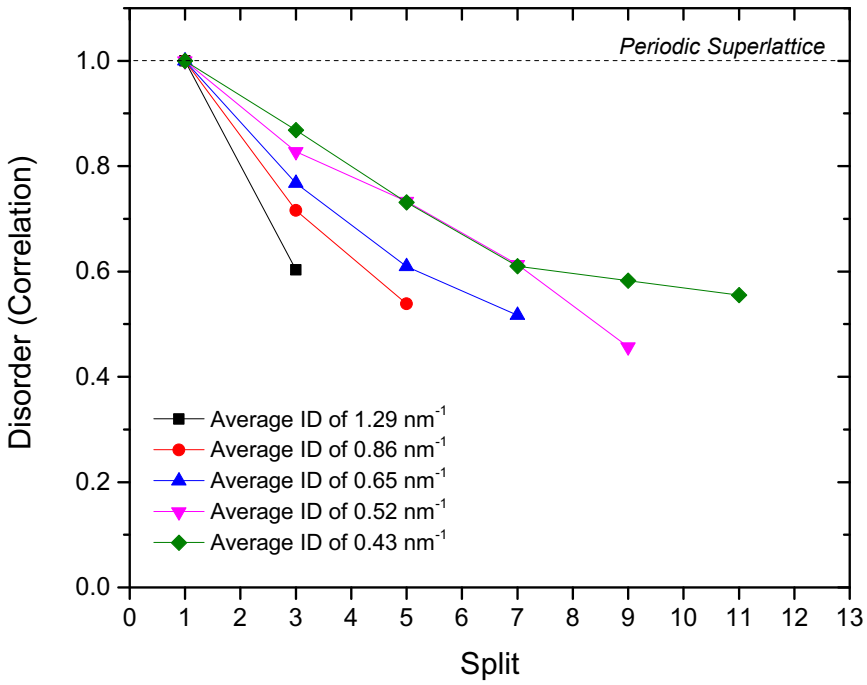

Figure 4.27: Degree of disorder calculated from the correlation function as a function of Split for various average interface density aperiodic superlattices.

One very natural measure of order in any system is a correlation function. For an 'n x n' periodic superlattice, any two layers separated by '$2(n \times a_{STO} + n \times a_{CTO})$', where '$a_{STO}$' and '$a_{CTO}$' are the lattice constants of STO and CTO respectively, will both be the same material, either STO or CTO. Thus we can define a correlation function as follows: for each pair of layers separated by '$2(n \times a_{STO} + n \times a_{CTO})$', if the layers are the same assign the value 1, else 0; then take the spatial average over all such pairs. Each periodic superlattice gives the value 1, corresponding to long-range order. Increasing the splitting leads to increasing disorder by this measure, as shown in Figure 4.27, which corroborates our initial claim of controlling disorder through the use of different Splits for a particular value of average interface density. We can also evaluate the consistency of this measure by applying it to the four different aperiodic sequences measured for average interface density of 1.29 nm^{-1}. This gives values from 0.5630 to 0.5970, indicating a high degree of consistency.

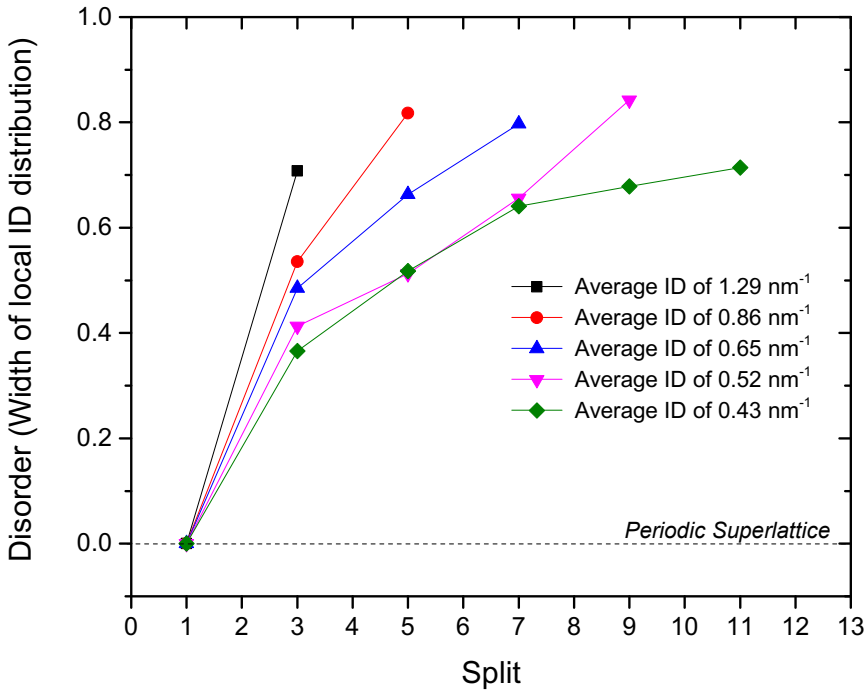

Figure 4.28: Degree of disorder calculated from the local interface density distribution, as a function of Split for various average interface density aperiodic superlattices.

Another measure of degree of disorder that correctly reports no disorder in the periodic case is the distribution of local interface densities across the whole structure. For an '*n* x *n*' periodic superlattice, we first find the local interface density for each (overlapping) segment of length '2(*n* x a_{STO} + *n* x a_{CTO})', and then use the width of the distribution of the local densities as the measure of disorder. This measure is also strictly increasing with splitting, as shown in Figure 4.28. Again applying the measure to all four different sequences of aperiodic superlattice with 1.29 nm^{-1} as the interface density, we get values from 0.6942 to 0.7131, once more indicating that splitting number is well correlated with real disorder present in the structure. Since both measures of "real disorder" correlate strongly with the splitting number, we can safely use that value as a proxy for the amount of disorder and will do so for the remainder of our analysis.

4.4.3.2 Quasi-incoherent model

As discussed above, a purely incoherent model cannot explain the trend in the thermal conductivity observed in Figure 4.26. This suggests the presence of coherent effects in the supposedly incoherent regime. It is unlikely, however, that transport could be coherent across the entire film thickness (200 nm) [267; 316]. Instead, we can look for coherent effects only on some length scale L_theta (< 200 nm), and then add the conductivities classically, using the standard equation: $(k_eff)^{-1} = \langle (k_local)^{-1} \rangle$.

To use this model, we must make two choices. First, we must choose the length scale L_theta on which we consider coherent effects. Second, we must choose how to evaluate the conductivity of each region of length L_theta. In this case we will consider the simplest model that incorporates any coherent effects – namely, in each region of length L_theta, we find the local interface density and assume that the conductivity of the region is the same as that of the periodic superlattice with the same interface density (with some interpolation for intermediate values). For example, a layering pattern AABBAABB within an aperiodic structure would be assumed to have a conductivity corresponding to a '2 x 2' periodic superlattice even if the overall interface density of the whole aperiodic sequence corresponds to a value different from the global interface density of the 2 x 2 periodic SL. This model captures the coherent effects that are present in the periodic superlattices and the incoherent effects of disorder. However, this approach ignores the coherent effects of disorder.

We can immediately draw some qualitative conclusions. First, this analysis predicts that thermal conductivity of the aperiodic superlattice with 0.86 nm^{-1} average interface density, will increase when disorder is added, as all other periodic superlattices have higher thermal conductivity. This partially explains the first of the surprising features we observed in the thermal data (Figure 4.26). For other aperiodic superlattices, the rough prediction is that thermal conductivity will tend to move towards that of a superlattice with lower interface density, since the effective overall thermal conductivity is a spatial average, and thus thicker layers (lower interface density) are overrepresented. In general, this implies that thermal conductivity of an aperiodic superlattice corresponding to average interface density of 1.29 nm^{-1} could be expected to decrease, while that corresponding to 0.65 nm^{-1}, 0.52 nm^{-1}, and 0.43 nm^{-1}, would exhibit a slight increase in thermal conductivity with disorder.

Quantitatively, however, some of these rough predictions fail. In particular, because the difference between the thermal conductivities of periodic '1 x 1' and '2 x 2' is much greater than that between '2 x 2' and '3 x 3', the thermal conductivity of 1.29 nm^{-1} aperiodic superlattice is actually predicted to increase with disorder. The precise results of these calculations are given in Figure 4.29, with the following details: (a) L_theta = 8 layers, linear interpolation; (b) L_theta = 8 layers, cubic interpolation; and (c) L_theta = 2*n* layers ('*n*' corresponds to '*n* x *n*' periodic superlattice), linear interpolation. These go to both extremes of assuming that L_theta does not depend on the average interface density at all and that it has no constant portion. Based on analyses of the mean free path in our previous paper, the former is a better approximation. L_theta = 8 was chosen because it is the order of magnitude corresponding to the period of the superlattice at the coherent – incoherent crossover. Other choices of L_theta at the same order of magnitude do not show significantly different results.

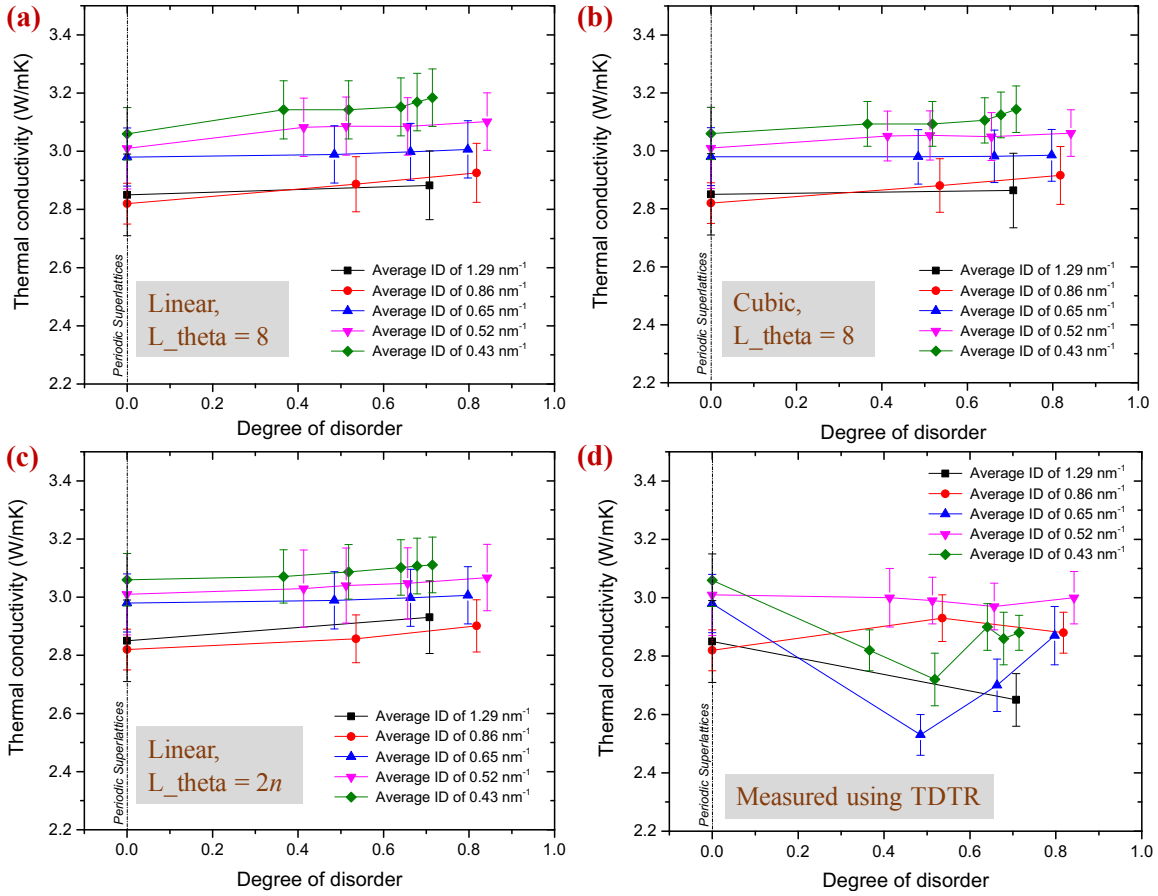

Figure 4.29: Thermal conductivity of aperiodic superlattices predicted using Quasi-incoherent model with L_theta value of (a) L_theta = 8, Linear Interpolation, (b) L_theta = 8, Cubic Interpolation, (c) L_theta = 2*n*, Linear Interpolation superlattices; (d) measured using TDTR.

The biggest flaw with this model is also the most interesting conclusion that we can draw from it: since it roughly captures all effects except for the coherent effects of disorder and simultaneously fails to describe the most interesting behavior observed in Figure 4.26, we are forced to conclude that the undescribed behavior does in fact arise from the effect of disorder on coherent phonon transport. More importantly, since we find 'k_eff' by an average of local thermal conductivities, each of which is no smaller than minimum thermal conductivity, we can never find an effective thermal conductivity below that value, whereas the experimental values show lower thermal conductivities in some of the aperiodic superlattices corresponding to average interface density of 0.43 nm^{-1}, 0.65 nm^{-1}, and 1.29 nm^{-1}.

4.4.3.3 Coherent Effects

As it is almost certainly the case that we only need to treat coherent effects on a short length scale and then can add the resulting conductivities semi-classically, we could simply try to improve our computation of the local thermal conductivity. Indeed, coherent effects of disorder have been convincingly demonstrated in small systems by several authors in recent publications using the technique of Molecular Dynamics simulations [310], with disorder suppressing conductivity by as much as 17%.

In order to capture the coherent effects of disorder, we can combine several different approaches to at least qualitatively explain the data. We begin by performing a calculation that assumes completely coherent transport. We apply the method described; as in the SM model [274], we consider the crystal as a system of masses with spring-type forces between them, and we find the transmission and reflection coefficients for an incoming phonon-wave at varying frequencies. From these data, we can calculate the "coherent thermal conductivity." To calculate the thermal conductivity [274]:

$$K(T) = \sum_{\lambda} \int \frac{d^d k}{(2\pi)^d} \, \hbar\omega_\lambda(k) |v_z(k)| \ell_\lambda(k) \, \frac{\partial n(\omega, T)}{\partial T} \tag{4.58}$$

, where 'λ' is the band index, '$v(k)$' the group velocity, 'ℓ' the mean free path, and 'n' the Bose-Einstein (BE) distribution. In the limit of high temperature and constant *mfp*, this reduces to:

$$K_\ell(T) = k_B(\ell) \sum_{\lambda} \int \frac{d^d k}{(2\pi)^d} \, |v_z(k)| \tag{4.59}$$

This formula assumed perfect transmission of each phonon described by the BE distribution, so to get thermal conductivity in our case, we can simply integrate the transmissions corresponding to each frequency. The results of this calculation are shown in Figure 4.30. Furthermore, while this calculation is moderately time-consuming, the predicted coherent conductivity scales very well with the interface density measure of disorder, as shown in Figure 4.30(a). Thus that very quick calculation can potentially be used in the future to estimate fully coherent thermal conductivities. Unfortunately, we have still failed to capture the effect that the conductivity increases again as disorder continues to increase as in the case of 0.65 nm^{-1} and 0.43 nm^{-1} interface densities. One possibility is that more weight should be given to phonons at low wave vector, since high wave vector phonons are more particle-like, due to scattering from thermal fluctuations, interdiffusion at the interface *etc.*, and thus more likely to lose coherence. If we follow this idea and integrate transmission as a function of frequency only up to some cutoff value, we do begin to see thermal conductivity increasing as the disorder continues to increase. This is demonstrated in Figure 4.30 (b-c) for two different cut-off values.

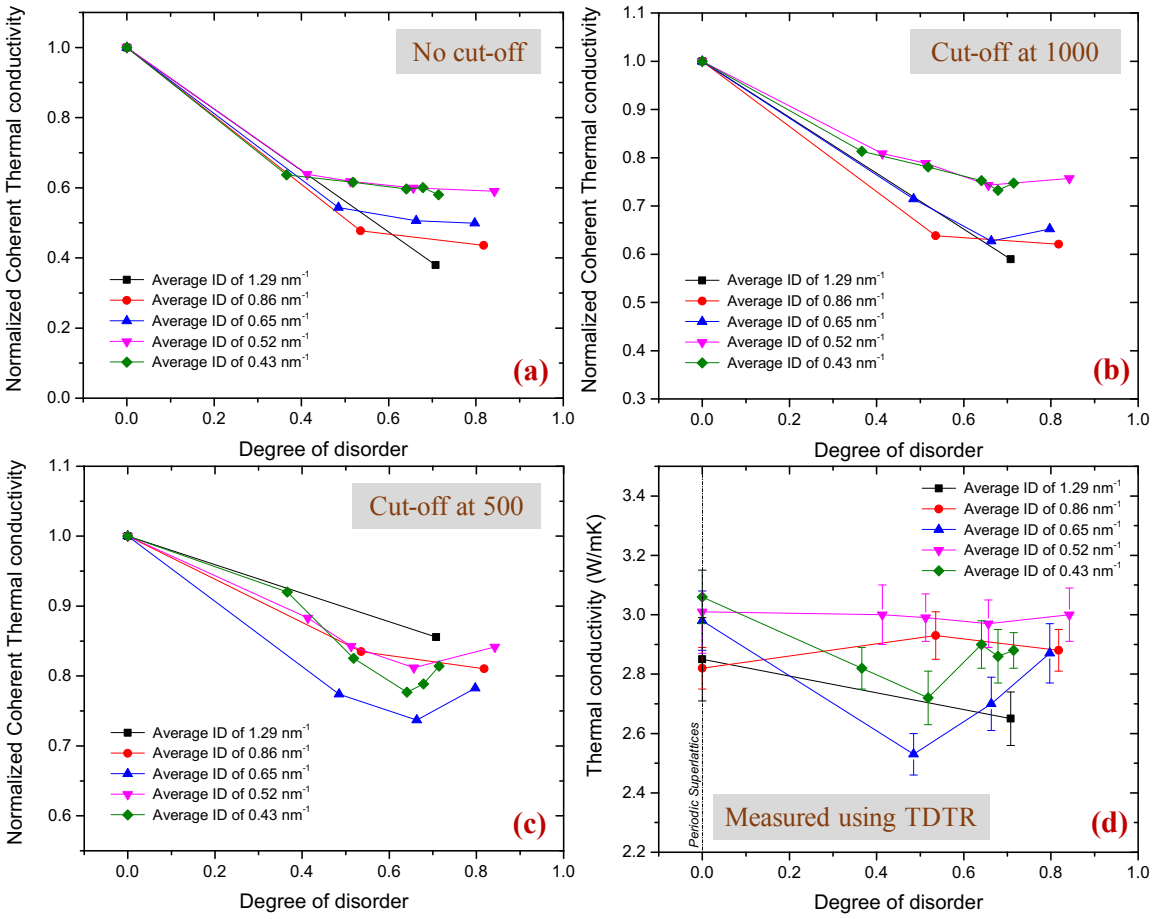

Figure 4.30: Normalized coherent thermal conductivity predicted for various aperiodic superlattices as a function of degree of Disorder with (a) no cut-off, and cut-off at (b) 1000, (c) 500. Normalization is done with respect to respective periodic superlattice; (d) Thermal conductivity of ASLs measured using TDTR.

Finally, I would like to explain the opposite trend observed in case of aperiodic superlattices corresponding to 0.1 nm^{-1}, where increasing the disorder first leads to increase in thermal conductivity and then saturates after certain degree of disorder. Both the quasi-incoherent calculation and the totally coherent calculation predict a conductivity that is essentially flat. Unfortunately, models discussed above does not explain this behavior of thermal conductivity with increasing disorder, and needs more sophisticated models which are currently the subject of investigation.

Our TDTR data on the thermal conductivity of aperiodic superlattices, Figure 4.27, presents several surprising features, which I have endeavored to explain. We first applied a quasi-incoherent model that estimated thermal conductivity of each small region of the aperiodic structure using the thermal conductivity of a periodic superlattice with equivalent interface density. I believe this model partially explains why the thermal conductivity of

0.86 nm^{-1} aperiodic superlattices increases, but it predicts relatively little change in thermal conductivity of aperiodic superlattices for other average interface densities. To explain the more interesting features, such as thermal conductivity of 0.65 nm^{-1} and 0.43 nm^{-1} aperiodic superlattices that initially decrease with disorder and then increases back again, we have considered several different approaches to coherent transport. I found that we could explain the observed features qualitatively, but if not quantitatively, by considering for which phonon wave-vectors coherent transport might be disallowed.

In summary, through the design of these aperiodic superlattices, not only I have shown that degree of disorder can be varied controllably, but also studied the effect of that controllable disorder on both the evolution of structural order in the system and the nature of phonon transport across a superlattice-like structure. Our work shows that both the local interface density in addition to global interface density, are equally important in manipulating phonon propagation across a multilayer structure. More importantly, evidence of coherent effects is observed in aperiodic superlattices for an average interface density, for which a periodic superlattice is found to be in the incoherent regime of phonon transport, in addition to an aperiodic superlattice whose average interface density lies completely in coherent regime of phonon transport.

4.5 Summary and future directions

In this chapter, I have discussed the observation of coherent scattering of phonons in superlattices and its effect on the thermal transport in superlattice films. I showed that the superlattice based on perovskite oxides (CTO, STO and BTO) proved to be a good model system to search for such coherent effects in phonons. STO-CTO system particularly, with both room temperature and low-temperature measurements, showed results in close agreement with the models predicting coherent phonon transport at short-period superlattices. These results show much stronger evidence of coherent phonon transport than recently reported ballistic-type phonon transport in a superlattice system [317].

The experimental findings of this work invite several immediate follow-up studies to further understand the coherent scattering of phonons in superlattice systems. The first parameter is increasing the strength of phonon reflection at the interfaces by choosing superlattice constituents that gives higher Acoustic Impedance Mismatch (AIM) between them. It has been predicted that increasing AIM results in much steeper decrease in thermal conductivity with interface density in the coherent regime, thereby resulting in deeper minimum observed in thermal conductivity trend (Figure 4.31). One viable option is substituting one component in the current superlattice system by, for example, $PbTiO_3$, which increases the AIM from 1.2 in $CaTiO_3$-$SrTiO_3$ to 1.88 in $CaTiO_3$-$PbTiO_3$. Such $PbTiO_3$-based superlattice systems would be a suitable candidate to study effect of increased AIM on coherent regime of phonon transport.

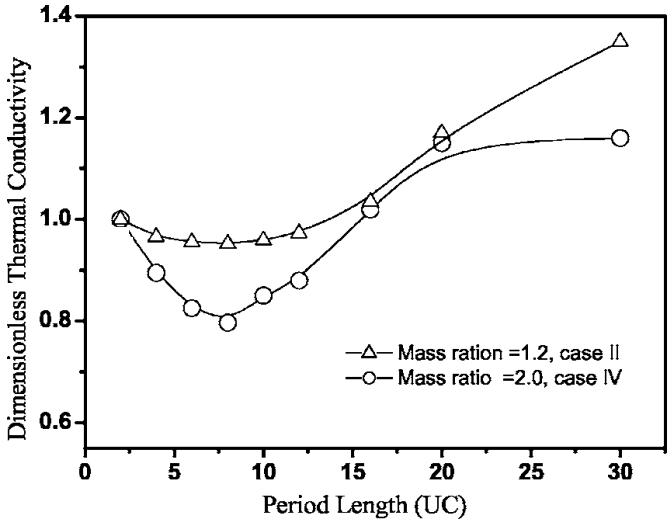

Figure 4.31: Normalized thermal conductivity as a function of superlattice period for two different mass ratio of superlattice constituents. From [275].

Second, is the phonon propagation in different crystallographic directions, for ex. superlattices oriented along [110], [111] directions, and their effect on coherent scattering of phonons at the superlattice interfaces, and finally their effect on measured thermal conductivity across the superlattice interfaces. Last, would be to study the coherent scattering at multiple interfaces in higher-order superlattice systems such as A – B – C (tri-color) superlattice whose one example could be CTO – STO – BTO, and A – B – C – D (quad-color) superlattice whose one example could be CTO – STO – BTO – PTO. Such higher-order superlattice structures adds more degrees of freedom to study coherent scattering of phonons in many possible superlattice sequences for the same average interface density of the structure.

After realization of coherent scattering of phonons at superlattice interfaces, immediate follow-up study would be to utilize coherent scattering in achieving other phonon wave interference effects on thermal conductivity. For instance, broadband localization of phonons in a crystalline structure using such correlated scattering of phonons, would be very promising for applications where extremely low thermal conductivity is required without compromising much on the electronic transport such as thermoelectric devices [237] *etc.* Although phonon localization in amorphous solids has been discussed at great length in literature [318-321], only theoretical studies have reported such wave effects in scattering of phonons in crystalline structures [183; 311-313; 322]. A number of theoretical studies has proposed phonon localization behavior in superlattice-like structures, for example, quasi-periodic structures [183; 322], aperiodic structures [312; 313; 323; 324], and artificially designed super cell [311]. A complete destructive interference of phonons, which carry majority of heat propagating through the superlattice structure, can result into significant localization of phonons leading to extremely low values of thermal conductivity in crystalline materials. With the capability to synthesize

superlattice systems with high quality interfaces in an optimally designed superlattice structure and with the presence of coherent scattering of phonon, localization of broadband of phonons is potentially realizable using optimized material parameters. Lastly, the effect of phonon wave interference on macroscopic properties motivates number of other studies where wave nature of phonon is crucial to the observation of phenomenon such as phonon filtering [258; 264] and phonon waveguides [325] in search for extremely low and high values of thermal conductivity respectively. The utilization of wave nature of phonons in manipulating heat flow in material systems can have enormous impact on thermal management, energy conversion and storage.

Chapter 5

Observation of Polarization Vortices in $PbTiO_3$-$SrTiO_3$ Superlattices

This chapter provides a second example of how artificially designed structures can enable observation of novel phenomenon in a subject of interest, which is not found in the bulk form. More specifically, I will present results on experimental observation of non-uniform polarization states such as Vortex-Antivortex structures, which has only been discussed in theoretical studies. The experimental evidence of long-standing theoretical predictions of such novel states in nanostructures, further supports the claim that superlattice structures has enormous potential in expanding the reach of material systems by utilizing various interacting degrees of freedom present within a material.

5.1 Introduction

Ferroelectricity has been a subject of intense research for past fifty years [326-328] or more because of its widespread application across various industries [329-333]. These existing applications are possible due to variety of physical properties exhibited by the ferroelectric materials. Such an important class of materials is known to exhibit properties such as piezoelectricity, pyroelectricity, electro-optic property, strong dielectric behavior and ferroelectric property. Based on their piezoelectric property, ferroelectric materials have found applications in micro actuators for Micro-electro-mechanical systems (MEMS) devices [334], transducer and sensors for submarines [335], piezoelectric gas igniters [336; 337] *etc.*, to name a few among its many applications across various industries. Based on pyroelectric behavior, ferroelectric materials have found applications in infrared thermal imaging [338], temperature sensors [339], intruder alarms [340] *etc.* Similarly, dielectric behavior of ferroelectric materials has found applications in DRAMs (based on their high dielectric constants) [341], in RF/microwave applications such as RF-tune and –filter [342], phase shifter in phased-array antennas for radar [343; 344] *etc.* Ferroelectric materials are also known to exhibit Electro-optic property, which has found applications in laser Q-switches [345], in optical shutters (tuning/altering amplitude, phase, frequency and propagation direction of light) [346], and in Holographic memory storage, which use photorefractive property of electro-optic materials [347; 348]. Lastly, ferroelectric

properties, *i.e.* possessing electrically-switchable spontaneous polarization, have found application in memory devices such as non-volatile Ferroelectric Random Access Memory (NFERAM) [349], Smart card or smart tags [349-351] *etc.*, and very recently they have showed potential to reduce the operating voltages of nanoscale devices such as ferroelectric-based Field-effect Transistors [352]. These examples clearly emphasize the importance of ferroelectric materials as being the key material in various technologies [353].

Ferroelectric materials can be synthesized in various forms, for example, in bulk form such as single crystal and polycrystalline [354], in 2D structures such as thin-films [355], in 1D structures such as nanowires [356] and nanotubes [357] *etc.* In bulk form, ferroelectric materials have been investigated intensively using both experimentally and theoretically. As a result, mechanism behind ferroelectric behavior, piezoelectric behavior, pyroelectric behavior *etc.*, in both simple systems such as BTO, PTO, $BiFeO_3$ *etc.* and solid solutions such as $PbZr_xTi_{1-x}O_3$ (PZT), $PbMg_xNb_{1-x}O_3$ (PMN) *etc.* have been studied and understood reasonably well [358-363]. These studies have led to several existing applications of these materials as discussed above. The solid solutions in particular have shown exceptionally high values of piezoelectric and dielectric constant owing to the discovery of morphotropic phase boundary (MPB) [364], which corresponds to a certain range of composition ('*x*') in the phase diagram where more than one phase coexists (such as tetragonal and rhombohedral in PZT). Such materials are anticipated to find applications in next generation piezoelectric devices [365].

In low-dimensional ferroelectrics such as thin-films (superlattices, heterostructures), nanowires, nanotubes, nanodots, however, ferroelectric behavior is not well understood as compared to bulk ferroelectrics. For example, the effect of reduced dimensions (down to few nanometers) on phase transition temperature, ferroelectric switching dynamics, polarization distributions *etc.*, is currently being investigated [366-368]. More detailed studies from both theoretical and experimental sides is needed to improve our understanding of ferroelectric behavior in nanostructures as they hold great promise for development of next generation devices. For example, nanoactuators for micro-electro-mechanical systems [369], integrated structures of ferroelectrics and semiconductors for development of next generation gate dielectrics for computer and tunable microwave devices [330; 368], non-volatile ferroelectric memories whose improvement in performance critically depends on the lower limits of ferroelectric film thickness [370]. Such great technological promises arise from the fact that nanostructured ferroelectric systems can enable geometries which can significantly alter the interactions between various fields leading to stabilization of new ferroelectric phases which are not present in bulk form [371-374]. More specifically, nanostructures can have significantly higher density of surface and/or interfaces which can dramatically affect the long-range dipole-dipole Coulomb interactions. It can also strongly affect the electrostrictive coupling due to change in mechanical boundary conditions owing to large increase in surface to volume ratio present in nanostructures. Lastly, the presence of strong depolarization fields, arising from the uncompensated bound surface charges, can interact so strongly with the ferroelectric order parameter that it can lead to complete suppression of ferroelectricity in the material [371]. The effect of reduced dimensions on ferroelectric behavior becomes

more apparent when case of simple single layer thin-films of ferroelectric materials is considered. For example, phase diagrams of thin-film ferroelectric materials may have additional parameters such as substrate-type (lattice constant, orientation), terminating layer of the film, thickness of the film, in addition to standard variable such as temperature and composition of the film [355]. Moreover, a large number of theoretical studies in ferroelectric nanostructures such as nanodisc and nanorods [371], superlattices composed of solid solutions ($Ba_{0.8}Sr_{0.2}TiO_3$-$Ba_{0.2}Sr_{0.8}TiO_3$ [375], $Pb(Zr_xTi_{1-x})O_3$-$Pb(Zr_yTi_{1-y})O_3$) [376], quantum dots and nanowires of PTO and BTO [377-379] *etc.*, have been done predicting number of unique properties which are absent in their bulk counterparts. Thus, it is anticipated that nanostructured ferroelectrics are likely to show various novel phenomenon enabling development of next generation devices for memories, sensors, actuators, and new functional devices.

One such example, which is drawing lot of attention in nanoscale ferroelectrics, is the novel polarization structure called as dipolar vortices or simply polarization vortices. The existence of vortex structures in low dimensional ferroelectric structure such as nanorods or nanodiscs have been predicted more than a decade ago [371]. And, since then many other theoretical studies have followed predicting the response of these vortex states to external fields such as electric field and their dependence on external parameters such as size and/or geometry of nanostructured system [372; 373; 380; 381]. Much interest in these novel polarization structures is due to its potential in achieving extremely high density of memory storage in non-volatile Ferroelectric RAMs (NFERAMs) [382]. It has been predicted that NFERAM based on these vortex structures can potentially have memory storage with density as high as 60 Terabits per square inch [369; 371] (which is higher than currently achievable with magnetic storage, *i.e.* 1.34 Terabits per square inch [17]). It has been discussed at great length that if the chirality of these vortex states (clockwise vs anticlockwise rotation), *i.e.* toroid moment of the vortex can be switched, it will open up the possibility of next generation "wunderbar" devices such as nanomemory, nanotransducers, nanosensors, nanomotors, nanoswitchers *etc.* [383].

Despite such long-standing predictions of vortex polarization states in low-dimensional ferroelectric nanostructures, experimental evidence to show their unequivocal existence remains largely missing. In this chapter, I will discuss experimental results, which will show the formation of such polarization vortices in ferroelectric layers of paraelectric/superlattice (*i.e.* PTO-STO) superlattice. The experimental studies presented here also discusses the evolution of dipolar vortices with layer thickness of PTO in superlattices of PTO/STO. This work further invites experimental investigations aimed at controlling the toroidal moment of these vortices by external stimuli for they're potential in novel applications discussed above.

In the following sections, I will first provide fundamentals of ferroelectricity followed by a discussion on various theoretical studies predicting polarization vortices in low-dimensional ferroelectric structures. Then, a detailed account of experiments employed to stabilize and observe such novel polarization distributions, is discussed. Finally, implications of the finding of dipolar vortices from both fundamental and technological perspective are discussed.

5.2 Theoretical predictions of Polarization Vortices in Ferroelectric Nanostructures

5.2.1 Fundamentals of Ferroelectricity

5.2.1.1 Definitions

Ferroelectricity is a property of a class of materials, which below certain temperature possess two, or more thermodynamically stable (or metastable) states in which the material has net non-zero electrical polarization under zero external electric field. This non-vanishing electrical polarization is commonly known as "spontaneous polarization" (P_s) of the ferroelectric material. Those states possessing (different) spontaneous polarization if can be switched from one state to another by the application of an electric field then only it's called a ferroelectric material [327]. The characteristics of the individual parameters involved in a ferroelectric property such as magnitude of spontaneous polarization, electric field needed to switch from one polarization state to another (also known as coercive field) and many others, further classify different types of ferroelectric behavior found in materials, and will be discussed in detail later. But, first we will discuss the crystallographic nature of ferroelectric behavior found in materials [327].

Crystals can be divided into 32-point groups whose dielectric behavior can be expressed as:

$$\boldsymbol{D}_i = \varepsilon_{ij}\, \boldsymbol{E}_j \tag{5.1}$$

, where 'D_i' is the dielectric displacement in the 'i' direction caused by the application of electric field ('E_j') in the 'j' direction, and 'ε_{ij}' is the dielectric (second-rank) tensor which is inherent property of the material (depends on the symmetry of the unit-cell, atoms constituting the unit-cell *etc.*). The unit of electric displacement is $\mu C/cm^2$. From these 32-point groups, 10 of them are centrosymmetric *i.e.* those possessing inversion symmetry and does not constitute the family of ferroelectric materials. The rest of the 21 point groups are noncentrosymmetric, *i.e.* those who do not possess have inversion symmetry, which except from one point group (*i.e.* 432), has at least one non-zero component of piezoelectric (third-rank) tensor (d_{ijk}) in the remaining 20 point groups. These 20 piezoelectric point groups allow the unit cell to show electric polarization when they are subjected to mechanical stress and conversely, obtaining expansion or contraction by subjecting to external electric field. These constitute the family of piezoelectric materials. In these piezoelectric materials, electric displacement can be writing as:

$$\boldsymbol{D}_i = \varepsilon_{ij}\, \boldsymbol{E}_j + d_{ik}\, \boldsymbol{Q}_k \tag{5.2}$$

, where 'd_{ik}' are piezoelectric coefficients (in Voight notation) and 'Q_k' is the mechanical stress field.

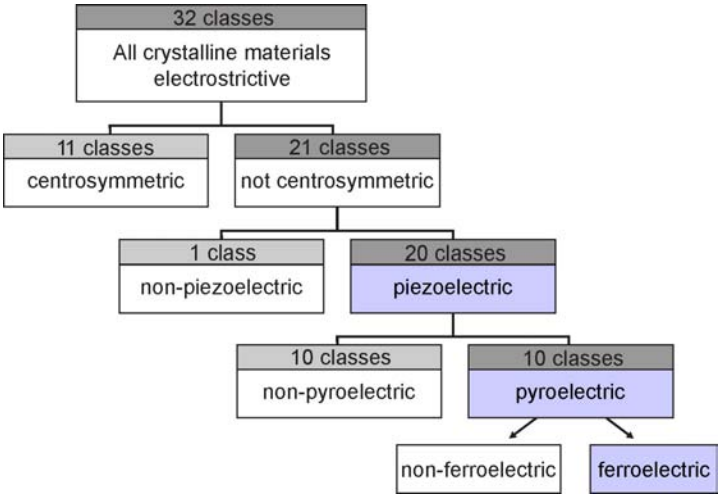

Figure 5.1: Classification of crystal classes based on their structure-property relationship. [384]

From these 20 noncentrosymmetric point groups, there are 10-point groups, which possess a unique polarization axis whose magnitude depends on the temperature field. These 10-point groups constitute the family of pyroelectric materials. If the crystal is subjected to external temperature gradient of magnitude 'ΔT', the electric displacement will have contribution from pyroelectric effects, and can be written as:

$$\boldsymbol{D}_i = \varepsilon_{ij}\,\boldsymbol{E}_j + d_{ik}\,\boldsymbol{Q}_k + p_i\,\Delta T \tag{5.3}$$

, where 'p_i' are pyroelectric coefficients. Those pyroelectric crystals, which have one or more stable states of non-zero polarization and can be switched from one to another by applying external electric field, will form the family of ferroelectric materials. The electric displacement in this case will have contribution from the spontaneous polarization (component in the '*i*' direction), *i.e.*,

$$\boldsymbol{D}_i = \varepsilon_{ij}\,\boldsymbol{E}_j + d_{ik}\,\boldsymbol{Q}_k + p_i\,\Delta T + (\boldsymbol{P}_s)_i \tag{5.4}$$

, where '$\boldsymbol{P}_s$' is the spontaneous polarization. Note that the units of electric displacement are same as the polarization, which is μC/cm^2. Thus the crystal symmetry is a key factor in observation of ferroelectric behavior (Figure 4.1) and will be discussed more later, where we will find that the mechanism leading to strong or weak ferroelectricity for the same crystal structures further depends on the atoms constituting the unit cell.

5.2.1.2 Hysteresis Loop

As discussed earlier, one of the requirements for the material to be ferroelectric is its ability to switch from one (meta)stable state to another by application of electric field. To experimentally verify whether a given material is ferroelectric or not, one has to perform polarization vs electric hysteresis measurement, where polarization as a function of external electric field is measured. A typical example of P-E hysteresis loop is shown in Figure 4.2, which demonstrates that polarization reversal is possible from spontaneous polarization '$-|\boldsymbol{P}_s|$' to '$|\boldsymbol{P}_s|$' with electric field. The hysteresis loop can be explained as follows: Starting from an polarized crystal where there is no external electric field (E = 0, point 'a' in the figure), distribution of polarization present within the material amounts to total of zero net polarization. For the case of very small electric field, the polarization will increase linearly with electric field as any normal dielectric, and if the electric field is removed polarization will go back to zero. But, if electric field is continued to increase its magnitude (curve 'A'), polarization will start to align along the electric field resulting into non-zero net polarization pointing along electric field, and eventually starts saturating beyond certain value. In order to reverse the polarization in the opposite direction, electric field in the opposite direction needs to be applied. But, first electric field is reduced to zero (indicated by curve 'B'), which reduces the polarization down to '$|\boldsymbol{P}_s|$', which is also referred to as spontaneous polarization. On further reducing the magnitude of electric field in the negative direction (indicated by curve 'C'), net polarization starts decreasing due to local polarization starts aligning along the direction of electric field. And, after decreasing the magnitude by certain amount, indicated by E_c, which is also, know as coercive field, the net polarization reverses the direction (from positive to negative). On further increasing the magnitude of electric field in negative direction leads to similar saturation of net polarization in the negative direction. Similar to before, when the external field is removed (indicated by curve 'D'), the materials are left in a state polarized with net polarization of $-|\boldsymbol{P}_s|$. One can again reverse this polarization state from $-|\boldsymbol{P}_s|$ to $|\boldsymbol{P}_s|$ by applying electric field in the opposite direction with magnitude more than coercive field (indicated by curve 'E').

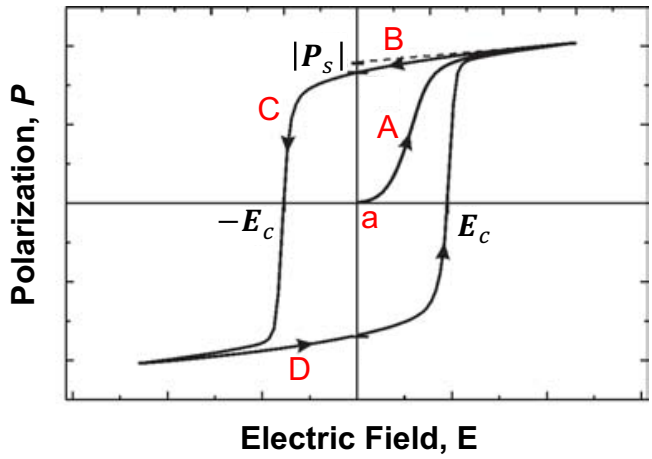

Figure 5.2: A schematic of Polarization-Electric field hysteresis loop is shown. [327]

Note that in practice, measurement of a P-E hysteresis loop requires making a device, usually a capacitor, which involves fabricating metal electrodes on either side of the material and may involve other parameters (such as electrode material, interface type/quality between electrode and ferroelectric) which come into play when performing the P-E measurement. And, sometimes these external factors may influence the electrical response from the device making it non-trivial to measure the intrinsic properties of the ferroelectric material [367]. Although hysteresis loops have been conventionnally used for establishing ferroelectric in a material, other technique such as PFM have also been utilized to characterize ferroelectricity in materials [158]. Finally, note that the ability of a ferroelectric material to retain non-zero spontaneous polarization under zero external electric field and to switch between two 'logic' states '-$|P_s|$' and '$|P_s|$', constitutes the basis of non-volatile and memory function respectively in application for non-volatile ferroelectric random access memory (NFERAM) [382].

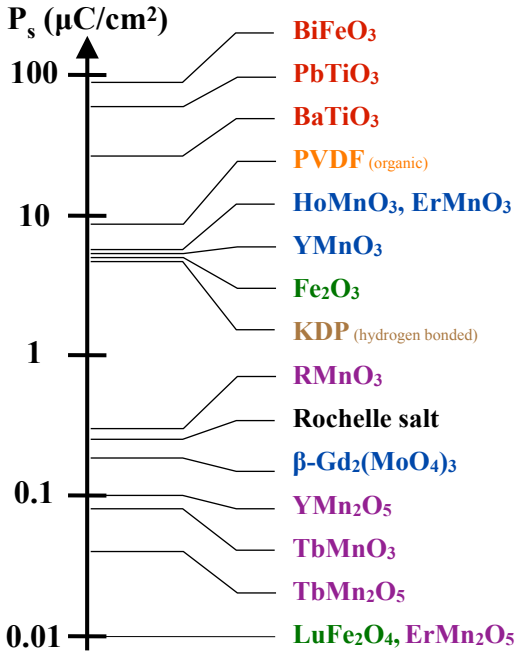

Figure 5.3: Spontaneous polarization of various ferroelectric materials is listed. From [367].

Based on these P-E hysteresis loops, spontaneous polarization of different class of ferroelectric materials have been measured and documented [367]. Figure 4.3 depicts spontaneous polarization of various types of ferroelectric materials. As can be seen from the figure, polarization values can vary over four orders of magnitude differentiating weak ferroelectric materials such $ErMn_2O_5$, $LuFe_2O_5$, from strong ferroelectric materials such as $BiFeO_3$, PTO. Further note that the list includes both inorganic (*e.g.* perovskites) and organic (*e.g.* PVDF) materials implying versatility of ferroelectric phenomenon in materials systems.

5.2.1.3 Ferroelectric Phase Transition

Usually in ferroelectric materials, when the temperature is increased beyond a critical value also called as Curie Temperature (T_c) there is a transition from the ferroelectric phase, which has many variants owing to the symmetry of the crystal, to a non-polar phase which has a single variant also called as Paraelectric phase. In the paraelectric phase, the spontaneous polarization goes to zero and the symmetry of this phase is higher than ferroelectric phase. Note that this paraelectric phase may not necessarily assume centrosymmetric crystal structure (for example $LiNbO_3$ whose high-symmetry paraelectric phase is rhombohedral). Also note the paraelectric phase is fundamentally different from dielectric phase, where in the former the electric permittivity

is a function of electric field, but in the latter it's constant. To explain the ferroelectric phase transition thermodynamically, we consider Devonshire-Ginzburg-Landau (DGL) phenomenological theory [367], which generally starts from identification of "order parameter" for the phase transition. Order parameter is a physical quantity such as polarization, which changes from a non-zero value in the ferroelectric phase to a zero value in the paraelectric phase. In this theoretical approach, free energy ('$\mathcal{F}(P)$') is represented as the Taylor series expansion of the order parameter and other variables close to phase transition temperature. For sake simplicity, we consider free energy expression with polarization as the order parameter assuming zero ground state energy of unpolarized crystal, which can be written as:

$$\mathcal{F}(P) = \frac{1}{2}\alpha_2 P^2 + \frac{1}{2}\alpha_4 P^4 + \frac{1}{2}\alpha_6 P^6 + .. \tag{5.5}$$

, where 'α_2', 'α_4', 'α_6' are expansion coefficients which are generally temperature-dependent but for a simple second order phase transition, we will consider 'α_4' and 'α_6' to be positive constant and 'α_2' to be linearly dependent on the temperature with a form: $\alpha_2 = C(T\text{-}T_c)$, with 'C' being a positive constant.

To minimize this free energy, we have to find values of 'P' for which $\frac{\partial \mathcal{F}}{\partial P} = 0$, *i.e.* minima's in free energy vs order parameter diagram. Note that this is the theoretical fingerprint of ferroelectric behavior in the material. The minimization of free energy will lead to:

$$\frac{\partial \mathcal{F}}{\partial P} = 0 \implies \alpha_2 P + \alpha_4 P^3 + \alpha_6 P^5 + .. = 0 \tag{5.6}$$

$$\implies P\,(\alpha_2 + \alpha_4 P^2 + \alpha_6 P^4 + ..) = 0 \tag{5.7}$$

$$\implies P\,(C(T - T_c) + \alpha_4 P^2 + \alpha_6 P^4 + ..) = 0 \tag{5.8}$$

For the case when $T > T_c$, only possible solution to above equation (5.8) is $P = 0$, at which free energy curve has the minima and this corresponds to non-polar paraelectric phase as described earlier. However, when $T < T_c$, there are more than one solution to equation (5.8), which implies there are non-zero values of P for which there exist one or more minima's in the free energy curve.

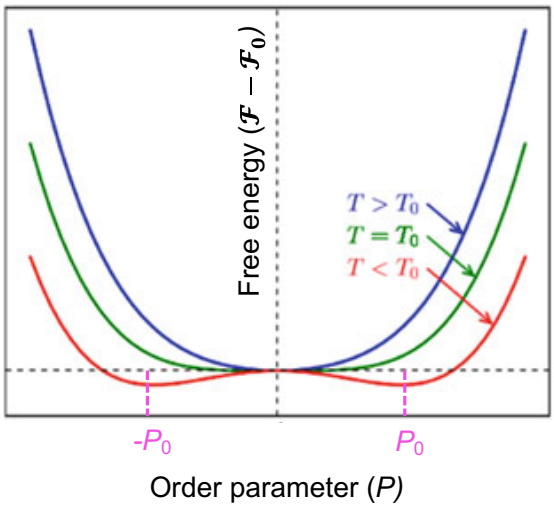

Figure 5.4: Ferroelectric phase transition described using Landau-Ginzburg-Devonshire theory. From [385].

To simplify the analysis, we ignore the higher order terms, *i.e.* 'α_6' or higher, and in which case the possible solutions to equation (5.8) would be:

$$P = \pm \sqrt{\frac{C(T_c - T)}{\alpha_4}} \tag{5.9}$$

This would result in double well in the free energy curve suggesting there are two non-zero 'P' values at which the system would be stable (Figure 4.4). These two non-zero values are generally related to the spontaneous polarization states ('-$|\boldsymbol{P}_s|$' and '$|\boldsymbol{P}_s|$') discussed earlier. Before we proceed further, it is important to mention the limitations of this phenomenological DGL theory. Although the coefficients of Taylor series expansion can be extracted by fitting to the experiments, this is approach is macroscopic and cannot be used to extract microscopic quantities such as atomic displacements associated with ferroelectric phase. Also note that the model is applied close to phase transition temperature, for the cases when temperature is far from T_c, additional care must be taken in applying this model. Thus, one has to do appropriate modifications in extending this method to length scales approaching few lattice constants (such as nanostructures), and to temperatures far from T_c. These obstacles are overcome by adopting other theoretical approaches such as First-principles or *ab-initio* simulations [367].

Let us take an example of such ferroelectric phase transition in a material system, which is widely studied (both experimentally and theoretically) such as PTO. The high-temperature paraelectric phase of PTO is cubic and it undergoes phase transition at 490°C to tetragonal low-symmetry ferroelectric phase. The spontaneous polarization is developed by atomic rearrangements of 'Pb', 'Ti' and 'O' atoms in the unit cell as illustrated in figure 5.5. The 'Pb' atoms and 'O' atoms move in a direction opposite to 'Ti' atoms. Due to

tetragonal symmetry along the '*c*' axis, two symmetry-equivalent polarization states exist, [001] and [00$\bar{1}$]. These two stable states corresponds to the '-$|\boldsymbol{P}_s|$' and '$|\boldsymbol{P}_s|$' spontaneous polarization states discussed above (see free energy vs polarization diagram, Figure 5.4). Note that the polar displacement of 'Pb', 'Ti' and 'O' atoms shown in Figure 5.5, driving the cubic phase to distort and form a tetragonal phase is the key for this material to show ferroelectricity. In general, such polar displacements of atoms in the unit cell during a phase transition results in 'small' distortion of the high-symmetry (paraelectric) phase breaking it to somewhat lower symmetry of the ferroelectric phase. This condition of requiring only 'small' distortion for the ferroelectric instability to occur is incredibly important and is the key reason for observed multiple stable states of different spontaneous polarization ($\pm\ |\boldsymbol{P}_s|$). Moreover, it also strongly affects the ability of the material to switch between these multivariant (stable) states under application of electric field, and thus, affecting ferroelectric parameters such 'P_s', 'T_c' *etc.* of the material. This important concept has been employed by several theoretical studies in developing other criteria for identifying ferroelectric instability in crystal structures [386; 387].

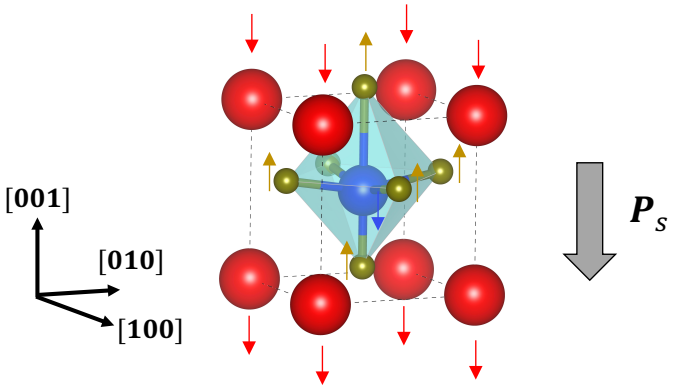

Figure 5.5: Ferroelectric distortion in a unit cell of PTO leading to a spontaneous polarization is shown.

We can again consider Landau approach to study other characteristics of the ferroelectric phase transitions. Using the same equation (5.5), *i.e.* polarization as the order parameter for describing free energy, one can derive that phase transition at $T < T_c$ (with $|T\text{-}T_c|$ being small) from paraelectric phase to ferroelectric phase is a second order phase transition with discontinuity in Polarization (P) and structural parameters (at T_c) [388]. Subsequently, one can also derive that the dielectric susceptibility at phase transition point ($T = T_c$) diverges to infinity. This divergence of dielectric susceptibility can be further used to determine the softening of phonon mode(s) [389; 390], which is one of key factors driving ferroelectric instability, using Lyddane-Sachs-Teller relation. The temperature dependent phonon spectroscopy has, thus, been employed immensely in studying ferroelectric phase transitions in materials [391] (a list of ferroelectric materials with their transition temperatures is shown in Figure 5.6). While most of the ferroelectric phase transitions are second order in nature, there are cases for example in some perovskites

which may involve small change in latent heat during the phase transition making them weakly first-order [388].

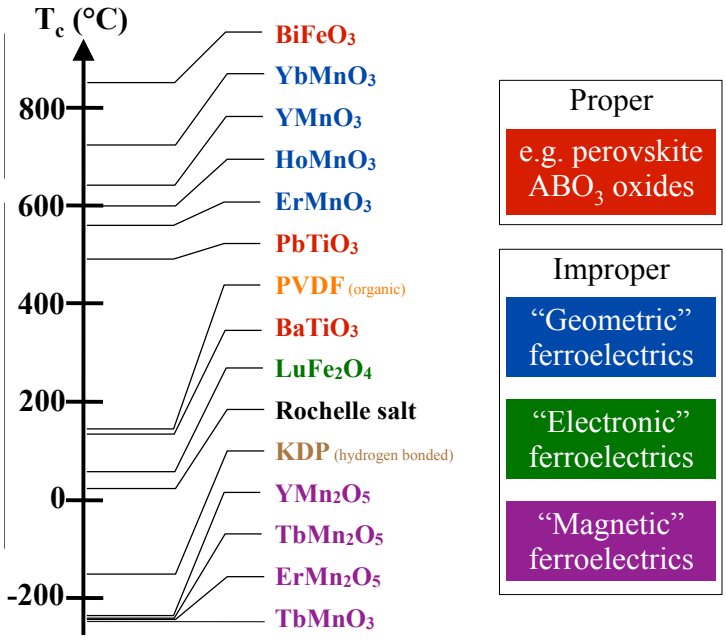

Figure 5.6: Ferroelectric phase transition temperature for various types of ferroelectric materials is listed. From [367]

Now, we turn our attention to one of the most critical parameter of the phase transition, *i.e.* order parameter, which differentiates various kinds of ferroelectricity found in materials such as those listed in Figure 4.6. When the primary order parameter is polarization they constitute the family of ferroelectric materials called as Proper Ferroelectrics. The examples of proper ferroelectrics include perovskite oxides such as $BiFeO_3$, BTO, and PTO *etc.* In these proper ferroelectrics materials, the driving force for ferroelectric instability is the polar lattice distortion, which eventually results into the development of spontaneous polarization in symmetry-equivalent states of the ferroelectric phase. An example of such a polar lattice distortion is shown earlier in Figure 5.5 and such off-centering of cations with respect to anions usually results from the hybridization of '3*d*' orbitals (of 'Ti' in BTO for ex.) and/or '6*p*' orbitals (of 'Bi' in $BiFeO_3$ for ex.) of cations with '2*p*' orbitals (of 'O' in BTO or $BiFeO_3$) of anions atoms leading to ferroelectricity in the materials [388]. There is other class of ferroelectric materials where the primary order parameter for the ferroelectric phase transition is not the polarization but a non-polar lattice distortion, which is coupled to secondary order parameter (polarization). These materials constitute the family of "Improper" Ferroelectrics. Depending on the primary order parameter in these improper ferroelectric materials, they can be further divided into three main categories: Improper 'Geometric,' 'Electronic,' and 'Magnetic' ferroelectrics. In improper geometric ferroelectrics, the primary order parameter is related to the structural

change of the unit cell such as rotation of oxygen polyhedral in $HoMnO_3$, $ErMnO_3$, $YbMnO_5$ (hexagonal manganites), which drives the symmetry-lowering of high-symmetry paraelectric state, giving rise to the ferroelectricity in the material [392; 393]. In improper electronic ferroelectrics, the primary order parameter is related to the charge-ordering phenomenon exhibited by the atoms present in the unit cell, which can assume multiple valence states such as 'Fe^{2+}' and 'Fe^{3+}'. In such cases, the charge ordering provides necessary symmetry-breaking instability for the materials to transition to ferroelectric state. Examples of electronic ferroelectrics include $LuFe_2O_4$, YFe_2O_4 [141; 394]. Note that there are no ion displacements involved during the phase transition making them improper ferroelectric materials. Lastly, in 'magnetic' ferroelectrics, the primary order parameter is magnetic order such as helical magnetic ordering in $CaMn_7O_{12}$ driving improper ferroelectricity in the material below T_c = 90 K [395]. Other examples of magnetic ferroelectrics include YMn_2O_5, $ErMn_2O_5$, $TbMnO_3$ [396-398]. It is important to mention that the order parameter being a differentiating criteria between proper vs improper ferroelectric, the criteria should be used with caution. For example, ferroelectric material Iron-iodine-boracite ($Fe_3B_7O_{12}I$) undergoes a sequence of phase transition from high symmetry cubic phase to orthorhombic phase, then from orthorhombic to monoclinic phase and finally from monoclinic phase to trigonal phase [399]. While the phase transition from the cubic phase to orthorhombic phase is an improper phase transition, the transition from orthorhombic to monoclinic is a proper phase transition [399]. Thus, proper vs improper ferroelectric term can be associated more appropriately with a ferroelectric phase transition rather than ferroelectric material itself. In conclusion, the presence of two (or more) order parameters with one being ferroelectric distortion and other being a magnetic order, electronic charge order *etc.*, in ferroelectric materials makes them a very promising candidate for electrically controllable novel functional devices.

5.2.1.4 Bulk Ferroelectrics

Owing to the remarkable piezoelectric and dielectric properties of ferroelectric material as mentioned earlier, several theoretical and experimental studies in bulk form (*i.e.* single crystal, polycrystalline *etc.*) have been performed to understand and explain various aspects of ferroelectric behavior found in these materials [358; 400]. In particular, perovskite oxides such as BTO [97; 388], PZT [362; 388; 401] *etc.*, have attracted much attention due to their relatively simple structure (especially useful for theoretical studies) along with their large spontaneous polarization (see Figure 5.3) to study various aspects of ferroelectricity. One example is the physical mechanism driving the materials towards ferroelectric instability, which have been studied and understood reasonably well in materials such as BTO, PTO *etc.* It is learned that ferroelectric behavior arises from the balance of two competing interactions. First are the short-range covalent interactions between the '2*p*' orbitals of oxygen anions and '3*d*' orbitals of B-site cation (and/or '6*p*' orbitals of A-site cation) due to the hybridization of these orbitals. Second is the dipole-dipole Coulomb interaction, which results from the collective displacement of group of atoms (or softening of a phonon mode). Thus, there exist a correlation volume within which

the balance between these two competing factors results into ferroelectric instability [386]. Note that this concept will become useful in anticipating dramatic changes in the physical mechanism leading to ferroelectric instability in nanostructures.

Another important example is the study of macroscopic ferroelectric state, *i.e.* presence of ferroelectric domains, domain walls *etc.*, of the bulk materials and how do they affect the associated ferroelectric properties such as coercive field [362; 402], ferroelectric switching dynamics [403] *etc.* Here, I will cover the basics of ferroelectric domain evolution with temperature as they are very relevant to the findings of the studies presented in this and the next chapter. Let us take an example of a cubic material transitioning to tetragonal ferroelectric phase which is cooled below its Curie temperature (T_c) say $PbZr_{0.8}Ti_{0.2}O_3$ (PZT). When the crystal is cooled below T_c, there are six-symmetry equivalent directions (including positive and negative) of the cubic high-symmetry reference state along which spontaneous polarization can develop. But, the actual electrical boundary condition and mechanical boundary condition imposed on the PZT crystal will finally decide the domain morphology of the crystal. An example of multivariant domain structure is shown in Figure 5.7 [362], where one can identify regions of uniformly oriented spontaneous polarization. For example, the shaded region in 'yellow' suggests that the polarization in individual unit cells within this region is all uniform and pointing along $[0\ \bar{1}\ 0]$ direction (shown as magnified image on left). Consequently, the net polarization in the yellow region is also pointing along $[0\ \bar{1}\ 0]$ direction. Similarly, the regions shaded in 'brown' corresponds to the spontaneous polarization of the unit-cells present in those regions pointing along $[0\ 1\ 0]$ direction, *i.e.* opposite to those present in 'yellow' regions. One can also identify the other two symmetry-equivalent directions, *i.e.* $[1\ 0\ 0]$ and $[\bar{1}\ 0\ 0]$, shaded in 'pink' and 'magenta' respectively, in this polydomain structure which contains four variants ($[1\ 0\ 0]$, $[\bar{1}\ 0\ 0]$, $[0\ 1\ 0]$, $[0\ \bar{1}\ 0]$).

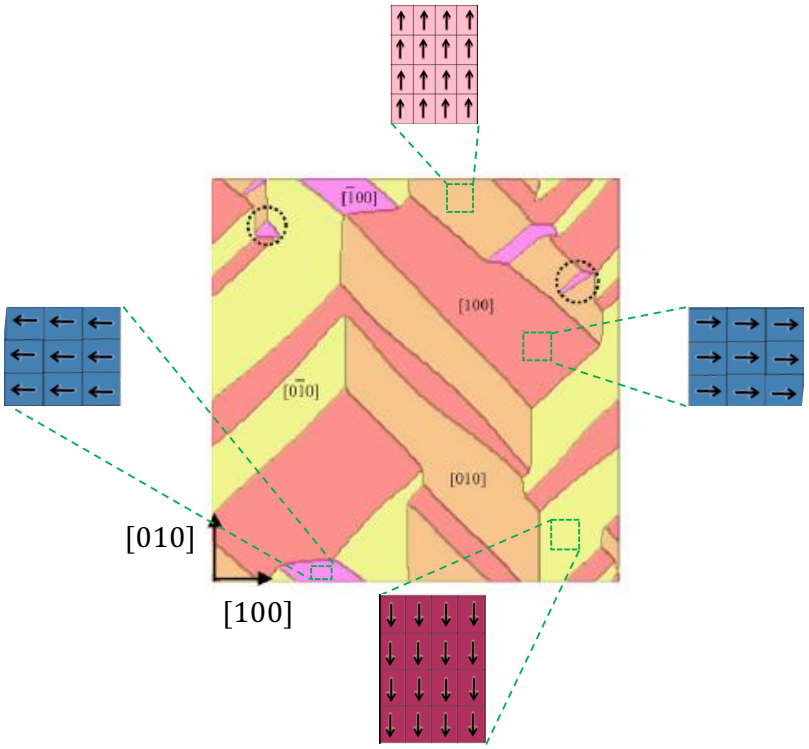

Figure 5.7: Domain structure of a PZT single crystal. Figure adapted from [362] and [404].

Another important characteristic of this multivariant domain structure is that the regions of uniform polarization are separated by what is called as *Domain Walls*. These domain walls can strongly affect the ferroelectric response of this polydomain domain structure and in some cases may exhibit properties, which are characteristically different from the parent ferroelectric material itself [405]. Domain walls are defined by the angle between the directions of the two spontaneous polarized regions, which are separated by respective domain wall. There are two types of domain walls: ferroelectric domain walls, which are by formed 180° domains vs. ferroelastic domain walls, which are formed by non-180° domains. Ferroelectric domain walls are formed due to electrical boundary conditions (depolarizing fields), while ferroelastic domain walls are formed due to mechanical boundary conditions (such as strains). For example, in the polydomain structure of PZT shown, 180° ferroelectric domain wall and 90° ferroelastic domain walls can be easily identified, the schematic of these domains walls is illustrated in Figure 5.8. Note that the distribution of polarization within a domain wall is highly non-uniform and it results in large gradient energy contribution from all domain walls towards the total energy of the ferroelectric crystal. The gradient energy is proportional to the square of the polarization gradient present in the region that is non-zero in the domain walls and zero in domains where polarization distribution is uniform. As will be discussed later, gradient energy becomes one of the dominating factor in deciding the novel polarization distributions found in nanostructures. Usually, the width of these ferroelectric domain walls is of the order of

few nanometers, thus one can anticipate their impact on ferroelectric nanostructures whose size is only few nanometers.

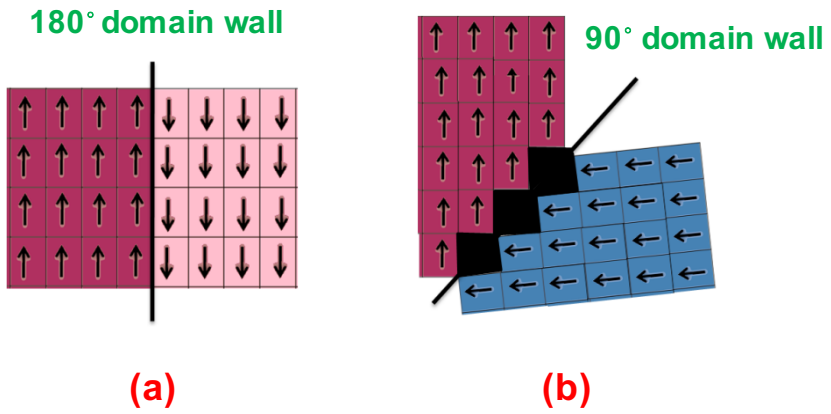

Figure 5.8: The schematic shows (a) 180° and (b) 90° degree domains walls which are commonly observed in multivariant domain structure. Figure adapted from [404].

The stabilization of a particular domain structure strongly depends on the mechanical and electrical boundary conditions imposed on the sample. The reason being the change in the contribution of electrostatic energy (arising from dipole-dipole interactions, from applied electric field *etc.*), elastic energy (arising from the mechanical strain applied to the sample and/or strain associated with the spontaneous polarization), and the gradient energy (arising from the non-uniform polarization regions, for example from domain walls) when either of electrical or mechanical (or both) are changed. The effect of this boundary condition is pronounced in thin-films and will be discussed next.

5.2.1.5 Thin-film Ferroelectrics

Ferroelectric properties of nanostructures, especially, in thin-film form, have attracted much attention given their huge potential in development of miniaturized actuator for MEMS devices, high-density memory storage for NFERAMs, and in lowering the operating voltage for integrated circuit devices due to smaller electric fields needed to switch owing to much smaller thickness (few hundreds of nanometers) compared to bulk (micrometer to millimeter thickness) [330; 382]. Scientifically, thin-films have raised many fundamental questions about the ferroelectric behavior when one of the dimensions of the materials is reduced to few unit-cells. For example, the fundamental limit on the thickness of the film for ferroelectricity to still exist [406; 407]. Similarly, the dependence of other ferroelectric properties such as coercive field (E_c), switching dynamics, Curie Temperature (T_c) *etc.* on the thickness of the film, have been subject of many intense investigations [366]. The quest to answer these fundamental questions was further fueled

by the advances made in thin-film synthesis and characterization techniques (both *in situ* and *ex situ*) in the last decade.

Hence, in the past decade or so, many research groups have devoted plenty of their time and resources in understanding various mechanisms involved in ferroelectric properties of thin-films. As mentioned earlier, the change in electrical and mechanical boundary conditions can significantly affect the ferroelectric ground state of the materials and thus its ferroelectric behavior. We will start our discussion with electrical boundary conditions, as they have proved crucial in study of ultrathin-films [367]. Electrical boundary condition decides the intrinsic stabilization of ferroelectric ground state and the measured properties of ferroelectric thin film (which is normally achieved through capacitance geometry). When a ferroelectric film is cooled below its T_c, the spontaneous polarization developed across the film leads to accumulation of bound charges on both ends of thin-film (see Figure 5.9(a)). These bound charges, if not screened externally or internally, will collectively form an electric field pointing in the opposite direction of spontaneous direction (see Figure 5.9(a)) also known as the depolarization field. This state is energetically unfavorable and thus the system will lower its energy by number of ways illustrated in Figure 5.9. Note that the magnitude of the depolarization field can be as high as 10^4 kV/cm [371], and thus, it is strong enough to completely suppress the polarization (a case depicted in Figure 5.9(b)). The external screening of these bound charges can be provided by either with help of free charges from metal electrodes placed on both sides of the films (normal geometry in which ferroelectric properties are measured as illustrated in Figure 5.9(c)), or ions (adsorbents) from the atmosphere as shown in Figure 5.9(d). These bound charges can also be screened by internally if the material has mobile charges such as in the case of semiconducting film (Figure 5.9(e)). In the case where there are no available charges to screen bound charges, ferroelectric film can still preserve its polarized state by forming ferroelectric domains within the film in such a way which will make the surface of the film charge neutral and net (overall) electric field within the materials zero. Two examples of domain structures formed in absence of free charges are shown in Figure 5.9(f) and Figure 5.9(g). Note that under externally applied mechanical strain, other domain structures can also be stabilized, as shown in (Figure 5.9(h) and Figure 5.9(i)). One case is subjecting to enough strain to drive the polarization go completely in plane, an example of this will be discussed in chapter 6. The other interesting example is stabilizing polarization distribution in the form of vortex structures (Figure 5.9(j)), which will be the focus of the work presented in this chapter. Thus, depending on the electrical boundary conditions thin films can be subjected to, ferroelectric ground state can adopt one of the possible states shown in Figure 5.9.

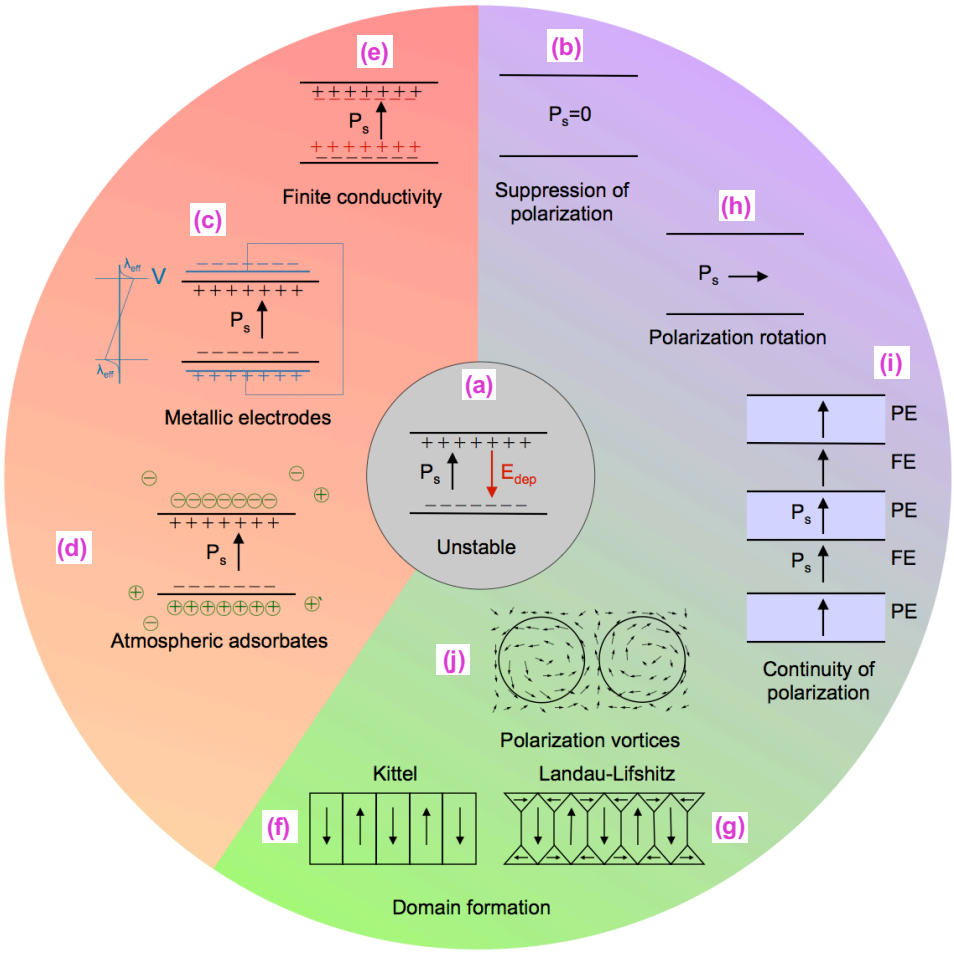

Figure 5.9: Effect of electrical boundary conditions on the polarization distribution within a slab of ferroelectric material. From [367].

The other important effect of electrical boundary conditions is observed when an attempt to measure the ferroelectric properties of thin-films using standard capacitance geometry (which is usually the method to measure coercive field, spontaneous polarization, dielectric constant, T_c *etc.*). When the thickness-dependent ferroelectric properties were measured using this geometry, a number of observations were made. For example, spontaneous polarization and T_c was observed to decrease with decrease in thickness of film, while coercive field was observed to increase with decreasing film thickness [367]. In addition to intrinsic contribution from ferroelectric material to the behavior observed above, there was another contribution coming from the extrinsic effect, which is the related to interface properties of metal and ferroelectric. In general, the cause of size effects was linked to the presence of *dead* layer at the metal/ferroelectric interface [408]. Note the existence of "dead" layer can be either external or internal. By external factor, it means poor quality of the interface formed during the fabrication of metal electrodes on ferroelectric. Examples include bombarding of sputtering ions on the ferroelectric film

during metal deposition; the top surface of the films contains defects such as off-stoichiometry *etc.* It is useful to mention that for many years (till late 1990s), it was believed that ferroelectricity does not exist below certain thickness, but the real reason, confirmed later, was the inadequate quality of the metal/ferroelectric interface used for measuring ferroelectric properties [388]. By internal factors, it means that even if the metal/ferroelectric interface were of high quality (defect-free), the effect of "intrinsic" dead would still be present. This is because the depolarization effect is an *interface* property and it depends on the materials (metals and ferroelectric) making that interface, crystallographic orientation of ferroelectric layer with respect to metal layer *etc.* The effect of depolarization field can also be described by 'effective screening length' (λ_{eff}), which is defined as the length over which the screening charges will spread at the metal/ferroelectric interface. One can derive the dependence of depolarization field on effective screening length [367], *i.e.*:

$$\boldsymbol{E}_d = -\frac{2\,\lambda_{\text{eff}}\,\boldsymbol{P}_o}{\epsilon_0 t} \tag{5.10}$$

, where '$\boldsymbol{P}_o$' is the spontaneous polarization, 't' is the thickness of the ferroelectric film, and '$\boldsymbol{E}_d$' is the depolarization field. From this equation (5.10), one can infer that the contribution of all electronic charges and ionic charges to the depolarization field is included in the λ_{eff}. This summarizes the effect of electrical boundary conditions on the measured ferroelectric properties of thin-film, and suggests that one has to be careful in performing ferroelectric measurements, especially, of thin-films.

Now, we will discuss the effect of mechanical boundary conditions on the ferroelectric ground state of thin-films. Similar to pressure-based studies in bulk ferroelectrics, which led to various pressure-based phase diagrams [97; 409; 410], epitaxial in-plane strain can be used to impose wide range of strain states in thin films [127], and thus, study their effect on ferroelectric properties thin films. Theoretically, the coupling between polarization and strain can be qualitatively discussed by revisiting the equation (5.5) from DGL model stated earlier, *i.e.*:

$$\mathcal{F}(P) = \frac{1}{2}\alpha_2 P^2 + \frac{1}{2}\alpha_4 P^4 + \frac{1}{2}\alpha_6 P^6 + .. \tag{5.11}$$

The coefficient of the quadratic term can be modified significantly by tuning the strain state of the film (below T_c), *i.e.* 'α_2' can be made more negative or less negative by choosing the appropriate amount of strain, thus leading to enhancement or suppression of ferroelectricity in the material. The coupling between ferroelectric distortion and mechanical strain/stress has proven to be extremely useful in exploring, enhancing and controlling the ferroelectric properties of materials in thin-films form. Such studies have been possible because of advances made in synthesis and characterization of thin-films,

and more importantly, the availability of wide range of substrate lattice parameters (see Figure 3.1), which allowed tuning the strain-state almost continuously.

The ability to synthesize thin-films in both compressive and tensile (in-plane biaxial) strain with high quality allowed researchers to build in-plane strain-based phase diagrams for ferroelectric thin-films [411-413]. I will discuss in detail in chapter 6 the effect of in-plane biaxial strain in stabilizing novel ferroelectric ground states by tuning the superlattice periodicity of paraelectric/ferroelectric superlattice. The other advantage of having biaxial strain as a controllable parameter is that ferroelectric domain morphology can be changed significantly [127; 414], owing to symmetry-equivalent directions of a crystal structure. Thus, allowing studies of ferroelectric behavior as a function of their domain structure in thin-film ferroelectrics [127]. Lastly, the *strain-engineering* of ferroelectric thin-films have enabled researchers to show unprecedented results such as inducing ferroelectricity in thin-films of STO strained by 1% (on DSO substrate) [415], enhancing the ferroelectric behavior of BTO, *i.e.* more than 100% increase in magnitude of spontaneous polarization and 500 K increase in T_c [416], by straining compressively on DSO or GSO substrate, and lastly, enabling novel ferroelectric phases and behavior in $BiFeO_3$ by subjecting to extraordinarily large amount of strain [126], *i.e.* more than 4%, on LAO substrate.

Thus, the controllability of epitaxial strain in thin-films has opened another phase space to explore ferroelectric behavior under both reduced dimensions (size effect) and mechanical strain/stress. This will invite more fundamental questions such as: Are there limits of *strain-engineering* combined with reduced dimensions of ferroelectric nanostructure, in, for example, enhancing the ferroelectric behavior of ferroelectric thin films, or in stabilizing novel ferroelectric phases such as non-uniform polarization structures akin to spin-topologies (ex. magnetic skyrmions, merons [417; 418]) found in magnetic systems? The work presented in this chapter makes an attempt to stabilize novel polarization structures, which are not found in bulk, by exploiting the interplay between both electrical and mechanical boundary conditions in ferroelectric layers of paraelectric/ferroelectric superlattice. Before I present the experimental results pertaining to the observation of such novel features, we will first discuss the theoretical predictions for the existence of these non-uniform polarization structures in low-dimensional nanostructures such as nanorods, nanodiscs, thin-films of superlattices *etc*.

5.2.2 Theoretical models predicting Vortex structures

There are number of different theoretical approaches which have been employed to study the physics of ferroelectrics [361; 419-421]. These methods include full first-principles (ab-initio) calculations, first-principle-derived calculations such as first-principles-based Effective-Hamiltonian method, and phenomenological models based on Landau theory such as Phase-field Simulations. These theoretical approaches have been applied extensively to study the properties of low-dimensional nanostructures such as nanorods, nanodisc, nanocomposites, superlattice structures *etc*. [369; 371-374; 380; 381; 383; 422-429]. The findings of these studies were rather remarkable, for example, non-

uniform polarization distributions were discovered in low-dimensional structures, which do not exist in bulk form. In contrast to uniform polarization distributions generally found in bulk materials (an example of which was shown earlier in Figure 5.7), the reduced size effect along with the different boundary conditions, such as those discussed in previous section, in nanostructures have stabilized polarization distributions in the form of Vortex structures [371; 373; 383; 430; 431]. These polarization structures find close resemblance to complex spin topologies found in magnetic systems such as spiral magnetic skyrmions [418], merons [417] *etc*. In fact, very recently, ferroelectric (or dipolar) skyrmions have been predicted in nanocomposite of BTO and STO (*i.e.* nanopiller of BTO embedded in a solid matrix of STO) [430]. Thus, these theoretical studies have provided enough evidence of complex topologies of electric polarization with only remaining is the experimental evidence. The theoretical studies have been further applied to predict the properties of dipolar vortices such as their switchability with electric field [380; 424], their phase transition characteristics with size of the nanostructure [371; 383], and many other novel characteristics based on these vortex states [369; 432]. Since this chapter focuses on observation of polarization vortices, I will limit our discussion to theoretical studies predicting their existence in nanostructures.

We will begin our discussion with the groundbreaking theoretical work done over a decade ago using first-principles-derived effective Hamiltonian method. In this method, first an effective Hamiltonian is constructed using variables involved in a ferroelectric instability such as local soft-mode amplitude vectors (u_i) and local strain tensor (η_l) in respective unit-cell (i) of the ABO_3 crystal structure [420], which gives the following expression for the total energy of the system in terms of those variables,

$$E_{\text{tot}} = E_{\text{self}}(\boldsymbol{u}_i) + E_{\text{dipole}}(\boldsymbol{u}_i) + E_{\text{short}}(\boldsymbol{u}_i) + E_{\text{elastic}}(\eta_l) + E_{\text{int}}(\boldsymbol{u}_i, \eta_l) \tag{5.12}$$

, where '$E_{\text{self}}(\boldsymbol{u}_i)$' is energy corresponding to local modes, '$E_{\text{dipole}}(\boldsymbol{u}_i)$' is energy corresponding to long-range dipole-dipole interactions, '$E_{\text{short}}(\boldsymbol{u}_i)$' is the energy corresponding to short-range interactions which results from short-range repulsion and hybridization from neighboring local modes, '$E_{\text{elastic}}(\eta_l)$' is the elastic energy corresponding to local strain, '$E_{\text{int}}(\boldsymbol{u}_i, \eta_l)$' is the energy corresponding to the interaction between local modes and local strain. Note that the local modes ($\boldsymbol{u}_i$) are related to local electrical dipoles ($\boldsymbol{p}_i$) in the ith unit cell by: $\boldsymbol{p}_i = Z^* \boldsymbol{u}_i$, where '$Z^*$' is the Born effective charge associated with local soft mode. The coefficients in these individual energy expressions were calculated from first-principles method (*i.e.* using density functional theory within the local density approximation [420]). Once the effective Hamiltonian is found for the system, Monte-Carlo Simulations were performed on given volume of the crystal ($L \times H \times B$) with periodic boundary conditions to solve for the local dipole moments in the ferroelectric system [420].

Prior to this work, it was believed that phase transition in low-dimensional systems is extremely difficult [433], thereby reducing the likelihood of exhibiting multi-stable ferroelectric states [434]. Choosing appropriate order parameter for such low-dimensional

systems made tremendous progress. This essentially means that if the development of non-zero net spontaneous polarization as a function of temperature is used as the evidence of ferroelectric phase transition, one would not notice any phase transition down to very low temperatures. This is primarily because the non-uniform polarization distribution developed (below a certain temperature) would result in zero net polarization (when summed over the entire volume of the system) before and after the phase transition. Thus, we have to choose an appropriate order parameter, which can register the onset of non-uniform polarization states with a nanostructure. In this pioneering work by Ivan *et al.*, [371] they discovered a new order parameter called as "spontaneous toroid moment" which shows a non-zero value below the phase transition temperature (T_c) and zero above T_c. The toroid moment, '$\boldsymbol{G}$', is defined as follows:

$$\boldsymbol{G} = \frac{1}{(2N)} \sum_i \boldsymbol{R}_i \times \boldsymbol{p}_i \tag{5.13}$$

, where 'N' is number of unit-cells in the simulation, '$\boldsymbol{R}_i$' is the position vector of ith unit cell, '$\boldsymbol{p}_i$' is the local dipole moment in the ith cell. In this simulation, PZT (0.5,0.5) composition was used with cylindrical geometry having diameter (D) and height (H) defined in terms of bulk lattice parameter (a_0 = 4 Å). When D > H, it is considered as nanodisc and for D < H it is considered as nanorod. The nanostructure is in general described as (D, H). For a particular case of (19, 14), *i.e.* $19a_0$ being the diameter and $14a_0$ being the height of nanodisc, '$\boldsymbol{G}$' was calculated from 768 K all the way down to 64 K. The components of '$\boldsymbol{G}$', *i.e.*, $\boldsymbol{G}_x$, $\boldsymbol{G}_y$, $\boldsymbol{G}_z$, are plotted as a function of Temperature (T) in Figure 5.10(a). Note the references axes, '*x*', '*y*', '*z*' are pointing along $[100]_{pc}$, $[010]_{pc}$, $[001]_{pc}$, where '*pc*' denotes pseudocubic, direction of the PZT unit cell. The figure shows that non-zero toroid moment along '*z*' direction (*i.e.* $\boldsymbol{G}_z$) starts developing when temperature is lowered below 600 K, while '$\boldsymbol{G}_x$' and '$\boldsymbol{G}_y$' remains almost zero at all temperatures. Figure 5.10(b) specifically plots the magnitude of '$\boldsymbol{G}_z$' component at different '*x*-*y*' planes or '*z*' planes or layers of the (19, 14) nanodisc. '$\boldsymbol{G}_z$' is zero at high temperatures (768 K) and assumes non-zero value at lower temperature (64 K), *i.e.* below T_c. The inset of Figure 5.10(b) shows the local dipoles with (19, 14) nanodisc present on *z* = 7 plane, clearly highlighting formation of polarization vortex structures in these nanodiscs. Similarly, when D < H case is considered, for example (7, 28) forming a nanorod, calculating toroid moment as a function of temperature, a phase transition was observed and corresponding formation of local polarization distribution is shown in Figure 5.11. The figure depicts x-plane and y-plane cross-section of the nanorod showing local dipoles within the nanorod. The formation of polarization vortices in these nanorods is highlighted in each cross section by the overlaid circles on the local profiles.

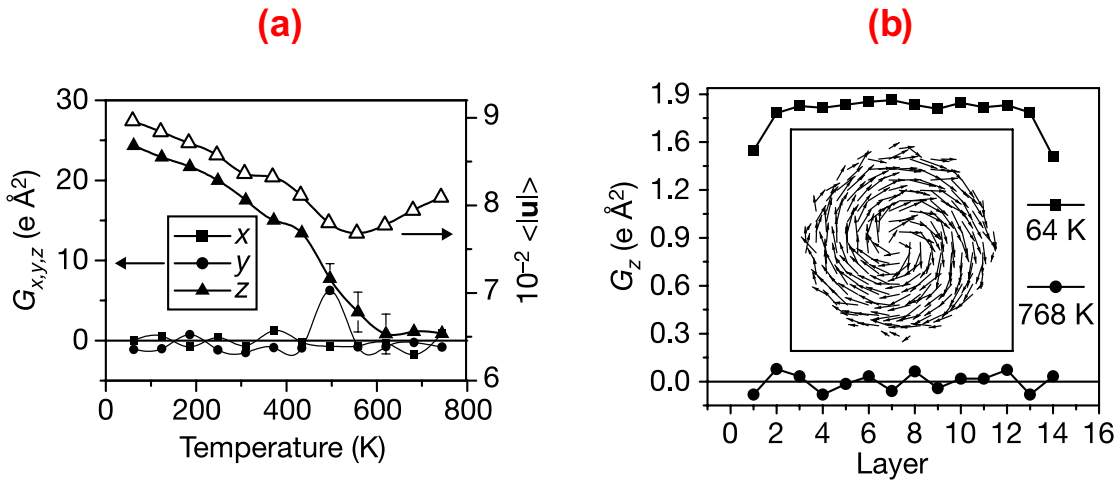

Figure 5.10: Toroidal moment for a nanodisc, as calculated from first-principles-derived effective Hamiltonian method. From [371].

It is important to realize that $\boldsymbol{G}_z$ can assume two equivalent values depending on whether local dipoles is rotating in clockwise or anticlockwise direction forming a vortex structure. Recall that toroid moment, $\boldsymbol{G}$, is also a vector quantity and similar to spontaneous polarization, $\boldsymbol{P}_s$, where there are two stable states ($\boldsymbol{P}_s$ and -$\boldsymbol{P}_s$), $\boldsymbol{G}$ can also possess two stable states: $\boldsymbol{G}$ and -$\boldsymbol{G}$. Note we shall call these states vortex and antivortex states. Having said that, it is also important to realize the other fundamental difference between these vortex states having non-zero toroid moment and uniformly polarized regions having non-zero spontaneous polarization. While in the latter case, where two stable states ('-$|\boldsymbol{P}_s|$' and '$|\boldsymbol{P}_s|$') can be accessed via application of static electric field, the former case needs a curling of electric field, *i.e.* $\nabla \times \boldsymbol{E} \neq 0$. In order to switch the toroid moment of a vortex from a positive (vortex) to negative (antivortex), we need to apply a time-dependent magnetic field which will generate a non-zero curl of electric field according to Maxwell equation, $\nabla \times \boldsymbol{E} = -\frac{\partial B}{\partial t}$. The coercive field for switching between vortex and antivortex will thus be calculated from magnitude of $\left|\frac{\partial B}{\partial t}\right|$ needed for switching. This particular characteristic of using magnetic field to switch ferroelectric states along with toroidal moment as the logic states ($\boldsymbol{G}$ and -$\boldsymbol{G}$) is anticipated to show superior performance [369; 371]. Note that these calculations are performed for free-standing PZT nanodisc or nanorod in vacuum, which implies electrical boundary conditions more importantly depolarization fields are playing crucial role in stabilizing these polarization vortex structures. Also, the calculations show that these vortex structures appear only for certain critical size of the nanodisc or nanorod, further suggesting the role of depolarization effects in the evolution of these non-uniform polarization modes.

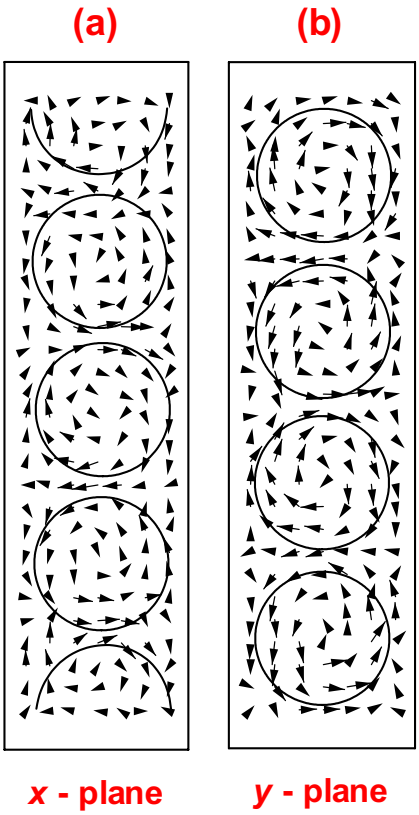

Figure 5.11: Local polarization profiles within a nanorod is shown on the cross-sectional plane of (a) $yz = 0$ and (b) $zx = 0$, as predicted from first-principles-derived effective Hamiltonian method. From [371].

In another theoretical study based on first-principles derived effective Hamiltonian method, prediction of polarization vortex structures was made in superlattices composed of PTO and STO. Particularly, 3 x 3 and 6 x 6 superlattice periodicities were shown to exhibit polarization vortex-antivortex structures in PTO ferroelectric layers [431] of the PTO-STO superlattice (see Figure 5.12). In this case also, the existence of polarization vortices is found to be dependent on periodicity of the superlattice structure. More specifically, the calculations suggest that there is a transition from a monodomain structure to a vortex structure as the superlattice peridocity is increased. In the monodomain structure, the polarization was found to stabilize with a constant out-of-plane polarization maintained throughout the superlattice structures, suggesting the STO layers are polarized as well. This domain structure was found to dominate at very short periodicities of the superlattice. On further increasing the periodicity, the polarization distribution starts confining within PTO layers forming vortex structures. Such a periodicity dependent transition is explained with the help of electrostatic coupling present between adjacent ferroelectric layers (PTO) of the superlattice structure. The presence of strong electrostatic coupling in short-period superlattice stabilizes the monodomain structure, while the presence of weak coupling in long-period superlattice results in polarization to be confined

within PTO layers stabilizing polarization vortices in alternating ferroelectric layers of the superlattice structure. Although the prediction was qualitatively good, the exact transition point for these phase transitions seems to be a bit-off from what was found experimentally (I will discuss this more later). The strain state of the superlattice structure, for example, was one reason among others, which was found to play a crucial role in this phase transition. Nevertheless, the main conclusion of the existence of polarization vortices in low-dimensional structure, along with the dependence on size for their existence, is found to be consistent with the previous studies on nanodisc/nanorod where similar size-dependent existence of these non-uniform polarization structures were predicted.

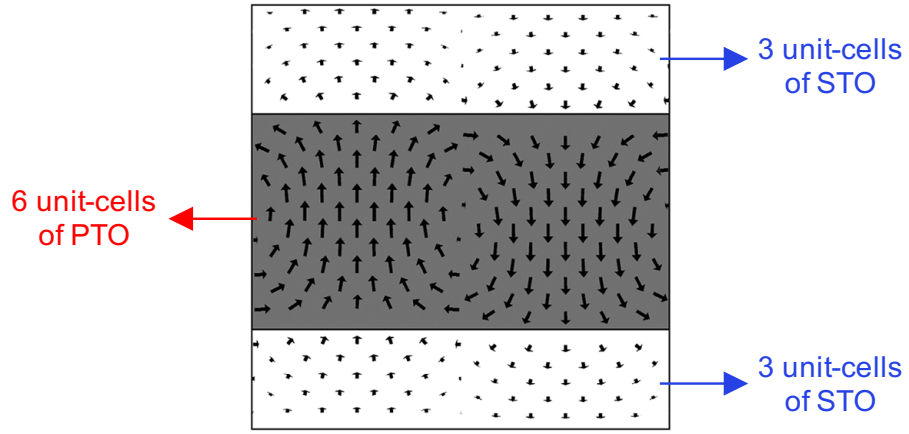

Figure 5.12: Local polarization profiles within a sub region of a 6 x 6 PTO-STO superlattice predicted using first-principles-derived effective Hamiltonian method, is shown. From [431].

There is another theoretical approach, which has been greatly used for studying domain structure evolution in ferroelectric thin-films [435; 436] and superlattices [428; 437], called *phase-field* models. Particularly, polarization vortex structures, using phase-field simulations, were also predicted in number of nanostructures such as nanodots [380], nanosheets [373], superlattices [381] *etc.* Using phase-field simulations also, it was predicted that the existence of polarization vortices depended critically on the size of the ferroelectric nanostructure [372], similar to previous predictions based on first-principles-derived methods. Phase-field simulation is a phenomenological approach in which the domain structure is described by a set of variables, also called as field variables [421]. In general, the total energy (F) of the system having poly- or mono-domain structure can be described by local free-energy density (f) corresponding to various interactions present in the system, which further depends on those field-variables. For example, in ferroelectrics, local free-energy density corresponding to various types of interactions such as long-range dipole-dipole interaction, elastic interactions, electrostatic interactions, with the local polarization vectors (P_x, P_y, P_z) as the field variable is formulated first. Then, the evolution of the field variable (which is local polarization vector) is obtained by solving a kinetic equation (time-dependent Landau-Ginzburg equation). The solution, thus, provides the

spatial distribution of local polarization vectors giving the domain structure of the ferroelectric system in question. Phase-field simulations to predict microstructure of ferroelectric domain has many advantages such as the size can be very large as compared to first-principles-derived method, for example, in simulating large-period superlattices, first-principles-derived method was experiencing scaling issues. Moreover, this method has been also successfully applied to obtain full three-dimensional ferroelectric domain structure for relatively large system with additional advantage of studying temperature-dependent evolution of domain structure. In addition, phase-field simulations were employed to predict domain structure evolution in more complicated boundary conditions [438]. The other major advantage of this simulation method is that it does not require *a priori* assumption of the domain structure of what the final domain structure might be [438]. Thus, we have used phase-field models to simulate spatial polarization distribution in superlattice structures of PTO-STO. Prof. Long-Qing Chen's group from Pennsylvania State University provided phase-field simulations for this superlattice system.

The evolution of polarization distribution in superlattices of PTO-STO on DSO substrate was obtained by solving the time-dependent Ginzburg-Landau equation with local polarization as the non-conserved field variable (or, order parameter in this case):

$$\frac{\partial P_i(x,t)}{\partial t} = -L\,\frac{\delta F}{\delta P_i(x,t)} \tag{5.14}$$

, where $x_i = x_1, x_2, x_3$ are the coordinates, 'P_i' is the local polarization component along 'i' direction, 't' is time, 'L' is a kinetic coefficient (which is related to interface mobility), 'F' is the total energy of the superlattice with contribution from various interaction [381]:

$$F = F_{landau}(P_i) + F_{grad}(\partial P_i/\partial x_j) + F_{elas}(P_i, \varepsilon_{ij}) + F_{elec}(P_i, E_i) \tag{5.15}$$

, where '$F_{landau}(P_i)$' is the Landau free energy which is the bulk free energy (a multi-well function of the order parameter), '$F_{grad}(\partial P_i/\partial x_j)$' is the Gradient energy which arises due to energy penalty for having regions of inhomogeneous polarization such as domain walls, '$F_{elas}(P_i, \varepsilon_{ij})$' is the elastic energy which has contribution from the strain imposed on the superlattice structure and from the strain due to spontaneous polarization, '$F_{elec}(P_i, E_i)$' is the electrostatic energy arising because of electrostatic interaction present within the polarized state of system. In this particular case of superlattice structure strained on DSO substrate, the expression for the individual energies is given:

$$F_{landau}(P_i) = \int \left[\frac{1}{2}\alpha_{ij}P_iP_j + \frac{1}{4}\gamma_{ijkl}P_iP_jP_kP_l + \frac{1}{6}\omega_{ijklmn}P_iP_jP_kP_lP_mP_n\right] d^3x \tag{5.16}$$

$$F_{grad}(\partial P_i/\partial x_j) = \int \left[\frac{1}{2} G_{ijkl} \frac{\partial P_i}{\partial x_j} \frac{\partial P_k}{\partial x_l}\right] d^3x \tag{5.17}$$

$$F_{elas}(P_i, \varepsilon_{ij}) = \int \left[\frac{1}{2} c_{ijkl}(\varepsilon_{ij} - Q_{ijkl}P_kP_l)(\varepsilon_{kl} - Q_{klij}P_iP_j)\right] d^3x \tag{5.18}$$

$$F_{elec}(P_i, E_i) = -\int \left[\frac{1}{2} k_b \varepsilon_0 E_i^2 + E_iP_i\right] d^3x \tag{5.19}$$

The constants appearing in these equations such as lattice constants, elastic coefficients (c_{ijkl}), background dielectric constants (k_b), Landau coefficients (α_{ij}, γ_{ijkl}, ω_{ijklmn}), gradient energy coefficients (G_{ijkl}), electrostrictive coefficients (Q_{ijkl}) were taken directly from literature [381].

The thermodynamic force, $\delta F/\delta P_i(x,t)$, which drives the system from a non-equilibrium state to an equilibrium by minimizing the total free energy as a function of order parameter (P_1, P_2, P_3), eventually gives us the polarization distribution at equilibrium. More details about the phase-field simulations can be found in [381; 438]. An example of polarization pattern in 10 x 10 superlattice is shown in Figure 5.13, where the formation of vortex structure can be clearly seen in successive layers of PTO. The simulations were also employed to find the evolution of polarization distribution as a function of superlattice periodicity. Similar to earlier theoretical predictions, phase-field simulations for PTO-STO superlattice also showed superlattice period-dependent existence of polarization vortices. This is the case only for a short window of superlattice periodicity where the interplay between depolarization energy, elastic energy, electrostatic and landau energy resulted in stabilization for these vortex ground states.

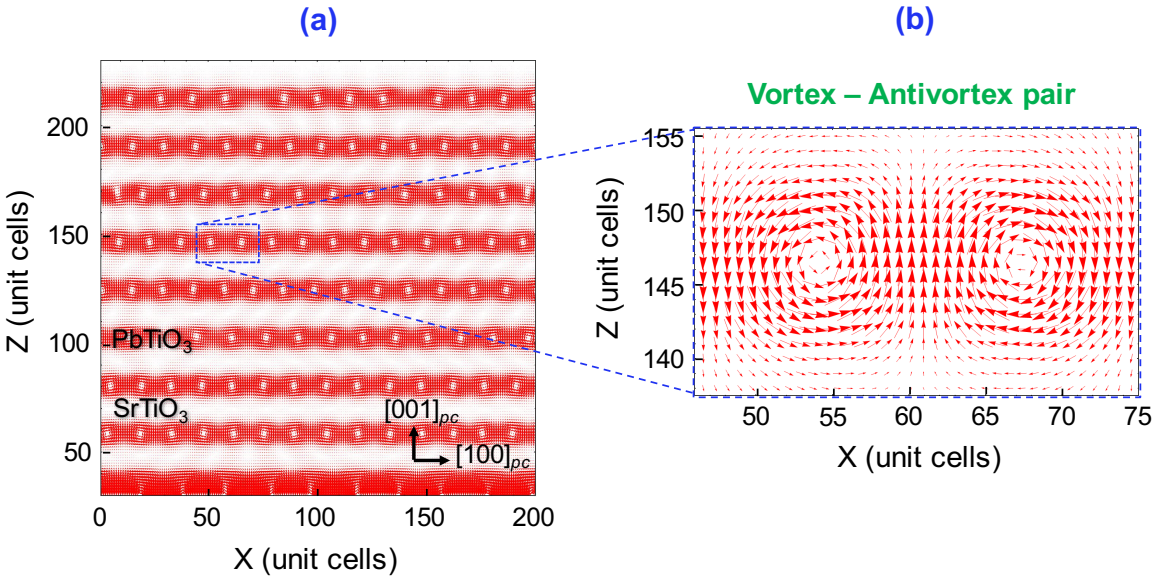

Figure 5.13: Phase-field simulations for a 10 x 10 PTO-STO superlattice epitaxially strained on a DSO (110) substrate is shown in (a), which suggests existence of array of vortex-antivortex pairs (b) present in PTO layers of the superlattice structure. Courtesy of Zijian Hong, Penn State University.

Thus, using various theoretical frameworks the existence of polarization vortices in nanostructures such as nanodots, nanorods, superlattices *etc.*, have been predicted. The findings of these studies suggest that there is a critical size range for these nanostructures, within which polarization vortices are predicted to exist. This further suggests that various energies involved (depolarization, elastic, electrostatic, landau) are competing with each other and their magnitude depends critically on size of the nanostructure. From the various theoretical approaches discussed, one particular approach *i.e.* Phase-field model was applied to PTO-STO superlattice structure to explain the phenomenon more comprehensively.

5.3 Experimental observation of Polarization Vortices in $PbTiO_3$-$SrTiO_3$ Superlattices

5.3.1 Background

Motivated by several theoretical predictions on the existence of non-uniform polarization modes in nanostructures, many experimental studies have been devoted for the search for such novel states. As these predictions are made for reduced dimension of ferroelectric material, thin-films [166; 439; 440] and superlattices [62] were mostly

targeted to search for this phenomenon. In thin-films, most of these efforts were based on direct observation of polarization patterns using high-resolution atomic-scale polar displacement mapping [166; 439; 440]. Although these studies have observed some signature of inhomogeneous polarization distributions, they were primarily enabled by the presence of an interface(s) which are formed between two (or more) ferroelectric domains walls within a material [439; 440], or, between a ferroelectric and dielectric (or metallic) material [166; 441]. Recall that ferroelectric domain walls are known to contain inhomogeneous polarization profiles and they contribute only partly to the total free energy, which may have equal (or more) contribution coming from uniform polarization regions. Thus, the above studies do not necessarily represent the stabilization of novel ferroelectric ground states, where there are no regions of uniform polarization. Superlattices such as PTO-STO, were also studied using TEM- and Synchrotron X-ray diffraction-based studies to understand the lattice distortions associated with inhomogeneous polarization distributions [62]. Despite prediction of ferroelectric vortices in PTO layer of PTO-STO, previous studies did not reveal the direct, unambiguous observation of polarization vortices. Interestingly, we note that ultra-thin periods (1 x 1, 2 x 3) of PTO-STO superlattices grown on STO (001), *i.e.* almost 0% strain state, stabilized a novel ferroelectric ground state (Figure 5.14) which showed emergence of novel phenomenon – 'improper' ferroelectricity, in the superlattice structures. The improper nature of the ferroelectricity in these ultra-thin superlattices was attributed to the order parameter associated with the tilting of oxygen octahedral in STO layers. A close observation of the theoretical work presented [86] to explain improper ferroelectricity in ultra-thin PTO-STO superlattices grown on 0% strained substrate, were extended to those grown on tensile-strained substrate (Figure 5.14). From Figure 5.14, one can conclude that the first-principle calculations is predicting another novel ground state in the tensile region with respect to STO misfit strain (indicated by dotted blue, with space group $Pmc2_1$). Surprisingly, the experimental efforts to observe this other novel ground state were largely missing. Although the calculation was performed for a 1 x 1 superlattice, one would expect the strain to play a significant role similarly in stabilizing fundamentally different ferroelectric ground states in relatively thicker period superlattices. As will be discussed more in this and the next chapter, the tensile strain was the key enabler in stabilizing novel polarization states associated with epitaxial-strained PTO-STO superlattices.

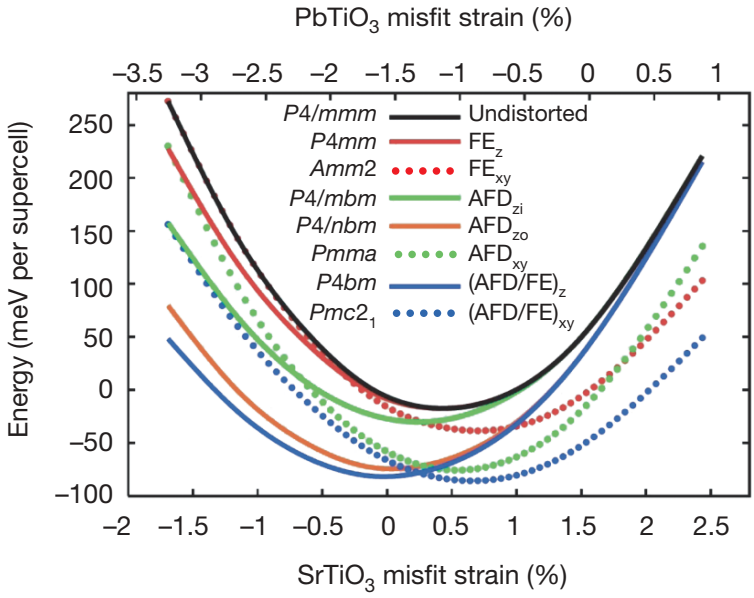

Figure 5.14: First-principles calculations for a 1 x 1 PTO-STO superlattice epitaxially strained on a substrate is shown, illustrating the relative stability of various instabilities (individual or coupled) with respect to misfit strain for respective STO and PTO layers in the superlattice structure. From [86].

It is important to mention a large number of studies reporting the formation of *vortex-like* domains patterns via Piezo Force Microscopy-based measurements. These studies were preformed on nanostructured ferroelectric samples with thicknesses ranging from few tens to hundreds of nanometer [440; 442; 443], or bulk samples such as BTO single-crystal lamella [444], where the ferroelectric domain structure observed under PFM was appearing to form a vortex-like domain structure, sometimes also referred as *flux-closure* domain structure [445-447]. The typical size of these flux-closure domains can range from tens to hundreds of nanometer or more [385; 448]. More recently, a periodic array of such flux-closure domains was reported in PTO layers of PTO-STO heterostructures [440]. In all of these studies, one would find that uniformly polarized regions or ferroelectric domains of size more than tens of nanometer form *flux-closure* or *vortex-like* domain structure. Such structures will again not represent the true vortex structure formed using completely non-uniform polarization distribution as predicted by several theoretical models. Thus, when the thickness of the ferroelectric material was relatively thick (more than few nanometers), they were observed to stabilize a domain morphology composed of uniformly polarized ferroelectric domains and domain walls, and when it was relatively thin (few unit cells) other interfacial phenomena were observed to decide the ferroelectric ground states. Therefore, along with the critical size dependence, the choice of the appropriate structure, ferroelectric material, its orientation and the strain state will all determine the observability of spatially non-uniform polarization modes.

5.3.2 Experimental Methods

Superlattices of $(PTO)_m/(STO)_n$ (short notation: '*m* x *n*') were synthesized via RHEED-assisted PLD, where '*m*' and '*n*' refers to the thickness in unit cells of respective materials oriented in the $[001]_{pc}$ (psuedocubic) direction. Superlattice with periodicities ranging from 2 x 2 to 27 x 27 were grown on a $(001)_{pc}$-oriented DSO and (001)-oriented STO substrates. STO substrates were first chemically treated with buffered HF and then heat treated at 1000°C for 3 hrs in flowing O_2 to obtain TiO_2-terminated STO substrate [154; 295]. DSO substrates were heat-treated at 1000°C for 4 hrs to obtain atomically-flat surface with (pseudocubic) unit-cell step height [299]. On both STO and DSO substrates, 100 nm thick superlattice films were grown at the chamber pressure of 100 mTorr and growth temperature of 630°C. PLD growth of PTO layers were achieved using a polycrystalline target having 20% excess Lead (Pb), *i.e.* using a target of composition $Pb_{1.2}TiO3$. The choice of the excess lead was found to be critical in stabilizing layer-by-layer growth of PTO layers. On the other hand, STO layers were grown using stoichiometric single crystal target. The laser fluence for both $Pb_{1.2}TiO_3$ and STO was set to 1.5 J/cm^2. Prior to growth of superlattices, a buffer SRO layer was grown at a growth pressure of 50 mTorr, growth temperature of 700°C and laser fluence of 1.5 J/cm^2. The SRO buffer was crucial in stabilizing in layer-by-layer growth of PTO and will be discussed in detail in the next section. After the growth of superlattice structure at 630°C, films were cooled down to room temperature at an oxygen pressure of 50 Torr to ensure full oxidation of oxide layers in superlattice structure. These superlattice films were characterized by both *in situ* and *ex situ* characterization techniques. RHEED was used as the *in situ* characterization method to monitor the layer-by-layer growth mode and thickness of individual layers. The RHEED oscillations were monitored for specular spots along $[\bar{1}10]$ (in-plane) direction of DSO and $[100]$ direction of STO substrate. Structural characterization of the superlattice films grown on DSO and STO, were achieved by Laboratory-based XRD and Synchrotron-based XRD methods. RBS was also used to confirm the stoichiometry of the films. High-resolution Scanning Transmission Microscopy (HRSTEM) was used to map polar lattice distortions present in the individual layers of PTO-STO superlattice.

5.3.3 Results and Discussion

Similar to previous superlattice growths discussed in chapter 4, first step was to optimize the growth parameters of individual components of the superlattice structure before growing superlattices of PTO-STO with varying periodicities. As mentioned earlier, the choice of substrate in-plane lattice parameter plays a crucial role in obtaining controlled synthesis of these materials, and thus, chosen carefully. In order to eliminate strain-effect when optimizing the growth, one would like to choose a substrate with in-plane lattice parameter as close to the film, ideally 0% misfit strain. In the case of optimizing growth parameters of PTO, (001)-oriented STO substrate becomes a perfect choice because its cubic lattice parameter, 3.905 Å, matches very closely with in-plane lattice parameter of

(001)-oriented PTO, 3.904 Å. In addition, this will facilitate growing PTO-STO superlattice structure with 0% in-plane misfit strain. Moreover, since the substrate surface can chemically- and thermal-treated to obtained single-termination (TiO_2) surface [154] further allows the growth of PTO to be highly controlled.

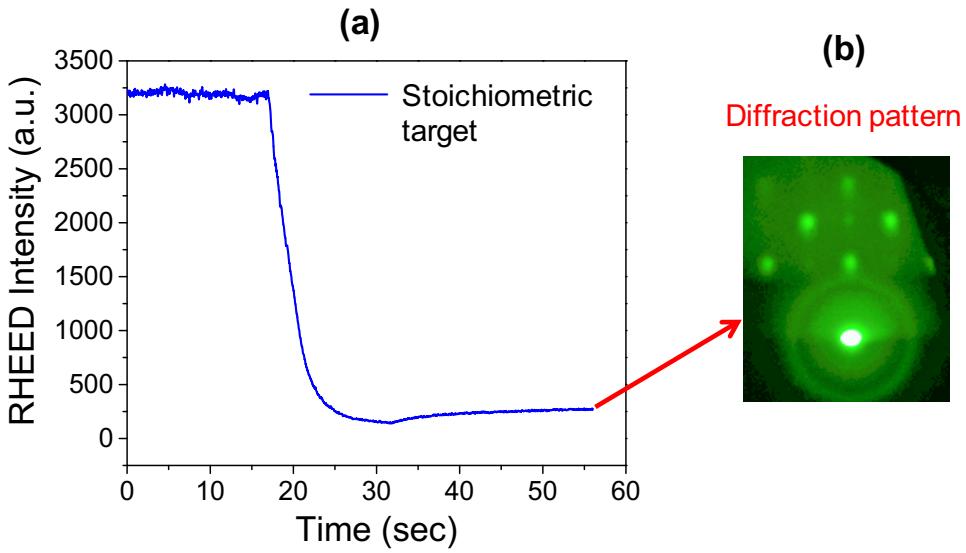

Figure 5.15: Variation of RHEED intensity corresponding to the growth of PTO from a stoichiometric polycrystalline target is shown in (a), along with a RHEED pattern observed at the end of the growth.

Since PbO is very volatile, most thin-films studies of PTO or doped-PTO (Example: $PbZr_{0.2}Ti_{0.8}O_3$ (PZT)) grown via PLD have observed a rapid transition to 3D growth mode when the growth begins [142; 449-451]. In order to synthesize superlattice structures with atomically sharp interfaces, it becomes almost a necessity to have the growth mode to be 2D or layer-by-layer, to ensure unit-cell-by-unit-cell accurate control of deposition of the individual components of the superlattice structure. Thus, allowing the growth of structures from ultra-thin period (2 x 2) to thick-period (27 x 27) superlattices with both high accuracy and repeatability. Now, when I used stoichiometric composition of PTO, *i.e.* Pb:Ti is 1:1, in the polycrystalline target to grow PTO on TiO_2-terminated STO (001) substrate via RHEED-assisted PLD, the diffraction pattern quickly transitioned to 3D as indicated by the RHEED pattern showing the 3D spots (see Figure 5.15(a)) corresponding to island growth of PTO pattern. If the key reason for the 3D growth were the high evaporation rate of PbO from the surface, one would naturally think to decrease the evaporation rate by increasing the oxygen pressure of the chamber or lowering temperature of the substrate. I varied growth parameters such as temperature and pressure to stabilize the 2D growth of PTO, but these attempts were largely unsuccessful. Even though the growth mode of PTO remained 3D with stoichiometric target, I was able to find the growth window in which good quality thin-films of PTO as characterized from X-ray diffraction and AFM, can be

grown. Now, instead of trying to lower the evaporation rate, I tried a different approach in which the flux of 'Pb' adatoms on the substrate was increased to suppress the effect of high volatility of PbO on the growth kinetics of PTO. This was achieved by increasing the 'PbO' content in the polycrystalline target of lead titanate to increase the flux of 'Pb' ions on the surface of the substrate. I found that when the lead content in the polycrystalline target was increased to a stage where the target became 20% rich in lead, *i.e.*, $Pb_{1.2}TiO_3$, the growth of PTO on TiO_2-terminated STO substrate did not go to 3D for sufficiently longer period time, under the optimized growth window found earlier. On continuing the same growth run and monitoring the growth using RHEED, I started observing RHEED oscillations (see Figure 5.16, Inset (a)) during the growth and accordingly the RHEED pattern changed to 2D (see Figure 5.16, Inset (b)). Thus, the use of lead-enriched polycrystalline PTO target was the key in enabling the layer-by-layer growth of PTO on treated STO substrate.

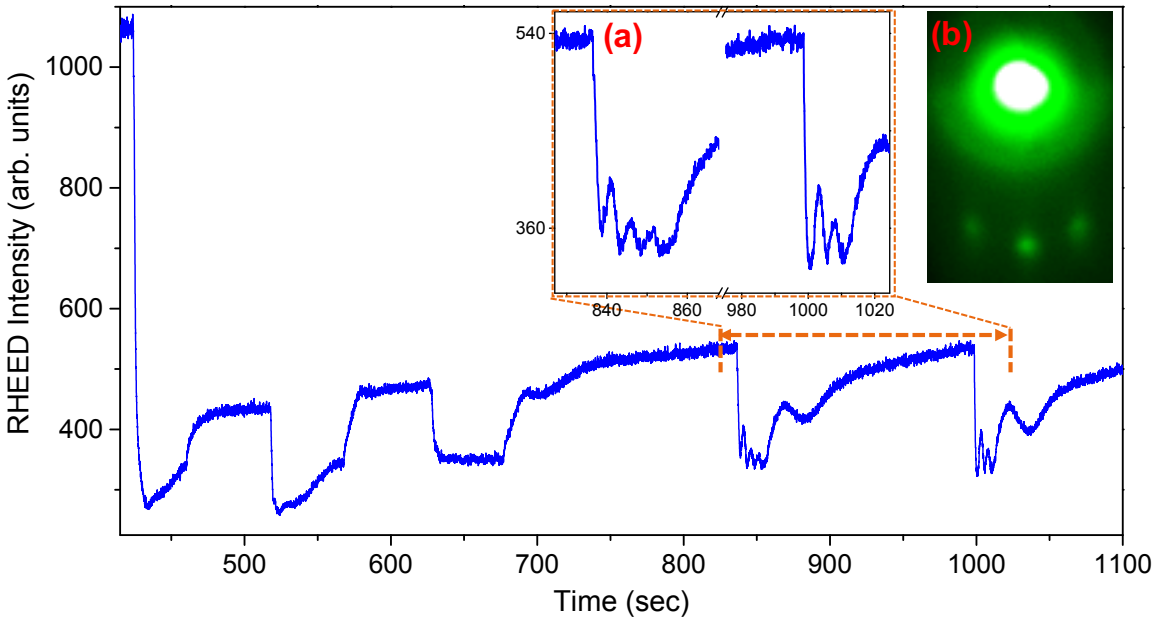

Figure 5.16: Variation in RHEED intensity during the growth of PTO from a 20% lead-rich PTO target on TiO_2-terminated STO substrate is shown. Inset (a) shows the zoomed-in region to highlighting the 2D growth mode, while inset (b) shows the RHEED pattern after continuing the layer-by-layer growth till 13 nm.

In an ideal scenario, one would like to have good control from the beginning of the growth, *i.e.* to use the atomic-steps of the (STO) substrate as the starting surface for the layer-by-layer growth of PTO. Recall that when I began the growth of PTO using lead-rich target, the starting, *i.e.* terminating, layer of the (001)-oriented STO substrate was TiO_2-atomic plane. In that case, when the first unit cell starts nucleating on the TiO_2-terminated surface, first atomic plane will be PbO-atomic plane as this will be more energetically favorable configuration. My hypothesis was that if I can switch the termination of the substrate to SrO-terminated; the first atomic plane of nucleating (PTO) phase will be TiO_2,

which are less volatile and much more stable than PbO. Now, there are number of ways in which one can switch the termination of treated STO substrate from TiO_2-terminated to SrO-terminated as discussed in literature [107; 452; 453]. I adopted the approach of using SRO growth on TiO_2-terminated STO substrate to switch the termination [107]. The growth kinetic of SRO on TiO_2-terminated STO allowed us to switch the termination by growing just one (or two) RHEED oscillation of SRO. Note that when SRO is grown on a TiO_2-terminated STO substrate, one would expect it to start from SrO-plane and end with RuO_2-plane. But, in reality, the first RHEED oscillation is always found to take 50% more time than the subsequent oscillations. The complex growth dynamics of SRO is discussed elsewhere [106; 113; 454]. In general, by growing one or two RHEED oscillations of SRO, it has been shown by various characterization techniques that the termination of the end layer can be switched from TiO_2-plane to SrO-plane [107]. So, I grew SRO corresponding to one RHEED oscillation on TiO_2-terminated STO substrate under optimized condition. To further support our hypothesis that SrO-termination is most crucial component, I grew 5 unit-cell of STO on the previously grown one RHEED oscillation of SRO, which will ensure that SrO-termination is kept preserved and the underlying layer is STO (not SRO). When PTO was grown on this stack of STO/SRO buffer layer using 20% lead-rich target and under the optimized condition, I found the PTO to start growing layer-by-layer immediately. Note that similar results were found for (001)-pseudocubic oriented DSO substrate, where similar termination switching was observed to assist in obtaining layer-by-layer growth directly (Figure 5.17). Thus, the terminating layer of the substrate was found to be another important factor in achieving controlled synthesis of PTO.

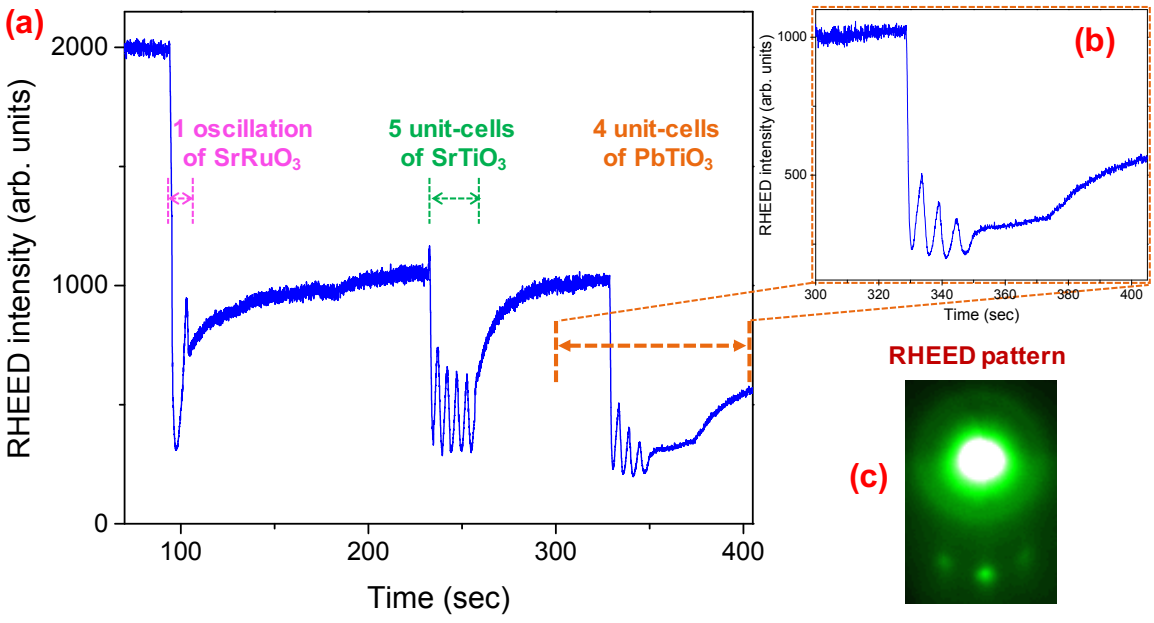

Figure 5.17: RHEED oscillations for 1 oscillation of SRO, 5 unit-cells of STO and then 4 unit-cells of PTO grown in that order is shown in (a), along with a zoomed-in section for

4 unit-cells PTO growth in (b). RHEED pattern after growing PTO layer-by-layer up to 13 nm is shown in (c).

After finding the recipe for the controlled-growth of PTO, the conditions for the growth of other component of the superlattice was optimized to find the overlap with the growth window of PTO. The use of STO as the other component of the superlattice greatly simplified this task as this material has very large growth window for obtaining RHEED-controlled growth. The growth condition for the superlattice is further narrowed down by the condition, which allowed sustainable RHEED oscillations for the growth of the PTO-STO superlattice. Under these optimum conditions, I grew superlattices of various periodicities ranging from 2 x 2 to 27 x 27. To provide an example, Figure 5.18(a) is showing RHEED oscillations for five periods of a 6 x 6 superlattice grown on DSO substrate. The RHEED oscillations of just one period are magnified in Figure 5.18(b) for better illustration. The sustainability of RHEED oscillations allowed us to synthesize superlattice structures, with varying periodicities, up to 200 nm thick films, maintaining layer-by-layer growth throughout the entire growth of the superlattice structure.

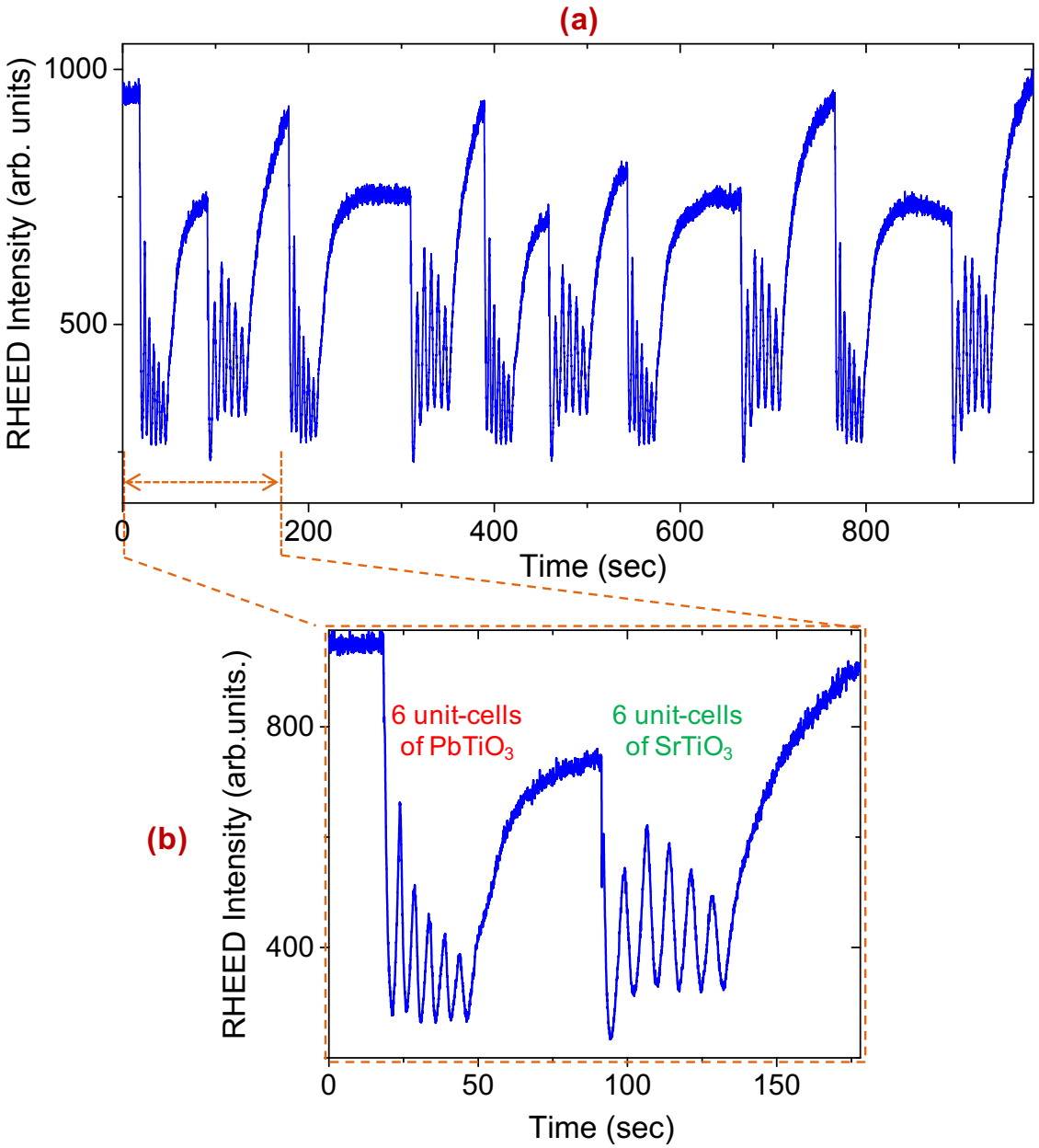

Figure 5.18: RHEED oscillations for five periods of a 6 x 6 PTO-STO superlattice grown on a DSO (110) substrate is shown in (a), along with a zoomed-in graph (b) showing oscillations for only one period. From [168].

Since I've used lead rich target to synthesize PTO, we measured the stoichiometry of PTO film using RBS to ensure there is no excess or deficiency of lead in the grown-PTO layers. Using the above described growth process and optimized growth condition; I grew 200 nm thick PTO on $(001)_{pc}$-oriented $GdScO_3$ substrate. The RBS spectrum of a 200 nm PTO film on $GdScO_3$ substrate along with the simulated spectrum is shown in Figure

2.37. Using the SIMNRA software package, the RBS spectrum was simulated and corresponding composition of the film was extracted. To evaluate the accuracy of the fit, R^2 analysis was done which for this case shows pretty good fit. The extracted composition of PTO confirmed that the films are stoichiometric and eliminated any spurious effects, which an off-stoichiometry may cause on the observations presented in this chapter.

After synthesizing superlattice films of STO/PTO with various periodicities with *in situ* characterization using RHEED, *ex situ* characterization to confirm the structural order in these films was performed by detailed X-ray diffraction measurements. First, using laboratory-based X-ray diffraction set-ups, I've characterized the crystallinity, structural order and strain state of the superlattices films. As a representative example, a high-resolution, *θ-2θ* symmetric scan of 100 nm-thick 10 x 10 superlattice is shown in Figure 5.19(a), where the presence of superlattice peaks ($SL_{(-1)}$ 002 and $SL_{(+1)}$ 002) along with their relative '*2θ*' position with respect to the central Bragg peak ($SL_{(0)}$ 002) confirmed the superlattice structural order in the out-of-plane direction ($[001]_{pc}$) and the periodicity corresponding to a 10 x 10 period. One can also notice the presence of thickness fringes, also known as *Pendellösung* fringes, around the Bragg ($SL_{(0)}$ 002) and superlattice peaks ($SL_{(-1)}$ 002 and $SL_{(+1)}$ 002), which attests to the precise nature of the interfaces, smoothness of the films and high crystallinity of the films. These superlattice films were checked with asymmetric scans (RSMs) to ensure that 100 nm-thick films are strained to the substrates. Figure 5.19(b) shows a representative RSM scan of a 6 x 6 superlattice around DSO $(113)_{pc}$ substrate peak. These RSMs confirm that the films are coherently strained to the substrate eliminating any effect of films relaxations on the results discussed in this chapter.

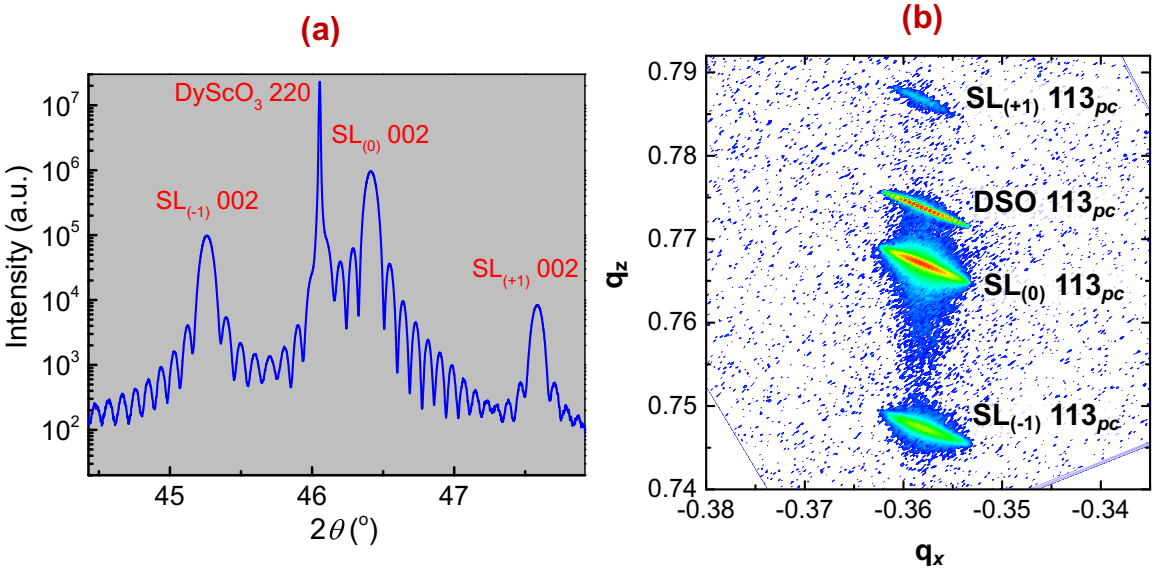

Figure 5.19: (a) A high-resolution symmetric XRD scan of a 10 x 10 PTO-STO superlattice [168] and a RSM around 113_{pc} of 6 x 6 PTO-STO superlattice (b), grown on DSO (110) substrate, are shown.

These superlattice films were also characterized by Synchrotron-based X-ray diffraction set-up to characterize features, which are extremely difficult to measure in laboratory-based XRD owing to their weak diffraction strength as compared to crystalline structural order (as discussed above). Thus, requiring a very strong source of X-ray to enable detection of weakly diffraction peaks associated with the novel features found in these superlattices. The advantage of using synchrotron-based X-ray diffraction set-up is that it allows acquiring diffraction peaks within a three-dimensional (3D) volume surrounding around a reciprocal lattice point. These full 3D reciprocal space maps can provide symmetric line scans and asymmetric scan around that respective lattice point allowing us to perform structural characterization in great depth. Symmetric line scans of superlattice films obtained from these synchrotron-based RSMs, showed the presence of many orders of superlattice reflections suggesting exceptionally high long range structural order with sharp interfaces (a representative line scan of a 16 x 16 superlattice is shown earlier, Figure 2.23). From the asymmetric scans, *i.e.* a two-dimensional cut from a 3D scan showed that the superlattice films are strained to the substrate (similar results were found using laboratory-based XRD as well, Figure 5.19 (b)). Figure 5.20 shows a representative example of 2D RSM map (or, in this case an LK-cut) of a 12 x 12 superlattice grown on a DSO (110) substrate. In addition to superlattice reflections present in the out-of-plane direction (L, $[001]_{pc}$) corresponding to the superlattice period, the presence of side-lobe diffraction peaks along the in-plane direction (K, $[010]_{pc}$) are also observed, which also corresponds to a 9–10 nm periodicity. This periodicity is arising from the polarization vortex ordering the PTO layers of PTO-STO superlattices and will be discussed in detail next.

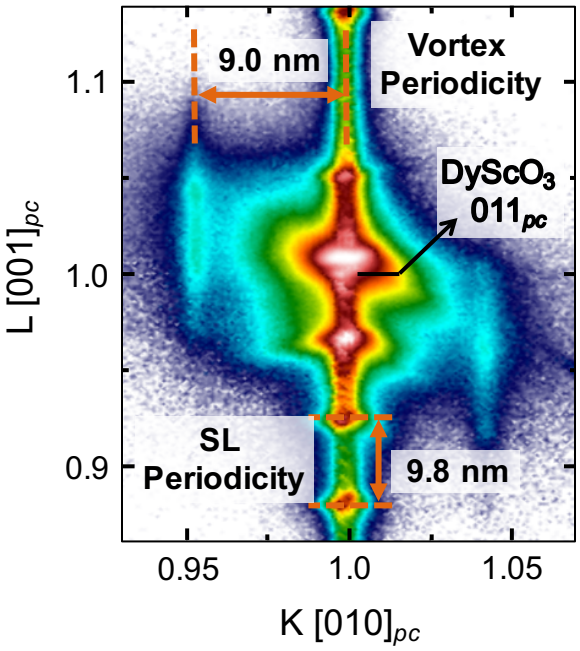

Figure 5.20: A 2D reciprocal space map, *i.e.* an LK-cut from 3D RSM around DSO 011_{pc} peak, of a 12 x 12 PTO-STO superlattice film grown on DSO (110) is shown. From [168].

High-resolution STEM was also employed to characterize the nature of PTO-STO interfaces in these superlattice films. A representative example is shown in Figure 5.21, which corresponding to a 10 x 10 superlattice grown on a DSO substrate with SRO buffer layer. Figure 5.21(a) is a low-magnification Z-contrast STEM image, which reveals the uniformity of superlattice structure, *i.e.* periodic stacking of PTO and STO layers, in these films. On the other hand, an atomic-scale high-resolution STEM image, shown in Figure 522(b), confirms the coherent and abrupt nature of interfaces present in these superlattice films.

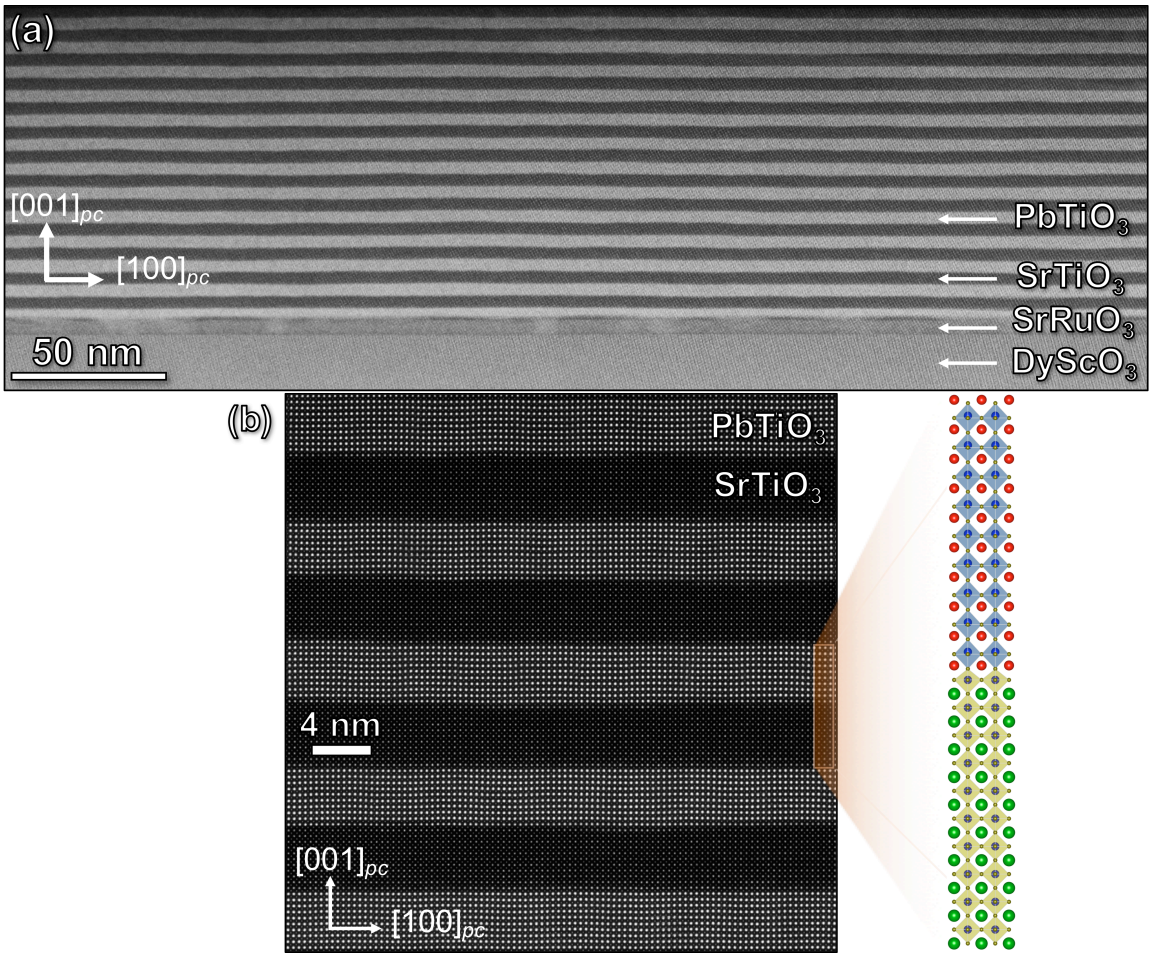

Figure 5.21: Low magnification STEM image of a 10 x 10 PTO-STO superlattice grown on a DSO (110) substrate is shown in (a), while (b) shows a High-resolution Z-contrast HAADF image of a sub region of the same 10 x 10 PTO-STO superlattice along with a schematic of one period of the superlattice structure. In the schematic, PTO (top) is drawn for the case of a $[001]_{pc}$ (upward) polarization, which results from the downward displacement of the Ti "centered" oxygen octahedral relative to Pb (Pb, red; Ti, blue; O, dark yellow). From [168].

Having established the high structural quality of the individual layers and the coherency of the interfaces as a function of superlattice periodicity through a combination of *in situ* RHEED analysis, X-ray diffraction and STEM imaging, I then proceeded to explore the atomic-scale evolution of the structural distortions and the feature responsible for the observed in-plane diffraction peaks. To do this, we combined atomic-resolution, cross-sectional STEM imaging (for example Figure 5.21(b)) from which we can extract local structural distortions in both the PTO and STO layers together with a vector-mapping algorithm (details of this algorithm are discussed elsewhere [166]) to understand the nature of local polarization evolution in various superlattice structures.

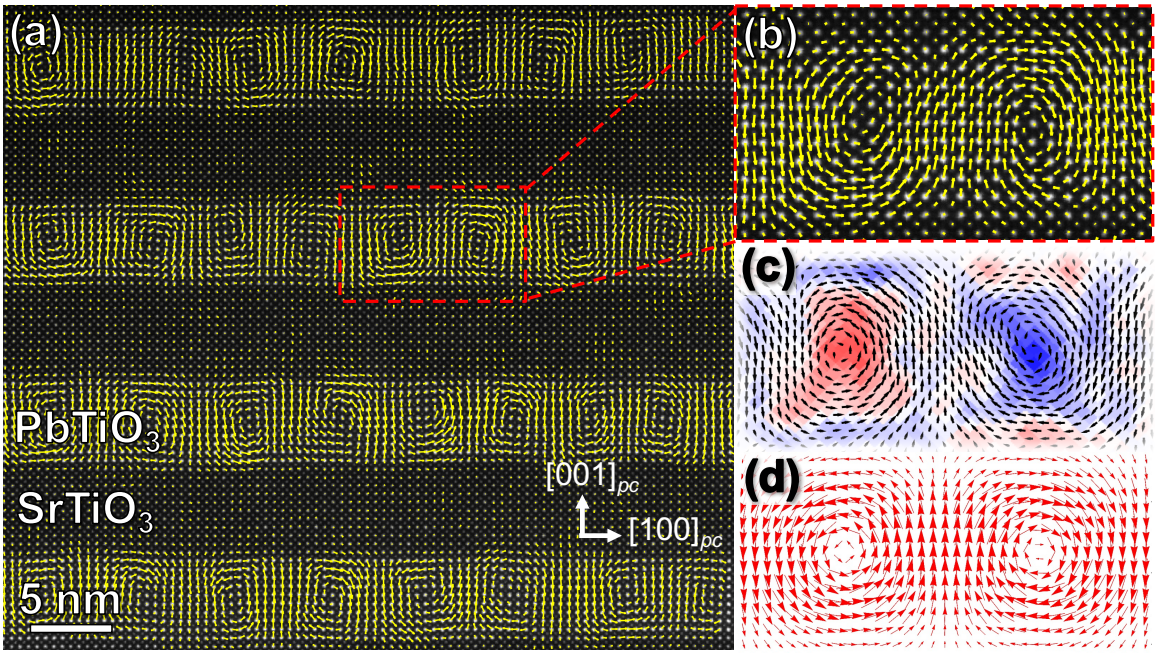

Figure 5.22: Cross-sectional HAADF STEM image with an overlay of the polar displacement vectors (yellow arrows) for a subregion of 10 x 10 PTO-STO superlattice showing an array of vortex-antivortex pairs, present in each PTO layers of the superlattice structure is shown in (a). A magnified image of a single vortex-antivortex pair (b) shows the full density of datapoints (displacement vectors are shown for both Pb-atoms and Ti-atoms) and the continuous rotation of the polarization state within such vortex-antivortex pairs. The curl of the polar displacement $(\nabla \times \boldsymbol{P_{PD}})_{[010]}$ for the same vortex-antivortex pair (c) reveals the alternating rotation directions the structures. Polarization distribution from a phase-field simulation of the same 10 x 10 superlattice (d), predicts vortex-antivortex pairs that closely matches the experimental observations. From [168].

The resulting analysis of the high-resolution STEM data for a 10 x 10 superlattice (corresponding to the STEM image in shown in Figure 5.21(b)) reveals interesting features: namely that the polarization in the PTO layer forms relatively long range, ordered arrays of vortex-like structures (Figure 5.22(a)). The yellow arrows indicate the polar displacement of respective atom located at that site. In Figure 5.22a, for better illustration, only 'Pb' site displacements have been plotted. A closer examination of these vortex patterns (Figure 5.22(b)), reveals that they are comprised of vortex-antivortex pairs, with a lateral width of approximately the superlattice periodicity. Here in Figure 5.22(b), note that the displacements corresponding to both 'Pb'-site and 'Ti'-site has been plotted. We also note that these vortices represent a continuous rotation of the local polarization vector, as predicted by number of theoretical studies, in contrast to macro scale domain-based vortices such as flux-closure-type domains [440; 444], uniformly polarized domains [442; 455]. The average spacing between these vortex-antivortex cores is ~ 5 nm and the vortex-

to-vortex core spacing is ~ (9-10) nm; matching closely the observed in-plane periodicity in the RSMs and suggesting that the periodicity arises from long-range ordered vortex states in the superlattice structures. To better understand the nature of these vortex-antivortex states, we carried out phase-field modeling of the polar state as a function of superlattice periodicity as discussed earlier (Courtesy of Prof. Long-Qing Chen). The corresponding phase-field calculated image for the same superlattice structure (Figure 5.22(c)) reveals strikingly close agreement to the experimentally obtained map of polarization. To quantify the vorticity of these structures, we have also extracted the curl of the polarization $(\nabla\times\boldsymbol{P}_{PD})_y$ from the experimental data for one vortex-antivortex pair, which is identified in red-blue coloring (Figure 5.22(d)). This illustrative pair clearly shows that the neighboring vortices have the opposite sense and uniformity of rotation.

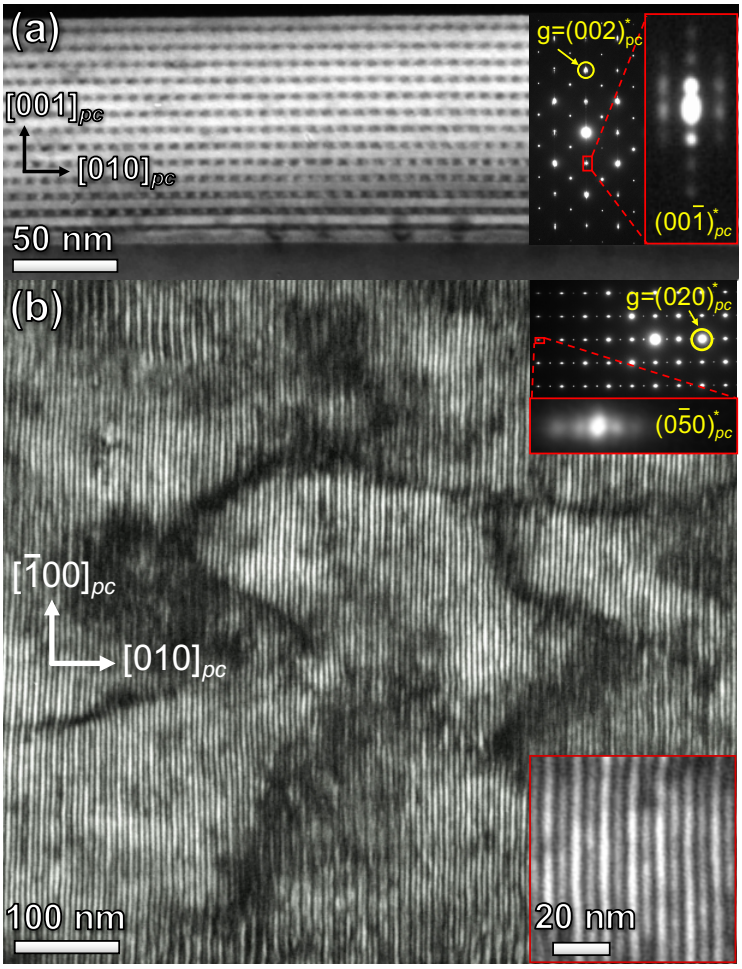

Figure 5.23: (a) Cross-section, DF-TEM images of a 10 x 10 PTO-STO superlattice revealing long-range ordering of vortices (where each bright/dark modulation corresponds to a period of the vortex-antivortex structure). The inset shows a SAED pattern for the sample with the g-vector of the two-beam imaging condition indicated by the yellow arrow.

Close inspection of the SAED pattern reveals superlattice reflections both in- and out-of-the plane suggesting long-range ordering of the vortex structures (magnified $(00\bar{1})_{pc}$ reflection inset). (b) Planar-view DF-TEM imaging of a 16 x 16 superlattice which likewise exhibits long-range in-plane ordering associated with the vortex-antivortex pairs along the $[\bar{1}00]_{pc}$ and confirms the widespread occurrence of these vortex pairs in the superlattice films. The upper inset shows the SAED pattern for the sample with the g-vector of the two-beam imaging condition indicated by the yellow arrow. Again, close inspection of the diffraction pattern reveals in-plane superlattice reflections indicating long-range ordering of the vortex structures. The lower inset shows a magnified view of the vortex structures – again revealing ~10 nm periodicities. From [168].

To further establish the long-range nature of such polarization vortices we studied the same sample using low magnification, dark-field imaging using a strongly excited $[\bar{1}10]_o$ g-vector (*i.e.*, a 2-beam condition). In turn, I observed a periodic, long-range array of "spots" (Figure 5.23(a)), with each spot corresponding to a vortex or antivortex. Again, the spacing between the bright spots is closely matched to that calculated from the X-ray RSM studies (*i.e.*, the in-plane satellite reflections, ~ (9-10) nm for the 10 x 10 superlattice). Thus far I have focused only on the nature of these vortex-antivortex states as imaged along the cross-sectional $[001]_o$ zone axis, we now turn to explore the layout of the vortices within the plane of the sample, using planar section TEM imaging along the $[110]_o$ zone axis of the DSO. A relatively large area image (~ 1x1 micron) view of a 16 x 16 superlattice (Figure 5.23(b)) reveals lattice fringe-like contrast across the entire sample, which are ordered along the $[\bar{1}10]_o$ of the DSO substrate. The measured spacing of the fringes is ~10 nm, which is illustrated in the higher magnification section (inset, Figure 5.23(b)) and is consistent with the periodicity measured from the cross-section image and in the RSMs. Last, from these dark-field TEM studies, I observed that these vortex structures exist along both in-plane directions as suggested by the two perpendicular zone-axis dark-field TEM images (see Figure 5.25).

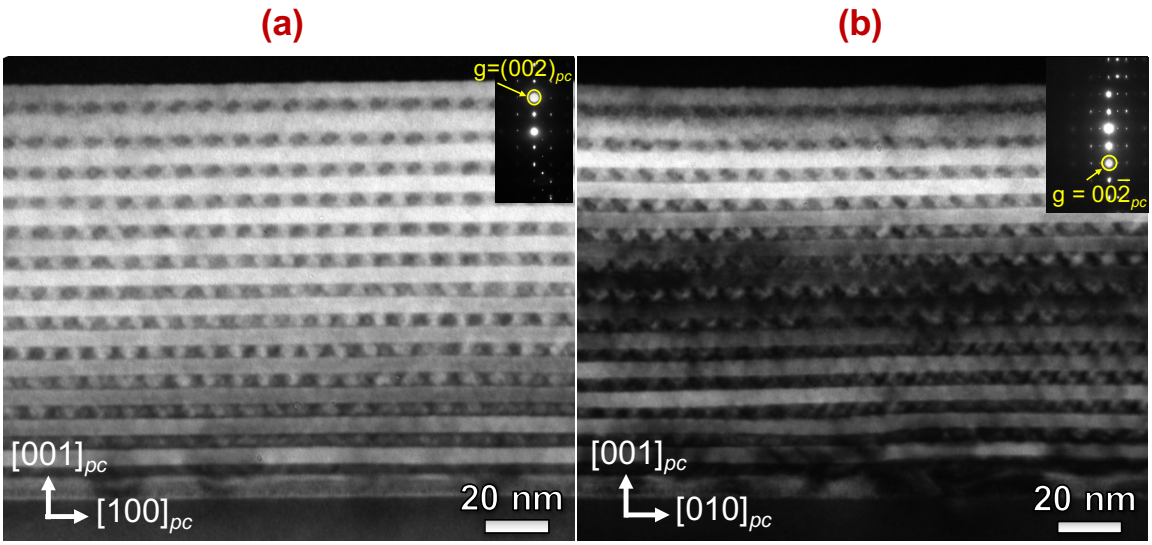

Figure 5.24: (a) Cross-sectional DF-TEM of a 10 x 10 PTO-STO superlattice taken along $[010]_{pc}$ zone axis (inset shows the SAED diffraction pattern at-tilt along with *g*-vector for image formation). (b) Cross-sectional DF-TEM of the same 10 x 10 superlattice sample taken orthogonal $[001]_{pc}$ zone axis (inset shows SAED diffraction pattern at-tilt along with g-vector for image formation). From [168].

Phase-field modeling of the PTO-STO superlattices was performed to study the energetics and to ascertain the 3D structure of the vortex–antivortex pairs. A range of superlattice periodicities were simulated, allowing each to evolve from a random initial state according to the time-dependent Ginzburg–Landau equation, as described earlier. More details about 3D simulation and parameters used therein can be found in [414]. The 3D polarization distribution in the 10 × 10 superlattice, corresponding to our experimental HR-STEM studies, is shown in Figure 5.25. With no *a priori* assumption of the polarization (***P***) distribution in these superlattice structures, the phase-field model was found to converge to an array of vortex–antivortex structures in each PTO layers of a STO/PTO superlattice. For comparison, sub-regions of the HR-STEM polar displacement map and planar-view dark-field TEM images are projected on the same 3D axes as the model (Figure 5.25). The tubular, ordered vortices, predicted from models, match closely with the experimentally observed polarization structures. The polarization rotation extracted from the phase-field models is mapped onto the *xz* plane and in 3D isosurfaces using a red/blue colour scale (see Figure 5.25) corresponding to alternating clockwise (vortices) and counterclockwise (antivortices) according to the $(\nabla \times \boldsymbol{P})_{[010]}$ curl of the polarization. The figure has two additional slices, *i.e. xz* planes, through the 3D polarization structure, which shows the polarization (***P***) components along the $[100]_{pc}$ ($\boldsymbol{P}_{[100]}$) and $[001]_{pc}$ ($\boldsymbol{P}_{[001]}$) using a green/yellow color scale. Similar to polar displacements from the HR-STEM, the model lacks discrete ferroelectric domains and, instead, exhibits a smooth rotation of the polarization forming vortex structure. The long-range order is also in good agreement with

the experiments and is exhibiting some degree of interlayer alignment with matching curl of polarization.

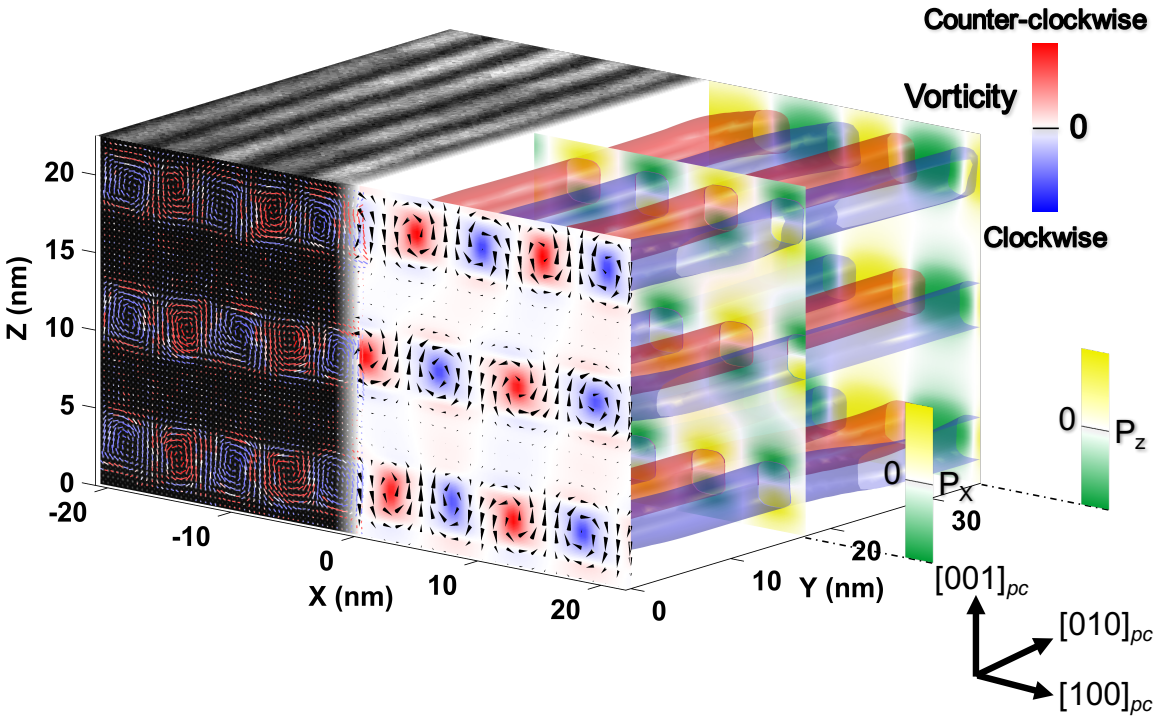

Figure 5.25: The 3D geometry of the vortex-antivortex array from phase-field simulation of a 10 x 10 PTO-STO superlattice is shown. The front cross-section of the model shows the polarization vector ***P*** ordered into clockwise (blue) and counterclockwise (red) vortex-antivortex states which extend along the y ($[001]_{pc}$) axis. **Left**. For comparison, a cross-section HR-STEM image overlaid with a polar displacement vector map and a planar-view DF-TEM image are projected onto the front and top planes of the axes. Red/blue color scales correspond to the curl of the polarization (phase field model) and polar displacement (HR-STEM). Scale bar on P_x and P_z is from [-37.76, 37.76] μC/cm^2 and [-47.45, 47.45] μC/cm^2, respectively, whereas the vorticity is from [-17.07, 17.07] μC/cm^{2}nm (phase field). From [168].

Using both experimental results and phase-film simulations, I explain the observation of vortex structure based on the competition between three different energies: Elastic energy, Electrostatic energy and Gradient energy. The elastic energy, which arises from the fact that the PTO layers in the superlattice structure are epitaxially strained in a tensile manner by the DSO substrate, which traditionally drives the c-axis, oriented PTO to adopt a mixture of in-plane $\boldsymbol{P}_{[100]}$ (or, $\boldsymbol{P}_{[010]}$) and out-of-plane $\boldsymbol{P}_{[001]}$ polarizations (that is, a *c/a*-type domain structure). Second is the electrostatic energy, which is thought to arise from built-in electric fields (or depolarization fields). At the interface of PTO and STO, there is likely to be a large polarization discontinuity normal to the interface, which drives

existence of bound charges according to $\nabla \cdot \boldsymbol{P} \neq 0$. The last competing energy is the gradient energy, which comes from the energy penalty to change the direction or magnitude of the polarization in an inhomogeneous polarization distribution. In this superlattice system, the competition between these three energies stabilizes a new topology of polarization, in which the structure localizes the in-plane $\boldsymbol{P}_{[100]}$ (or, $\boldsymbol{P}_{[010]}$) components at the superlattice interfaces and forms alternating out-of-plane $\boldsymbol{P}_{[001]}$ components mid-layer of PTO layers, thereby creating a rotating polarization distribution in the in-plane direction of PTO layers.

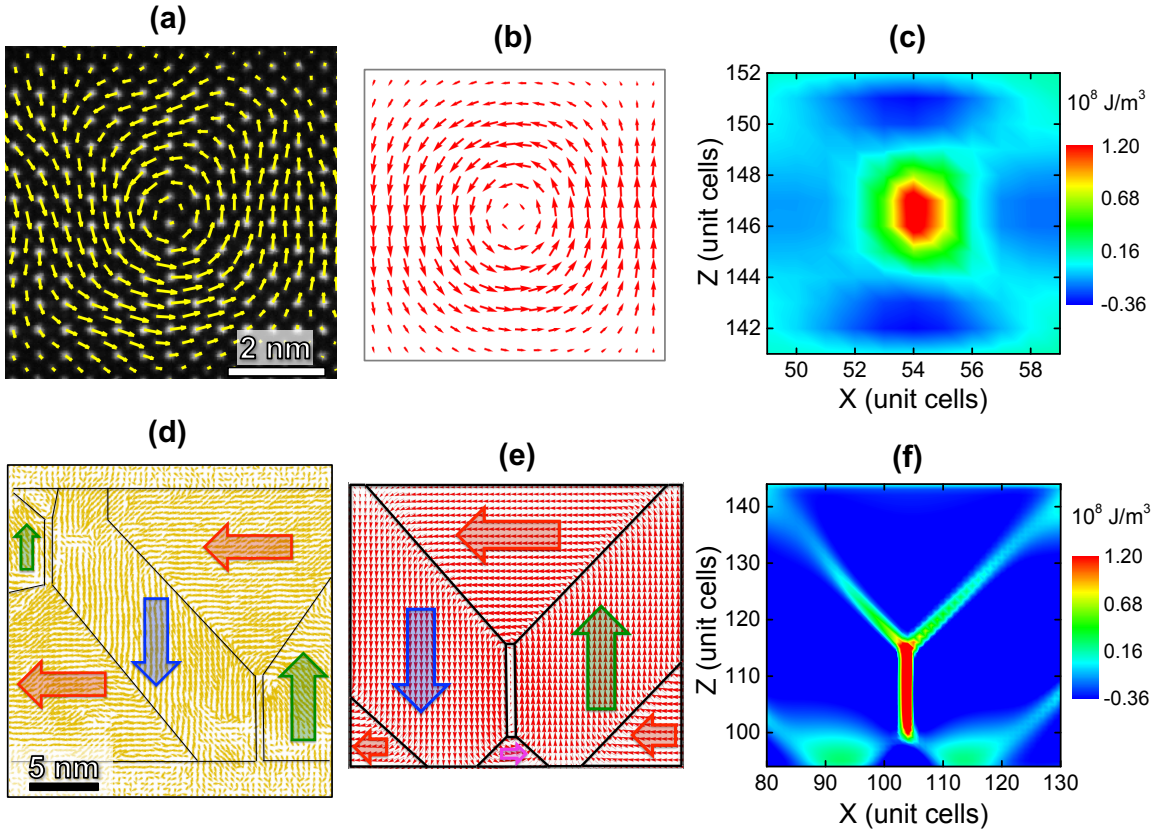

Figure 5.26: (a) HR-STEM polar displacement vector map of a single vortex in a 10 x 10 PTO-STO superlattice. (b) Phase-field calculated polarization vector map of a single vortex in a 10 x 10 PTO-STO superlattice. (c) Total energy density variation within a single vortex in a 10 x 10 PTO-STO superlattice calculated from Phase-field simulations. (d) HR-STEM polar displacement vector map of a 20 nm PTO in a heterostructure having same layer stacking as Tang *et. al.* [440] (e) Phase-field calculated polarization vector map of a flux-closure domain in a 20 nm PTO heterostructure. (f) Total energy density variation within a flux-closure domain calculated using Phase-field simulations. From [168].

As pointed our earlier in theoretical studies predicting vortex structures, the ferroelectric ground state strongly depends on the size of ferroelectric materials. We have

performed phase-field simulations of evolution of polarization vortices with superlattice periodicity. Thus, a complete phase diagram of superlattice period-dependent evolution of ferroelectric ground states was obtained using models. Although, here I will use these calculations for qualitative discussion, in the next the chapter I will provide experimental results on superlattice period-dependent evolution of polarization states and compare it with theoretical models. In short-period superlattices, *i.e.* $n < 10$, the polarization distribution associated with a vortex structure becomes energetically unfavorable and the electrostatic and gradient energy is minimized at the expense of elastic energy by driving the polarization to adopt in-plane $\boldsymbol{P}_{[100]/[010]}$ components (that is, a_1/a_2-type domain structures) only. As the superlattice periodicity in increased to intermediate length scales, *i.e.*, $10 < n < 16$, a discontinuity in the total free energy appears in the phase diagram, as derived from the phase-field models and total energy calculations, and thus a co-existence of the a_1/a_2 and vortex phases is observed. In long-period superlattices, *i.e.* $n \gtrsim 18$, the polarization structure begins to evolve into classical flux-closure-type domain structures, which are characterized by the formation of discrete uniformly polarized domains separated by domain walls having localized polarization gradients. A side-by-side comparison of experimental results and phase-field simulations for a single vortex (in 10 × 10) and flux-closure (in 50 × 50) structures is shown in Figure 5.26. In a vortex structure, polarization is continuously changing about a vortex core-giving rise to a completely inhomogeneous polarization distribution. Such a state is demonstrated using both HR-STEM displacement vector mapping (Figure 5.26(a)) and phase-field simulations (Figure 5.26(b)) in a 10 × 10 superlattice. In flux-closure-type domain structure, on the other hand, regions of homogeneous polarization (with a net non-zero polarization) can be identified, along with domain walls separating those regions. The overall domain morphology is very similar to those observed in bulk materials. For example, free-standing single crystal lamellae of BTO were probed using piezoresponse force microscopy [444] and the results show formation of flux-closure domains at the length scale of micrometers, which are very similar to the domain patterns reported earlier [440] and the one shown in Figure 5.26 for the case of 50 x 50 structure.

5.4 Summary and future directions

Ferroelectric materials are known to exhibit strong coupling between lattice, charge and orbital degrees of freedom. By utilizing the interaction between these degrees of freedom in a ferroelectric-paraelectric (PTO-STO) superlattices, I have produced complex topologies of electric polarization, namely vortex-antivortex arrays, which are reminiscent of spin topologies such as magnetic skyrmions [418], merons [417] *etc.* The experimental observation of polarization vortices provides evidence for long-standing theoretical prediction of such non-uniform polarization states in ferroelectrics nanostructures. The superlattice-period dependent existence of these polarization vortices also agrees with theoretical predictions of size-dependent existence of non-uniform polarization modes in nanodisc/nanorods [371], nanocomposites [430] *etc.*

The experimental findings of this work invite further investigations to improve the understanding of these non-uniform polarization states. For example, the effect of changing the mechanical boundary conditions such as the stiffness of paraelectric/insulating layer for example by replacing STO with softer material such as DSO, changing in-plane epitaxial strain, and changing the symmetric (*n* x *n*) to asymmetric (*m* x *n*) structure of the superlattice *etc.*, on the evolution of polarization vortices. Second, is the controllability of these polarization states achievable with external stimuli such as an electric field or temperature? For example, if the electrical field can be used to switch a vortex to an antivortex (or vice-versa), or switch between vortex to uniform polarization or vice-versa, are the questions, which remain to be answered. Especially, switching the toroidal moment from vortex to antivortex (or vice-versa) using a curling of electric field, is expected to enable tremendous improvement in the storage capacity of non-volatile ferroelectric RAMs [371]. Another example of external stimuli could be temperature, if changing the temperature of the superlattice films can control vortex polarization states. Third, is the studying the fundamental properties of vortex states itself. For example, the origin of optical chirality associated with vortex-antivortex structures, which could potentially open up possibilities of electrical control of optical behavior, remains to be explored. Fourth is the presence of these vortex states on the ferroelectric properties of superlattice structures such as dielectric response, switching dynamics *etc.* In addition, the presence of long-range ordered vortex-antivortex in alternating layers of a superlattice on other physical properties such thermal conductivity across (out-of-plane) and along (in-plane) the superlattice interfaces would be interesting. Thus, there is a huge parameter space in which understanding the nature of their existence, the fundamental properties associated with them, and their effect of other physical properties of the material, are still to be investigated.

The other prospect of stabilizing vortex structure of electrical polarization is the one in which such non-uniform polarization states can be induced in ferroelectric perovskites with other fundamental degrees of freedom such as multiferroic $BiFeO_3$. Previous studies have shown that ferroelectric polarization in $BiFeO_3$ can couple to the antiferromagnetic and canted moment in the material [224]. If the polarization order parameter can be made to undergo a uniform rotation as in the PTO layer, then it is quite conceivable that the magnetic sublattice will follow suit and thus provide us with a powerful pathway to manipulate (and potentially enhance) the canted moment that arises due to Dzyalozhinski-Moriya interactions in this system.

Chapter 6

Novel Phenomena associated with Polarization Vortices

This chapter provides another example of how superlattice structures can be used to achieve fundamentally different physical behavior as compared to their bulk counterparts. In this chapter, first I will present the ferroelectric domain evolution of PTO-STO superlattice films with superlattice periodicity, which is found to be fundamentally different from what is observed in traditional ferroelectrics. Second, I will present intriguing results on fundamental characteristic of these vortex structures, which showed that vortex-antivortex structures are optically chiral. This aspect of their optical behavior is anticipated to open novel pathways to control properties such as electric control of optical behavior. Thus, these studies further substantiate the immense potential in these artificial structures in enabling novel features, which are otherwise absent in bulk.

6.1 Introduction

Ferroelectric materials have found numerous applications owing to inherent properties exhibited by them such as large dielectric constant, piezoelectricity, pyroelectricity and spontaneous polarization *etc.*, as detailed in the introduction of chapter 5. Piezoelectricity is particularly important property, which has applications in sensors, actuators *etc.* In piezoelectric behavior, major development in the last decade or so has been made possible because of optimization of domain configuration [96; 456]. For example, in PMN-PT or PZT-PT the enhancement in their piezoelectric strains is achieved by optimizing the domain structure, which contained both rhombohedral and tetragonal phases (at morphotropic phase boundary) [96]. Another example could be discovery of lead-free ceramics [456] such as $(K,Na)NbO_3$-$LiTaO_3$, $(K,Na)NbO_3$-$LiTaO_3$-$LiSbO_3$ *etc.* These lead-free piezoelectric ceramics was also reported to exhibit remarkable enhancement in piezoelectric constant by texturing the crystal [456]. Thus, the technological importance of studying the domain structure on piezoelectric behavior is paramount.

The study of domain structure has been central to the understanding of ferroelectric properties of materials in bulk [401; 457], thin-film form [458; 459] and other

nanostructures such as nanocomposites constituting nanotubes [374], nanowires [432] and superlattices [143; 460] *etc.* It is primarily because ferroelectric ground state is strongly dependent on the boundary conditions (mechanical and electrical), in addition to characteristics of ferroelectric material itself. The other interesting aspect of domain structure is the presence of domain walls, which are boundaries between different (uniformly) polarized domains. In past decade or so, these domain walls have exhibited physical characteristics, which are not even present in their parent ferroelectric material. These observations can be attributed to spatial symmetry breaking in the domain wall regions, and thus, they can add more functionality to the ferroelectric material if their density is increased. For example, the domain walls in multiferroic $BiFeO_3$ have been found to be electrically conducting [405], while $BiFeO_3$ itself is insulating in nature. Another example can be the paraelectric CTO that is found to have spontaneous polarization in its (100) twin walls [461]. Such unique characteristics of domain walls have led to tuning of ferroelectric properties using what is called *domain-wall engineering* [462]. Thus, domain configuration and its evolution with external parameters remain critical to the understanding of physics of ferroelectrics. In the first section of this chapter, I will show how superlattice period can be used as the structural parameter to stabilize different ferroelectric ground states and associated anomalous domain evolution with change in superlattice periodicity.

Apart from the macroscopic domain configuration having uniformly distributed regions separated by domain walls, completely non-uniform polarization profiles in nanostructures has attracted much attention owing to their promise in the development of next generation devices [424] and fundamentally different physics (compared to bulk) offered by them. Vortex structures, as an example, were discussed earlier in chapter 5 with regard to observing such non-uniform polarization structures. Recall that, a new term was defined to describe this type of non-uniform polarization structure, *i.e.* toroidal moment. Since dipole vortices having non-zero toroidal moment, do not couple to homogeneous static electric field [369], one has to apply curling of electric field ($\boldsymbol{\nabla} \times \boldsymbol{E}$) or apply inhomogeneous electric field to control the toroidal moment of the vortices. Theoretical investigations exploring different ways in which toroidal moment of a vortex can be controlled, have predicted novel electromechanical coupling coefficients to exist along with these vortex phases. Example of these novel tensors is 'axial peizotoroidic tensor', 'pyrotoroidic tensor' and 'electrical toroidal susceptibility' tensor. Based on these novel-coupling coefficients, the possibility of next generation nanodevices such as nanotransducers, nanosensors, nanoswitchers, nanomotors [369; 424] have been discussed. In any case, the first step would be to achieve the controllability of toroidal moment of vortex states, as all technological applications including the most promising application of nanomemory devices in ferroelectric RAMs [369; 371], hinges on that capability. In order to control vortex states, a deeper understanding of the nature of these non-uniform polarization states is needed. Thus, all experimental techniques available at our disposal need to be employed to allow for their full characterization and to assist in paving the pathway to achieve desired controllability. In the second section of this chapter, experimental results of spectroscopic measurements will be presented, which will provide evidence of presence of chirality in vortex-antivortex pairs. Finally, I will conclude with a

discussion on possibility of localizing propagative phonons due to the presence of vortex *lattice* in PTO-STO superlattices.

6.2 Unusual ferroelectric domain evolution with Superlattice periodicity

6.2.1 Background

As discussed in chapter 5, when a ferroelectric material is cooled below its Curie temperature (T_c), depending on the boundary conditions and symmetry equivalent directions of ferroelectric distortion, a multivalent domain structure is formed. In that section, we covered some characteristics of domain morphology including discussion on domain walls (180°, 90°). In this section, I will provide a deeper discussion on fundamentals of domain formation and the law, which govern their evolution with ferroelectric thickness.

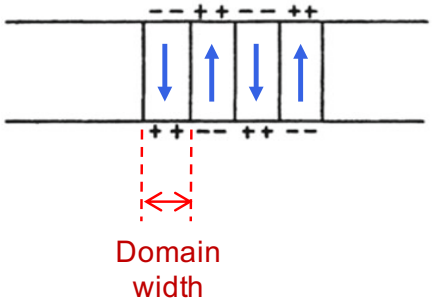

Figure 6.1: A schematic of Kittel domains in a ferroelectric slab (blue arrows indicate net polarization vectors within respective domains). From [445].

The most widely used law to describe domain evolution with ferroelectric thickness is Kittel's law. This law was originally formulated for ferromagnetic domains [445], but later extended to ferroelectric systems as well [463; 464]. If we consider a ferroelectric slab of thickness '*t*' in scenario where there are no free charges or ions from adsorbents to screen the bound charges, ferroelectric domains will form to preserve the polar state. Figure 6.1 shows one example of how a ferroelectric slab might stabilize its ground state. By adopting this domain structure, also known as Kittel's domains, notice how the ferroelectric layer has achieved charge neutrality on the surface of the slab. In general, charge neutrality on the surface of the ferroelectric layer along with its material parameters dictates the final domain formation. As a result of this charge neutrality on the surface, ferroelectric material has suppressed the net depolarization field significantly and achieved a ground state with significantly lower electrostatic energy.

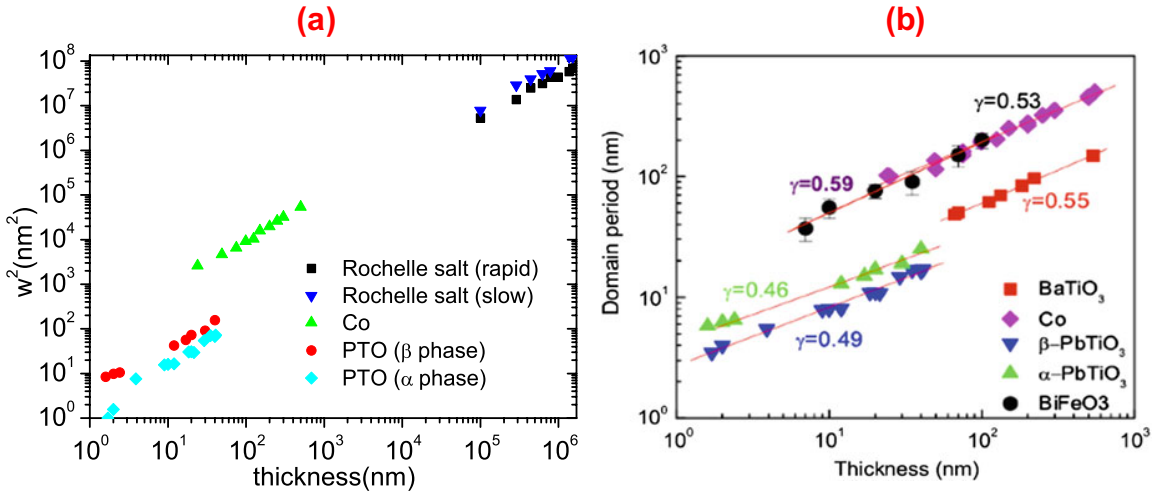

Figure 6.2: Domain scaling law for 180° domain width as a function of thickness. Figure adapted from [385; 448].

Now, one can find the stable ground state by minimizing the total free energy of the system using a simple phenomenological model. Although here we are going to build a simple model to derive the Kittel's law, this has been verified by first-principles Hamiltonian approach as well [465]. For the case of Kittel domains, there are two major contributions, which compete to form the stable state. One is the interaction between antiparallel alignment of domains (forming 180° domain walls) and the other is the short-range interaction between dipoles present within domain walls. The energy expression for the first term can be derived [464] from the electric field present between antiparallel domains near the surface of the slab, whose final expression comes out to be:

$$F_{domain} \sim P_0^2 D \tag{6.1}$$

, where 'D' is width of domain walls and 'P_0' is magnitude of spontaneous polarization. According to this relation, the antiparallel domains will tend to reduce the width of domains to lower their energy. But, decreasing the width of domains will result into increase in density of domain walls, thereby increasing the contribution of domain wall energy to the total free energy [464]. Thus, the domain wall energy will scale inversely with domain thickness. If we assume σ_0 as the domain wall energy per unit cross-section area of the slab, the energy expression for the second term comes out to be:

$$F_{wall} \sim \frac{\sigma_0 t}{D} \tag{6.2}$$

, where 't' is thickness of slab and 'D' is domain width. The total free energy can be written as:

$$F_{domain} = P_0^2 D + \frac{\sigma_0 t}{D} \tag{6.3}$$

If we minimize this free energy expression with respect to domain width, we will find:

$$\frac{\partial F_{domain}}{\partial D} = P_0^2 - \frac{\sigma_0 t}{D^2} \tag{6.4}$$

$$\frac{\partial F_{domain}}{\partial D} = 0 \quad \Rightarrow \quad D = \sqrt{\frac{\sigma_0 t}{P_0^2}} \tag{6.5}$$

$$D = \frac{\sqrt{\sigma_0 t}}{P_0} \tag{6.6}$$

This width dependence of domains on the thickness of ferroelectric layer, $D \propto \sqrt{t}$, is called Kittel's law and it suggests that the domain width will reduce as the dimensions are reduced. This simple scaling law is so powerful that is has been found to be applicable for a very wide range over six orders of change in ferroelectric thickness and across various ferroelectric material systems (see Figure 6.2). The constant of proportionality generally depends on the material parameters. It has been noted that if the finite thickness (a) of domain walls is also included into the above law, one can define a universal quantity – $D/\sqrt{at}$ [448]. Moreover, the existence of these Kittel domains have been experimentally shown and were observed to follow Kittel's law of square root-dependence all the way down to 4-10 unit cells of PTO grown on STO substrate [466].

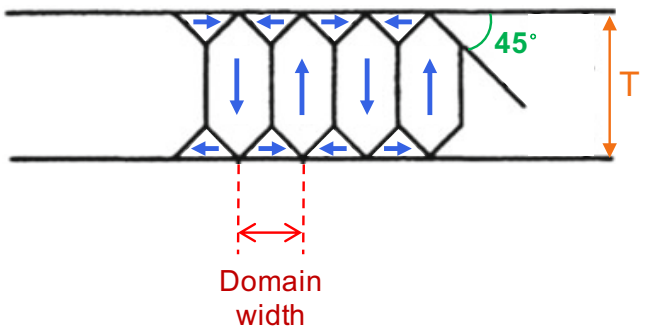

Figure 6.3: A schematic of Landau-Lifshitz domain in a ferroelectric slab of thickness 'T.' Figure adapted from [445].

One other possibility of preserving polar state of the ferroelectric slab is by adopting a different domain configuration such as Landau-Lifshitz domain (Figure 6.3), which is also known as flux-closure domains. Although similar square scaling law for domain width with thickness (*i.e.* $D \propto \sqrt{t}$) was observed for Landau-Lifshitz domains [385], very recently thin-film heterostructures of PTO and STO epitaxially strained on $GdScO_3$ (110), was found to exhibit linear dependence [440], *i.e.* $D = A + B\,t$. This experimental result was supported by earlier theoretical work [467]. It was predicted that under certain strain state a non-monotonic dependence of domain size with thickness is expected, when the film thickness is below certain value (see Figure 6.4). On further increasing the thickness of ferroelectric layer, the non-monotonic dependence changes to linear dependence and with more increase in ferroelectric thickness Kittel's behavior of square-root dependence ($D \propto \sqrt{t}$) was observed. Interestingly, we note that in their theoretical study of equilibrium domain width variation with ferroelectric layer thickness, there is specific range of thicknesses for which inverse scaling behavior was also predicted. This essentially means that, in that specific range of thicknesses, the equilibrium domain width is predicted to decrease with increase in the thickness of ferroelectric layer (as highlighted in yellow in Figure 6.4). The experimental evidence of this qualitative trend will be discussed more in this chapter. We must note that by reducing the dimensions of the ferroelectric material in not just one dimension (as in thin-film) but all three dimensions, for example in a nanodot, one report of such inverse behavior was recently reported [379].

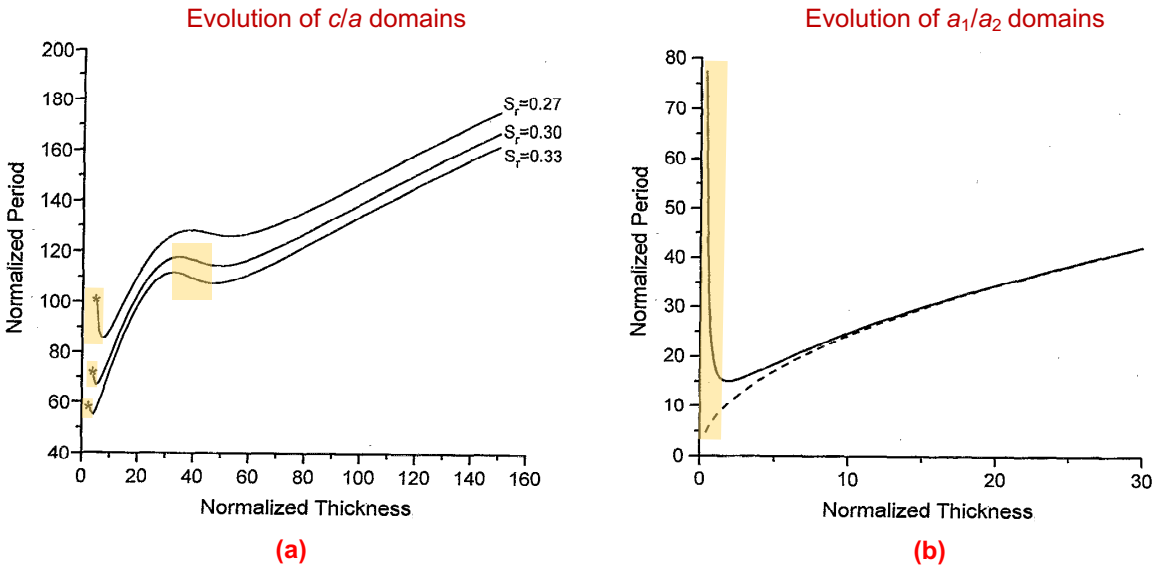

Figure 6.4: Theoretically predicted evolution of domain width with film thickness, for (a) *c*/*a* and (a) a_1/a_2 domains formed in tetragonal ferroelectric thin films strained on a cubic substrate. Regions exhibiting inverse domain scaling with thickness are highlighted in yellow. Figure adapted from [467].

6.2.2 Experimental Methods

Superlattices of $(PTO)_n/(STO)_n$ (short notation: '*n* x *n*') were synthesized on $(001)_{pc}$-oriented DSO and (001)-oriented STO via RHEED-assisted PLD under the same growth conditions described earlier in Chapter 5. Superlattice films corresponding to 4 x 4, 6 x 6, 8 x 8, 10 x 10, 12 x 12, 13 x 13, 14 x 14, 16 x 16, 18 x 18 and 27 x 27 periodicities of total thickness 100 nm were grown on both STO (001) and DSO (110) substrates, to characterize the superlattice period dependent evolution of ferroelectric ground state. Structural characterization of these superlattice films was performed by Laboratory-based XRD and Synchrotron-based X-ray diffraction methods. High-resolution Scanning Transmission Electron Microscopy (HRSTEM) was employed to map polar lattice distortions present in the individual layers of PTO-STO superlattice. PFM was used to characterize the variation in ferroelectric domain structure with superlattice periodicity.

6.2.3 Results and Discussion

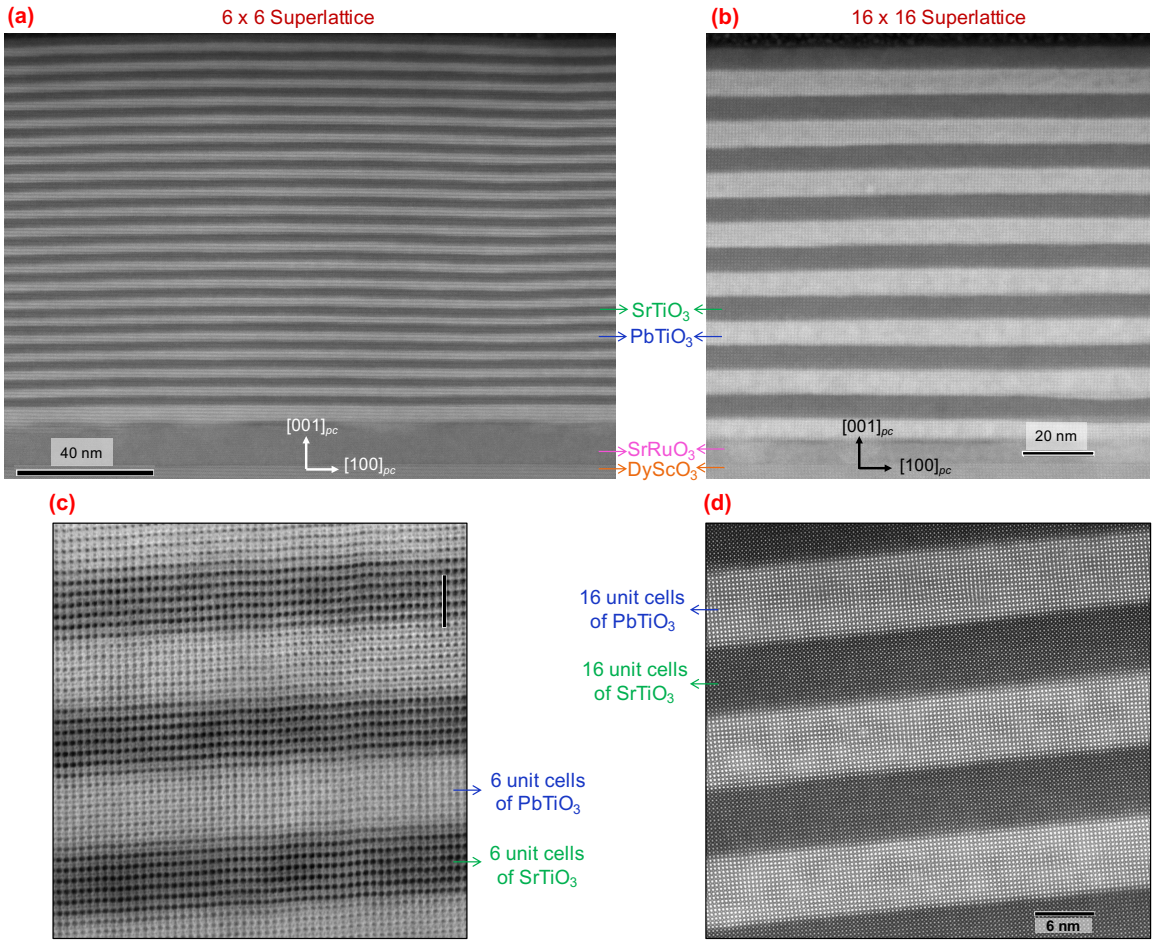

Figure 6.5: Low magnification STEM image of (a) 6 x 6 and (b) 16 x 16 PTO-STO superlattice is shown along with a zoomed-in sub region of the respective lattices in (c) and (d) showing high quality of superlattice interfaces.

Superlattice films of varying periodicity from 4 x 4 to 27 x 27 were grown via *in situ* characterized RHEED of total 100 nm thickness on both STO and DSO substrates. The uniformity of superlattice structure with different superlattice periodicities across the thickness of film was confirmed by low-magnification STEM imaging, a representative example of two superlattice structure (6 x 6 and 16 x 16) which are in characteristically different regimes (as characterized by PFM and XRD) is shown in Figure 6.5(a-b). The quality of superlattice interfaces can also be seen in high-magnification Z-contrast HAADF STEM image shown for both superlattices in Figure 6.5(c-d). These results attest to the coherency of the superlattice interfaces and structural uniformity in these superlattice films.

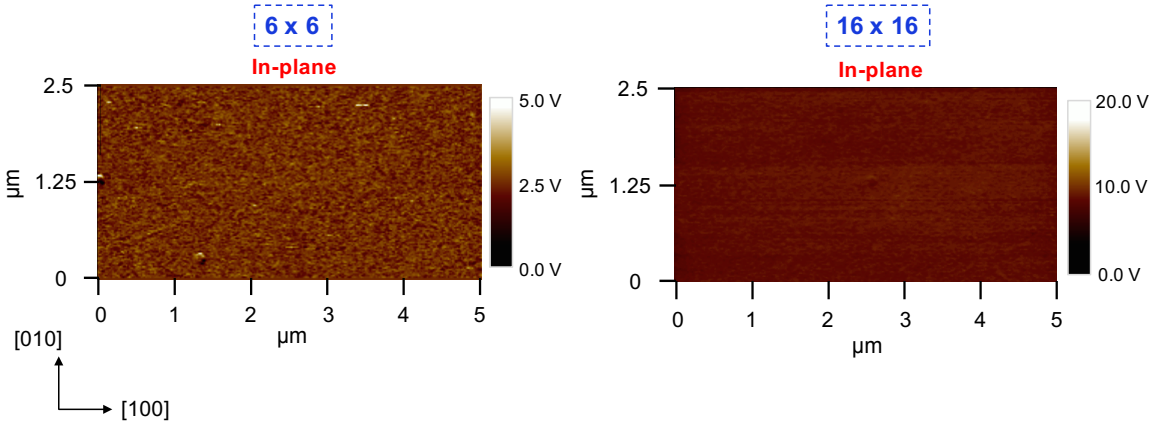

Figure 6.6: In-plane PFM of (a) 6 x 6 and (b) 16 x 16 PTO-STO superlattice grown on STO (001) substrate is shown.

I will begin characterizing the domain structure evolution with PFM measurements. First, I noticed that the superlattices grown on STO (001) substrate did not show any domain contrast or domain structure when measured using PFM. Figure 6.6 shows two representative (in-plane) PFM scans, one for 6 x 6 and other for 16 x 16 superlattice, grown for 100 nm on STO (001) substrate. A representative PFM scans for a 6 x 6 superlattice film grown on STO is shown in Figure 6.6. The absence of any domain structure was found to be true for all superlattices with different periodicities grown on a STO (001) substrate. These results were found to be consistent with previous reports of PTO-STO superlattice grown on STO (001) substrate [460].

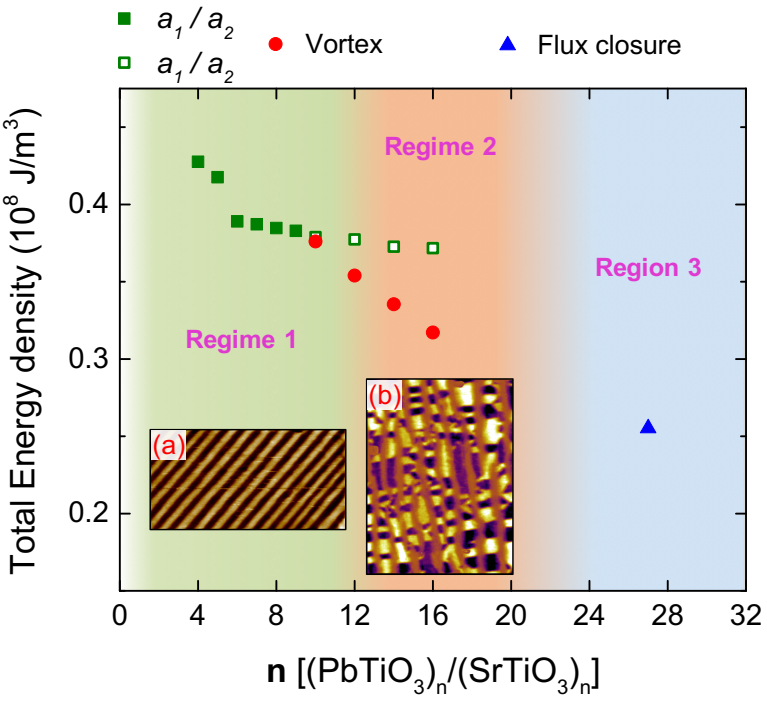

Figure 6.7: Phase diagram as function of superlattice periodicity with characteristic domain structure for the respective regimes in insets (a, b).

Second, on applying epitaxial strain on superlattice structures using a DSO (110) substrate, I observed domain structure contrast in PFM. Depending on the superlattice periodicity, the domain structure was observed to evolve with superlattice periodicity suggesting the role of both strain and superlattice structure. Figure 6.7 shows the domain structure evolution with superlattice period. Based on the characteristic domain configuration, phase diagram can be divided into three different regimes. Regime 1 was characterized by the presence of a_1/a_2-type domain structure [160], whose features was observed to change with superlattice periodicity, *i.e.* going from 4 x 4 to 12 x 12. The inset of Figure 6.7(a) shows a typical a_1/a_2 domain structure observed (via PFM) for range of superlattices present in this regime. In Regime 2, the domain structure changes to completely different configuration and it were characterized by a specific type of domain contrast as shown in the inset Figure 6.7(b). In this regime also, as the superlattice periodicity was increased from 14 x 14 to 18 x 18, the features were observed to evolve with increasing superlattice periodicity. In the regime 3, the domain structure evolved into domain morphology, which is different from both regime 1 and regime 2. I will now discuss these three characteristically different regimes with regard to their domain evolution with superlattice periodicity, thereby forming a superlattice-period-dependent phase diagram.

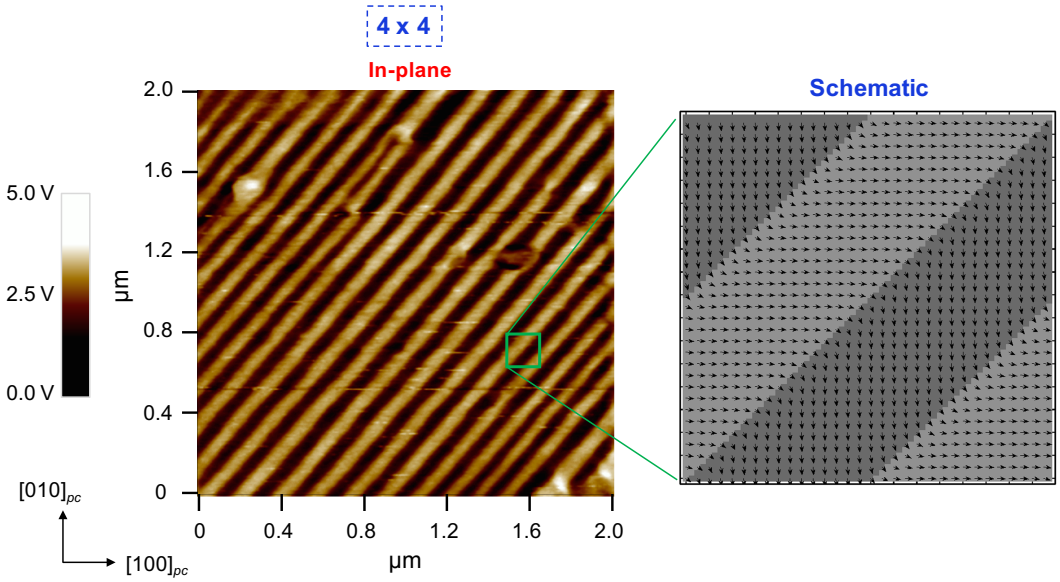

Figure 6.8: In-plane PFM of 4 x 4 PTO-STO superlattice grown on DSO (110) substrate is drawn, which shows a_1/a_2 type domain structure, along with a schematic of polarization distribution inside a_1 and a_2 domains. The schematic is taken from [468].

In regime 1, the characteristic domain looks similar to that of a typical a_1/a_2 domain structure known to exist in PTO film epitaxially strained on a substrate (examples: $SmScO_3$ and $TbScO_3$ [469]). Due to mechanical strain applied by the substrate along $[100]_{pc}$ and $[010]_{pc}$, the c-axis of PTO unit-cell sitting along two symmetry-equivalent in-plane directions ($[100]_{pc}$ and $[010]_{pc}$). Since the *a*-axis of PTO is along out-of-plane direction of the substrate, *i.e.* $[001]_{pc}$, they are called 'a_1' or 'a_2' domains. The two possible symmetry equivalent directions give rise to a domain structure in which mixture of both 'a_1' and 'a_2' domains exist, where one of them ('a_1') is pointing along $[100]_{pc}$ and other one ('a_2') is pointing along $[010]_{pc}$ (vice-versa). The domain walls formed between these domains (existing because of mechanical constraints imposed by epitaxial strain) are 90° domain walls, thus making them ferroelastic in nature [463].

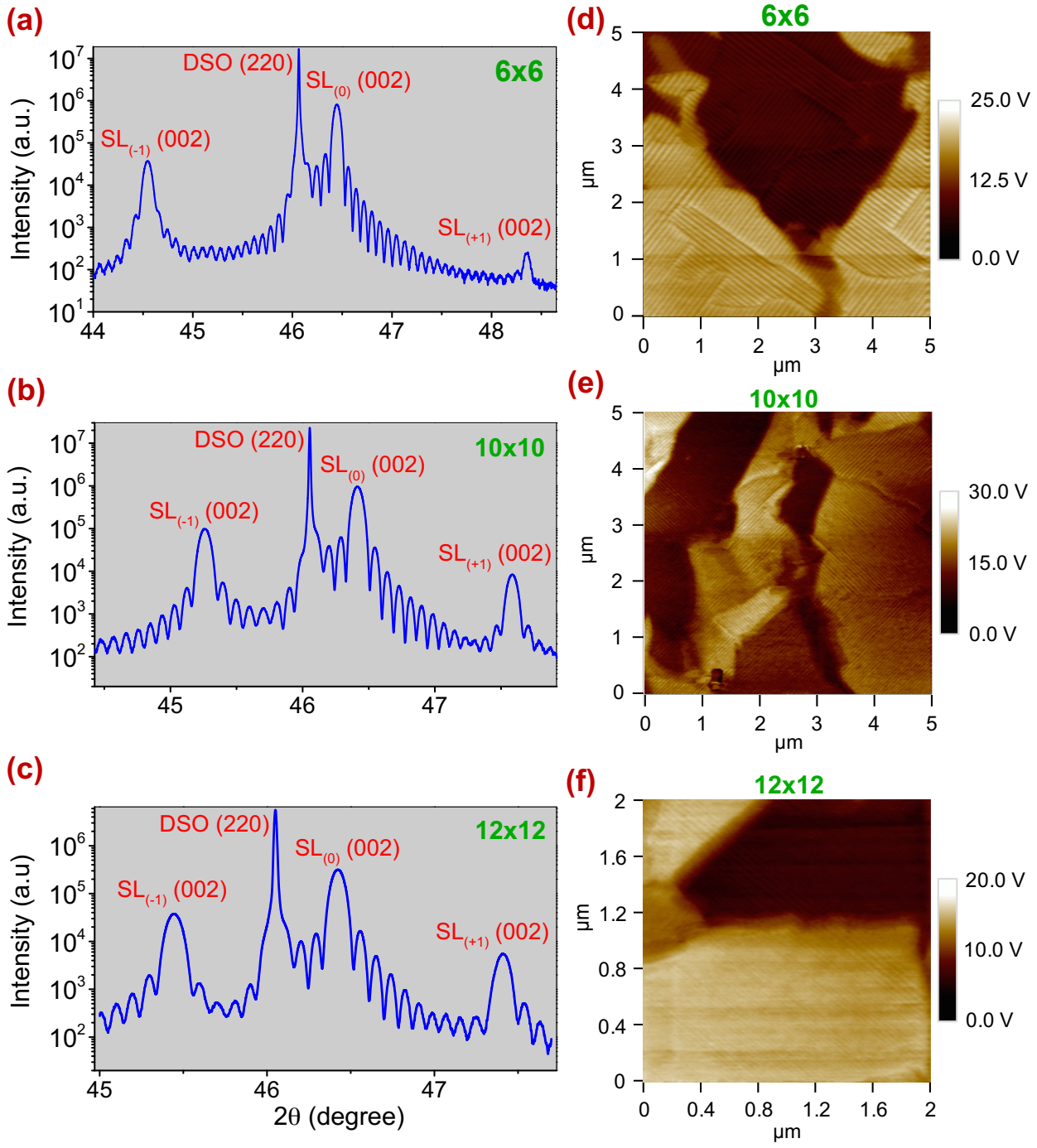

Figure 6.9: Symmetric XRD of (a) 6 x 6, (b) 10 x 10 and (c) 12 x 12 PTO-STO superlattice films is drawn along with the in-plane PFM scans shown on right (d), (e) and (f) respectively.

When a superlattice of PTO and STO is grown on a DSO substrate, the domain contrast in PFM looks similar to typical a_1/a_2-type domains, an example of 4 x 4 superlattice periodicity is shown in Figure 6.8(a) along with a schematic on the side highlighting the local polarization vectors within those a_1/a_2-type domains (Figure 6.8(b)). The average domain width for 'a_1/a_2' type domains found for this periodicity was about 65.5 nm. On increasing the periodicity to 6 x 6, PFM showed similar domains structure having 'a_1'- and 'a_2'-type domains (Figure 6.9(d)). And, the average width of these a_1/a_2 domains was found to be about 77 nm. When the periodicity was increased to 10 x 10 (Figure 6.9(e)), significant reduction in average domain width of a_1/a_2 domains was observed. The average domain width for a 10 x 10 superlattice was found to be 40.1 nm. For a 12 x 12 superlattice, which is almost at the end of Regime 1, PFM domain contrast (Figure 6.9(f)) shows a very fine a_1/a_2 domains with average domain width further reduced to 20.4 nm. As a function of PTO thickness in superlattice period, when average domain is plotted (as in Figure 6.10 (a)) an inverse Kittle behavior or negative scaling coefficient with superlattice period thickness is observed. Note that the total thickness of these superlattices is kept constant at 100 nm; only the superlattice periodicity is increased from 4 x 4 to 12 x 12, which means that only the thickness of PTO layer in superlattice period is increased. For comparison, the domain scaling law for standard Landau-Lifshitz-Kittel domains is replotted in Figure 6.10(b) from previous section (Figure 6.2). The negative scaling of average domain width with increase in only superlattice period suggest a dramatic change in depolarization field across the PTO layers in the superlattice structure. Such a drastic change in depolarization field is playing a significant role in the observed anomalous domain evolution. One might wonder the role of epitaxial strain in the observed evolution of domain structure. So, I carried out extensive X-ray diffraction studies to evaluate their crystal structure and strain state of the film.

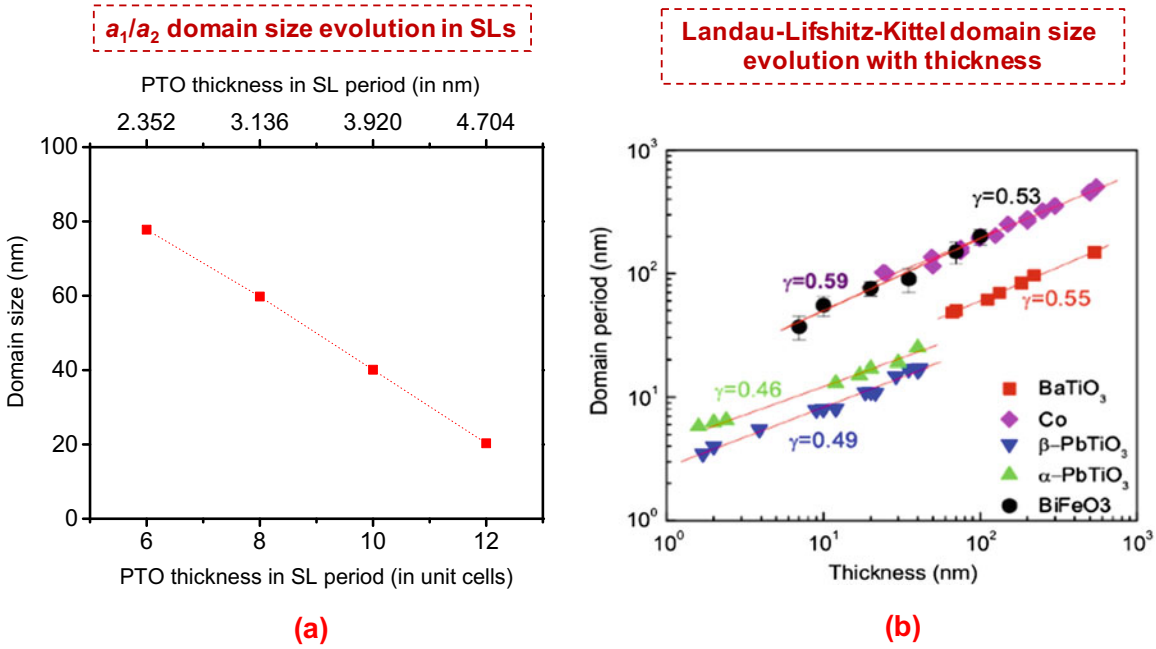

Figure 6.10: (a) Average domain width of a_1 or a_2 domains observed in superlattice structures is plotted as a function of PTO thickness in superlattice periodicity. For comparison, domain size evolution of Landau-Lifshitz-Kittel domains is plotted in (b).

The symmetric XRD scans performed using laboratory-based set-ups are summarized in Figure 6.9(a-c). The presence of superlattice reflections, *i.e.* $SL_{(-1)}$ 002 and $SL_{(+1)}$ 002 in each cases, correspond to superlattice ordering of their respective superlattice structure confirming the *in situ* RHEED characterization of superlattice thin films during the growth. The presence of *Pendellösung* fringes around both Bragg peak ($SL_{(0)}$ 002) and superlattice reflection ($SL_{(-1)}$ 002 and $SL_{(+1)}$ 002) further attests to the precise nature of interfaces in these superlattice films grown on DSO (110). Since the superlattice structure is strained on the DSO substrate in the in-plane directions by 1%, I noticed a systematic shift of both superlattice peaks and Bragg peaks as compared to the superlattice structure grown on a 0% strained substrate such as STO (001) (Figure 6.11). When the reciprocal space map was measured of the same 6 x 6 superlattice film sample around $(103)_{pc}$ of DSO using laboratory-based XRD, it confirmed that the 100 nm superlattice films is strained to the DSO substrate (see earlier Figure 5.19). Similarly, 2D reciprocal space maps were used to confirm the strain state of other superlattice films. These RSM results suggest that the superlattice films are strained and further implies that strain may not be taking part in observed negative scaling of domain width as the superlattice periodicity is increased from 4 x 4 to 12 x 12.

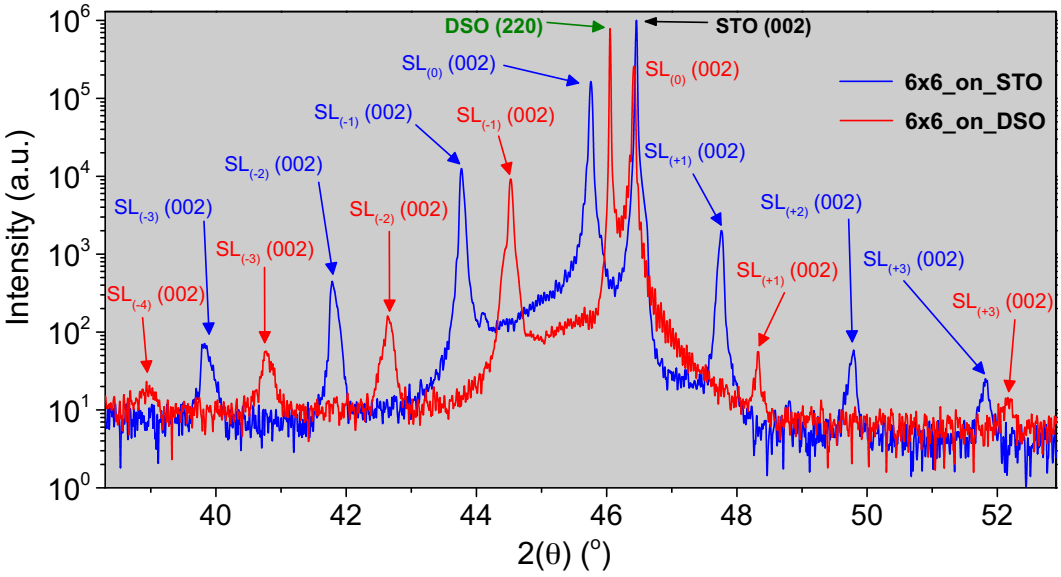

Figure 6.11: Symmetric XRD of 6 x 6 PTO-STO superlattice films grown on STO (001) (in blue) vs DSO (110) (in red) substrate.

Synchrotron based XRD was employed to obtain full three dimensional (3D) Reciprocal Space Maps to investigate the crystallographic nature of domains present in the superlattice films. For regime 1, we again take the example of 6 x 6 superlattice grown on DSO (110) substrate, whose HK-cut and LHK-cut of 3D RSM done around DSO (202) peak, are shown in Figure 6.12. The HK-cut reveals the diffraction peaks arising form the domain ordering in the in-plane directions of the DSO substrate (*i.e.* $[\bar{1}10]_o/[100]_{pc}$ and $[001]_o/[010]_{pc}$). The observed diffraction peaks in this HK-plot suggest that domains are ordered along 45° to the $[010]_{pc}/[100]_{pc}$ of the substrate, *i.e.* H = K and H = - K, which is suggesting ordering of a_1/a_2-type domains observed earlier in PFM as periodic domains along those directions. When we take LHK-cut at H = K (or H = - K) around the same reciprocal lattice points, we find that the diffraction peaks corresponding to both superlattice reflections (along L direction) and peaks corresponding to crystallographic ordering of a_1/a_2 domains. It is interesting to note that the diffraction peaks corresponding to a_1/a_2-type domain structure are observed along H = K (in Figure 6.12(b)) for all those values of 'L' for which superlattice reflections (out-of-plane) were observed. This may suggest the presence of a super cell or repeating unit for a_1 or a_2 domains, which is repeating along 'L' direction with the same characteristics period.

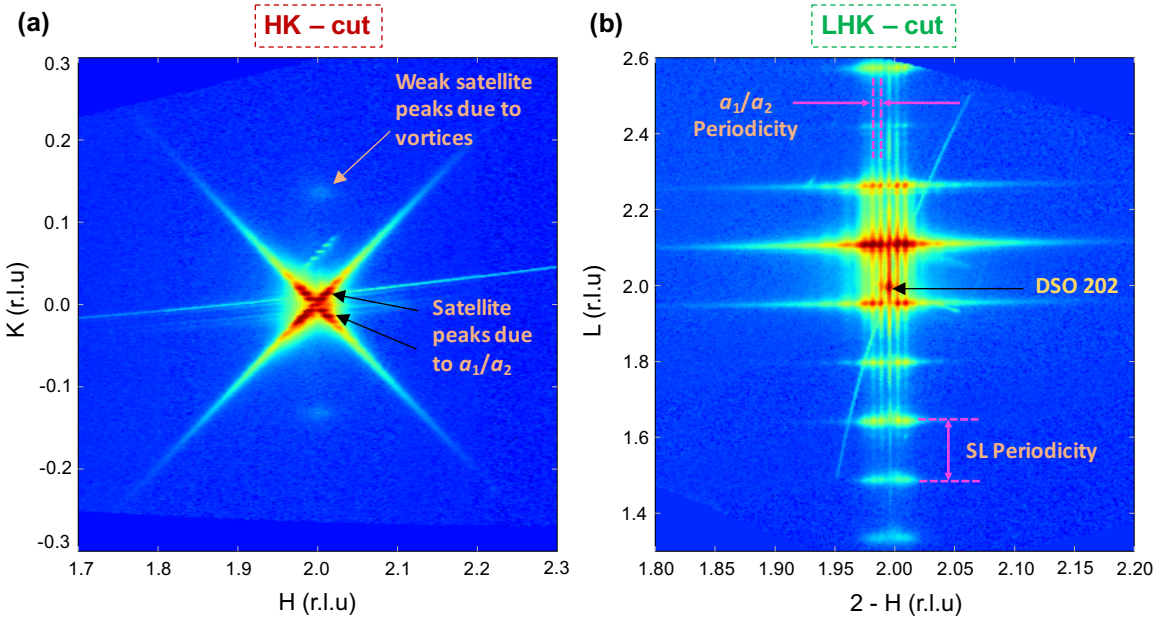

Figure 6.12: HK-cut (a) and LHK-cut (b) obtained from a 3D RSM around DSO 202 peak is shown for a 6 x 6 PTO-STO superlattice film grown on DSO (110) substrate.

We have also performed high-resolution polar displacement mapping to study the evolution of polarization distribution within PTO layers of superlattices as a function of superlattice period (or PTO thickness in the superlattice structure). Figure 6.13 shows the polar displacement mapping for various periodicities – 4 x 4, 6 x 6, 12 x 12, which depicts the evolution of polarization distribution. In 4 x 4, due to large depolarization field across PTO layers, polarization is found to be aligned in plane (Figure 6.13(a)) to attain low-energy configuration as discussed in chapter 5 (Figure 5.9). As the thickness is increased the depolarization field reduces and polarization within each PTO layers begins to evolve into a non-homogeneous distribution such as one shown in 6 x 6 (Figure 6.13(b)), where it seems to have formed a "wave"-like polarization structure. On further increasing the thickness of PTO layer by increasing the superlattice periodicity to 10 x 10, polarization distribution within PTO layers has matured to a vortex structure with alternating rotation directions (see earlier Figure 5.22). Similar vortex-structure formation was found for 12 x 12 superlattice as well (Figure 6.13(c)). Such significant change in the polarization distribution as a function of PTO thickness (or superlattice period) may play a role in observed negative scaling of domain size with ferroelectric thickness. In addition to experimental polar displacement mapping for these superlattice periodicities, the corresponding phase-field simulations were also plotted in the same figure, which shows close agreement with the experimental data.

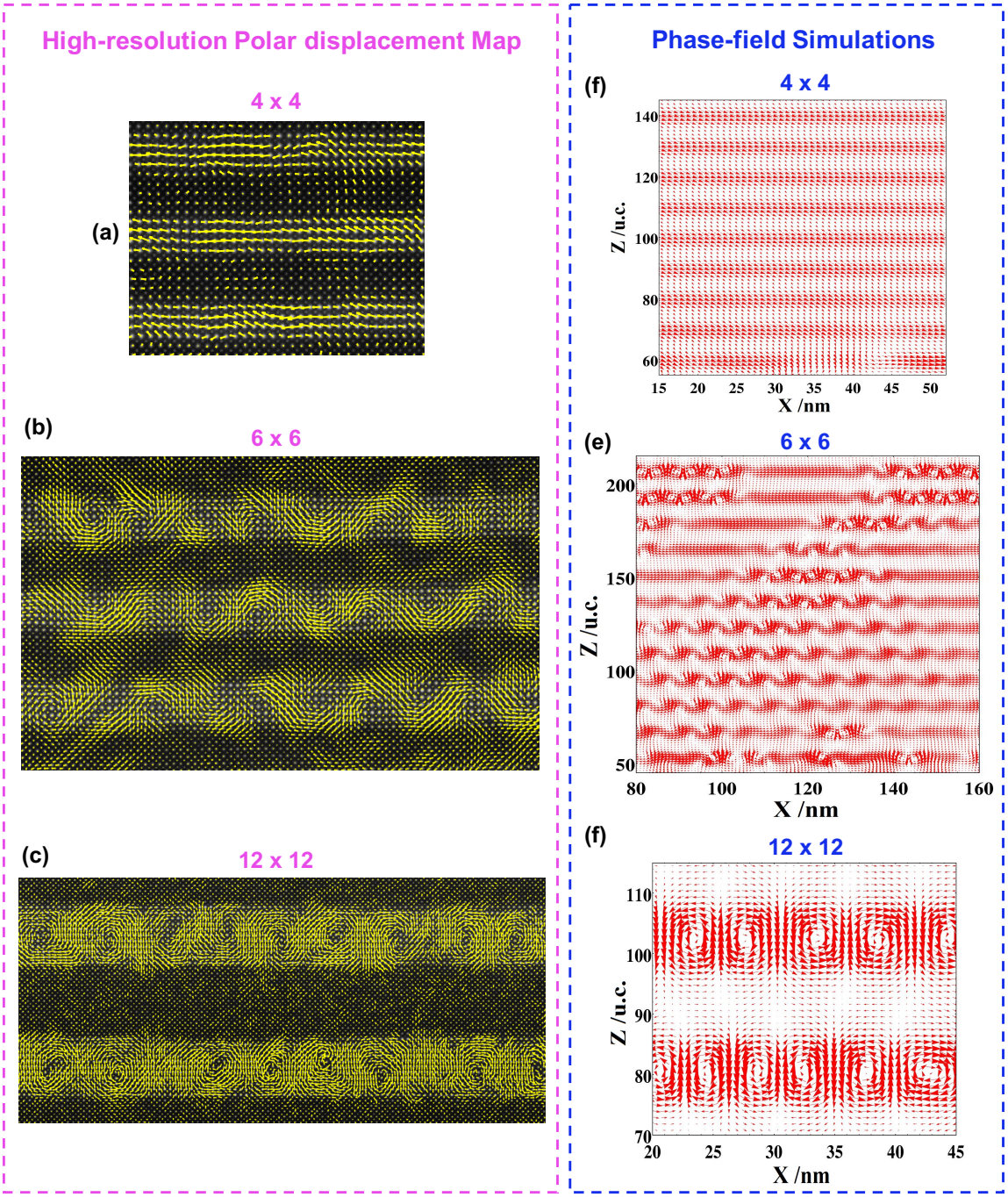

Figure 6.13: Evolution of polarization distribution for superlattice periodicity 4 x 4, 6 x 6, 12 x 12, as obtained experimentally from HR-TEM polar displacement map (a, b, c) and phase field simulations (d, e, f) respectively.

Thus, using combination of characterization methods (XRD, PFM and TEM), I have studied the nature of domain structure evolution observed in the first regime of the

phase diagram. I observed an inverse Kittel's law behavior for domain size variation with the thickness of the PTO in the superlattice structure. Such anomalous behavior can be linked to significant change in the depolarization field as function of superlattice periodicity.

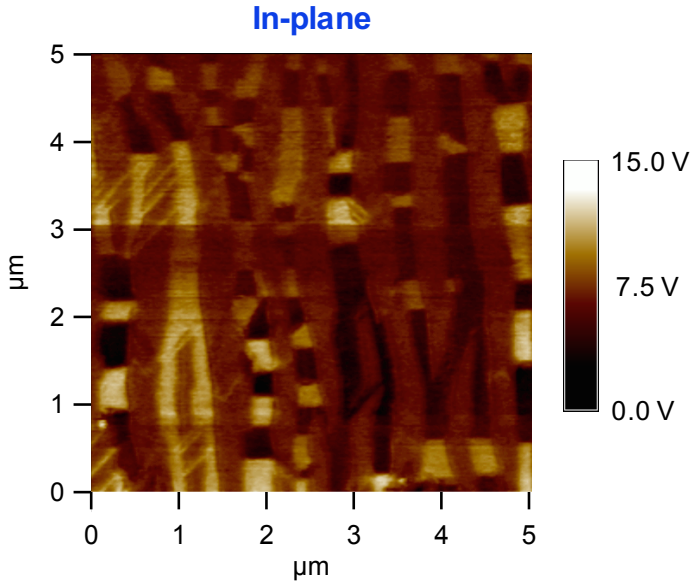

Figure 6.14: In-plane PFM of 16 x 16 PTO-STO superlattice film grown on a DSO (110) substrate.

In regime 2, superlattice films on DSO showed a characteristically different domain contrast, a representative PFM scan of 16 x 16 superlattice film is shown in Figure 6.14. The domain contrast in the in-plane PFM shows two types of the pattern, stripe-like features in a 5x5 µm image. First, is the stripe along $[010]_{pc}$, which has uniform contrast within and seems to have low piezoresponse as compared to other regions. The second set of stripe-like pattern include those with black/white alternating contrast within those stripes and occurring adjacent to first set of stripes. On taking a closer look at the surface topography of the corresponding PFM scan (of same 16 x 16 film), I noticed that first set of stripes are approximately 0.8 Å lower than second set of stripes (with black/white contrast). A representative surface topography of the superlattices, via AFM, in Regime 2 is depicted in Figure 6.15, where contrast in the image is arising from the height difference between the two phases.

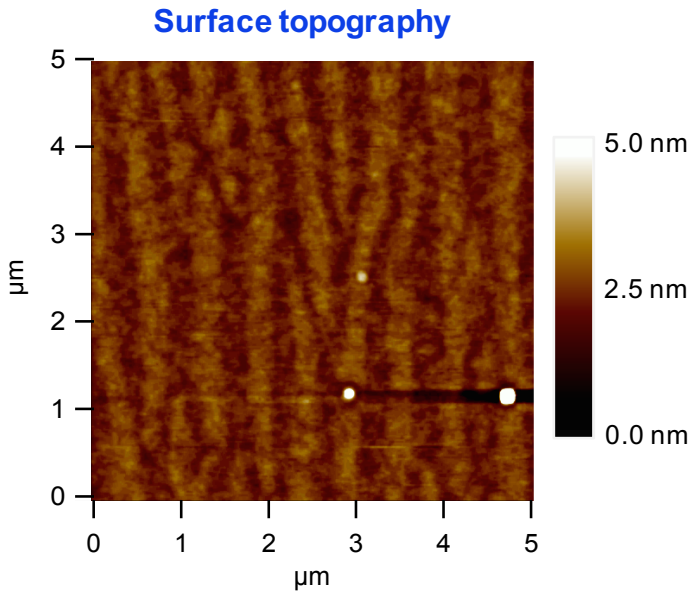

Figure 6.15: AFM image of 16 x 16 PTO-STO superlattice film grown on DSO (110) substrate.

To understand the characters of this type of domain structure, I again performed extensive X-ray diffraction studies using both Laboratory- and Synchrotron-based XRD. In the symmetric XRD scans of the same 16 x 16 superlattice on DSO, I noticed very interesting diffraction pattern (see Figure 6.16(a)). One would expect a set of superlattice reflection (labeled in red and indicated by black arrows) corresponding to 16 x 16 periodicity in a symmetric scan. For comparison, symmetric XRD scan of a 16 x 16 superlattice on STO (001) substrate is shown in Figure 6.16(b) for reference. Following the same trend of superlattices (from 12 x 12 onwards), only one set of superlattice reflections would be expected corresponding to a_1/a_2 and further reduction of domain size of a_1/a_2-type domains. Thus, one might anticipate that one set of superlattice reflections still corresponds to a_1/a_2-type domain structure. And, PFM was not able to resolve the contrast within those black/white stripes as the periodicity of the domain size is approaching the resolution limit of PFM measurement. In this case, however, we observe one more set of peaks, labeled in pink and indicated by pink arrows, which it turns out also corresponds to the same 16 x 16 periodicity as the other set labeled in red. Interestingly, when I extracted the d-spacing (d') of Bragg peaks corresponding to both set of superlattice reflections, I made the following observation. The difference in the average out-of-plane lattice parameters ($2\Delta d$') is approximately equals to 0.8 Å, same height difference we found in surface topography from scanning probe measurements. This result further suggests that region of low piezoresponse corresponds to higher average 'd' spacing between (00l) plane of the (001)-oriented superlattice structure.

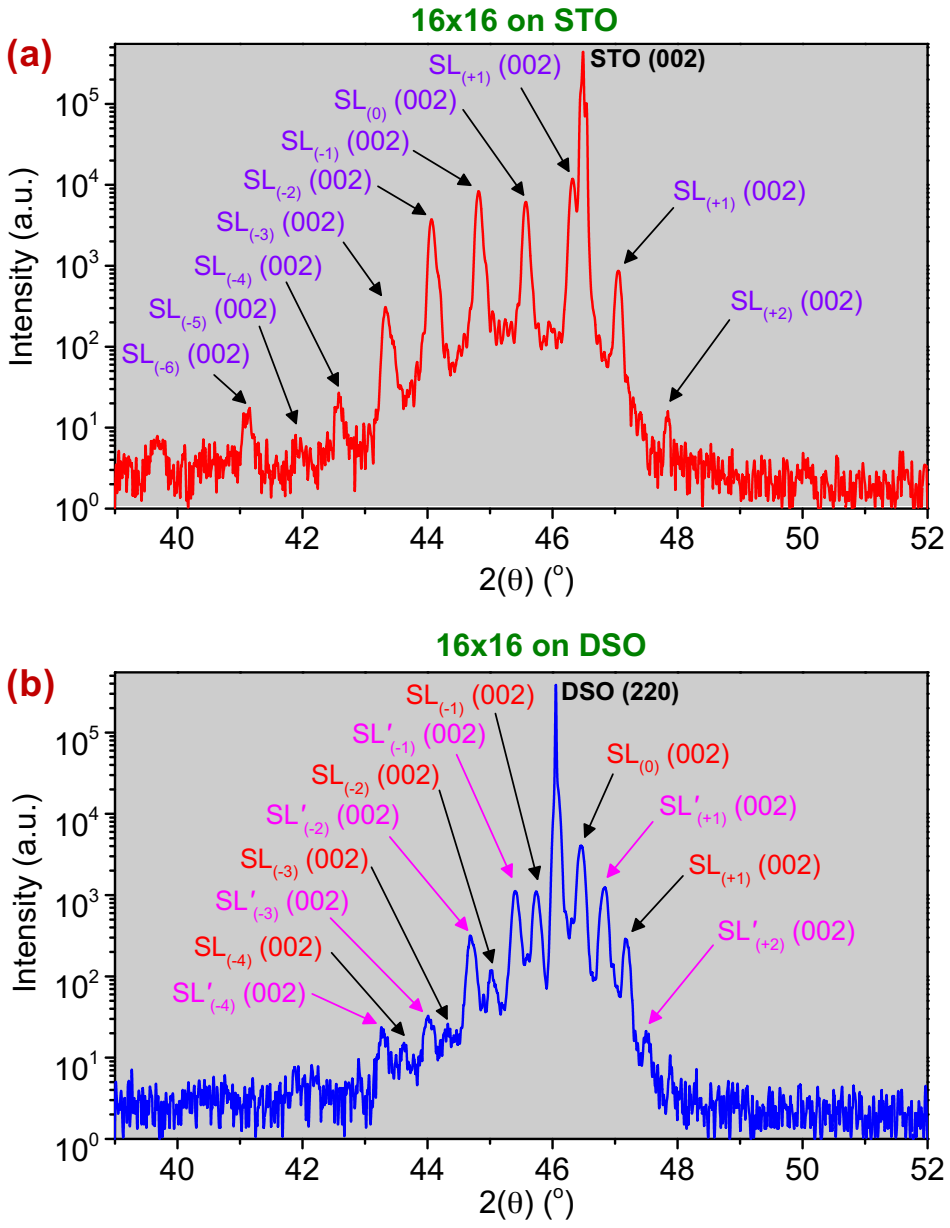

Figure 6.16: Symmetric XRD of 16 x 16 PTO-STO superlattice films grown on (a) STO (001) and (b) DSO (110) substrate.

The second confirmation for this hypothesis was found when I analyzed the symmetric XRD scans as a function of superlattice period (from 14 x 14 to 18 x 18). Figure 6.17(a-c) shows the symmetric scans of 14 x 14, 16 x 16 and 18 x 18 on a DSO (110) substrate. From the Intensity vs '2θ' scans, I noticed that relative change in the intensity of superlattice reflections corresponding to two sets of peaks as the periodicity is increased from 14 x 14 to 18 x 18. The intensity corresponding to one set (with lower piezoresponse)

is increasing at the expense of second set (with black/white contrast). The corresponding evolution in the domain structure is depicted side-by-side in the same Figure 6.17(d-f). From the PFM contrast, we note the regions with lower piezoresponse are increasing at the expense of the regions with black/white contrast, which correlated well with the X-ray diffracted intensity evolution with superlattice periodicity. The results suggest that the volume fraction of one type of phase (with lower piezoresponse) is growing with superlattice periodicity at the expense of other phase. To understand the features present within this complex domain structure, I again used Synchrotron-based XRD to characterize in-plane and out-of-plane ordering of these domains.

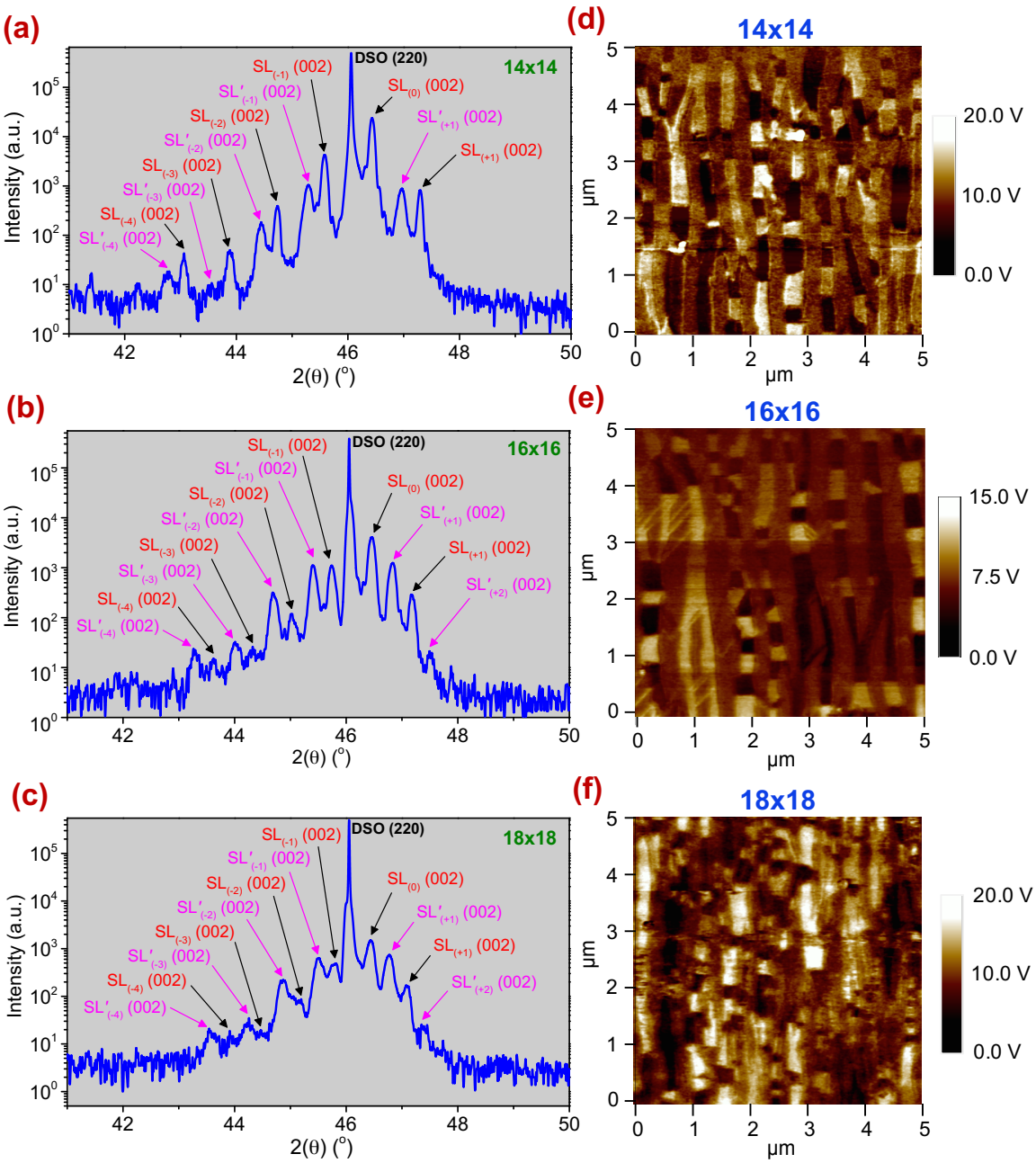

Figure 6.17: Symmetric XRD of (a) 14 x 14, (b) 16 x 16 and (c) 18 x 18 PTO-STO superlattice films is shown along with the in-plane PFM scans shown on right (d), (e) and (f) respectively.

Synchrotron-based XRD of the same representative 16 x 16 superlattice sample on DSO (110) is shown in Figure 6.18. The 3D RSM was done around $(011)_{pc}$ DSO reciprocal lattice peak. In the HK-cut passing through the substrate peak L = 0.92 (shown in Figure

6.18(a)), one can identify two types of domains ordered along (H = K, H = - K) and K direction. The domain ordering along H = K and H = - K (Figure 5.17(b)) are the same a_1/a_2-type domain structure observed in previous 3D RSMs (Figure 6.12(b)). As expected from the continuation of the peaks in the OOP direction in symmetric line scans (Figure 6.17(a-c)), in 3D RSMs the in-plane peaks along 45° to $[110]_{pc}$ and $[1\bar{1}0]_{pc}$ directions of the DSO substrate correspond to a_1/a_2-type domains ordered along these directions. One can also use the position of 'L' values corresponding to a_1/a_2-type domains by taking line profile along H = K (H = - K) to further confirm that in-plane peaks along 45° to $[100]_{pc}$ ($[010]_{pc}$) corresponding to a_1/a_2. When an LK-cut along H = K (or H = - K) is taken (Figure 6.18(b)), we see similar characteristics of in-plane peaks following superlattice reflections along L-direction as observed in a_1/a_2 of regime 1 (Figure 6.12(b)). This result confirms the existence of a_1/a_2-type domains in those black/white stripes observed in PFM. Moreover, as can be seen from Figure 6.18(a), a_1/a_2 in-plane peaks have shifted much farther in the reciprocal lattice direction (H = K or H = - K) compared to for example in 6 x 6 shown in Figure 6.12(a), with domain size further reduced to 13.63 nm.

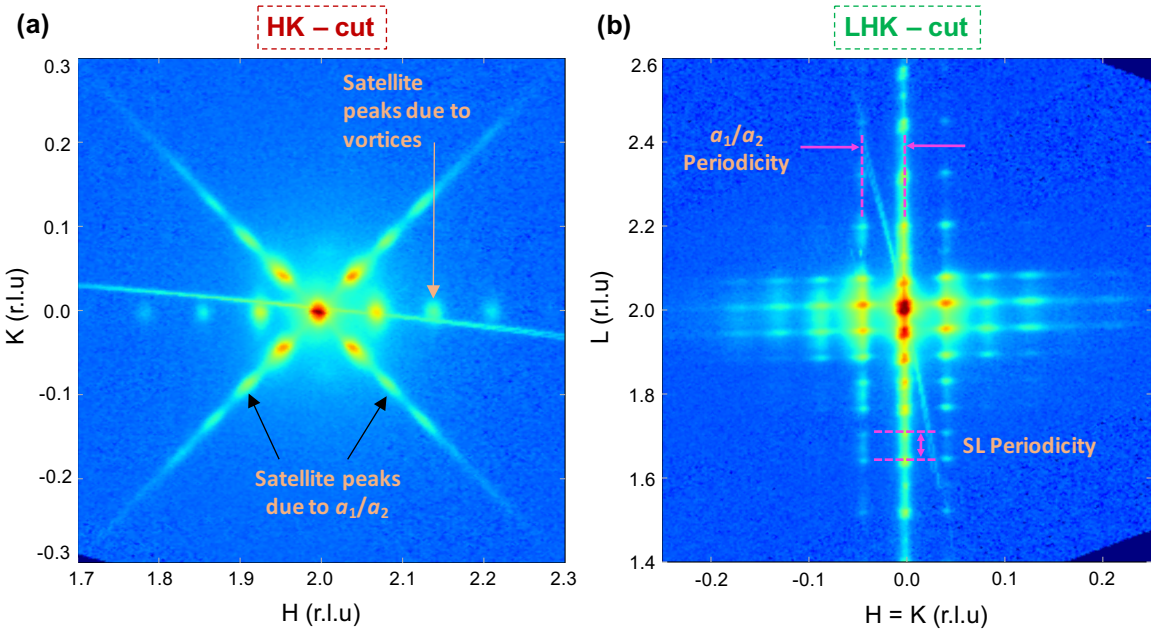

Figure 6.18: An HK-cut (a) and LHK-cut (b) is shown to highlight the a_1/a_2 periodicity in 16 x 16 superlattice film grown on DSO (110) substrate along specific crystallographic directions.

The second set of in-plane peaks, corresponding to the other set of stripes discussed in PFM (having large average '*c*'-axis lattice parameter), is observed to show diffraction peaks along K direction, indicating their ordering along that direction. When the periodicity of these in-plane peaks is extracted from a line, it came around 10.9 nm. This set of in-plane peaks corresponds to the vortex-antivortex ordering along the in-plane direction in

PTO layers of the superlattice structure. A representative LK-cut along K direction is shown in Figure 6.19, from which a number of observations can be made. First, the two sets of superlattice reflections found in symmetric scan of 16 x 16 earlier can also be seen in this map along the L-direction as doublet peaks (note that doublet peaks can also be seen in the LHK-cut taken along H = K as shown previously in Figure 6.18(b)). The in-plane diffraction peaks associated with both doublet-peaks, when analyzed with a line scan it gave a non-zero intensity profile as a function of K values (when taken along K-direction). The periodicity associated with these diffraction peaks along K direction came out to be 10.9 nm. Similar to earlier observations, I noted that in-plane peaks corresponding to vortex structure is also following the superlattice reflections along L direction, suggesting that vortex structure are present in subsequent PTO layers of superlattice structure. More diffused nature of diffracted peaks in L direction, reflects on vortex ordering in adjacent PTO layers and is consistent with TEM-based observations (discussed earlier in chapter 5). Also note that diffraction peaks corresponding to vortex phase is less crystallographic in nature as compared to sharply defined a_1/a_2 peaks in Figure 6.18(b) (and earlier observation of a_1/a_2 in 3D RSMs). The weakly diffused nature of diffraction peaks from vortex phase can be attributed to non-uniform polarization distribution present whose origin is not crystallographic. Thus, based on results from PFM, XRD and 3D RSM measurements, I conclude that vortex regions corresponds to the low-piezoresponse phase observed in PFM showing uniform contrast within, while a_1/a_2-type domains were found to exist in the black/white regions of the other phase present in the superlattice film. The advantage of using large flux of photons in a synchrotron X-ray source becomes apparent in this particular case where the existence of a_1/a_2-type domains and in-plane ordering can be easily characterized which otherwise be difficult using laboratory-based characterization tools. I also found that the domain width associated with a_1/a_2 domains got further reduced from 20.8 nm in 12 x 12 to 13.73 nm in 16 x 16. The coexistence of a_1/a_2-type ferroelastic domains with vortex phase provides the experimental evidence of the phase diagram predicted for STO/PTO superlattices using Phase-field simulations (Figure 6.7).

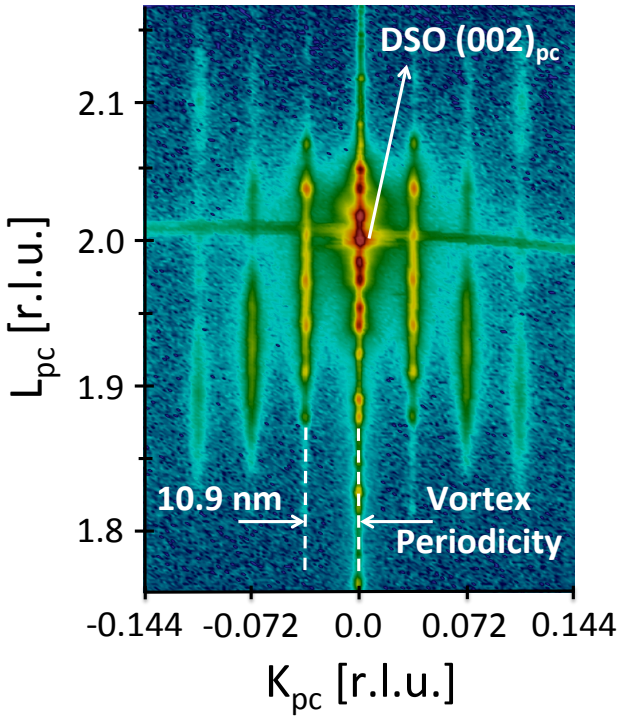

Figure 6.19: An LK-cut of 16 x 16 PTO-STO superlattice film grown on DSO (110) substrate showing vortex diffraction peaks.

In regime 3, the superlattice films were observed to transition to a different domain structure, a representative PFM scan of 27 x 27 superlattice grown on DSO (110) is shown in Figure 6.20. The domain structure has evolved into less-ordered domain structure, which lacks repeating pattern. The domain size has become very large at these periodicities and does not show any signature of a_1/a_2 domains compared to Regime 1 and 2. The symmetric XRD scans of superlattices on DSO in this regime shows broader diffracted intensities with few sharp peaks (see Figure 6.21). This result can be attributed to a combination of several factors such as formation of less-ordered domains and large strain from substrate. For instance, when a similar superlattice periodicity (27 x 27) is grown on a 0% strained STO substrate, sharp ordered diffraction peaks were observed in the symmetric XRD scans (see Figure 5.20). Note that PFM measurement on a 27 x 27 superlattice grown on STO (001) substrate did not show any domain contrast, consistent with regime 1 and 2.

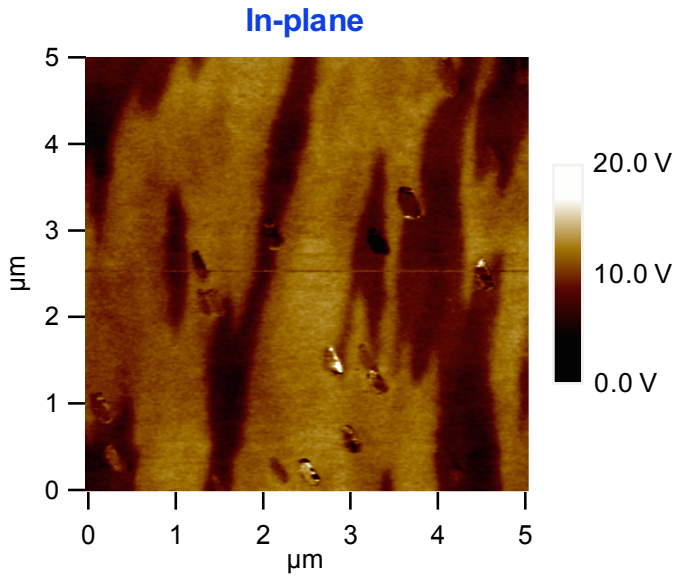

Figure 6.20: In-plane PFM of a 27 x 27 PTO-STO superlattice film grown on DSO (110) substrate.

At these large periodicities of the superlattice structures grown on DSO (110) substrate, both TEM-based experimental observations and phase-field simulations showed the presence of flux-closure type polarization domain structure present in subsequent PTO layers of the PTO-STO superlattice (see earlier Figure 5.26 in chapter 5). As mentioned earlier in this chapter, a linear dependence of domain periodicity in flux-closure domains on the thickness of PTO layers has already been observed experimentally [440]. However, the domain evolution of overall PTO-STO structure, for example. via PFM, has not been discussed in their report [440]. Finally, I conclude that, in regime 3, the thickness of PTO layers in superlattice structures has increased to a state where it is tending towards bulk-like behavior, *i.e.* the net result in the polarization distribution has evolved into flux-closure type domains, which is often reported in bulk-like ferroelectric samples [444].

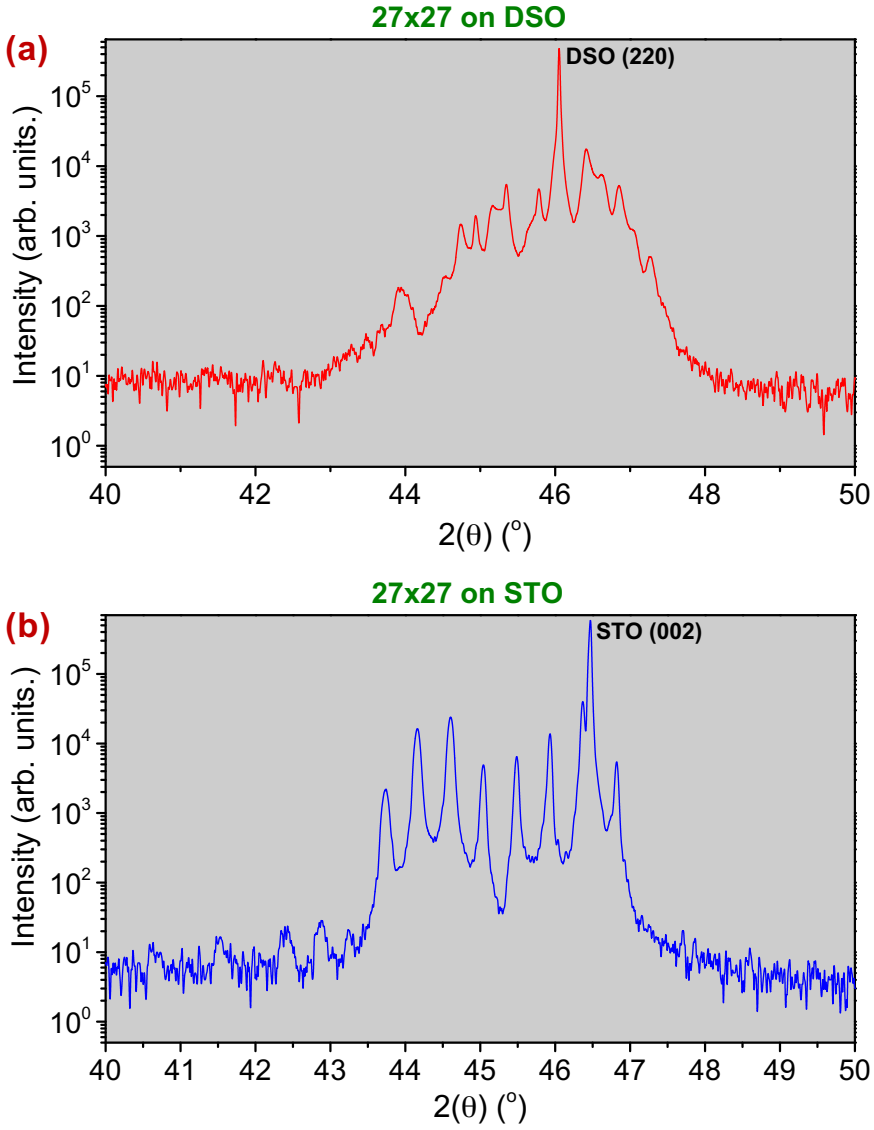

Figure 6.21: Symmetric XRD of 27 x 27 PTO-STO superlattice film grown on (a) DSO (110) and (b) STO (001) substrate.

In summary, using combination of various characterization methods, I have observed the evolution of macroscopic domain structure as a function of superlattice periodicity. In the superlattice structures grown on a 0% strained substrate such as STO (001), PFM did not show any domain contrast for all periodicities. While those grown on a DSO (110) substrate, *i.e.* 1% in-plane epitaxial strain, a rich spectrum of domain configurations was observed, suggesting a dominant role played by in-plane strain in stabilizing ferroelectric domains in these superlattice films. When the superlattice periodicity is varied from 4 x 4 to 27 x 27, the domain structure was found to be strongly dependent on the superlattice period. Based on the characteristic features of the domain

configuration, the phase diagram was divided into three regimes. In regime 1, *i.e.* from 4 x 4 to 12 x 12, a_1/a_2 type domain (with 90° ferroelastic domain walls) was found to exist in the superlattice films. As the superlattice period was increased within this regime, domain size was observed to decrease which implies a negative scaling coefficient (or inverse Kittel behavior) for domain size evolution with ferroelectric thickness. In contrast to normal behavior of positive scaling coefficient (0.5) observed in general [448], also known as Kittel's law for ferroelectric domain evolution, these superlattices show inverse behavior indicating the presence of other factors such as strong depolarization fields playing a significant role in the observed anomalous behavior. Pertsev *et al.* [467] theoretically predicted the negative scaling coefficient for the specific range of thicknesses of a tetragonal ferroelectric thin-film strained on a cubic substrate. The experimental evidence for this prediction was observed when superlattice periodicity was increased from lower to higher periodicity in regime 1. Upon transitioning to even higher periodicities, *i.e.* in regime 2, we found a characteristically different domain structure as compared to regime 1. We found the coexistence of vortex phase and a_1/a_2-type domains occurring in a unique domain configuration, which supported theoretical calculations (Figure 6.7). Lastly, in regime 3, I observed a completely different domain structure compared to the previous regimes, 1 and 2. The domain structure in this last regime lacked repeating patterns with no signature of a_1/a_2-type crystallographic domains.

6.3 Emerging Chirality in Polarization Vortices

6.3.1 Background

Resonant X-ray Absorption spectroscopy has been applied extensively to study ferroelectricity in both single crystals [470-473] and thin films [211; 474-476]. The presence of ferroelectric order has been shown to introduce a difference in absorption spectra when measured using linearly polarized light. The large X-ray linear dichroism (XLD) found in absorption spectra measured with light polarized parallel and perpendicular to polarization vector is expected for a normal ferroelectric (or multiferroic) system. An example of XLD from a ferroelectric film (PZT) grown on STO (001) substrate buffered with a bottom electrode (either SRO or LSMO) layer is shown in Figure 6.22. Tuning the incoming X-ray energy to $L_{2,3}$ edges of 'Ti' leads to observation of well known Ti-spectrum shown in Figure 6.22 (a), which corresponds to, from the left, (t_{2g}, e_g) levels of $2p_{3/2}$ (L_3) to (t_{2g}, e_g) levels of $2p_{1/2}$ (L_2) respectively. The splitting of Ti *d*-orbitals observed in this absorption spectrum is a result of the spin-orbit interaction [42] and crystal field interactions [45]. When the incoming light is linearly polarized with one parallel and other perpendicular to polarization vector (Figure 6.22, inset (c)), the difference in the absorption spectra (Figure 6.22 (b)) can reveal useful information about ferroelectric order and associated characteristics, for example structural changes associated with reversal of polarization of PZT before (as-grown) and after switching [211].

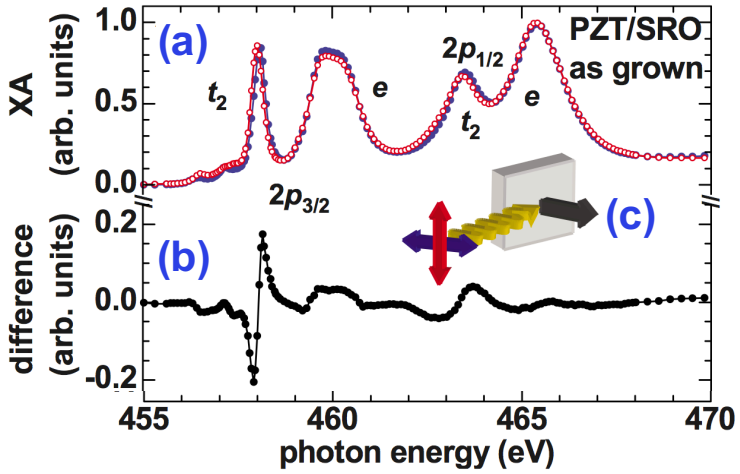

Figure 6.22: XAS spectra of PZT thin film grown on SRO/STO (001) are shown in (a), along with X-ray Linear Dichroism signal shown in (b). Inset (c) shows the sample orientation with respect to incoming polarized soft X-ray light. From [211].

6.3.2 Experimental Methods

Superlattices of $(PTO)_n/(STO)_n$ (short notation: '*n* x *n*') were synthesized on $(001)_{pc}$-oriented DSO via RHEED-assisted PLD under the same growth conditions as described earlier in Chapter 5. Superlattice periodicity corresponding to 14 x 14 and 16 x 16 grown on DSO substrate was used to study the optical behavior of long-range ordered vortex structures present in these superlattices. Structural characterization of these superlattice films was performed by Laboratory-based XRD and Synchrotron X-ray diffraction methods. High-resolution Scanning Transmission Microscopy was employed to map polar lattice distortions present in the individual layers of PTO-STO superlattice. Resonant soft X-ray Absorption Spectroscopy was performed at 'Ti' *L*-edge to measure X-ray Circular Dichroism (XCD) from vortex-antivortex arrays.

6.3.3 Results and Discussion

Several *ex situ* techniques such as XRD, PFM, first characterized superlattice films grown via RHEED-assisted PLD and TEM to ensure good quality of films, as discussed in great detail in previous and this chapter. After ensuring high quality of superlattice films, we measured X-ray Circular Dichroism of vortex structures using Resonant Soft X-ray Absorption Spectroscopy. With the unique capability of RSXS to combine resonant scattering with absorption spectroscopy allowed to us to specifically probe only vortex polarization structure in the superlattice structure. The in-plane diffraction from the vortex

structures giving rise to peaks along H and K direction ($[100]_{pc}$ and $[010]_{pc}$) were first tuned to resonate with 'Ti' *L*-edge to enhance the scattering cross-section from the vortex structures. Then, for a given diffraction geometry, *i.e.* a given vortex diffraction peak, X-ray absorption spectroscopy was performed using a circularly polarized light. The difference in the absorption spectra of left- vs right-circularly polarized light amounts to the X-ray Circular Dichroism (XCD) possessed by the features being RSXS probed.

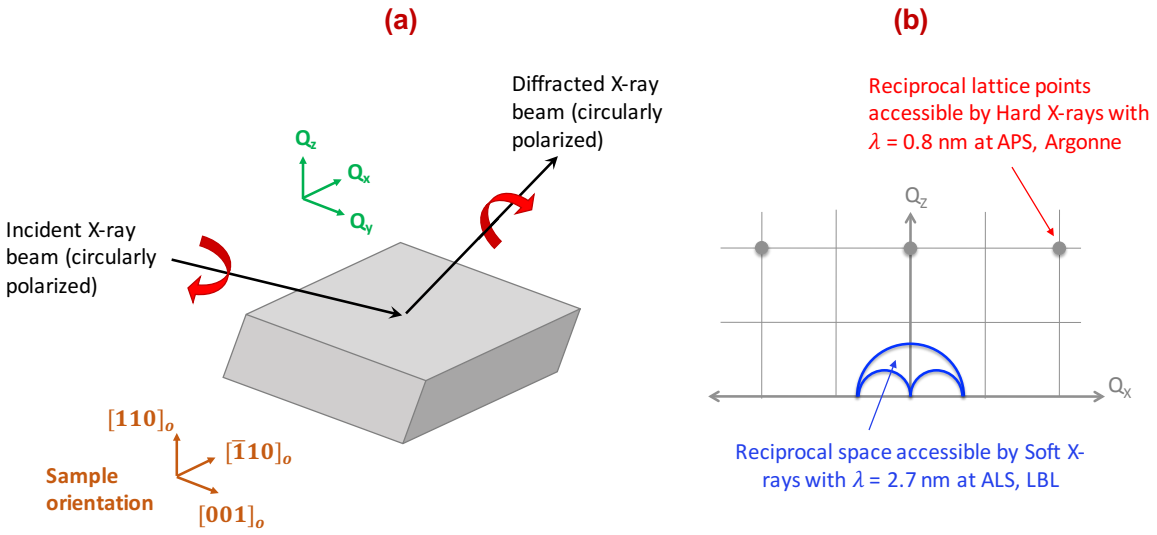

Figure 6.23: A schematic of RSXS measurement is drawn in (a), with reciprocal space highlighting the difference between the spaces accessible by soft vs. hard X-rays.

In the Figure 6.23, the sample orientation with respect to the incident circularly polarized X-ray light used for measuring XCD signal from polarization vortices is illustrated. From the knowledge gained from the previous 3D RSM that vortex structure align along $[100]_{pc}$ and $[010]_{pc}$ directions giving rise to diffraction peaks along H and K (shown as Q_x and Q_y in Figure 6.23(a)), which repeats in the L-direction (or Q_z in the Figure 6.23(a)) with superlattice period as found in previous 3D RSM studies (see Figure 6.19). The presence of vortex diffraction peaks occurring repeatedly along L-direction with periodicity same as the superlattice period, greatly simplified this experiment and allowed us to conveniently choose an L-value corresponding to vortex diffraction and perform XCD on vortex diffraction peaks present in the in-plane directions (a schematic of which is shown in Figure 6.24(b)). In addition, the advantage of superlattice structure in increasing the volume fraction of the vortex phase becomes apparent in this measurement.

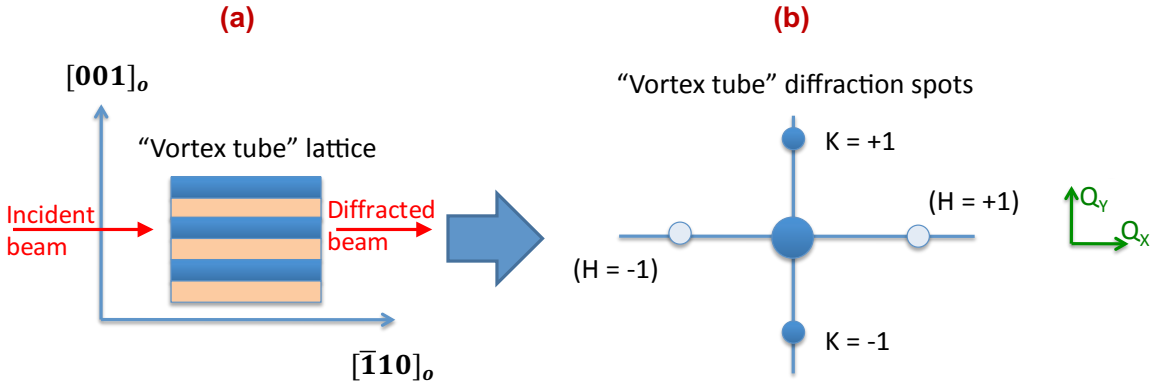

Figure 6.24: A schematic of diffraction geometry is drawn in (a) showing the vortex orientation with respect to incoming X-ray beam, which results in diffracted intensities along H- and K-direction as shown in the schematic (b). Figure courtesy of Dr. Padraic Shafer, Prof. Elke Arenholz.

Using the diffraction geometry described above, XCD was performed on the vortex diffraction peaks on a 14 x 14 superlattice grown on a DSO (110) substrate. The result of the measurements is presented in Figure 6.25, which shows the X-ray absorption spectrum obtained in Fluorescence Yield (FY) mode. For a given diffraction peak (for this case, K = + 1), FY spectra obtained for a left- (in blue) vs right-circularly polarized light (in red) was recorded is shown Figure 6.25 (a). The difference in the absorption spectra shows a non-zero Circular Dichroism signal as shown in Figure 6.25(b). Similarly, XCD was measured for other three diffraction peaks shown in the schematic Figure 6.25(c), all of which exhibited a non-zero XCD signal with similar sign in the difference of absorption spectra from left- vs right-circularly polarized. Other superlattice periodicities such as 16 x 16 was also measured using this method, which exhibited a slightly stronger magnitude of XCD signal from the vortex diffraction peaks. These measurements indicate that the vortex-antivortex structures are chiral in nature. This result agrees well with the theoretical studies predicting a handedness associated with such polarization vortex structures.

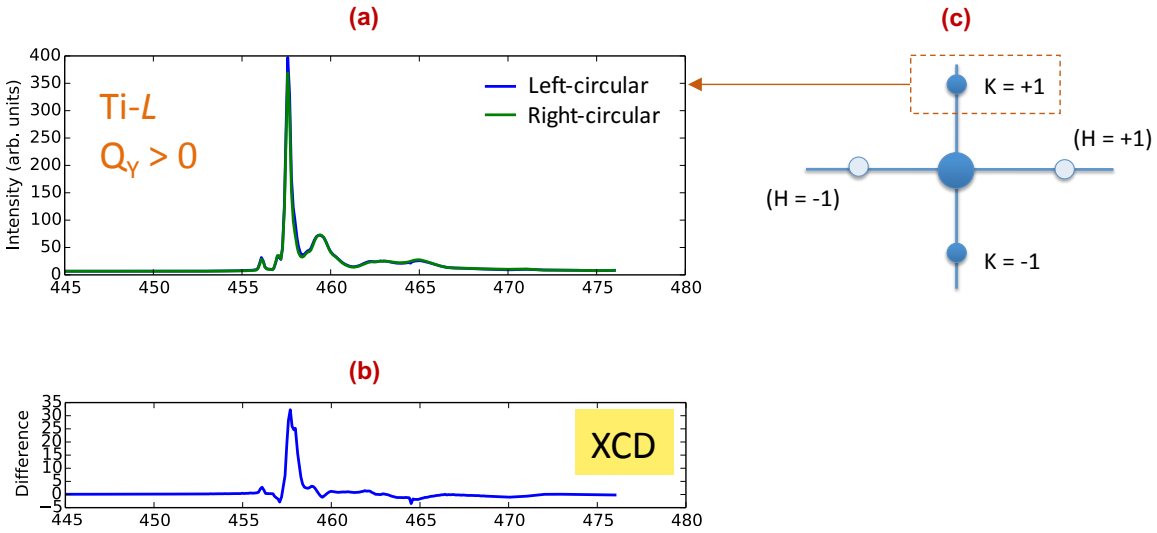

Figure 6.25: XAS spectra from a vortex diffraction peak in a 14 x 14 PTO-STO superlattice film grown on a DSO (110) substrate, obtained in FY mode is shown in (a) for both left- and right-circular polarized X-ray light. The difference in the absorption spectra between left- and right-circular polarized lights is shown in (b). The schematic of the particular diffraction peaks used for the XCD measurement is shown in (c). Figure courtesy of Dr. Padraic Shafer, Prof. Elke Arenholz.

6.4 Possibility of Phonon Localization due to Vortex *Lattice*

6.4.1 Background

Phonon localization has been pursued for long in both ordered [477-479] and disordered media [318-320; 480]. Although disordered media such as amorphous materials (glass [321]), have been studied in great detail for localization of phonons, ordered media are still being pursued for observation of this phenomenon [481; 482]. This is primarily because disordered media has degraded electronic (and other) properties due to lack of mass or structural order, which makes them at disadvantage for applications such as thermoelectric and thermal management. And, thus, there is an active search for localization of phonon modes in crystalline materials. One possible route to search for this phenomenon is through scattering of phonons, where optimum degree of correlated scattering of phonons within the material can significantly reduce propagation of extended states. The localization of those states, or significant percentage of those, which carry large portion of heat in the system, will result in massive reduction of thermal conductivity, which is highly desirable for certain applications [258].

For correlated scattering to occur depends strongly on whether phonon wave packets can retain their phase information between successive scattering events. For most systems, since significant heat is carried by those states whose wavelengths are less than few nanometers, nanostructured systems becomes the most suited candidates to realize correlated scattering and their effect on heat transport. Superlattices are one possible option and have been employed in demonstrating the effect of correlated scattering on heat transport across thin films, as discussed greatly in chapter 5. Coherent transport of phonons observed in superlattice structures is one consequence of correlated scattering phonon, where the constructive interference between phonon waves leads to non-zero states in BZ zone and deconstructive interference leads to disallowed states forming minibands in the (superlattice) phonon dispersion curve. Building on theoretical studies predicting this coherent scattering in superlattice systems, there have been many theoretical predictions of significant degree of phonon localization in random multilayers [261; 313] and quasi-periodic structures [322], utilizing correlated scattering of phonons. For instance, when average phonon transmission rate is calculated for random multilayers composed of GaAs and AlAs, significant reduction in transmission rate of phonon spectrum was observed (Figure 6.26(a)). The reduction in transmission rate for random multilayers (circles plus black solid line) becomes apparent when compared to a periodic superlattice (red solid line) also plotted in Figure 6.26(a) [313].

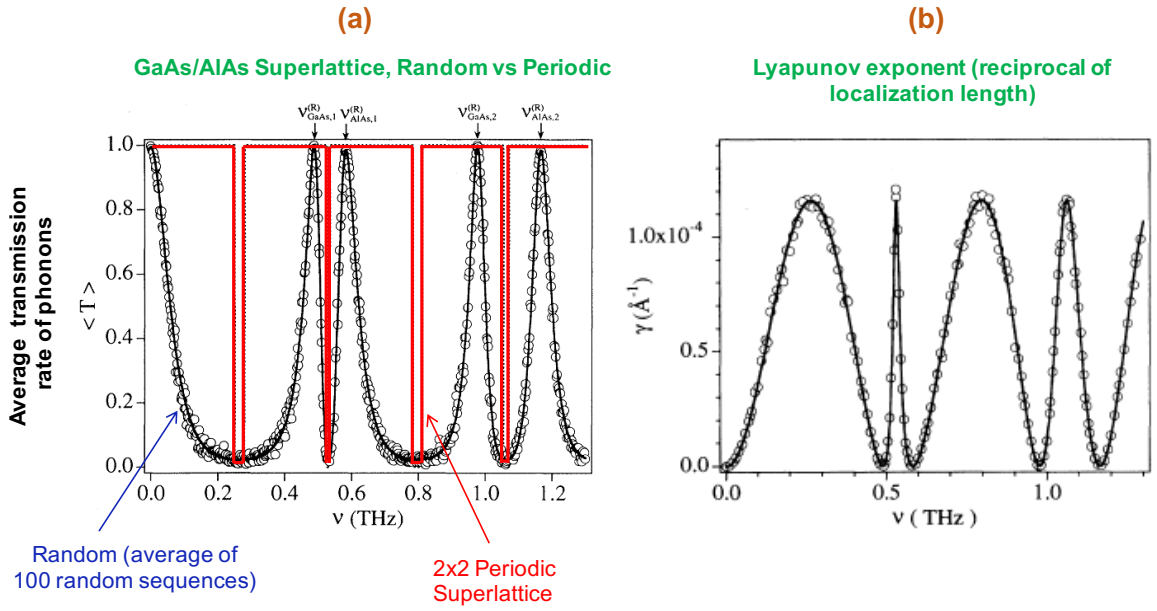

Figure 6.26: (a) Average phonon transmission rate of phonon across a random multilayer of GaAs-AlAs vs a periodic superlattice (2 x 2). (b) Lyapunov exponent for a random multilayer as a function of phonon frequency corresponding to which the average transmission rate is shown in (a). For both graphs, solid lines correspond to analytical solution, while open circles indicate numerical data. From [313].

Phonon localized states are often characterized by the localization length (ξ) or more conveniently by inverse of localization length, also known as Lyapunov exponent (γ). Localization length or Lyapunov exponent represents the rate at which the amplitude of eigen modes decay due to the presence of large amount of disorder in the random multilayers. Corresponding to the transmission rate of random multilayer (vs periodic superlattice) shown in Figure 6.26(a), Lyapunov exponent is computed and plotted as a function of phonon frequency in Figure 6.26(b) [313]. There are plenty of observations that can be made from this calculation. First, the frequencies corresponding to which superlattice phonon dispersion curve have band gaps or forbidden modes, show maxima in Lyapunov exponent. The presence of non-zero Lyapunov exponent (γ) for all other frequencies indicates that the large amount of randomness in mass distribution has introduced sufficient coherent backscattering of phonons to possess non-zero γ decay constant. Using these optimized structures, which allows significant reduction of phonon propagation by localizing them, presents one possible route to search for (or induce) phonon localization in crystalline materials.

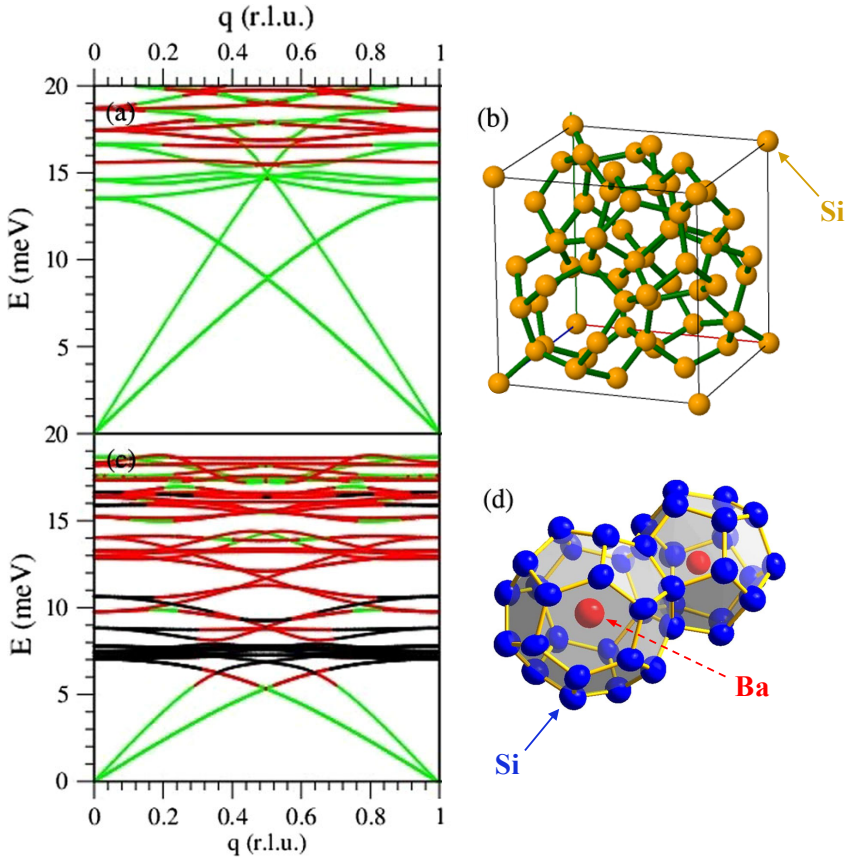

Figure 6.27: (a), (c) present simulated phonon dispersion relation for clathrates Si_{46} and Ba_8Si_{46} respectively. (b) shows the crystal structure of Si_{46}, while (d) show building units

of Ba_8Si_{46} with 'Ba' atoms occupying empty polyhedral cavities of 'Si' network. Figure adapted from [244; 482].

In contrast to above route which relies on manipulating propagation of phonons by inducing a unique type of scattering, one could pursue another route which depends on the design of material itself. This essentially means that structure of the material will allow a phonon dispersion curve which will promote increased percentage of localized modes in the spectrum of phonon states, thereby increasing the portion of non-conducting phonons in the heat-carrying phonon states. Thus, will greatly reduce the lattice thermal conductivity of the materials. Perhaps, the most suitable example to explain this approach is type-I clathrates materials [482]. Si_{46} is a type-I clathrate with a simple cubic structure having 46 atoms per unit cell (Figure 6.27 (b)) and it is formed by a covalent bonding between Si framework which leaves large polyhedral cavities in the crystal structure. The thermal conductivity of this ordered framework of Si atoms (in Si_{46}) is reasonably high, of about ~ 120 W/mK [483]. For this clathrate material system, Si_{46}, simulated phonon dispersion curve is plotted in Figure 6.27(a), with the modes coded in color to highlight the strength of their participation ratio (Green and Red suggesting high and intermediate strength). When 'Ba' atoms are used to fill those empty cavities formed by Si framework (Figure 6.27(d)) making another clathrate compound Ba_8Si_{46}, whose thermal conductivity was found to reduced by orders of magnitude. At room temperature, single crystals of Ba_8Si_{46}, was found to exhibit ultralow thermal conductivity of 1.7 W/mK [482]. The corresponding phonon dispersion curve for Ba_8Si_{46} is shown in Figure 6.27(c), along with the mode color coded according to their participation ratio. This drastic reduction in lattice thermal conductivity is attributed to the localization of propagative acoustic phonons having wave vectors beyond a critical value (q_c) (Figure 6.28 (b,d)). This localization of acoustics phonons originates from the strong entanglement of phonons corresponding to 'Si' (host) and 'Ba' (guest) sublattices. It has been experimentally verified that there is spectral weight transfer from Si-dominated acoustics phonons to flat optical phonons (Figure 6.28 (b, d)). The dynamical structure factor (which represents phonon intensity, position *etc.*) measured as a function of wave vectors using inelastic x-ray scattering, shows drastic decrease in the Longitudinal acoustic (LA) and Transverse acoustic (TA) intensities beyond q_c, with simultaneous increase in the intensity corresponding to optical phonons (at E_1, Figure 6.28 (b, d)). Such spectral transfer results in the bending of dispersion curve related to acoustic mode, eventually leading to zero slope frequency (or, E) vs wave vector (q) (at E_1, Figure 6.28 (a, b)). This approach of manipulating phonon dispersion relation by carefully designing the material crystal structure gives us another route to search for broadband localization of phonons in materials.

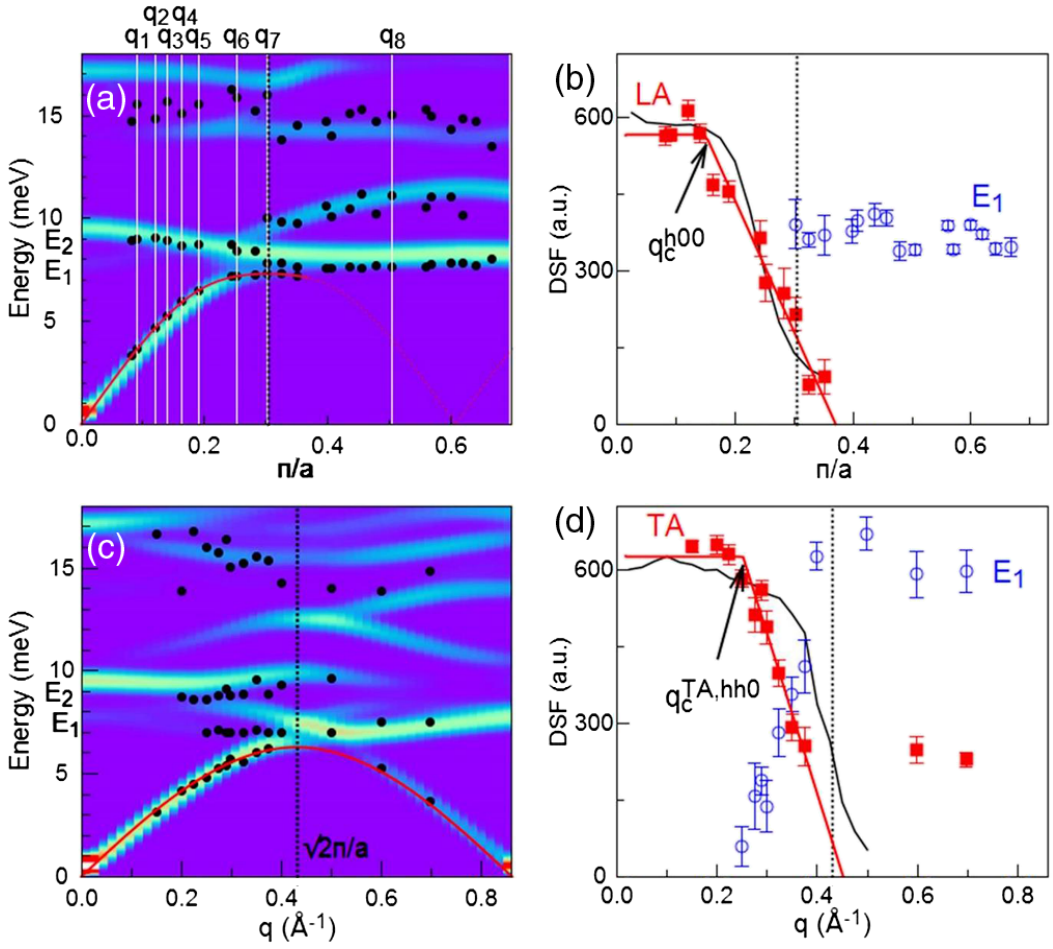

Figure 6.28: (a) and (c) shows the map of simulated Inelastic X-ray Scattering (IXS) intensities of Longitudinal acoustic (LA_{001}) and Transverse acoustic (TA_{001}^{110}) phonons propagating along [001] respectively. The black dots in (a) and (c) represent the experimentally measured data points. (b) and (d) plots dynamic structure factor (DSF), measured in red squares, simulated in solid black line, for longitudinal and transverse acoustic phonons respectively, along with the intensities of optical phonons corresponding to 'Ba' guest sublattice at E_1. From [482].

6.4.2 Hypothesis

From the discussion in chapter 5, we learned that there is stabilization of non-uniform polarization modes in the form of vortex-antivortex structures in ferroelectric (PTO) layers of PTO-STO superlattice grown on DSO (110) substrate. In that chapter, I discussed both theoretical results (Figure 5.13) and experimental observation (Figure 5.22), while in this section I will discuss time-evolution of polarization distribution as calculated from Phase-field simulations.

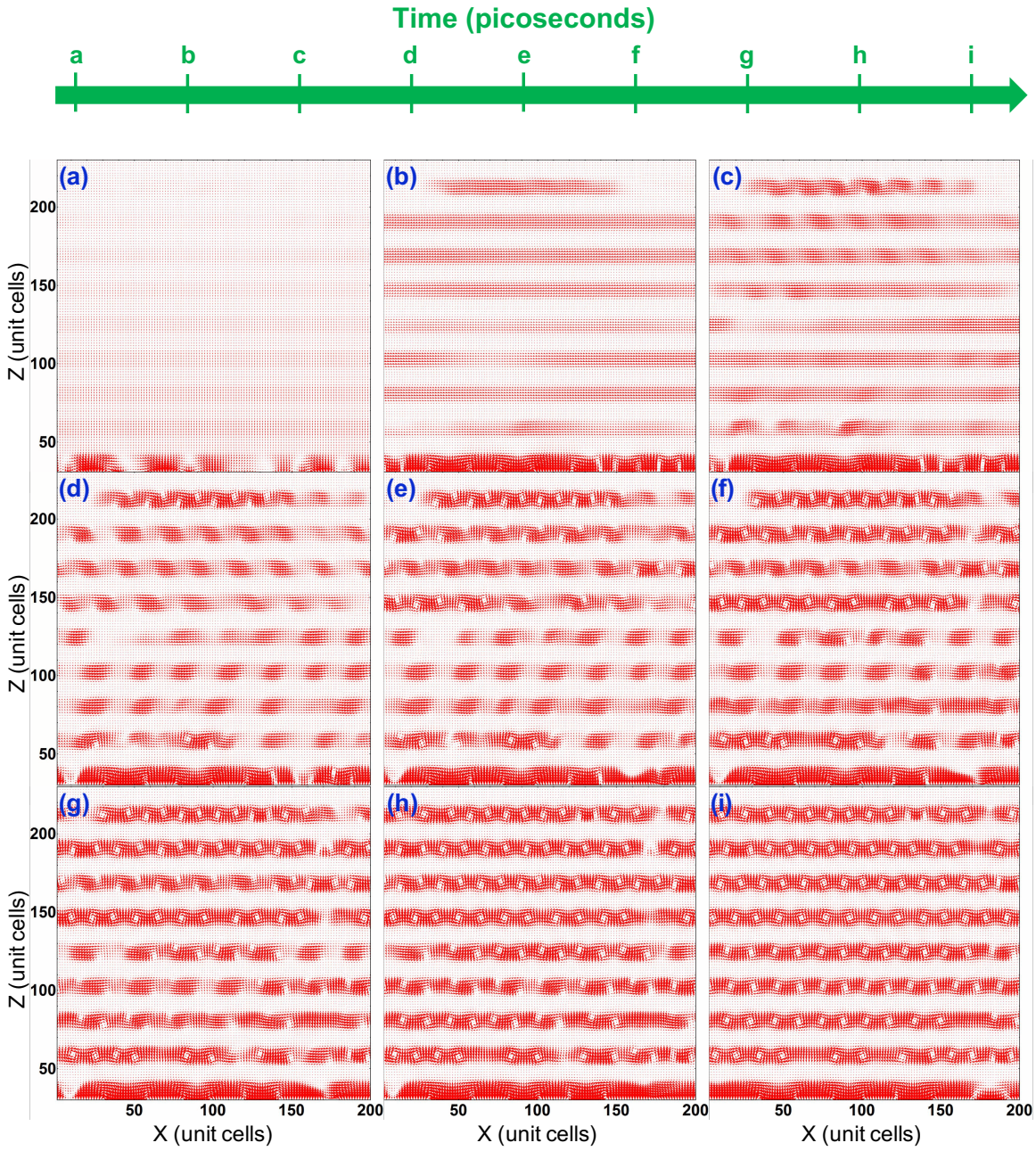

Figure 6.29: Time evolution of polarization distribution in 10 x10 PTO-STO superlattice as simulated using Phase-field Simulations is shown from (a) to (i) in chronological order. Time axis is also shown to highlight the evolution of vortex state from an unpolarized state. Courtesy of Zijian Hong.

In Figure 6.29, time-evolution of polarization distribution in a 10 x 10 superlattice structure as simulated using Phase-field models at room temperature is illustrated. In this

theoretical experiment, starting from a very weakly and randomly polarized state at time equal to 0, the kinetics of polarization distribution is recorded as a function of time at intervals of 2.5 picosecond (ps) and is shown in Figure 6.29. Just after a time span 2.5 ps (Figure 6.29(a)), PTO layers shows mostly in-plane polarized region with very small magnitude of polarization. After additional 2.5 ps (Figure 6.29(b)), most PTO layers of superlattice structure begin to have significant amount polarization, again polarized along in-plane direction. But, after 7.5 ps (Figure 6.29(c)), some PTO layers of the superlattice structures begin to form non-uniform polarization distribution, resembling wave-like structure (see the top PTO layer of the superlattice structure). Given additional 2.5 ps (Figure 6.29(d)), *i.e.* after 10 ps, some layers of PTO start to form vortex-antivortex polarization structures while the rest of PTO regions begins to form wave-like polarization structure. Further recording the polarization distribution with time ((Figure 6.29(e-i))), reveals that first wave-like modulation is formed, followed by vortex-antivortex structures.

Since PTO is a displacive ferroelectric (Figure 5.5), local polarization in PTO layers relates directly to the lattice distortion present at those respective locations. The periodic occurrence of vortex-antivortex structures in PTO layers and associated periodic lattice distortion leads to formation of Vortex *Lattice* with periodicity ~ 9-10 nm (Figure 6.30). The periodic lattice distortions due to this vortex lattice give rise to in-plane satellite peaks observed in 3D RSMs of superlattice films (Figure 5.20 and Figure 6.19). Similar to previous example of Si_{46} vs Ba_8Si_{46}, phonons corresponding to vortex sublattice may entangle with those corresponding to PTO unit-cell lattice leading to localization of acoustic phonons beyond a critical value of (phonon) wave vector. If there is a significant spectral weight transfer from acoustic (LA, TA or both) phonons, corresponding to PTO sublattice, to flat-optical phonons corresponding to vortex sublattice, one may observe drastic reduction in phonon propagation especially in the in-plane direction leading to extremely low value of thermal conductivity. It would very interesting to simulate the phonon dispersion curve for PTO-STO superlattice structure having vortex lattice in subsequent PTO layers and experimentally study the dispersion relation from Inelastic X-ray Scattering. Moreover, if we can stabilize the metastable states shown in Figure 6.29 in that order using controlled cooling rate from the (high) growth temperature, systematic evolution of phonon dispersion relation and corresponding evolution of phonon propagation and thermal conductivity in the in-plane direction, can be studied in detail.

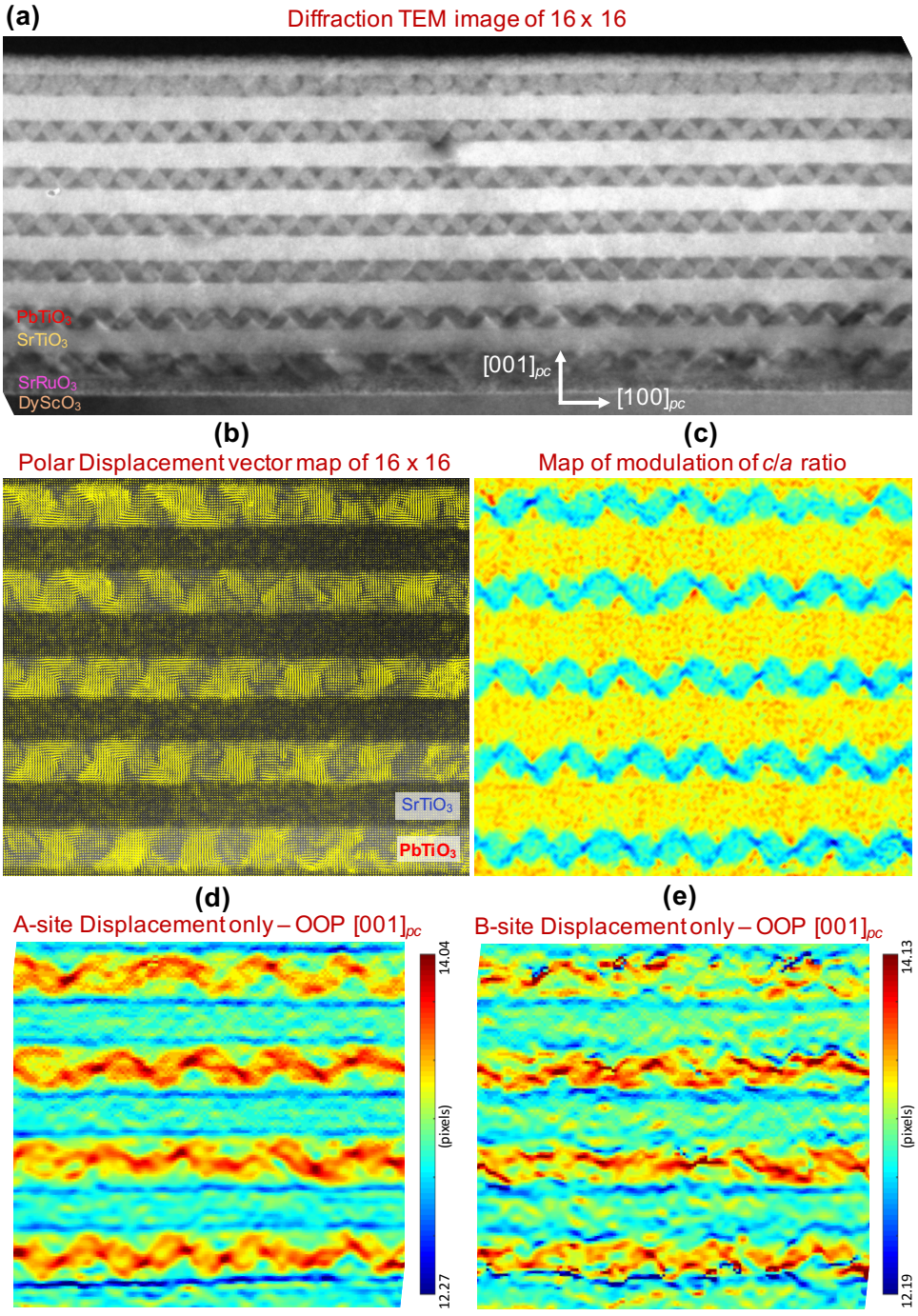

Figure 6.30: (a) Contrast in diffraction TEM shows the wave-like modulation of lattice associated with polarization vortices in PTO layers of 16 x 16 PTO-STO superlattice film grown on DSO (110) substrate. (b) Polar displacement map showing the displacement vectors (in yellow) corresponding to A-site only, overlaid on HRSTEM image. The colorized map of '*c*/*a*' ratio of the same superlattice film as extracted from a high-resolution

STEM image is shown in (c). The displacement maps corresponding to both A-site (d) and B-site (e) extracted from HRSTEM image is shown in (d) and (e) respectively. Courtesy of Dr. Christopher Nelson.

If there is indeed significant localization of acoustic modes due to the presence of vortex sublattice, one can design optimized superlattice structures which will have increased volume fraction of PTO layers to further reduce overall thermal conductivity of the thin-film structure. For example, decreasing the STO layers in the superlattice structure to say 4 unit-cell or 1 unit-cell, making a 10 x 4 (or 10 x 1) asymmetric superlattice, where the volume of vortex structure is greatly increased leading to even larger reduction in thermal conductivity (as compared to symmetric 10 x 10 superlattice structure). In addition, it would also be interesting to measure thermal conductivity in the out-of-plane direction and study the scattering of phonons propagating in that direction by localized modes corresponding to vortex sublattice. The other prospects of phonon localization leading to ultralow thermal conductivity are that they open possibility of controlling thermal conductivity via Electric field. Preliminary measurements using PFM and *in situ* TEM shows that these vortex polarization states can be controlled via Electric field. Using PFM, it was found that vortex state could be switched to uniformly polarization (a_1/a_2) states and to-and-fro, in 16 x 16 for example. If phonon localization leads to large reduction in thermal conductivity compared to uniformly polarized state (a_1/a_2), electric field can be used to control thermal conductivity by significant amount. In sum, designing material structure in a way to induce significant localization of heat-carrying phonons by modifying the phonon dispersion relations, presents a unique way to alter heat flow and potentially achieve ultralow thermal conductivity in crystalline material.

6.5 Summary and implications

In this chapter, two main observations on the unique characteristics associated with superlattices of PTO-STO were discussed. First, anomalous ferroelastic domain size evolution with superlattice periodicity was described, where inverse Kittel behavior was observed which is opposite to what has been reported in bulk-like ferroelectric systems. Such behavior may have arisen from the large changes in the depolarization fields when the periodicity of the superlattice structure is increased. Second, the nature of polarization vortices was studied using resonant soft x-ray scattering, which revealed that distribution of polarization vectors forming a vortex structure possesses optical chirality. This result aligns with theoretical studies, which associate a handedness to polarization vortex predicted in ferroelectric nanostructures.

This study invites further investigations to fully characterize the properties discussed here and other associated properties with such novel polarization structures. First, studies focused on finding the origin of observed inverse Kittel behavior of domain size evolution would be fundamentally interesting. For instance, changing the superlattice structure from symmetric to asymmetric superlattice with the strain state kept same and

characterizing the ferroelectric domain structure. The other interesting study would be to combine this superlattice structure-dependent ferroelectric domain evolution with strain to understand the role of epitaxial strain in the observed behavior. One more potentially interesting study could be to synthesize tricolor superlattice structure with one ferroelectric component (PTO) and two other non-ferroelectric components and study the domain evolution with superlattice periodicity and structure. This study can be further combined with different strain states of the superlattice structure. Second would be to study the ferroelectric characteristics of the domains observed in these superlattice structures. For instance, polarization hysteresis loops from the characteristic domains (ex. d_{33} loop) and the effect of temperature on domain evolution measured via PFM. The coexistence of vortex domains and uniformly polarized a_1/a_2 domains on the ferroelectric properties of superlattice phases would also be interesting as they will provide more physical understanding about these ferroelectric phases and their associated properties. Third, would be further investigations to fully understand the origin of optical chirality in polarization vortices. And, investigate the implications of chirality on the existence non-vanishing components of novel peizotoroidic tensor predicted for these polarization vortices. The other important study is to control the chirality of polarization vortices using an external stimulus such as electric field, temperature *etc.* These studies are much needed for the novel applications anticipated for these polarization vortices in the development of next generation devices such as nanomemory, nanotransducers, nanosensors, nanomotors and nanoswitchers.

Chapter 7

Conclusion and future prospects

I conclude this dissertation by revisiting the major findings of the studies presented and their implications. In the first chapter, I have shown a unique heat transport phenomenon by utilizing the lattice degree of freedom available in the complex oxide material systems. By synthesizing bicolor superlattices of STO-CTO and BTO-STO, I demonstrated a heat transport behavior dominated by the wave characteristics of phonons, called as Coherent phonon transport, which has not been observed in bulk-like systems. In short-period superlattices, when the coherence length of heat-carrying phonons becomes comparable to period the superlattice phonon dispersion curve begins the dictate the phonon transport behavior. In contrast to conventional incoherent heat transport where phonon transport can be described by energy-carrying particles, in coherent transport the scattering of phonons becomes correlated meaning the interference between phonon waves leads to significant change in the dispersion curve. This leads to formation phonon minibands in the superlattice dispersion curve which significantly alters their group velocity and hence their transport behavior. With the inherent capability of superlattice structures to reduce the dimensions of a material down to length scale of phonon coherence length and at the same time have enough volume (*i.e.* no. of superlattice repeats) to be able to measure transport properties using conventional techniques, allowed us to tune the thermal transport behavior as a function of superlattice period. In large period superlattices, incoherent phonon transport behavior was observed, *i.e.* decrease in thermal conductivity with increase in superlattice period, which is expected due to their much larger lengths as compared to coherence length. As the periodicity is reduced to length scales comparable to coherence length, due to interference between the phonons waves getting scattering at the superlattice interfaces the transport behavior was dominated by the superlattice phonon dispersion which is further decided by the superlattice period. In this coherent regime, thermal conductivity was observed to increase with the increase in superlattice period, *i.e.* opposite to what was observed in the incoherent regime. These results of phonon wave interference affecting macroscopic properties such as thermal conductivity invites other investigations searching for phenomenon such as phonon localization, phonon filtering *etc.*, which could have significant impact on expanding the limits of thermal conductivity found in material systems. More broadly, utilizing wave nature of phonons in controlling heat flow can have huge implications for thermal management, energy storage and conversion.

In chapter 5, I have combined the lattice degree of freedom with charge and orbital degrees available in complex oxides, to demonstrate another unique physical phenomenon, which has been only discussed in theoretical studies. By synthesizing superlattice structures of a ferroelectric and paraelectric material and utilizing the complex interplay between these degrees of freedom, I have stabilized complex topologies of electric polarization, namely vortex-antivortex arrays, which are reminiscent of spin topologies such as magnetic skyrmions, merons *etc.* The experimental observation of polarization vortices in this superlattice structure provides unambiguous evidence for long-standing theoretical prediction of such non-uniform polarization states in ferroelectrics nanostructures. In contrast to normal bulk-like ferroelectric systems, where in the ferroelectric state regions of uniform polarization exist separated by domain walls, the uniqueness of this phenomenon is highlighted from the fact the polarization distribution adopts a completely non-uniform distribution and arranging into a specific kind of structures, *i.e.* vortex-antivortex arrays. Such non-uniform polarization distributions are understood to have arisen from the competition between various energies such as elastic (strain) energy, depolarization energy and electrostatic energy. I also noticed that the superlattice-period dependent existence of these polarization vortices agrees well with the theoretical prediction of size-dependent existence of non-uniform polarization modes in nanostructures. These polarization vortices if controllable via electric field for example, are anticipated to enhance the storage capacity of non-volatile ferroelectric RAMs. One important prospect of stabilizing vortex structures of electrical polarization is the one in which such non-uniform polarization distributions can be induced in ferroelectric perovskites (such as $BiFeO_3$), where ferroelectric polarization is coupled to other order parameters (such as antiferromagnetic order) in the system. Such studies could provide pathways to improve physical properties in materials, such as magnetization in $BiFeO_3$ using enhanced Dzyalozhinski-Moriya interactions.

In the last chapter (6), I have discussed unique and unusual characteristics observed in PTO-STO superlattices as the periodicity is varied. An anomalous ferroelastic domain size evolution was observed which is opposite what is usually observed in bulk-like ferroelectric systems. In normal ferroelectric, with increase in ferroelectric thickness the domain size increases obeying Kittel's law. In PTO-STO superlattice, however, a negative scaling coefficient with ferroelectric (PTO) thickness in superlattice period was observed following an inverse Kittel behavior, *i.e.* with increase in the ferroelectric thickness the domain size reduces. As the superlattice periodicity was increased from short period (6 x 6) to long period (12 x 12), the domain size was found to decrease monotonically. Such behavior may stem from the large changes in depolarization fields as the superlattice periodicity is increased from short period to long period. More interesting domain evolution may be observed when system parameters such as strain state, superlattice structure, superlattice-type *etc.*, are varied. And, the associated change in the ferroelectric properties would be an interesting avenue to explore the potential of superlattice structures in tailoring properties. In this chapter, I have also briefly discussed the preliminary results characterizing the nature of polarization vortices observed in PTO-STO superlattices. Using Resonant Soft X-ray absorption studies, I showed that the vortex-antivortex structures possess chirality as measured from the difference in the X-ray absorption spectra

of left- vs right-circularly polarized light. The existence of chirality is interesting because if the vortices can be controlled by external electric field, it opens the possibility of controlling the chirality in materials using electric field.

Thus, using the studies presented in this dissertation, I have shown enough evidence to substantiate the claim that superlattice structures continues to provide a phase space where unique, hidden and novel physical phenomena exists and remains largely untapped.

Bibliography

[1] Z.I. Alferov, Reviews of Modern Physics 73 (2001) 767-782.

[2] A.I. Gubanov, Zh. Tekh. Fiz. 20 (1950).

[3] S. William, Circuit element utilizing semiconductive material, Google Patents, 1951.

[4] A.I. Gubanov, Zh. Tekh. Fiz. 21 (1951).

[5] N.G. Basov, O. N. Krokhin, and Yu. M. Popov, Sov. Phys. JETP 12 (1961).

[6] D.N. Nasledov, A. A. Rogachev, S. M. Ryvkin, and B. V. Tsarenkov, Sov. Phys. Solid State 4 (1962).

[7] R.H. Hall, G. E. Fenner, J. D. Kingsley, T. J. Soltys, and R. O. Carlson, Phys. Rev. Lett. 9 (1962).

[8] N. Holonyak, Jr., and S. F. Bevacgua, Appl. Phys. Lett. 1 (1962).

[9] M.I. Nathan, W. P. Dumke, G. Burns, F. H. Dill, Jr., and G. I. Lasher, Appl. Phys. Lett. 1 (1962).

[10] A.Y. Cho, Applied Physics Letters 19 (1971) 467-468.

[11] R. Dingle, W. Wiegmann, C.H. Henry, Physical Review Letters 33 (1974) 827-830.

[12] R.D. Dupuis, P.D. Dapkus, N. Holonyak, E.A. Rezek, R. Chin, Applied Physics Letters 32 (1978) 295-297.

[13] L.L. Chang, L. Esaki, R. Tsu, Applied Physics Letters 24 (1974) 593-595.

[14] L. Esaki, and R. Tsu, IBM J. Res. Dev. 14 (1970).

[15] R.F. Kazarinov, and R. A. Suris, Sov. Phys. Semicond. 5 (1971).

[16] R.F. Kazarinov, and R. A. Suris, Sov. Phys. Semicond. 7 (1973).

[17] R. Tsu, L. Esaki, Applied Physics Letters 22 (1973) 562-564.

[18] R. Dingle, H.L. Störmer, A.C. Gossard, W. Wiegmann, Applied Physics Letters 33 (1978) 665-667.

[19] D. Delagebeaudeuf, P. Delescluse, P. Etienne, M. Laviron, J. Chaplart, N.T. Linh, Electronics Letters 16 (1980) 667-668.

[20] M. Takashi, H. Satoshi, F. Toshio, N. Kazuo, Japanese Journal of Applied Physics 19 (1980) L225.

[21] J.P. van der Ziel, R. Dingle, R.C. Miller, W. Wiegmann, W.A. Nordland, Applied Physics Letters 26 (1975) 463-465.

[22] W.T. Tsang, Applied Physics Letters 40 (1982) 217-219.

[23] Z.I. Alferov, et al., Sov. Tech. Phys. Lett. 14 (1988).

[24] K.v. Klitzing, G. Dorda, M. Pepper, Physical Review Letters 45 (1980) 494-497.

[25] D.C. Tsui, H.L. Stormer, A.C. Gossard, Physical Review Letters 48 (1982) 1559-1562.

[26] J. Seidel, Complex oxides : materials physics, synthesis, characterization and applications, De Gruyter, Berlin, 2015.

[27] P. Zubko, S. Gariglio, M. Gabay, P. Ghosez, J.-M. Triscone, Annual Review of Condensed Matter Physics 2 (2011) 141-165.

[28] J.A. Sulpizio, S. Ilani, P. Irvin, J. Levy, Annual Review of Materials Research 44 (2014) 117-149.

[29] C.N.R. Rao, Annual Review of Physical Chemistry 40 (1989) 291-326.

[30] L.W. Martin, Y.H. Chu, R. Ramesh, Materials Science and Engineering: R: Reports 68 (2010) 89-133.

[31] S. Havelia, Epitaxial Stabilization of Kinetically Frustrated Metastable Materials, Carnegie Mellon University, 2009.

[32] N.A. Benedek, Inorganic Chemistry 53 (2014) 3769-3777.

[33] T. Tomio, H. Miki, H. Tabata, T. Kawai, S. Kawai, Journal of Applied Physics 76 (1994) 5886-5890.

[34] H. Suzuki, H. Bando, Y. Ootuka, I. H. Inoue, T. Yamamoto, K. Takahashi, Y. Nishihara, Journal of the Physical Society of Japan 65 (1996) 1529-1532.

[35] L.A. Knauss, J.M. Pond, J.S. Horwitz, D.B. Chrisey, C.H. Mueller, R. Treece, Applied Physics Letters 69 (1996) 25-27.

[36] P. Ravindran, A. Kjekshus, H. Fjellvåg, A. Delin, O. Eriksson, Physical Review B 65 (2002) 064445.

[37] A. Hammouche, E.J.L. Schouler, M. Henault, Solid State Ionics 28 (1988) 1205-1207.

[38] J.B. Goodenough, Reports on Progress in Physics 67 (2004) 1915.

[39] T.T. Fister, D.D. Fong, in: S. Ramanathan (Ed.), Thin Film Metal-Oxides: Fundamentals and Applications in Electronics and Energy, Springer US, Boston, MA, 2010, pp. 1-49.

[40] J.M. Rondinelli, S.J. May, J.W. Freeland, MRS Bulletin 37 (2012) 261-270.

[41] Schematic of d orbitals, http://folk.uio.no/ravi/activity/ordering/orbitalordering.html.

[42] in, Magnetism: From Fundamentals to Nanoscale Dynamics, Springer Berlin Heidelberg, Berlin, Heidelberg, 2006, pp. 167-220.

[43] T. Hashimoto, S. Ishibashi, K. Terakura, Physical Review B 82 (2010) 045124.

[44] Schematic of orbital ordering in LaMnO3, http://www.fkf.mpg.de/645706/10_Spin-orbital-and-charge-order.

[45] in, Magnetism: From Fundamentals to Nanoscale Dynamics, Springer Berlin Heidelberg, Berlin, Heidelberg, 2006, pp. 221-310.

[46] S.J. Moon, H. Jin, W.S. Choi, J.S. Lee, S.S.A. Seo, J. Yu, G. Cao, T.W. Noh, Y.S. Lee, Physical Review B 80 (2009) 195110.

[47] S. Jin, T.H. Tiefel, M. McCormack, R.A. Fastnacht, R. Ramesh, L.H. Chen, Science 264 (1994) 413-415.

[48] J.-C. Lin, et al., Advanced Materials 28 (2016) 764-770.

[49] C.H. Ahn, J.M. Triscone, J. Mannhart, Nature 424 (2003) 1015-1018.

[50] L. Li, C. Richter, J. Mannhart, R.C. Ashoori, Nat Phys 7 (2011) 762-766.

[51] K. Ueda, H. Tabata, T. Kawai, Science 280 (1998) 1064-1066.

[52] L.W. Martin, D.G. Schlom, Current Opinion in Solid State and Materials Science 16 (2012) 199-215.

[53] H.Y. Hwang, Y. Iwasa, M. Kawasaki, B. Keimer, N. Nagaosa, Y. Tokura, Nat Mater 11 (2012) 103-113.

[54] J. Mannhart, D.G. Schlom, Science 327 (2010) 1607-1611.

[55] M. Dawber, N. Stucki, C. Lichtensteiger, S. Gariglio, P. Ghosez, J.M. Triscone, Advanced Materials 19 (2007) 4153-4159.

[56] K.-S.K.a.Y.H.J. Abhijit Biswas, in: L.P.a.G. Zhu (Ed.), Perovskite Materials - Synthesis, Characterisation, Properties, and Applications, 2016.

[57] K. Rogdakis, J.W. Seo, Z. Viskadourakis, Y. Wang, L.F.N. Ah Qune, E. Choi, J.D. Burton, E.Y. Tsymbal, J. Lee, C. Panagopoulos, Nat Commun 3 (2012) 1064.

[58] Y. Ogawa, H. Yamada, T. Ogasawara, T. Arima, H. Okamoto, M. Kawasaki, Y. Tokura, Physical Review Letters 90 (2003) 217403.

[59] H.N. Lee, H.M. Christen, M.F. Chisholm, C.M. Rouleau, D.H. Lowndes, Nature 433 (2005) 395-399.

[60] W. Tian, J.C. Jiang, X.Q. Pan, J.H. Haeni, Y.L. Li, L.Q. Chen, D.G. Schlom, J.B. Neaton, K.M. Rabe, Q.X. Jia, Applied Physics Letters 89 (2006) 092905.

[61] L.F. Kourkoutis, J.H. Song, H.Y. Hwang, D.A. Muller, Proceedings of the National Academy of Sciences 107 (2010) 11682-11685.

[62] P. Zubko, N. Jecklin, A. Torres-Pardo, P. Aguado-Puente, A. Gloter, C. Lichtensteiger, J. Junquera, O. Stephan, J.M. Triscone, Nano Lett 12 (2012) 2846-51.

[63] L. Xiaomin, K. Tomoji, K. Shichio, Japanese Journal of Applied Physics 33 (1994) L18.

[64] D.P. Norton, B.C. Chakoumakos, J.D. Budai, D.H. Lowndes, B.C. Sales, J.R. Thompson, D.K. Christen, Science 265 (1994) 2074-2077.

[65] I. Bozovic, J.N. Eckstein, M.E. Klausmeier-Brown, G. Virshup, Journal of Superconductivity 5 19-23.

[66] J.M. Triscone, O. Fischer, O. Brunner, L. Antognazza, A.D. Kent, M.G. Karkut, Physical Review Letters 64 (1990) 804-807.

[67] H. Tabata, T. Kawai, S. Kawai, Applied Physics Letters 58 (1991) 1443-1445.

[68] H.U. Habermeier, G. Cristiani, R.K. Kremer, O. Lebedev, G. van Tendeloo, Physica C: Superconductivity 364–365 (2001) 298-304.

[69] A.I. Buzdin, Reviews of Modern Physics 77 (2005) 935-976.

[70] Z. Sefrioui, D. Arias, V. Peña, J.E. Villegas, M. Varela, P. Prieto, C. León, J.L. Martinez, J. Santamaria, Physical Review B 67 (2003) 214511.

[71] T. Holden, et al., Physical Review B 69 (2004) 064505.

[72] J. Chakhalian, et al., Nat Phys 2 (2006) 244-248.

[73] A. Pimenov, A. Loidl, P. Przyslupski, B. Dabrowski, Physical Review Letters 95 (2005) 247009.

[74] A. Wold, W. Croft, The Journal of Physical Chemistry 63 (1959) 447-448.

[75] J. Kanamori, Journal of Physics and Chemistry of Solids 10 (1959) 87-98.

[76] A.V. Boris, et al., Science 332 (2011) 937-940.

[77] R. Eguchi, A. Chainani, M. Taguchi, M. Matsunami, Y. Ishida, K. Horiba, Y. Senba, H. Ohashi, S. Shin, Physical Review B 79 (2009) 115122.

[78] J. Mizusaki, I. Yasuda, J.i. Shimoyama, S. Yamauchi, K. Fueki, Journal of The Electrochemical Society 140 (1993) 467-471.

[79] K.S. Takahashi, M. Kawasaki, Y. Tokura, Applied Physics Letters 79 (2001) 1324-1326.

[80] Z. Zeng, M. Greenblatt, M. Croft, Physical Review B 59 (1999) 8784-8788.

[81] G.L. Catchen, T.M. Rearick, D.G. Schlom, Physical Review B 49 (1994) 318-326.

[82] M. Gibert, P. Zubko, R. Scherwitzl, J. Íñiguez, J.-M. Triscone, Nat Mater 11 (2012) 195-198.

[83] E.J. Monkman, C. Adamo, J.A. Mundy, D.E. Shai, J.W. Harter, D. Shen, B. Burganov, D.A. Muller, D.G. Schlom, K.M. Shen, Nat Mater 11 (2012) 855-859.

[84] X. Zhai, et al., Nat Commun 5 (2014).

[85] G. Rijnders, D.H.A. Blank, Nature 433 (2005) 369-370.

[86] E. Bousquet, M. Dawber, N. Stucki, C. Lichtensteiger, P. Hermet, S. Gariglio, J.M. Triscone, P. Ghosez, Nature 452 (2008) 732-6.

[87] J. Kim, Y. Kim, Y.S. Kim, J. Lee, L. Kim, D. Jung, Applied Physics Letters 80 (2002) 3581-3583.

[88] J. Sinsheimer, S.J. Callori, B. Bein, Y. Benkara, J. Daley, J. Coraor, D. Su, P.W. Stephens, M. Dawber, Physical Review Letters 109 (2012) 167601.

[89] S. Heinze, H.-U. Habermeier, G. Cristiani, S. Blanco Canosa, M. Le Tacon, B. Keimer, Applied Physics Letters 101 (2012) 131603.

[90] H. Ohta, et al., Nat Mater 6 (2007) 129-134.

[91] L.D. Hicks, M.S. Dresselhaus, Physical Review B 47 (1993) 12727-12731.

[92] A.I. Abutaha, S.R.S. Kumar, K. Li, A.M. Dehkordi, T.M. Tritt, H.N. Alshareef, Chemistry of Materials 27 (2015) 2165-2171.

[93] K. Koumoto, Y. Wang, R. Zhang, A. Kosuga, R. Funahashi, Annual Review of Materials Research 40 (2010) 363-394.

[94] P. Jha, T.D. Sands, P. Jackson, C. Bomberger, T. Favaloro, S. Hodson, J. Zide, X. Xu, A. Shakouri, Journal of Applied Physics 113 (2013) 193702.

[95] H. Ohta, R. Huang, Y. Ikuhara, physica status solidi (RRL) – Rapid Research Letters 2 (2008) 105-107.

[96] S.-E. Park, T.R. Shrout, Journal of Applied Physics 82 (1997) 1804-1811.

[97] J.J. Wang, P.P. Wu, X.Q. Ma, L.Q. Chen, Journal of Applied Physics 108 (2010) 114105.

[98] R. Eason, Pulsed laser deposition of thin films : applications-led growth of functional materials, Wiley-Interscience, Hoboken, N.J., 2007.

[99] D.G. Schlom, J.H. Haeni, J. Lettieri, C.D. Theis, W. Tian, J.C. Jiang, X.Q. Pan, Materials Science and Engineering: B 87 (2001) 282-291.

[100] J.J. Tietjen, Annual Review of Materials Science 3 (1973) 317-326.

[101] D.B. Chrisey, G.K. Hubler, Pulsed laser deposition of thin films, Wiley, New York, 1994.

[102] M. Aliofkhazraei, Advances in Graphene Science, 2013.

[103] E.W. Schlag, Time-of-flight mass spectrometry and its applications, Elsevier, Amsterdam; New York, 1994.

[104] G. Siegel, Y.P. Venkata Subbaiah, M.C. Prestgard, A. Tiwari, APL Mater. 3 (2015) 056103.

[105] H.-U. Krebs, et al., in: B. Kramer (Ed.), Advances in Solid State Physics, Springer Berlin Heidelberg, Berlin, Heidelberg, 2003, pp. 505-518.

[106] J. Choi, C.B. Eom, G. Rijnders, H. Rogalla, D.H.A. Blank, Applied Physics Letters 79 (2001) 1447-1449.

[107] G. Rijnders, D.H.A. Blank, J. Choi, C.-B. Eom, Applied Physics Letters 84 (2004) 505-507.

[108] G. Koster, Artificially layered oxides by pulsed laser deposition, University of Twente, Enschede, 1999.

[109] C. Ristoscu, Mihailescu, I. N., in, 2011.

[110] G. Koster, in, In Situ Characterization of Thin Film Growth, Woodhead Publishing, 2011, pp. 3-28.

[111] A. Ichimiya, P.I. Cohen., Reflection High-Energy Electron Diffraction, Cambridge University Press, 2004.

[112] K. Oura, M. Katayama, A.V. Zotov, V.G. Lifshits, A.A. Saranin, in: K. Oura, M. Katayama, A.V. Zotov, V.G. Lifshits, A.A. Saranin (Eds.), Surface Science: An Introduction, Springer Berlin Heidelberg, Berlin, Heidelberg, 2003, pp. 47-75.

[113] G. Koster, M. Huijben, A. Janssen, G. Rijnders, in, Epitaxial Growth of Complex Metal Oxides, Woodhead Publishing, 2015, pp. 3-29.

[114] C. Daumont, Multiferroic perovskites under epitaxial strain: The case of TbMnO3 thin films, University of Groningen, 2009.

[115] J. Klein, Epitaxial heterostructures of doped manganites, University of Cologne, 2001.

[116] Stages of layer by layer growth, http://lippmaa.issp.u-tokyo.ac.jp/rheed/.

[117] J. Nichols, O.B. Korneta, J. Terzic, L.E. De Long, G. Cao, J.W. Brill, S.S.A. Seo, Applied Physics Letters 103 (2013) 131910.

[118] D.-W. Kim, D.-H. Kim, B.-S. Kang, T.W. Noh, S. Shin, Z.G. Khim, Physica C: Superconductivity 313 (1999) 246-254.

[119] G.J.H.M. Rijnders, G. Koster, D.H.A. Blank, H. Rogalla, Applied Physics Letters 70 (1997) 1888-1890.

[120] S. Martini, A.A. Quivy, Brazilian Journal of Physics 32 (2002) 359-361.

[121] D.L. Proffit, H.W. Jang, S. Lee, C.T. Nelson, X.Q. Pan, M.S. Rzchowski, C.B. Eom, Applied Physics Letters 93 (2008) 111912.

[122] M. Lee, X-ray diffraction for materials research : from fundamentals to applications, 2016.

[123] B.D. Cullity, Elements of X-ray diffraction, Addison-Wesley Pub. Co., Reading, Mass., 1956.

[124] X-Ray Diffraction set up schematic, http://lipidlibrary.aocs.org/Biochemistry/content.cfm?ItemNumber=40299.

[125] D. Fuchs, E. Arac, T. Schwarz, R. Schneider, in: R. Haug (Ed.), Advances in Solid State Physics, Springer Berlin Heidelberg, Berlin, Heidelberg, 2008, pp. 271-275.

[126] R.J. Zeches, et al., Science 326 (2009) 977-980.

[127] D.G. Schlom, L.-Q. Chen, C.-B. Eom, K.M. Rabe, S.K. Streiffer, J.-M. Triscone, Annual Review of Materials Research 37 (2007) 589-626.

[128] D.G. Schlom, L.-Q. Chen, X. Pan, A. Schmehl, M.A. Zurbuchen, Journal of the American Ceramic Society 91 (2008) 2429-2454.

[129] M.D. Smith, et al., Journal of Materials Chemistry C 2 (2014) 5787-5792.

[130] P. Padhan, P. LeClair, A. Gupta, M.A. Subramanian, G. Srinivasan, Journal of Physics: Condensed Matter 21 (2009) 306004.

[131] U. Pietsch, V. Holý, T. Baumbach, Determination of Layer Thicknesses of Single Layers and Multilayers, Springer New York, New York, NY, 2004.

[132] Schematic of Symmetric and Asymmetric XRD scans, TU Munich, http://www.ph.tum.de/studium/praktika/fopra/text/userguide-08.en.pdf, 2009.

[133] U. Pietsch, V. Holý, T. Baumbach, in: U. Pietsch, V. Holý, T. Baumbach (Eds.), High-Resolution X-Ray Scattering: From Thin Films to Lateral Nanostructures, Springer New York, New York, NY, 2004, pp. 179-203.

[134] Y. Hu, D. Stender, M. Medarde, T. Lippert, A. Wokaun, C.W. Schneider, Applied Surface Science 278 (2013) 92-95.

[135] C. Merckling, M. El-Kazzi, G. Delhaye, V. Favre-Nicolin, Y. Robach, M. Gendry, G. Grenet, G. Saint-Girons, G. Hollinger, Journal of Crystal Growth 306 (2007) 47-51.

[136] R.A. Coppeta, H. Ceric, D. Holec, T. Grasser, Critical thickness for GaN thin film on AlN substrate, 2013, 133-136.

[137] Y.B. Chen, H.P. Sun, M.B. Katz, X.Q. Pan, K.J. Choi, H.W. Jang, C.B. Eom, Applied Physics Letters 91 (2007) 252906.

[138] U. Pietsch, V. Holý, T. Baumbach, Diffractometers and Reflectometers, Springer New York, New York, NY, 2004.

[139] P.J. Withers, in, Practical Residual Stress Measurement Methods, John Wiley & Sons, Ltd, 2013, pp. 163-194.

[140] Application of Sychrotron light source, http://science.energy.gov/~/media/bes/pdf/Synchrotron_Techniques.pdf.

[141] N. Ikeda, M. Tanaka, H. Kitô, S. Sasaki, Y. Yamada, Ferroelectrics 222 (1999) 227-235.

[142] K. Lee, H. Han, H. Yi, Y.J. Park, J.Y. Choi, S. Baik, in: J.Y. Choi, S. Rah (Eds.), Synchrotron Radiation Instrumentation, Pts 1 and 2, Amer Inst Physics, Melville, 2007, pp. 1411-1414.

[143] P. Zubko, N. Stucki, C. Lichtensteiger, J.M. Triscone, Physical Review Letters 104 (2010).

[144] B. Dupé, I.C. Infante, G. Geneste, P.E. Janolin, M. Bibes, A. Barthélémy, S. Lisenkov, L. Bellaiche, S. Ravy, B. Dkhil, Physical Review B 81 (2010) 144128.

[145] C.M. Schleputz, S.O. Mariager, S.A. Pauli, R. Feidenhans'l, P.R. Willmott, Journal of Applied Crystallography 44 (2011) 73-83.

[146] C.M. Schleputz, R. Herger, P.R. Willmott, B.D. Patterson, O. Bunk, C. Bronnimann, B. Henrich, G. Hulsen, E.F. Eikenberry, Acta Crystallographica Section A 61 (2005) 418-425.

[147] N. Tomczak, K.E.J. Goh, Scanning probe microscopy, World Scientific Pub. Co., Singapore; Hackensack, NJ, 2011.

[148] Tip as sharp as single atom, http://www.standford.edu/.

[149] H.-J. G¸ntherodt, Scanning tunneling microscopy, Springer, Berlin, 1992.

[150] T.R. Corle, G.S. Kino, Confocal scanning optical microscopy and related imaging systems, Academic Press, San Diego, 1996.

[151] G. Haugstad, Atomic force microscopy understanding basic modes and advanced applications, 2012.

[152] SPM schematic, http://www.eng.utah.edu/~lzang/images/Lecture_4_SPM.pdf.

[153] F. Sanchez, C. Ocal, J. Fontcuberta, Chemical Society Reviews 43 (2014) 2272-2285.

[154] G. Koster, B.L. Kropman, G.J.H.M. Rijnders, D.H.A. Blank, H. Rogalla, Applied Physics Letters 73 (1998) 2920-2922.

[155] T. Ohnishi, K. Takahashi, M. Nakamura, M. Kawasaki, M. Yoshimoto, H. Koinuma, Applied Physics Letters 74 (1999) 2531-2533.

[156] S. Iakovlev, C.-H. Solterbeck, M. Kuhnke, M. Es-Souni, Journal of Applied Physics 97 (2005) 094901.

[157] PFM schematic, https://www.asylumresearch.com/Applications/PFMAppNote/PFMAppNote.shtml.

[158] S. Lepadatu, M.G. Cain, in: G.M. Cain (Ed.), Characterisation of Ferroelectric Bulk Materials and Thin Films, Springer Netherlands, Dordrecht, 2014, pp. 191-219.

[159] PFM basics, http://www.parkafm.com/images/spmmodes/dielectric/Piezoelectric-Force-Microscopy-(PFM).pdf.

[160] S. Matzen, O. Nesterov, G. Rispens, J.A. Heuver, M. Biegalski, H.M. Christen, B. Noheda, Nat Commun 5 (2014) 4415.

[161] Y.H. Chu, et al., Applied Physics Letters 90 (2007) 252906.

[162] T. Zhao, et al., Nat Mater 5 (2006) 823-829.

[163] B. Fultz, J.M. Howe, Transmission electron microscopy and diffractometry of materials, Springer, Berlin; New York, 2008.

[164] TEM schematic, http://ocw.mit.edu/courses/materials-science-and-engineering/3-225-electronic-and-mechanical-properties-of-materials-fall-2007/lecture-notes/lecture_3.pdf.

[165] T. Egami, S.J.L. Billinge, Underneath the Bragg peaks : structural analysis of complex materials, Elsevier, Amsterdam, 2012.

[166] C.T. Nelson, et al., Nano Letters 11 (2011) 828-834.

[167] Schematic of STEM, http://what-when-how.com/nanoscience-and-nanotechnology/electron-microscopy-imaging-techniques-in-environmental-and-geological-science-part-1-nanotechnology/.

[168] A.K. Yadav, et al., Nature 530 (2016) 198-201.

[169] L. Palmetshofer, in, Surface and Thin Film Analysis, Wiley-VCH Verlag GmbH & Co. KGaA, 2011, pp. 191-202.

[170] Rutherford Backscattering Spectroscopy, Springer Berlin Heidelberg, Berlin, Heidelberg, 2007.

[171] C. Jeynes, N.P. Barradas, P.K. Marriott, G. Boudreault, M. Jenkin, E. Wendler, R.P. Webb, Journal of Physics D: Applied Physics 36 (2003) R97.

[172] L.C. Feldman, J.M. Poate, Annual Review of Materials Science 12 (1982) 149-176.

[173] W. Savin, L.C. Feldman, Nuclear Instruments and Methods in Physics Research Section B: Beam Interactions with Materials and Atoms 45 (1990) 417-419.

[174] J.H. Seol, et al., Science 328 (2010) 213-216.

[175] C.A. Heusch, H.G. Moser, A. Kholodenko, Nuclear Instruments and Methods in Physics Research Section A: Accelerators, Spectrometers, Detectors and Associated Equipment 480 (2002) 463-469.

[176] J.M. Corsan, in: K.D. Maglić, A. Cezairliyan, V.E. Peletsky (Eds.), Compendium of Thermophysical Property Measurement Methods: Volume 2 Recommended Measurement Techniques and Practices, Springer US, Boston, MA, 1992, pp. 3-31.

[177] L. Lu, W. Yi, D.L. Zhang, Review of Scientific Instruments 72 (2001) 2996-3003.

[178] S. David, Measurement Science and Technology 12 (2001) R89.

[179] A.J. Schmidt, R. Cheaito, M. Chiesa, Review of Scientific Instruments 80 (2009) 094901.

[180] A.S. Iyengar, A.R. Abramson, Journal of Heat Transfer 131 (2009) 064502-064502.

[181] S. Alvarado, E. Marín, A.G. Juárez, A. Calderón, R. Ivanov, European Journal of Physics 33 (2012) 897.

[182] A.J. Schmidt, X. Chen, G. Chen, Review of Scientific Instruments 79 (2008) 114902.

[183] R. Merlin, K. Bajema, R. Clarke, F.Y. Juang, P.K. Bhattacharya, Physical Review Letters 55 (1985) 1768-1770.

[184] D.-W. Oh, et al., Applied Physics Letters 98 (2011) 221904.

[185] Y.K. Koh, S.L. Singer, W. Kim, J.M.O. Zide, H. Lu, D.G. Cahill, A. Majumdar, A.C. Gossard, Journal of Applied Physics 105 (2009) 054303.

[186] D.G. Cahill, F. Watanabe, Physical Review B 70 (2004) 235322.

[187] M.S. Aubain, P.R. Bandaru, Journal of Applied Physics 110 (2011) 084313.

[188] A. Giri, J.-P. Niemelä, C.J. Szwejkowski, M. Karppinen, P.E. Hopkins, Physical Review B 93 (2016) 024201.

[189] R.B. Wilson, B.A. Apgar, W.-P. Hsieh, L.W. Martin, D.G. Cahill, Physical Review B 91 (2015) 115414.

[190] D.G. Cahill, et al., Applied Physics Reviews 1 (2014) 011305.

[191] Y. Wang, J.Y. Park, Y.K. Koh, D.G. Cahill, Journal of Applied Physics 108 (2010) 043507.

[192] R.B. Wilson, B.A. Apgar, L.W. Martin, D.G. Cahill, Optics Express 20 (2012) 28829-28838.

[193] B.M. Foley, C.S. Gorham, J.C. Duda, R. Cheaito, C.J. Szwejkowski, C. Constantin, B. Kaehr, P.E. Hopkins, The Journal of Physical Chemistry Letters 5 (2014) 1077-1082.

[194] E. Bozorg-Grayeli, Z. Li, M. Asheghi, G. Delgado, A. Pokrovsky, M. Panzer, D. Wack, K.E. Goodson, Applied Physics Letters 99 (2011) 261906.

[195] W.-P. Hsieh, A.S. Lyons, E. Pop, P. Keblinski, D.G. Cahill, Physical Review B 84 (2011) 184107.

[196] J. Heidmann, Metrology for contactless measurement of electrical resistance change in magnetoresistive samples, Google Patents, 2013.

[197] Z. Guo, A. Verma, X. Wu, F. Sun, A. Hickman, T. Masui, A. Kuramata, M. Higashiwaki, D. Jena, T. Luo, Applied Physics Letters 106 (2015) 111909.

[198] Y.K. Koh, M.-H. Bae, D.G. Cahill, E. Pop, Nano Letters 10 (2010) 4363-4368.

[199] L. Shi, Nanoscale and Microscale Thermophysical Engineering 16 (2012) 79-116.

[200] J.-C. Zhao, X. Zheng, D.G. Cahill, Scripta Materialia 66 (2012) 935-938.

[201] H.-S. Yang, G.R. Bai, L.J. Thompson, J.A. Eastman, Acta Materialia 50 (2002) 2309-2317.

[202] S. Huxtable, D.G. Cahill, V. Fauconnier, J.O. White, J.-C. Zhao, Nat Mater 3 (2004) 298-301.

[203] C. Monachon, L. Weber, Emerging Materials Research 1 (2012) 89-98.

[204] X. Wang, C.D. Liman, N.D. Treat, M.L. Chabinyc, D.G. Cahill, Physical Review B 88 (2013) 075310.

[205] C. Chiritescu, D.G. Cahill, N. Nguyen, D. Johnson, A. Bodapati, P. Keblinski, P. Zschack, Science 315 (2007) 351-353.

[206] Soft X-rays Sychrotron source, https://www-als.lbl.gov/index.php/about-the-als/quick-facts.html.

[207] E.J. Nordgren, S.M. Butorin, L.-C. Duda, J.-H. Guo, SOFT X-RAY EMISSION AND RESONANT INELASTIC X-RAY SCATTERING SPECTROSCOPY, Springer US, Boston, MA, 2006.

[208] J. Guo, in, X-Rays in Nanoscience, Wiley-VCH Verlag GmbH & Co. KGaA, 2010, pp. 211-254.

[209] J. Fink, E. Schierle, E. Weschke, J. Geck, Reports on Progress in Physics 76 (2013) 056502.

[210] H. Li, Synthesis of CMR manganites and ordering phenomena in complex transition metal oxides, 2008.

[211] E. Arenholz, G. van der Laan, A. Fraile-Rodríguez, P. Yu, Q. He, R. Ramesh, Physical Review B 82 (2010) 140103.

[212] D. Yi, J. Liu, S. Okamoto, S. Jagannatha, Y.-C. Chen, P. Yu, Y.-H. Chu, E. Arenholz, R. Ramesh, Physical Review Letters 111 (2013) 127601.

[213] N. Reyren, et al., Science 317 (2007) 1196-1199.

[214] J. Chakhalian, J.W. Freeland, H.U. Habermeier, G. Cristiani, G. Khaliullin, M. van Veenendaal, B. Keimer, Science 318 (2007) 1114-1117.

[215] P. Van der Heide, X-ray photoelectron spectroscopy an introduction to principles and practices, Wiley-Blackwell, Hoboken, N.J., 2012.

[216] W. Zhang, Angle-Resolved Photoemission Spectroscopy, Springer Berlin Heidelberg, Berlin, Heidelberg, 2013.

[217] A. Frano, The Technique: Resonant X-ray Scattering, Springer International Publishing, Cham, 2014.

[218] S.C.B. Mannsfeld, Nat Mater 11 (2012) 489-490.

[219] R. Comin, A. Damascelli, Annual Review of Condensed Matter Physics 7 (2016) 369-405.

[220] Y. Murakami, Synchrotron Radiation News 17 (2004) 22-27.

[221] J.P. Goff, R.S. Sarthour, D.F. McMorrow, F. Yakhou, A. Stunault, A. Vigliante, R.C.C. Ward, M.R. Wells, Journal of Physics: Condensed Matter 11 (1999) L139.

[222] Schematic of X-ray Absorption Spectroscopy, http://cheiron2008.spring8.or.jp/lec_text/Oct.3/2008_Dj_J.Huang.pdf.

[223] B.A. Collins, et al., Nat Mater 11 (2012) 536-543.

[224] J.T. Heron, et al., Nature 516 (2014) 370-373.

[225] A. Bhattacharya, S.J. May, Annual Review of Materials Research 44 (2014) 65-90.

[226] G. Chen, Nanoscale energy transport and conversion : a parallel treatment of electrons, molecules, phonons, and photons, Oxford University Press, Oxford, 2005.

[227] G.P. Srivastava, Lattice Thermal Conduction Mechanism in Solids, Springer New York, New York, NY, 2006.

[228] D.T. Morelli, G.A. Slack, High Lattice Thermal Conductivity Solids, Springer New York, New York, NY, 2006.

[229] I. Lake Shore Cryotronics, Range of thermal conductivity in materials, http://www.physics.udel.edu/~nowak/phys646/serial/serial.html.

[230] Electronic conductivity in materials, http://www.britannica.com/science/electrical-conductivity.

[231] A.S. Shanmuga, Velraj, R., Thermal Science 12 (2008) 5-26.

[232] G. Jiang, L. Diao, K. Kuang, in: G. Jiang, L. Diao, K. Kuang (Eds.), Advanced Thermal Management Materials, Springer New York, New York, NY, 2013, pp. 1-10.

[233] K. Jones, Mitra, A., Ramsey, J., SAE Technical Paper (2004) 13.

[234] J. Wilson, Thermal Issues in GaAs Analog RF Devices, http://www.electronics-cooling.com/2002/02/thermal-issues-in-gaas-analog-rf-devices/, 2002.

[235] S.C. Lin, K. Banerjee, IEEE Transactions on Electron Devices 55 (2008) 245-255.

[236] L.L.N. Laboratory, US Energy Demand and Supply Chart Flow, https://flowcharts.llnl.gov/content/energy/energy_archive/energy_flow_2011/LLNLUSEnergy2011.png, 2012.

[237] G.J. Snyder, E.S. Toberer, Nat Mater 7 (2008) 105-114.

[238] C.J. Vineis, A. Shakouri, A. Majumdar, M.G. Kanatzidis, Advanced Materials 22 (2010) 3970-3980.

[239] W. Kim, Journal of Materials Chemistry C 3 (2015) 10336-10348.

[240] H. Alam, S. Ramakrishna, Nano Energy 2 (2013) 190-212.

[241] G. Chen, M.S. Dresselhaus, G. Dresselhaus, J.P. Fleurial, T. Caillat, International Materials Reviews 48 (2003) 45-66.

[242] J.R. Sootsman, D.Y. Chung, M.G. Kanatzidis, Angewandte Chemie International Edition 48 (2009) 8616-8639.

[243] K. Biswas, J. He, I.D. Blum, C.-I. Wu, T.P. Hogan, D.N. Seidman, V.P. Dravid, M.G. Kanatzidis, Nature 489 (2012) 414-418.

[244] P. Norouzzadeh, C.W. Myles, D. Vashaee, Scientific Reports 4 (2014) 7028.

[245] N.P. Padture, M. Gell, E.H. Jordan, Science 296 (2002) 280-284.

[246] D.R. Clarke, M. Oechsner, N.P. Padture, MRS Bulletin 37 (2012) 891-898.

[247] G. Chen, International Journal of Thermal Sciences 39 (2000) 471-480.

[248] D.G. Cahill, K. Goodson, A. Majumdar, Journal of Heat Transfer 124 (2002) 223.

[249] K. Schwab, E.A. Henriksen, J.M. Worlock, M.L. Roukes, Nature 404 (2000) 974-977.

[250] W. Lee, K. Kim, W. Jeong, L.A. Zotti, F. Pauly, J.C. Cuevas, P. Reddy, Nature 498 (2013) 209-212.

[251] J. Ma, et al., Nat Nanotechnol 8 (2013) 445-51.

[252] R.M. Costescu, D.G. Cahill, F.H. Fabreguette, Z.A. Sechrist, S.M. George, Science 303 (2004) 989-990.

[253] A.I. Hochbaum, R. Chen, R.D. Delgado, W. Liang, E.C. Garnett, M. Najarian, A. Majumdar, P. Yang, Nature 451 (2008) 163-7.

[254] S. Berber, Y.-K. Kwon, D. Tománek, Physical Review Letters 84 (2000) 4613-4616.

[255] P. Kim, L. Shi, A. Majumdar, P.L. McEuen, Physical Review Letters 87 (2001) 215502.

[256] A.A. Balandin, S. Ghosh, W. Bao, I. Calizo, D. Teweldebrhan, F. Miao, C.N. Lau, Nano Letters 8 (2008) 902-907.

[257] D.G. Cahill, W.K. Ford, K.E. Goodson, G.D. Mahan, A. Majumdar, H.J. Maris, R. Merlin, S.R. Phillpot, Journal of Applied Physics 93 (2003) 793.

[258] W. Kim, R. Wang, A. Majumdar, Nano Today 2 (2007) 40-47.

[259] C. Kittel, Introduction to solid state physics, Wiley, New York, 1966.

[260] M. Maldovan, Nat Mater 14 (2015) 667-674.

[261] A. Frachioni, B. White, MRS Proceedings 1404 (2012).

[262] W. Kim, J. Zide, A. Gossard, D. Klenov, S. Stemmer, A. Shakouri, A. Majumdar, Physical Review Letters 96 (2006).

[263] G. Pernot, et al., Nat Mater 9 (2010) 491-5.

[264] D.L. Nika, E.P. Pokatilov, A.A. Balandin, V.M. Fomin, A. Rastelli, O.G. Schmidt, Physical Review B 84 (2011) 165415.

[265] M. Bachmann, M. Czerner, C. Heiliger, Semiconductor Science and Technology 29 (2014) 124008.

[266] C.J. Glassbrenner, G.A. Slack, Physical Review 134 (1964) A1058-A1069.

[267] G. Chen, Journal of Heat Transfer 119 (1997) 220-229.

[268] G. Chen, Journal of Nanoparticle Research 2 199-204.

[269] K.E. Wilkes, R.B. Dinwiddie, R.S. Graves, C. International Thermal Conductivity, Thermal conductivity 23, Technomic Pub., Lancaster, Pa.

[270] K. Termentzidis, P. Chantrenne, P. Keblinski, Physical Review B 79 (2009) 214307.

[271] P. Hyldgaard, G.D. Mahan, Physical Review B 56 (1997) 10754-10757.

[272] G.D. Mahan, Physical Review B 83 (2011).

[273] G. Chen, Physical Review B 57 (1998) 14958-14973.

[274] M.V. Simkin, G.D. Mahan, Physical Review Letters 84 (2000) 927-930.

[275] Y. Chen, D. Li, J.R. Lukes, Z. Ni, M. Chen, Physical Review B 72 (2005) 174302.

[276] J. Garg, G. Chen, Physical Review B 87 (2013) 140302.

[277] G. Chen, M. Neagu, Applied Physics Letters 71 (1997) 2761-2763.

[278] S.-i. Tamura, Y. Tanaka, H.J. Maris, Physical Review B 60 (1999) 2627-2630.

[279] W.S. Capinski, H.J. Maris, Physica B: Condensed Matter 219–220 (1996) 699-701.

[280] W.S. Capinski, H.J. Maris, T. Ruf, M. Cardona, K. Ploog, D.S. Katzer, Physical Review B 59 (1999) 8105-8113.

[281] T. Borca-Tasciuc, et al., Superlattices and Microstructures 28 (2000) 199-206.

[282] M.N. Touzelbaev, P. Zhou, R. Venkatasubramanian, K.E. Goodson, Journal of Applied Physics 90 (2001) 763-767.

[283] Y.K. Koh, Y. Cao, D.G. Cahill, D. Jena, Advanced Functional Materials 19 (2009) 610-615.

[284] H.K. Lipsanen, V.M. Airaksinen, Journal of Electronic Materials 23 465-470.

[285] U. Schmid, N.E. Christensen, M. Cardona, F. Luke, K. Ploog, Physical Review B 45 (1992) 3546-3551.

[286] B. Samson, T. Dumelow, A.A. Hamilton, T.J. Parker, S.R.P. Smith, D.R. Tilley, C.T. Foxon, D. Hilton, K.J. Moore, Physical Review B 46 (1992) 2375-2392.

[287] Z.V. Popović, M. Cardona, E. Richter, D. Strauch, L. Tapfer, K. Ploog, Physical Review B 41 (1990) 5904-5913.

[288] Y. Hsu, W.I. Wang, T.S. Kuan, Physical Review B 50 (1994) 4973-4975.

[289] J. Ravichandran, et al., Nat Mater 13 (2014) 168-172.

[290] J.C. Jiang, X.Q. Pan, W. Tian, C.D. Theis, D.G. Schlom, Applied Physics Letters 74 (1999) 2851-2853.

[291] Y. Ezzahri, S. Grauby, J.M. Rampnoux, H. Michel, G. Pernot, W. Claeys, S. Dilhaire, C. Rossignol, G. Zeng, A. Shakouri, Physical Review B 75 (2007).

[292] R.P. Beardsley, P.M. Walker, A.J. Kent, M. Henini, Journal of Physics: Conference Series 92 (2007) 012014.

[293] T. Kohmoto, K. Tada, T. Moriyasu, Y. Fukuda, Physical Review B 74 (2006) 064303.

[294] C. Thomsen, J. Strait, Z. Vardeny, H.J. Maris, J. Tauc, J.J. Hauser, Physical Review Letters 53 (1984) 989-992.

[295] A. Biswas, P.B. Rossen, C.-H. Yang, W. Siemons, M.-H. Jung, I.K. Yang, R. Ramesh, Y.H. Jeong, Applied Physics Letters 98 (2011) 051904.

[296] A. Soukiassian, et al., Journal of Materials Research 23 (2008) 1417-1432.

[297] B.F. Lewis, T.C. Lee, F.J. Grunthaner, A. Madhukar, R. Fernandez, J. Maserjian, Journal of Vacuum Science & Technology B 2 (1984) 419-424.

[298] O. Auciello, A.R. Krauss, In situ real time characterization of thin films / edited by Orlando Auciello, Alan R. Krauss, Wiley, New York, 2001.

[299] J.E. Kleibeuker, et al., Advanced Functional Materials 20 (2010) 3490-3496.

[300] B. Yang, G. Chen, Physical Review B 67 (2003) 195311.

[301] P.E. Hopkins, J.R. Serrano, L.M. Phinney, S.P. Kearney, T.W. Grasser, C.T. Harris, Journal of Heat Transfer 132 (2010) 081302-081302.

[302] R. Cheaito, J.C. Duda, T.E. Beechem, K. Hattar, J.F. Ihlefeld, D.L. Medlin, M.A. Rodriguez, M.J. Campion, E.S. Piekos, P.E. Hopkins, Physical Review Letters 109 (2012) 195901.

[303] M.G. Holland, Physical Review 134 (1964) A471-A480.

[304] A.G. Beattie, G.A. Samara, Journal of Applied Physics 42 (1971) 2376-2381.

[305] A.I. Lebedev, Ab initio calculations of phonon spectra in ATiO3 perovskite crystals (A = Ca, Sr, Ba, Ra, Cd, Zn, Mg, Ge, Sn, Pb), 2009.

[306] R. Wang, Zhou, J., Sun, C., Kang, L., Zhao, Q., Sun, J., Progress In Electromagnetics Research Letters 10 (2009) 145-155.

[307] in: O. Madelung, U. Rössler, M. Schulz (Eds.), Ternary Compounds, Organic Semiconductors, Springer Berlin Heidelberg, Berlin, Heidelberg, 2000, pp. 1-12.

[308] M.I. Flik, C.L. Tien, Journal of Heat Transfer 112 (1990) 872-881.

[309] A.J. Griffin, F.R. Brotzen, P.J. Loos, Journal of Applied Physics 75 (1994) 3761-3764.

[310] E.S. Landry, M.I. Hussein, A.J.H. McGaughey, Physical Review B 77 (2008) 184302.

[311] S. Tamura, F. Nori, Physical Review B 40 (1989) 9790-9801.

[312] S.-i. Tamura, F. Nori, Physical Review B 41 (1990) 7941-7944.

[313] N. Nishiguchi, S.-i. Tamura, F. Nori, Physical Review B 48 (1993) 2515-2528.

[314] P.K. Schelling, S.R. Phillpot, P. Keblinski, Physical Review B 65 (2002) 144306.

[315] Y. Wang, H. Huang, X. Ruan, Physical Review B 90 (2014).

[316] B. Latour, S. Volz, Y. Chalopin, Physical Review B 90 (2014).

[317] M.N. Luckyanova, et al., Science 338 (2012) 936-9.

[318] J.J. Freeman, A.C. Anderson, Physical Review B 34 (1986) 5684-5690.

[319] R. Biswas, A.M. Bouchard, W.A. Kamitakahara, G.S. Grest, C.M. Soukoulis, Physical Review Letters 60 (1988) 2280-2283.

[320] L.D. Van Ee, B.J. Thijsse, J. Sietsma, Journal of Non-Crystalline Solids 205–207, Part 2 (1996) 641-644.

[321] J.E. Graebner, B. Golding, L.C. Allen, Physical Review B 34 (1986) 5696-5701.

[322] D.H.A.L. Anselmo, A.L. Dantas, S.K. Medeiros, E.L. Albuquerque, V.N. Freire, Physica A: Statistical Mechanics and its Applications 349 (2005) 259-270.

[323] A. Frachioni, B.E. White, Journal of Applied Physics 112 (2012) 014320.

[324] Y. Wang, C. Gu, X. Ruan, Applied Physics Letters 106 (2015) 073104.

[325] C.W. Chang, D. Okawa, H. Garcia, A. Majumdar, A. Zettl, Physical Review Letters 99 (2007) 045901.

[326] J. Valasek, Physical Review 17 (1921) 475-481.

[327] M.E. Lines, A.M. Glass, Principles and Applications of Ferroelectrics and Related Materials, Oxford University Press, Oxford, 2001.

[328] A.F. Devonshire, The London, Edinburgh, and Dublin Philosophical Magazine and Journal of Science 40 (1949) 1040-1063.

[329] C.R. Bowen, H.A. Kim, P.M. Weaver, S. Dunn, Energy & Environmental Science 7 (2014) 25-44.

[330] J.F. Scott, Science 315 (2007) 954-959.

[331] J.D. Jain, IETE Technical Review 5 (1988) 351-382.

[332] H. Takasu, Journal of Electroceramics 4 327-338.

[333] D.-W. Fu, et al., Science 339 (2013) 425-428.

[334] S. Trolier-McKinstry, P. Muralt, Journal of Electroceramics 12 7-17.

[335] M. Kraft, M. Jakusch, M. Karlowatz, A. Katzir, B. Mizaikoff, Applied Spectroscopy 57 (2003) 591-599.

[336] S. Herbert, Manually operable piezoelectric gas igniter, Google Patents, 1971.

[337] H. Banno, Ferroelectrics 50 (1983) 3-12.

[338] R. Watton, Ferroelectrics 91 (1989) 87-108.

[339] R.W. Whatmore, A. Patel, N.M. Shorrocks, F.W. Ainger, Ferroelectrics 104 (1990) 269-283.

[340] R.W. Whatmore, P.C. Osbond, N.M. Shorrocks, Ferroelectrics 76 (1987) 351-367.

[341] L.H. Parker, A.F. Tasch, IEEE Circuits and Devices Magazine 6 (1990) 17-26.

[342] A.K. Tagantsev, V.O. Sherman, K.F. Astafiev, J. Venkatesh, N. Setter, Journal of Electroceramics 11 5-66.

[343] R. Babbitt, T. Koscica, W. Drach, L. Didomenico, Integrated Ferroelectrics 8 (1995) 65-76.

[344] S. Chen, D.F. DiFonzo, E.P. Ekelman, Phased array antennas incorporating voltage-tunable phase shifters, Google Patents, 2003.

[345] M. Roth, M. Tseitlin, N. Angert, Glass Physics and Chemistry 31 86-95.

[346] H. Jiang, Y.K. Zou, Q. Chen, K.K. Li, R. Zhang, Y. Wang, H. Ming, Z. Zheng, Transparent electro-optic ceramics and devices, 2005, 380-394.

[347] L. Hesselink, S.S. Orlov, A. Liu, A. Akella, D. Lande, R.R. Neurgaonkar, Science 282 (1998) 1089-1094.

[348] J.P. Wilde, Utilization of ferroelectric domain screening for high capacity holographic memory, Google Patents, 1998.

[349] O. Auciello, Scott, J. F., R. Ramesh, Physics Today 51 (1998) 22-27.

[350] H. Takasu, Integrated Ferroelectrics 14 (1997) 1-10.

[351] R.M. Paratore, P.A. Maltseff, RFID tag having timing and environment modules, Google Patents, 2001.

[352] S. Salahuddin, S. Datta, Nano Letters 8 (2008) 405-410.

[353] J.F. Scott, ISRN Materials Science 2013 (2013) 24.

[354] C. Galassi, in, Multifunctional Polycrystalline Ferroelectric Materials: Processing and Properties, Springer Netherlands, Dordrecht, 2011, pp. 1-37.

[355] N. Setter, et al., Journal of Applied Physics 100 (2006) 051606.

[356] W.S. Yun, J.J. Urban, Q. Gu, H. Park, Nano Letters 2 (2002) 447-450.

[357] Y. Luo, I. Szafraniak, V. Nagarajan, R.B. Wehrspohn, M. Steinhart, J.H. Wendorff, N.D. Zakharov, R. Ramesh, M. Alexe, Integrated Ferroelectrics 59 (2003) 1513-1520.

[358] P. Weaver, M.G. Cain, in: G.M. Cain (Ed.), Characterisation of Ferroelectric Bulk Materials and Thin Films, Springer Netherlands, Dordrecht, 2014, pp. 115-145.

[359] D. Damjanovic, M. Budimir, M. Davis, N. Setter, in: S.B. Lang, H.L.W. Chan (Eds.), Frontiers of Ferroelectricity: A Special Issue of the Journal of Materials Science, Springer US, Boston, MA, 2007, pp. 65-76.

[360] R. Whatmore, in: G.M. Cain (Ed.), Characterisation of Ferroelectric Bulk Materials and Thin Films, Springer Netherlands, Dordrecht, 2014, pp. 65-86.

[361] K.M. Rabe, P. Ghosez, in, Physics of Ferroelectrics: A Modern Perspective, Springer Berlin Heidelberg, Berlin, Heidelberg, 2007, pp. 117-174.

[362] S. Choudhury, L.Q. Chen, Y.L. Li, Applied Physics Letters 91 (2007) 032902.

[363] R. Jiménez, B. Jiménez, in: L. Pardo, J. Ricote (Eds.), Multifunctional Polycrystalline Ferroelectric Materials: Processing and Properties, Springer Netherlands, Dordrecht, 2011, pp. 573-616.

[364] A.J. Bell, in: S.B. Lang, H.L.W. Chan (Eds.), Frontiers of Ferroelectricity: A Special Issue of the Journal of Materials Science, Springer US, Boston, MA, 2007, pp. 13-25.

[365] R.F. Service, Science 275 (1997) 1878-1878.

[366] C. Lichtensteiger, M. Dawber, J.-M. Triscone, in, Physics of Ferroelectrics: A Modern Perspective, Springer Berlin Heidelberg, Berlin, Heidelberg, 2007, pp. 305-338.

[367] C. Lichtensteiger, P. Zubko, M. Stengel, P. Aguado-Puente, J.-M. Triscone, P. Ghosez, J. Junquera, in, Oxide Ultrathin Films, Wiley-VCH Verlag GmbH & Co. KGaA, 2011, pp. 265-230.

[368] I.A. Kornev, H. Fu, L. Bellaiche, in, Frontiers of Ferroelectricity: A Special Issue of the Journal of Materials Science, Springer US, Boston, MA, 2007, pp. 137-145.

[369] S. Prosandeev, I. Ponomareva, I. Naumov, I. Kornev, L. Bellaiche, Journal of Physics: Condensed Matter 20 (2008) 193201.

[370] J.F. Scott, Annual Review of Materials Science 28 (1998) 79-100.

[371] I.I. Naumov, L. Bellaiche, H. Fu, Nature 432 (2004) 737-740.

[372] J. Wang, M. Kamlah, T.-Y. Zhang, Y. Li, L.-Q. Chen, Applied Physics Letters 92 (2008) 162905.

[373] W.J. Chen, Y. Zheng, B. Wang, Applied Physics Letters 100 (2012) 062901.

[374] Y. Nahas, S. Prokhorenko, L. Louis, Z. Gui, I. Kornev, L. Bellaiche, Nat Commun 6 (2015).

[375] J.M. Gregg, D. O'Neill, G. Catalan, R.M. Bowman, MRS Online Proceedings Library Archive 656 (2000) DD6.9 (6 pages).

[376] J.-W. Chen, H.-X. Cao, L. Fang, Current Applied Physics 11 (2011) S197-S199.

[377] W. Ma, Applied Physics A 96 (2009) 915-920.

[378] H. Fu, L. Bellaiche, Physical Review Letters 91 (2003) 257601.

[379] J.Y. Son, arXiv:1301.3293 (2013).

[380] W.J. Chen, Y. Zheng, B. Wang, J.Y. Liu, Journal of Applied Physics 115 (2014) 214106.

[381] P. Wu, X. Ma, Y. Li, V. Gopalan, L.-Q. Chen, Applied Physics Letters 100 (2012) 092905.

[382] J.F. Scott, C.A. Paz de Araujo, Science 246 (1989) 1400-1405.

[383] S. Prosandeev, L. Bellaiche, Physical Review B 75 (2007) 094102.

[384] F. Peter, Piezoresponse force microscopy and surface effects of perovskite ferroelectric nanostructures, Techn. Hochsch. Aachen, PUB:(DE-HGF)11 ; PUB:(DE-HGF)3, 2006.

[385] J. Guyonnet, in, Ferroelectric Domain Walls: Statics, Dynamics, and Functionalities Revealed by Atomic Force Microscopy, Springer International Publishing, Cham, 2014, pp. 7-24.

[386] G. Geneste, E. Bousquet, P. Ghosez, Journal of Computational and Theoretical Nanoscience 5 (2008) 517-520.

[387] G. Ph, X. Gonze, J.P. Michenaud, EPL (Europhysics Letters) 33 (1996) 713.

[388] K.M. Rabe, M. Dawber, C. Lichtensteiger, C.H. Ahn, J.-M. Triscone, in, Physics of Ferroelectrics: A Modern Perspective, Springer Berlin Heidelberg, Berlin, Heidelberg, 2007, pp. 1-30.

[389] W. Cochran, Physical Review Letters 3 (1959) 412-414.

[390] A.A. Sirenko, C. Bernhard, A. Golnik, A.M. Clark, J. Hao, W. Si, X.X. Xi, Nature 404 (2000) 373-376.

[391] P.M. Gehring, S. Wakimoto, Z.G. Ye, G. Shirane, Physical Review Letters 87 (2001) 277601.

[392] F. Yen, C. dela Cruz, B. Lorenz, E. Galstyan, Y.Y. Sun, M. Gospodinov, C.W. Chu, Journal of Materials Research 22 (2007) 2163-2173.

[393] B.B. Van Aken, T.T.M. Palstra, A. Filippetti, N.A. Spaldin, Nat Mater 3 (2004) 164-170.

[394] N. Ikeda, R. Mori, K. Kohn, M. Mizumaki, T. Akao, Ferroelectrics 272 (2002) 309-314.

[395] N.J. Perks, R.D. Johnson, C. Martin, L.C. Chapon, P.G. Radaelli, Nat Commun 3 (2012) 1277.

[396] J.H. Kim, et al., Physical Review B 78 (2008) 245115.

[397] Y. Koyata, K. Kohn, Ferroelectrics 204 (1997) 115-124.

[398] T. Aoyama, K. Yamauchi, A. Iyama, S. Picozzi, K. Shimizu, T. Kimura, Nat Commun 5 (2014).

[399] V. Dvořák, Ferroelectrics 7 (1974) 1-9.

[400] M.G. Cain, M. Stewart, in: G.M. Cain (Ed.), Characterisation of Ferroelectric Bulk Materials and Thin Films, Springer Netherlands, Dordrecht, 2014, pp. 15-35.

[401] S. Anteboth, A. Brückner-Foit, M.J. Hoffmann, U. Sutter, T. Schimmel, M. Müller, Computational Materials Science 41 (2008) 420-429.

[402] J.S. Liu, S.R. Zhang, H.Z. Zeng, C.T. Yang, Y. Yuan, Physical Review B 72 (2005) 172101.

[403] Y.-H. Shin, I. Grinberg, I.W. Chen, A.M. Rappe, Nature 449 (2007) 881-884.

[404] R.P. Potnis, N.-T. Tsou, E.J. Huber, Materials 4 (2011).

[405] J. Seidel, et al., Nat Mater 8 (2009) 229-234.

[406] D.D. Fong, G.B. Stephenson, S.K. Streiffer, J.A. Eastman, O. Auciello, P.H. Fuoss, C. Thompson, Science 304 (2004) 1650-1653.

[407] N.A. Spaldin, Science 304 (2004) 1606-1607.

[408] M. Stengel, N.A. Spaldin, Nature 443 (2006) 679-682.

[409] I.A. Kornev, L. Bellaiche, P. Bouvier, P.E. Janolin, B. Dkhil, J. Kreisel, Physical Review Letters 95 (2005) 196804.

[410] G.A. Samara, Ferroelectrics 2 (1971) 277-289.

[411] N.A. Pertsev, A.G. Zembilgotov, A.K. Tagantsev, Physical Review Letters 80 (1998) 1988-1991.

[412] D.A. Tenne, et al., Physical Review B 69 (2004) 174101.

[413] Q.Y. Qiu, V. Nagarajan, S.P. Alpay, Physical Review B 78 (2008) 064117.

[414] Y.L. Li, S.Y. Hu, Z.K. Liu, L.Q. Chen, Acta Materialia 50 (2002) 395-411.

[415] J.H. Haeni, et al., Nature 430 (2004) 758-761.

[416] K.J. Choi, et al., Science 306 (2004) 1005-1009.

[417] M. Ezawa, Physical Review B 83 (2011) 100408.

[418] N. Nagaosa, Y. Tokura, Nat Nano 8 (2013) 899-911.

[419] M. Stengel, N.A. Spaldin, D. Vanderbilt, Nat Phys 5 (2009) 304-308.

[420] W. Zhong, D. Vanderbilt, K.M. Rabe, Physical Review B 52 (1995) 6301-6312.

[421] L.-Q. Chen, Annual Review of Materials Research 32 (2002) 113-140.

[422] Z. Gui, L.-W. Wang, L. Bellaiche, Nano Letters 15 (2015) 3224-3229.

[423] I. Kornev, H. Fu, L. Bellaiche, Physical Review Letters 93 (2004).

[424] S. Prosandeev, I. Ponomareva, I. Kornev, I. Naumov, L. Bellaiche, Physical Review Letters 96 (2006) 237601.

[425] D. Sichuga, L. Bellaiche, Physical Review Letters 106 (2011).

[426] D. Sichuga, W. Ren, S. Prosandeev, L. Bellaiche, Physical Review Letters 104 (2010).

[427] L. Baudry, A. Sené, I.A. Luk'yanchuk, L. Lahoche, J.F. Scott, Physical Review B 90 (2014) 024102.

[428] L. Hong, Y. Li, P. Wu, L.-Q. Chen, Journal of Applied Physics 114 (2013) 144103.

[429] K. Kathan-Galipeau, P. Wu, Y. Li, L.-Q. Chen, A. Soukiassian, X. Xi, D.G. Schlom, D.A. Bonnell, ACS Nano 5 (2011) 640-646.

[430] Y. Nahas, S. Prokhorenko, L. Louis, Z. Gui, I. Kornev, L. Bellaiche, Nat Commun 6 (2015) 8542.

[431] P. Aguado-Puente, J. Junquera, Physical Review B 85 (2012) 184105.

[432] M. Anoufa, J.M. Kiat, I. Kornev, C. Bogicevic, Physical Review B 88 (2013) 144106.

[433] N.D. Mermin, H. Wagner, Physical Review Letters 17 (1966) 1133-1136.

[434] I.P. Batra, P. Wurfel, B.D. Silverman, Physical Review Letters 30 (1973) 384-387.

[435] G. Sheng, J.M. Hu, J.X. Zhang, Y.L. Li, Z.K. Liu, L.Q. Chen, Acta Materialia 60 (2012) 3296-3301.

[436] B. Winchester, P. Wu, L.Q. Chen, Applied Physics Letters 99 (2011) 052903.

[437] K. Kathan-Galipeau, P.P. Wu, Y.L. Li, L.Q. Chen, A. Soukiassian, Y. Zhu, D.A. Muller, X.X. Xi, D.G. Schlom, D.A. Bonnell, Journal of Applied Physics 112 (2012) 052011.

[438] L.-Q. Chen, Journal of the American Ceramic Society 91 (2008) 1835-1844.

[439] G. Catalan, A. Lubk, A.H.G. Vlooswijk, E. Snoeck, C. Magen, A. Janssens, G. Rispens, G. Rijnders, D.H.A. Blank, B. Noheda, Nat Mater 10 (2011) 963-967.

[440] Y.L. Tang, et al., Science 348 (2015) 547-551.

[441] C.-L. Jia, K.W. Urban, M. Alexe, D. Hesse, I. Vrejoiu, Science 331 (2011) 1420-1423.

[442] Y. Ivry, D.P. Chu, J.F. Scott, C. Durkan, Physical Review Letters 104 (2010).

[443] A. Gruverman, D. Wu, H.J. Fan, I. Vrejoiu, M. Alexe, R.J. Harrison, J.F. Scott, Journal of Physics: Condensed Matter 20 (2008) 342201.

[444] R.G. McQuaid, A. Gruverman, J.F. Scott, J.M. Gregg, Nano Lett 14 (2014) 4230-7.

[445] C. Kittel, Physical Review 70 (1946) 965-971.

[446] L.W. Chang, V. Nagarajan, J.F. Scott, J.M. Gregg, Nano Letters 13 (2013) 2553-2557.

[447] T. Shimada, S. Tomoda, T. Kitamura, Physical Review B 81 (2010) 144116.

[448] G. Catalan, J.F. Scott, A. Schilling, J.M. Gregg, Journal of Physics: Condensed Matter 19 (2007) 022201.

[449] I.B. Misirlioglu, A.L. Vasiliev, S.P. Alpay, M. Aindow, R. Ramesh, Journal of Materials Science 41 697-707.

[450] G.L. Yu, J.L. Zhu, Q.L. Zhang, J.Z. Tan, Y.F. Tian, J.G. Zhu, D.Q. Xiao, Integrated Ferroelectrics 78 (2006) 93-101.

[451] J.X. Zhang, J.Y. Dai, W. Lu, H.L.W. Chan, B. Wu, D.X. Li, Journal of Physics D: Applied Physics 41 (2008) 235405.

[452] S. Roy, A. Solmaz, J.D. Burton, M. Huijben, G. Rijnders, E.Y. Tsymbal, T. Banerjee, Physical Review B 93 (2016) 115101.

[453] L. Aballe, S. Matencio, M. Foerster, E. Barrena, F. Sánchez, J. Fontcuberta, C. Ocal, Chemistry of Materials 27 (2015) 6198-6204.

[454] G. Koster, L. Klein, W. Siemons, G. Rijnders, J.S. Dodge, C.-B. Eom, D.H.A. Blank, M.R. Beasley, Reviews of Modern Physics 84 (2012) 253-298.

[455] A. Schilling, D. Byrne, G. Catalan, K.G. Webber, Y.A. Genenko, G.S. Wu, J.F. Scott, J.M. Gregg, Nano Letters 9 (2009) 3359-3364.

[456] Y. Saito, H. Takao, T. Tani, T. Nonoyama, K. Takatori, T. Homma, T. Nagaya, M. Nakamura, Nature 432 (2004) 84-87.

[457] Y.C. Shu, K. Bhattacharya, Philosophical Magazine Part B 81 (2001) 2021-2054.

[458] D. Dragan, Reports on Progress in Physics 61 (1998) 1267.

[459] S.B. Ren, C.J. Lu, J.S. Liu, H.M. Shen, Y.N. Wang, Physical Review B 54 (1996) R14337-R14340.

[460] M. Dawber, C. Lichtensteiger, M. Cantoni, M. Veithen, P. Ghosez, K. Johnston, K.M. Rabe, J.M. Triscone, Physical Review Letters 95 (2005).

[461] L. Goncalves-Ferreira, S.A.T. Redfern, E. Artacho, E.K.H. Salje, Physical Review Letters 101 (2008) 097602.

[462] E. Salje, H. Zhang, Phase Transitions 82 (2009) 452-469.

[463] A.L. Roitburd, physica status solidi (a) 37 (1976) 329-339.

[464] T. Mitsui, J. Furuichi, Physical Review 90 (1953) 193-202.

[465] S. Prosandeev, S. Lisenkov, L. Bellaiche, Physical Review Letters 105 (2010) 147603.

[466] S.K. Streiffer, J.A. Eastman, D.D. Fong, C. Thompson, A. Munkholm, M.V. Ramana Murty, O. Auciello, G.R. Bai, G.B. Stephenson, Physical Review Letters 89 (2002) 067601.

[467] N.A. Pertsev, A.G. Zembilgotov, Journal of Applied Physics 78 (1995) 6170-6180.

[468] P. Marton, J. Hlinka, Ferroelectrics 373 (2008) 139-144.

[469] F. Borodavka, I. Gregora, A. Bartasyte, S. Margueron, V. Plausinaitiene, A. Abrutis, J. Hlinka, Journal of Applied Physics 113 (2013) 187216.

[470] T. Higuchi, et al., Physical Review B 78 (2008) 085106.

[471] R.V. Vedrinskii, V.L. Kraizman, A.A. Novakovich, V.D. Ph, S.V. Urazhdin, Journal of Physics: Condensed Matter 10 (1998) 9561.

[472] A.M. Mulders, S.M. Lawrence, A.J. Princep, U. Staub, Y. Bodenthin, M. García-Fernández, M. Garganourakis, J. Hester, R. Macquart, C.D. Ling, Physical Review B 81 (2010) 092405.

[473] M.E.M. Cabrera, in, Multifunctional Polycrystalline Ferroelectric Materials: Processing and Properties, Springer Netherlands, Dordrecht, 2011, pp. 281-346.

[474] K.-T. Ko, et al., Nat Commun 2 (2011) 567.

[475] V. Garcia, et al., Science 327 (2010) 1106-1110.

[476] J.X. Zhang, et al., Physical Review Letters 107 (2011) 147602.

[477] J. Jäckle, Solid State Communications 39 (1981) 1261-1263.

[478] S.G. Cloutier, R.S. Guico, J.M. Xu, Applied Physics Letters 87 (2005) 222104.

[479] J.L. Cohn, G.S. Nolas, V. Fessatidis, T.H. Metcalf, G.A. Slack, Physical Review Letters 82 (1999) 779-782.

[480] J.T. Edwards, D.J. Thouless, Journal of Physics C: Solid State Physics 5 (1972) 807.

[481] W. Zhao, et al., Nat Commun 6 (2015).

[482] S. Pailhès, H. Euchner, V.M. Giordano, R. Debord, A. Assy, S. Gomès, A. Bosak, D. Machon, S. Paschen, M. de Boissieu, Physical Review Letters 113 (2014) 025506.

[483] J.C. Li, C.L. Wang, M.X. Wang, H. Peng, R.Z. Zhang, M.L. Zhao, J. Liu, J.L. Zhang, L.M. Mei, Journal of Applied Physics 105 (2009) 043503.